Probing the Intergalactic medium properties using X-ray absorption from multiple tracers

TONY DALTON

How to cite:

DALTON, TONY (2022) Probing the Intergalactic medium properties using X-ray absorption from multiple tracers. Doctoral thesis, Durham University.

Probing the Intergalactic medium properties using X-ray absorption from multiple tracers

Tony Dalton

Supervisors:

Simon L. Morris

Chris Done

A thesis presented for the degree of

Doctor of Philosophy

Centre for Extragalactic Astronomy

The University of Durham

United Kingdom

2022

Probing the Intergalactic medium properties using X-ray absorption from multiple tracers

Tony Dalton

Abstract

Based on the Lambda Cold Dark Matter concordance cosmological model (ΛCDM), the majority of baryons exist in the Intergalactic medium (IGM). It is extremely challenging to observationally trace the IGM, especially at higher temperatures and low densities. Post reionisation, the vast majority of hydrogen and helium is ionized in the IGM and therefore, the observation of metals is essential for parametrising the IGM properties.

My hypothesis is that there is significant absorption in the diffuse highly ionisied IGM, and that this IGM column density increases with redshift. I use X-ray absorption in multiple tracers which yields information on the total absorbing column density of the matter between the observer and the source. Clear IGM detections require tracer sources that are bright, distant, and common enough to provide a good statistical sample of IGM lines of sight (LOS). To more accurately isolate any IGM contribution to spectral absorption, I examine each tracer host type to realistically model it, in addition to using appropriate intrinsic continuum curvature models. I test the robustness of the result from a number of perspectives. I examine the impact of the key underlying assumptions that affect the column density calculations including metallicity, ionisation and location of absorption. I look for any evidence of evolution in the parameters.

In Chapters 2, 3, 4 and 5, I use gamma-ray bursts (GRBs), blazars and quasars (QSOs) to estimate IGM baryon column densities, metallicity, temperature, ionisation parameters and redshift distributions. My results for each tracer are presented in each of the respective chapters and collectively in Chapter 5 which includes comparative analysis.

In conclusion, through the work in this thesis I demonstrate a consistent case for strong X-ray absorption in the IGM on the LOS to three different tracer types and that it is related to redshift. The results are consistent with the ΛCDM model for density, temperature and metallicity. Given these results, I would recommend that studies of distant objects should not follow the convention of assuming all X-ray absorption in excess of our Galaxy is attributed to the host galaxy, that the host is neutral and has solar metallicity. Instead, particularly at higher redshift, absorption in the IGM should be accounted for to give more accurate results for the tracer host properties.

Acknowledgements

I am very grateful to my primary supervisor, Simon Morris. I sent my thesis proposal to Simon in 2019, with some "requests" including doing the work remotely from Ireland. Thankfully, he agreed to take me on board and allowed me considerable freedom in pursuing this work. Simon was very generous with his time including our weekly zoom meetings from which useful insights and considerations always arose. Thanks to his support and thorough reviews, I managed to complete four journal papers as part of this thesis.

I want to thank Michele Fumagalli. Michele started as my second supervisor but soon left Durham for Milan. I was grateful and flattered when he said that he would be happy to continue as a collaborator. His deep knowledge of aspects of the IGM were very helpful, and indeed any comment of his warranted serious attention.

I want express my appreciation to my external examiner, Sergio Campana and internal examiner, Ryan Cooke who made my viva a very enjoyable and productive experience. They posed many challenging questions and gave me plenty of food for thought for future work.

Contents

Declaration

No part of this thesis has been submitted elsewhere for any other degree or qualification. It is the sole work of the author, apart from the data reduction for the *XMM-Newton* QSO and blazar spectra which was completed by Efrain Gatuzz as referenced in the relevant chapters.

The substantial part of the work presented in this thesis has been published in, or submitted to, the Monthly Notices of the Royal Astronomical Society (MNRAS) journal and reproduced in full with minor formatting changers in Chapters 2, 3, 4 and 5 as follows:

Using realistic host galaxy metallicities to improve the GRB X-ray equivalent total hydrogen column density and constrain the intergalactic medium density, Dalton, T. and Morris, S.L., 2020, MNRAS, 495(2), pp.2342-2353.

Probing the physical properties of the intergalactic medium using gamma-ray bursts, Dalton, T., Morris, S.L. and Fumagalli, M., 2021, MNRAS, 502(4), pp.5981-5996.

Probing the physical properties of the intergalactic medium using blazars, Dalton, T., Morris, S.L., Fumagalli, M. and Gatuzz, E., 2021, MNRAS, 508(2), pp.1701-1718.

Probing the parameters of the intergalactic medium using quasars, Dalton, T., Morris, S.L, ., Fumagalli, M. and Gatuzz, E., submitted to the MNRAS January, 2022. (Accepted 18 March, 2022 with some edits - see https://doi.org/10.1093/mnras/stac814)

Tony Dalton
Date February, 2022

How to cite:

DALTON, TONY (2022) Probing the Intergalactic medium properties using X-ray absorption from multiple tracers, Durham theses, Durham University. Available at Durham E-Theses Online: http://etheses.dur.ac.uk

List of Figures

List of Tables

Abbreviations

AGN Active galactic nuclei

BC Bulk Comptonisation

BL Lac BL Lacertae

BLR Broad line region

CGM Circum-galactic medium

CIB Ultra-violet and X-ray background radiation

CIE Collisional ionisation equilibrium

Cstat C-statistic based on Cash (1979)

DLA Damped lyman α system

FRB Fast Radio Burst

FSRQ Flat spectrum radio quasar

GRB Gamma-ray burst

IGM Intergalactic medium

LOS Line of sight

LSS Large scale structure

MCMC Markov chain Monte Carlo

n_0 hydrogen density at redshift zero

NHXGAL Galactic hydrogen column density

NHX Hydrogen equivelent column density

NH I Neutral hydrogen column density

NHXIGM IGM hydrogen column density

PIE Photionisation equilibrium

QSO Quasi-stellar object or quasar

T/K Temperature in Kelvin

WHIM Warm-hot intergalactic medium

$[X/\mathrm{H}]$ metallicity $= Z/Z_{\odot}$

CHAPTER 1

Introduction

This chapter sets out the overall aim, hypothesis and key objectives of the thesis. It gives a summary of the focus area of the IGM, the tracer background objects used, the instruments from which the data is drawn and the spectral analysis software used.

1.1 Thesis aims and hypothesis

Based on the ΛCDM cosmological model, the minority of the baryons reside in galaxies and inter-cluster medium (ICM), with the majority existing in the IGM, distributed in a web of tenuous sheets and filaments and the diffuse space in between (McQuinn, 2016, hereafter M16).

Highly accurate measurements of the cosmic microwave background temperature, polarization, and anisotropies from projects such as the Planck Collaboration (e.g. Planck Collaboration et al., 2020) have supported the continued preference for ΛCDM as the concordance model of cosmology, and led to the term ‘precision cosmology’ .

It is extremely challenging to trace the IGM, especially at higher temperatures and low densities with actual observational methods. There are many different direct and indirect methods to detect and observe the IGM including, but not limited

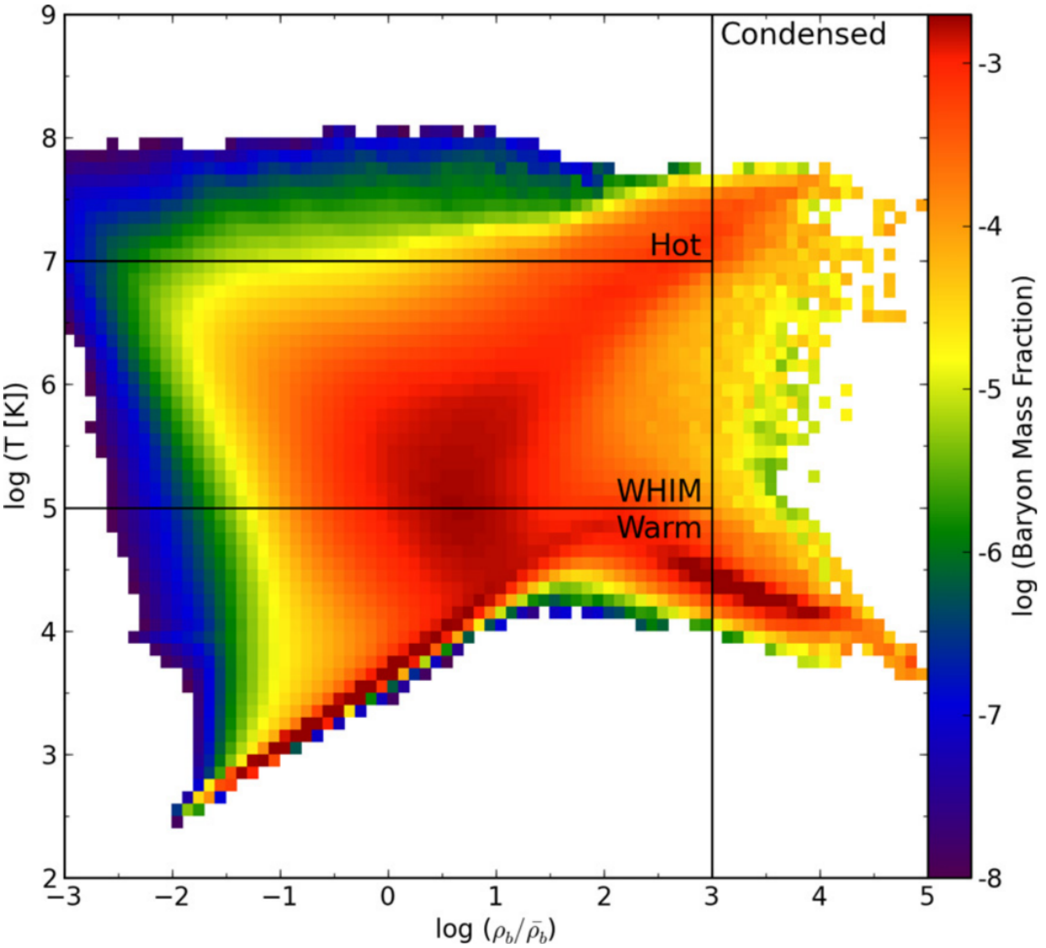

Figure 1.1: Thermal phases of the IGM for temperature (T/K) and baryon overdensity $\Delta_b = \rho_b/\overline{\rho}_b$, colour-coded by baryon mass fraction (image credit (Shull et al., 2012)

to, emission and absorption features, dispersion and rotation measures e.g. in Fast Radio Bursts, the Sunyaez-Zel'dovich effect, etc. In absorption, a very broad spectrum of energies can provide information on IGM properties. Optical /UV observations of absorption in the spectra of QSOs have provided a highly sensitive probe of the cool IGM ($\sim 10^4 T/K$) (e.g. Morris et al., 1991; York et al., 2000; Fumagalli et al., 2016). The vast majority of hydrogen is ionised in the IGM post the reionisation era $z \sim 6$, and helium by $z \sim 3.5$. Therefore, the observation of metals is essential for parametrising the IGM properties.

There are many absorption line studies of individual systems which have used the ionisation states of abundant heavy metals in optical to UV (e.g. Danforth and

Shull, 2008; Shull et al., 2012; Raghunathan et al., 2016). While these surveys have been very successful, most very highly ionised metals are not observed in optical to UV. Therefore, high-resolution X-ray observations are required as they are sensitive to a broad range of cross-sections over the full integrated line-of-sight (LOS). However, due to the resolution of current instruments, tracing individual features of the IGM metals in X-ray is very limited. Fig 1.1 shows the distribution of IGM phases for temperature (T/K) and baryon overdensity $\Delta_b = \rho_b/\overline{\rho}_b$, colour-coded by baryon mass fraction (Shull et al., 2012).

Given these circumstances, I use X-ray absorption in multiple tracers which yields information on the total absorbing column density of the matter between the observer and the source. Tracers in this sense are distant objects whose spectra are absorbed by intervening baryonic matter on the LOS. In Section 1.3, I provide a brief overview of the tracers used, which are GRBs, blazars and QSOs. Clear IGM detections require tracer sources that are bright, distant, and common enough to provide a good statistical sample of IGM lines of sight. Such tracers are the only way of directly confirming the predictions of the ΛCDM model on the IGM baryon inventory and other properties, and without such evidence it would appear premature to use the term 'precision cosmology' for baryon IGM properties.

My hypothesis is that there is significant absorption in the diffuse highly ionised IGM, and that this IGM column density increases with redshift. There is increasing evidence that the IGM shows significant metal enrichment at all redshifts and at all densities. Indeed, it is thought that a substantial fraction of metals are to be found in the IGM, with significant enrichment at high redshifts with little evidence for metal evolution (e.g. Aguirre et al., 2001; Schaye et al., 2003; Shull et al., 2012; Fumagalli, 2014; McQuinn, 2016; Peroux and Howk, 2020; Flores et al., 2021). My approach is different to most other tracer studies which are primarily focused on individual absorbers either in the tracer host or on the LOS. In this regard, the convention adopted is to typically attribute to the tracer host, any spectral hardening due to excess absorption over our Galaxy and known LOS individual absorbers (e.g Bottacini et al., 2010; Schady et al., 2011; Watson, 2011; Paliya et al., 2016; Ricci et al., 2017; Buchner et al., 2017). Instead, I focus on the possible absorption in X-ray due to the IGM using a sophisticated model for the highly ionised absorption component. Further, to more accurately isolate any IGM contribution to spectral absorption, I examine each tracer host type to realistically model it, in addition to best fit intrinsic continuum curvature models.

This thesis will use different types of tracers to estimate the key IGM properties of baryon column densities, metallicity, temperature, ionisation and redshift distributions, to determine if the tracers show consistent results that can parameterise the properties, and whether the results are consistent with or challenge the current ΛCDM concordance model in terms of baryonic matter. I examine past observations and simulations to set the parameters ranges and priors for our models. I test the robustness of the result from a number of perspectives. I examine the impact of the key underlying assumptions that affect the column density calculations including metallicity, ionisation and location of absorption. I look for any evidence of evolution in the parameters.

The structure of this thesis is as follows: In chapter 2, I isolate a more accurate estimate for the IGM contribution to column densities using GRBs as tracers, using actual or realistic GRB host metallicities, and by approximating the GRB host intrinsic hydrogen column density using the measured neutral column adjusted for the ionisation fraction. In chapter 3, I use GRB spectra to estimate the key IGM properties of hydrogen column density, metallicity, temperature and ionisation parameter over a redshift range of $1.6 \leq z \leq 6.3$, using ionisation equilibrium models for the ionised plasma. In chapter 4, I use blazar spectra and in chapter 5 QSO spectra to estimate the key IGM properties. In chapter 5, I also combine the results of all tracers used to do comparative analysis on the IGM properties and in Chapter 6, I conclude on the findings of the thesis.

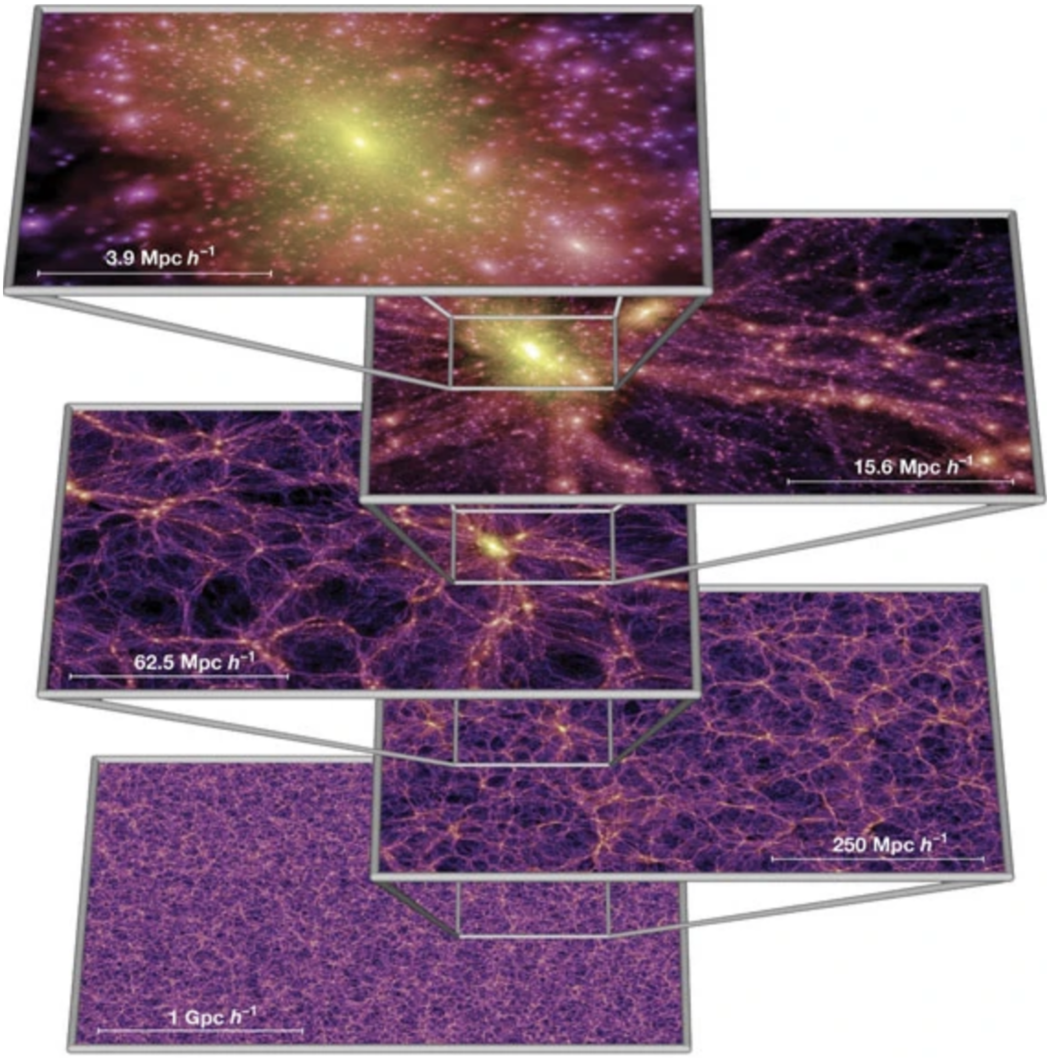

Figure 1.2: A simulated image of the cosmic web where each image zooms in by a factor of 4 (image credit (Springel et al., 2005)

1.2 IGM

As there is no standard or single definition of the IGM, I give here a very brief overview of the IGM for contextual purposes, given the aim of this thesis is the comparative tracer analysis of the IGM. This brief review summarises the current accepted picture of the large scale structure (LSS) and homogeneity of the universe, the ionisation processes in the IGM, equilibrium conditions, and the main observable parameters investigated in this thesis.

1.2.1 Large scale structure

The LSS of the Universe forms a ‘cosmic web’ (Bond et al., 1996) of filaments, sheets, and voids, which evolved via gravitational instability from small density perturbations in the near-homogeneous early Universe (see Fig. 1.2 for simulated image). These structures have been observed on $\gtrsim$ 14 Mpc scales going back many decades (e.g. Lapparent et al., 1986; Gott III et al., 2005). The LSS has been detected using many different methodologies and observational techniques e.g. weak lensing of background galaxies (Yang et al., 2020, and references therein), use of the CMB (e.g. He et al., 2018), ionised gas by the Sunyaev-Zel’dovich effect (De Graaff et al., 2019), Lyman α forest absorption, and emission (Umehata et al., 2019). The large-scale spatial distribution of galaxies in the Universe is thought to follow the distribution of matter in the LSS and is far from uniform, as observed by wide-area surveys such as the Two-Degree Field Galaxy Redshift Survey (Colless et al., 2001), the Galaxy And Mass Assembly survey (Driver et al., 2009), the Sloan Digital Sky Survey (SDSS) (York et al., 2000), the Dark Energy Survey (Planck Collaboration et al., 2020, and prior Planck Collaboration studies), and the VIMOS Public Extragalactic Redshift Survey (Scodeggio et al., 2018).

Any assumption regarding homogeneity and isotropy in the Universe is time and distance dependant. On smaller scales of Mpc or less, the distribution of matter density, temperature and metallicity can be highly inhomogeneous. In terms of evolution, inhomogeneity exists over a large range in redshift. The ΛCDM model is based upon the cosmological principle, that states that the Universe is spatially homogeneous and isotropic. The cosmological principle is considered to be valid on very large scales ($>$ 100 Mpc), even at low redshifts. For the assumption of homogeneity to be reasonably valid therefore, we should be looking at scales greater than the known large scale structures. There is now evidence that homogeneity decreases with redshift (Gonçalves et al., 2020). This makes the assumption of homogeneity increasingly valid with higher redshift. As the bulk of matter in the IGM post reionisation is ionised and exists outside of gravitationally bound structures, and I use tracer objects that have LOS orders of magnitude greater than the LSS, in this thesis I use the assumption of homogeneity i.e. that the absorbing matter on the LOS to tracers is uniformly distributed.

1.2.2 Ionisation processes and equilibrium conditions in the IGM

Generally, there are two processes that determine the ionisation state of plasma in the IGM i.e. photoionisation by the cosmic UV background, and collisional ionisation caused by the high temperature of the gas which can be caused by shock heating processes in the warm-hot IGM (WHIM) or by the cosmic X-ray background. I term both the UV and X-ray background as cosmic ionisation background (CIB), and an overview of the CIB is given in Section 1.2.3. Different physical processes are therefore involved and any assumptions regarding whether collisional, photoionisation or a combination dominates will impact any attempts to model the IGM for observational methods. The photoionisation rate (Γ_{Hi}) depends on the ionising radiation field in the IGM provided by the UV background. Becker et al. (2013) found a remarkably constant Γ_{Hi} and hence the ionising background is generally assumed to be spatially uniform and constant up to redshifts as high as $z \sim 5$. Photoionisation for metals, which can be either neutral or fully ionised, is similar to hydrogen, except they have several electrons available and are, even at very high temperature, usually only partly ionised. Thus, electronic transitions exist for such highly-ionised metals in the IGM. Therefore, for photoionisation IGM modelling, the key variables are density, metallicity and the ionisation parameter (the ratio of ionising photon density to electron density).

Temperature measurements of the cooler diffuse IGM over $2 \leq z \leq 4$, generally agree at $T_0 = (1 - 2) \times 10^4$ K, where T_0 is the kinetic gas temperature at the baryonic mean cosmic density (M16 and references therein). Collisions by thermal electrons ionise hydrogen to a high degree for gas temperatures $> 1.5 \times 10^4$ K. At generally accepted densities for the diffuse IGM, collisional ionisation dominates at $\log(T/K) > 5.4$ (Shull et al., 2012). Therefore, for IGM modelling with the collisional assumption for ionisation, the key variables are density, metallicity and temperature.

Nicastro et al. (1999) compared models of collisional and photoionisation. They found that the fractional abundances of metals are more smoothly distributed in photoionised gas i.e. lower ionised metals can co-exist over a range of photionisation levels, but different types of highly ionised metals exist within narrow ranges of temperature in collisional ionisation. They also found that for collisional ionisation to dominate, the ionisation parameter (U) had to be very low ($U < 0.3$). However, this was in high density environments and may not be relevant to IGM plasma. In summary, it is likely that both photoionisation and collisional processes contribute to the IGM plasma state in different regions and phases.

The above summary largely assumed ionisation equilibrium (hereafter CIE for collisional and PIE for photoionisation equilibrium). The relation between ionisation state and gas temperature (CIE) and ionisation parameter (PIE) explicitly assumes that the gas is in an ionisation equilibrium (Richter et al., 2008, hereafter R08). Opinions on the WHIM plasma equilibrium state differ greatly. There is a substantial amount of literature on this area, and so I am providing a limited number of examples. Some argue that WHIM filaments may have a large range of density and are not isothermal (e.g. R08). Others were of the view that plasma had densities of $n_e \sim 10^{-5}$ cm^{-3} and was virtually in CIE, and photoionisation plays a negligible role (e.g. Nicastro et al., 2018). In contrast, Branchini et al. (2009), for example were of the view that the bulk of the WHIM is not in CIE. In non-equilibrium, the plasma remains over-ionised compared to CIE at any temperature, as recombination lags behind cooling (Gnat and Sternberg, 2007, hereafter G07). They noted that this affects all elements including hydrogen and helium. For CIE, the column density ratios depend only on the gas temperature. However, for non-equilibrium cooling the ion fractions and therefore the column densities also depend on metallicities. It is important to note that G07 assumed there is no impact from any background radiation. While there is still debate on the equilibrium state of the WHIM, in the cooler diffuse IGM, extremely low densities and ionisation equilibrium conditions persist (M16). Importantly for IGM modelling, well outside the influence of galaxies and clusters, the CIB becomes more important.

1.2.3 Cosmic ionising radiation background

The abundance of ionic species is partially dependent on the CIB. In modelling the IGM, it is conventional to assume a spatially uniform shape and intensity of the ionising background (Simcoe, 2011). Many studies have been completed on the sources of the CIB, being primarily star forming galaxies and AGN (e.g. De Luca and Molendi, 2004; Luo et al., 2011; Moretti et al., 2012; Haardt and Madau, 2012). General practice is to adopt a fixed power law for the background radiation. Oppenheimer and Schaye (2013a) noted that non-equilibrium effects are smaller in the presence of the CIB. In Chapter 2, I examine the impact of different power law assumptions for the CIB on the total column density estimates for the IGM, and also which software models are therefore appropriate for IGM modelling.

In summary, for our IGM models, I assume ionisation equilibrium which is reasonable in the bulk of the IGM. However, the equilibrium assumption could result in an underestimation of column density if the IGM plasma remains over-ionised in a non-equilibrium state (G07). I also assume a single gas phase in the IGM, while acknowledging that a multi-phase gas may be more realistic in some regions such as the WHIM.

1.2.4 IGM observable properties from X-ray absorption

Most baryonic matter resides in the IGM (M16), which is highly ionised. We are using X-ray spectra to analyse the IGM properties. Following the above overview of the IGM properties and conditions, the IGM properties examined in this thesis are:

- hydrogen density which is typically reported as an equivalent total hydrogen column density (hereafter $N\mathrm{HX}/\mathrm{cm}^{-2}$) (an integrated quantity over the column length), even though the X-ray absorption cross-section is mostly dominated by metals.
- metallicity $[X/\mathrm{H}]$* or $Z/Z_{\odot}$. In this thesis, the term 'metallicity' is used synonymously with metal abundance.
- temperature measured in Kelvin, typically reported in this thesis as $\log(T/\mathrm{K})$ and relevant for CIE assumed conditions.
- ionisation parameter (dimensionless $\log(\xi)$) for PIE assumed conditions

Simulations predict that up to 50% of the baryons by mass have been shock-heated into the WHIM at low redshift $z < 2$, with $T = 10^5 - 10^7$ K and $n_b = 10^{-6} - 10^{-4}$ cm^{-3} where n_b is the baryon density (e.g Cen and Ostriker, 1999, 2006; Davé and Oppenheimer, 2007; Schaye et al., 2015). It is currently estimated that the cool diffuse IGM constitutes ~ 39% and the WHIM ~ 46% of the baryons at redshift $z = 0$ (Martizzi et al., 2019, using the IllustrisTNG simulations †). Observations of the IGM are essential for effective tracing of matter across time and to validate the simulations (Danforth et al., 2016). The observation of metals is necessary for observing the IGM properties including density, temperature and metallicity as post reionisation, the vast majority of hydrogen and helium is ionised in the IGM. Most very highly ionised metals are not observed in the optical to UV wavelength range where the bulk of prior studies have been carried out on individual systems using the ionisation states of abundant heavy elements (e.g. Shull et al., 2014; Raghunathan et al., 2016; Selsing et al., 2016). In the cool phases of the IGM, $40-60\%$ of the universe by mass has $[\mathrm{X/H}] > -3$ (Fumagalli, 2014, and references therein). Both Schaye et al. (2003) and Aguirre et al. (2008) found metalicity had a strong dependency on density but had virtually no evolution in the cool IGM

---

[*] $[X/\mathrm{H}] = \log(X/\mathrm{H}) - \log(X/\mathrm{H})_{\odot}$, where X is number density of the metal element, and H is the number density of Hydrogen.

[†] http://www.tng-project.org/

in the range $z = 1.8 - 4.1$. A significant fraction of the cool gas probed by dense Lyman systems ($\log(N_{\rm HX}/{\rm cm}^{-2}) > 20$) has been associated with galaxy haloes and the circum-galactic medium (CGM) (e.g. Pieri et al., 2014; Fumagalli et al., 2016). The metallicity rises from very low values of [X/H] ~ -3 to -2, to approximate values of > -1.5 for dense Damped Lyα systems (DLAs) as we move from the diffuse IGM to virialised luminous matter (e.g Fumagalli et al., 2016; Wotta et al., 2019).

For some time since their first prediction at low redshift, the expected baryons were not observed in the WHIM, giving rise to the "missing" baryon problem (e.g. Danforth and Shull, 2005; Shull et al., 2014). Recent literature points to the CGM as a reservoir for a large fraction of this matter (e.g. Tumlinson et al., 2011; Werk et al., 2013; Lehner et al., 2016). Other claims to have detected the WHIM include excess dispersion measure over our Galaxy and the host galaxy in Fast Radio Bursts, possible detection of O VII lines in the X-ray, and stacked X-ray emission from cosmic web filaments using the thermal Sunyaev Zelodovich effect (e.g. Macquart et al., 2020; Nicastro et al., 2018; Tanimura et al., 2020b).

There appears to be a consensus that, at least for $z < 2$, the predicted mean metallicity of the WHIM from simulations and O VI absorption studies is $\sim 0.1Z_\odot$ (e.g. Wiersma et al., 2011; Danforth et al., 2016; Pratt et al., 2018, S12).

Tracing individual features of the IGM metals in X-ray with current instruments is very limited. Athena, the proposed European Space Agency X-ray observatory, aims to study the IGM through detailed observations of O VII (E = 573 eV) and O VIII (E = 674 eV) absorption features (Walsh et al., 2020). In the meantime, we trace the IGM parameters based on the integrated effect of the full LOS to tracers as seen in their X-ray spectra.

In conclusion, in this thesis, I follow a similar definition of the IGM to M16 as being baryonic matter outside of the virial radius of galaxies and clusters. It is essentially all highly ionised baryonic matter on the LOS to our distant tracer objects existing outside our Galaxy and the host galaxy of the tracer. I assume conditions of CIE and PIE when exploring the IGM parameters of density, metallicity, temparature and ionisation as seen in the X-ray spectra of tracers. The parameter ranges used when fitting the tracer spectra are informed by prior studies such as those referenced above. I now turn to the tracers used in this thesis.

1.3 Tracers

The ideal tracers, or background X-ray sources, would have all of the following characteristics:

- Extremely bright or luminous so that they can be observed at great distances.
- Relatively simple intrinsic spectra in the X-ray bandwidth i.e. the intrinsic continuum is a simple power law model. The simple intrinsic model reduces any error in isolating absorption due to the IGM from degeneracies with the tracer continuum curvature, or absorption in the host environment.
- Broad sky distribution as I am examining general IGM properties,
- Available across low and high redshift ranges.
- Minimal or simple host galaxy contribution to the spectral shape.
- Long emission duration for extended observation, preferably with minimal time variability.

What follows is a very brief overview of the tracers used in this thesis to provide context only. This is primarily to highlight the advantages and disadvantages of the tracers types in terms of ideal criteria. Further, it is to draw attention to the key issues and assumptions on aspects that can affect and influence the determination of IGM properties derived from tracer X-ray spectra. The actual data selection and methodologies for each tracer are contained in the later chapters dealing with each tracer research completed.

1.3.1 GRBs

GRBs are among the most powerful explosions known in the universe, (see Schady, 2017, for a recent general review). GRBs provide a valuable probe of all baryonic matter along their LOS given the huge range in distances to GRBs, and their extremely high luminosities, combined with the broad energy range of observed emissions. In the energy band that I use (mainly 0.3-10 keV), X-ray absorption yields information on the total absorbing column density of the matter between the observer and the source as any element that is not fully ionised contributes to the absorption of X-rays (scattering by electrons becomes important above 10 keV (Wilms et al., 2000)).

Though I am primarily interested in absorption seen in the afterglow spectra of GRBs, I give a brief overview next of the GRB progenitor, the current favoured GRB model, and GRB afterglow types.

1.3.1.1 GRB progenitor and fireball model

GRBs were first discovered by US Vela military satellites in the 1960s, though their discovery was not published until 1973 (Klebesadel et al., 1973). It was not until the late 1990s that they were confirmed as extra-galactic (Metzger et al., 1997; Costa et al., 1997). GRB are thought to result from massive stars undergoing a colossal energy release event towards the end of their evolution (van Paradijs et al., 1997). The burst durations follow a bi-modal distribution (typically quantified as t_{90}, the time in which 90% of the source photons are collected), with a division around 2 seconds (Kouveliotou et al., 1993). Long GRB afterglows can last from ~ 2 to several hundred seconds, with a typical burst lasting ~ 30 seconds (e.g. Butler et al., 2007). For long GRBs ($t_{90} > 2$ s), the progenitor is thought to be a rapidly-rotating massive star that core-collapses into a black hole (Woosley, 1993). This model is known as the collapsar model. For short GRBs ($t_{90} < 2$ s) the progenitors are thought to be mergers of neutron star binaries or neutron star-black hole binaries

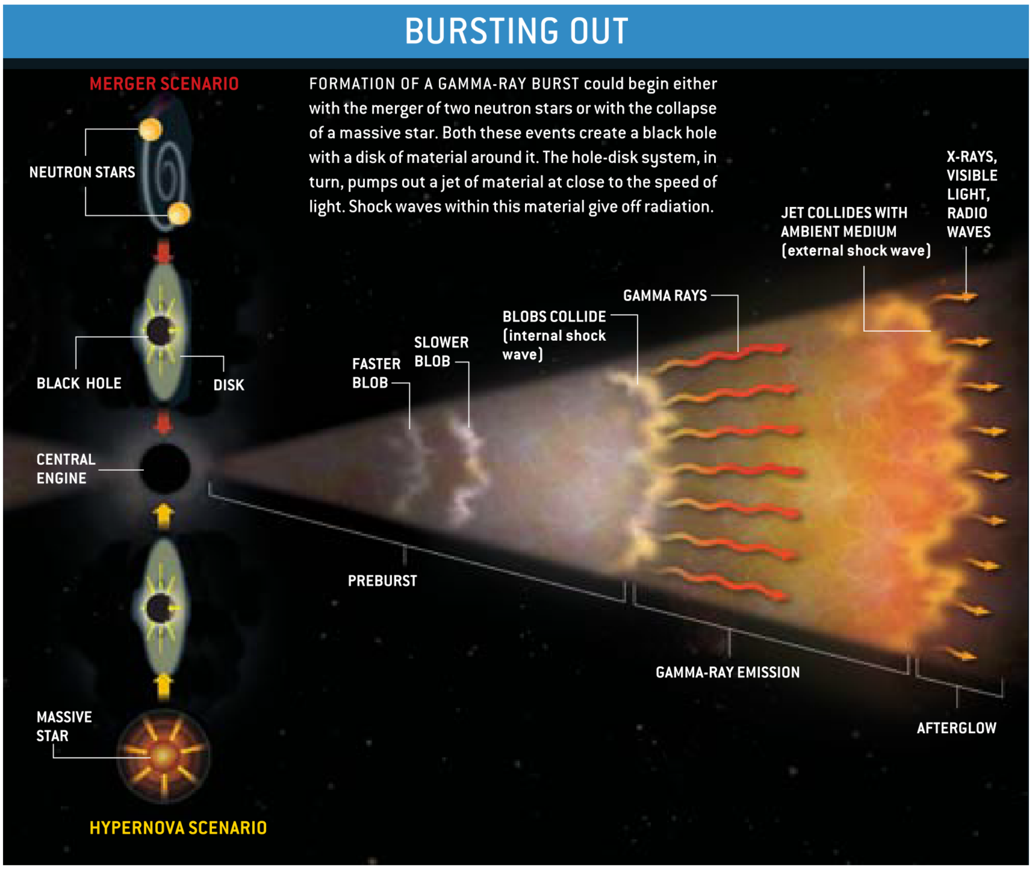

Figure 1.3: Illustration of the GRB fireball model. The black hole with an accretion disk around it drives a relativistic jet into space. The observed prompt gamma-ray and afterglow X-ray to radio spectra arise from the hot gas near the black hole, shell collisions within the jet, and from the jet's interaction with host galaxy environment or progenitor wind (Gehrels et al., 2002).

(Paczynski, 1986). While the two GRB progenitors are physically distinct, the initial emission mechanisms are thought to be similar. The energy output of GRBs are separated into the prompt and afterglow emission phases. The prompt emission phase is characterized by an intense gamma-ray flux, produced by ultra-relativistic flows that get dissipated in internal collisions along the jet direction. The afterglow phase occurs when the jet of gamma-rays subsequently collide with the surrounding medium, slowing it down by external shocks. It then emits synchrotron radiation which is observed as the X-ray to optical and radio afterglow (Piran, 2004). The spectral shape of the afterglow typically follows a simple power-law (Sari et al., 1999). This simple consistent afterglow spectra makes it very attractive as a tracer.

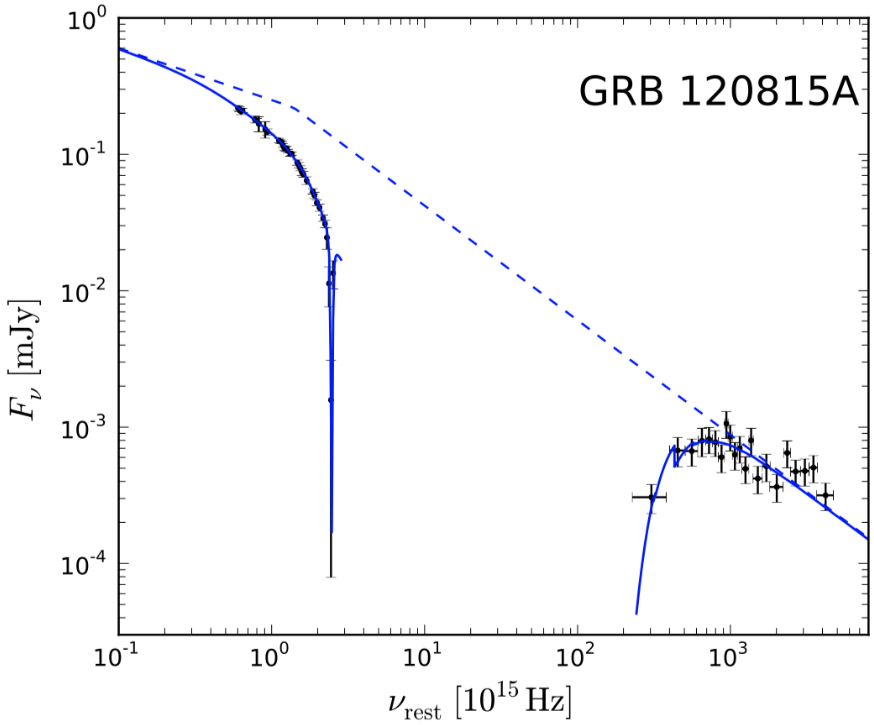

Figure 1.4: Rest-frame afterglow broadband SED analysis of GRB 120815A. Optical and X-ray data are plotted with black points. The best-fitted model is plotted with solid blue lines and the intrinsic afterglow spectrum with dashed-blue line. Image credit: Japelj et al. (2016)

Figure 1.3 (image credit: Gehrels et al. (2002)) depicts the process of producing the GRB prompt emission and the afterglow through internal and external shocks, respectively.

The afterglows of GRBs are generated from synchrotron radiation thought to be caused by the interaction between the ultra-relativistic jet and the GRB host environment. Electron cooling in the GRB postshock causes an observable break in the synchrotron spectrum (Zafar et al., 2018, and references therein) . This cooling break is typically located between the optical and X-ray bands (see Fig. 1.4 which shows the broadband spectral energy distribution(SED) for GRB120815A as an example, image credit: Japelj et al. (2016)). The X-ray part of the SED in Fig.1.4, shows the typical shape for GRBs of an absorbed simple power law.

1.3.1.2 GRB host

Because GRBs are observed across a very large redshift range, are extremely luminous and have a simple intrinsic continuum spectra, they have been used many times as tracers. As it is often not possible to determine the location of absorbers in X-ray, it is essential to account properly for any non-IGM contribution to the full LOS column density. This entails examining GRB host properties including gas density, neutral fraction and metallicity. By convention, most studies with GRBs as tracers used the same assumptions i.e. all absorption in excess of our Galaxy attributed to the GRB host, and a neutral host with solar metallicity. Several studies have tried to justify the resulting high column densities attributed to the GRB host using fairly extreme host environment theories e.g. dust extinction bias (Watson and Jakobsson, 2012), ultra-ionised gas in the environment of the GRB (Schady et al., 2011) and a host galaxy mass $N_{\rm HX}$ relation (Buchner et al., 2017). I explore in detail in Chapter 2, specific GRB host properties including using actual metallicities, dust corrected where available for detections, and a more realistic average host metallicity using a standard adjustment from solar. I also examine using the measured host neutral column adjusted for the ionisation fraction as a proxy for the GRB host column density.

1.3.1.3 GRBs as tracers

In conclusion, GRBs are excellent tracers of the IGM. From the ideal tracer criteria, they satisfy extreme luminosity, huge redshift range and simple intrinsic continuum spectra in the X-ray band. However, they are very short lived transient events for observational purposes and can have complex host environments.

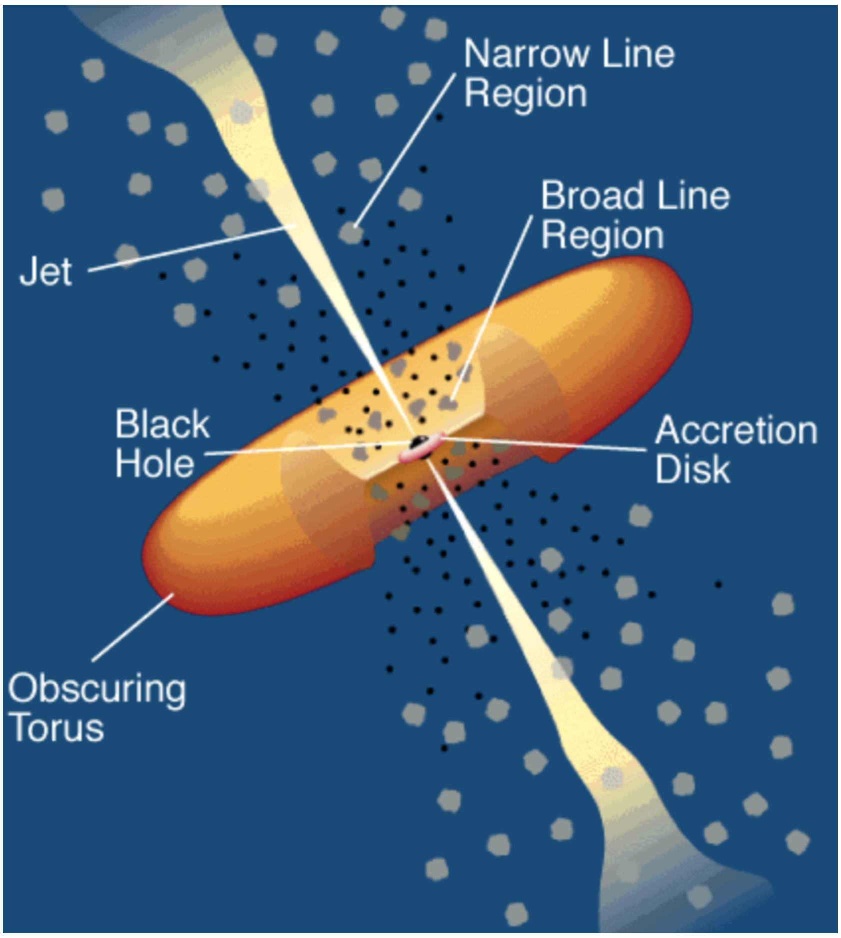

Figure 1.5: Schematic representation of an active galactic nucleus (AGN) basic components (adapted from Urry and Padovani, 1995)

1.3.2 QSOs

Though sequentially in this thesis, blazars are the second tracer type, I give a brief overview next for QSOs, as blazars are a sub-type of QSO. In this section, I summarise Active Galactic Nuclei (AGN) of which QSOs are a sub-type, the AGN engine model, the QSO host environment, and concluding with QSO as tracers.

1.3.2.1 AGN engine model and classification

The conventional basic components (not all necessarily occur) of an AGN traditionally represented as in Fig. 1.5 (adapted from Urry and Padovani (1995)) are:

- Super-massive central black hole, $10^6 - 10^9 M_{\odot}$.
- Accretion disk of hot, luminous gas accreting onto the black hole.
- Jets, charged particles moving at relativistic speeds out of the nucleus.
- Broad-line region: gas clouds (density $n \approx 8 - 12$ cm^{-3} typically within 1pc of the accretion disk.
- Dusty torus: a ring of denser gas and dust surrounding the nucleus.
- Narrow-line clouds: gas clouds ($n \approx 3 - 6$ cm^{-3} further out up to several kpc, moving more slowly.

The observational history of AGN spans most of the 20th century. Without the current accepted understanding of the AGN model, and due to the various components in AGN, initially many different types of AGN related objects were thought to exist including Seyfert galaxies, broad and narrow line galaxies, QSO, BL Lac objects, flat spectrum radio quasars etc. Given the overlapping components and features, many attempts were made a developing unification models (see Urry and Padovani, 1995, for a comprehensive review). These models were based on the hypothesis that most AGN were intrinsically the same and the differing features could be explained primarily due to the viewing orientation relative to the torus. The current picture is that there are intrinsically different components in the AGN resulting in differing features e.g. the mass of the black hole, the accretion rate, obscuration by dust and whether the AGN is radio loud or quiet (e.g. Done, 2010).

1.3.2.2 QSOs

QSOs are among the most luminous, non-transient sources in the Universe. Though most QSOs are characterised by spectral time variability, they have very long lifetimes with current estimates ranging between ~ 0.01 Myr and ~ 1 Gyr (Khrykin et al., 2021, and references therein) . The discovery of dormant SMBH at the centres

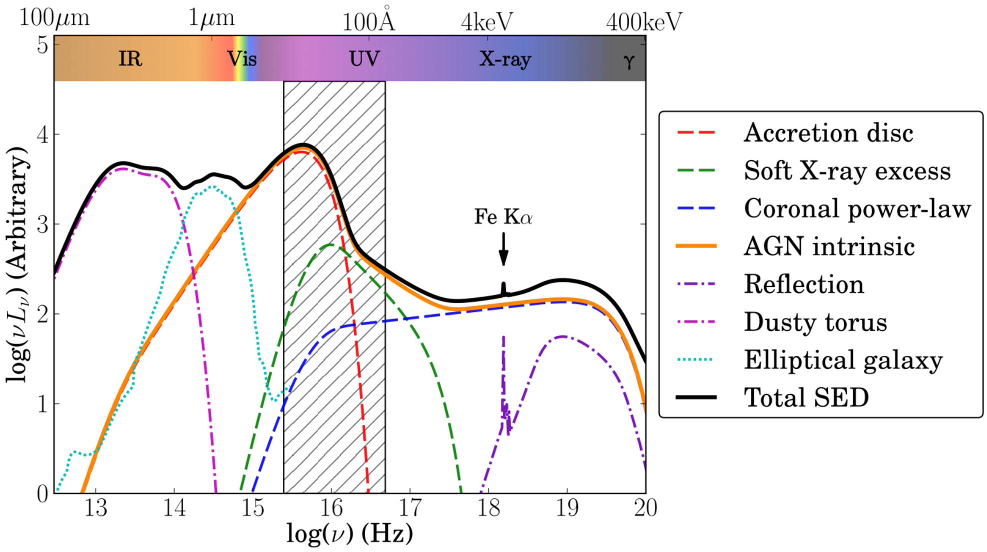

Figure 1.6: A schematic diagram of an AGN SED, showing the typical shape of the various components. The hatched region highlights the spectral range that is obscured by optical/UV absorption in the galaxy and the IGM. Image credit: Collinson et al. (2017)

of most bulge-dominated galaxies led to the hypothesising that they were once active QSOs. The term “quasar” was first created as the acronym of “quasi–stellar radio source”, due to the original, radio based discoveries. In the following years, an increasing number of QSOs with no radio emission were found, and the term “quasi–stellar object” was introduced. Nowadays, the two terms are used synonymously.

QSOs are the most luminous subclass of AGN and can outshine their host galaxies such that only the core is visible with bolometric luminosities of ($\approx 10^{45} - 10^{49}$ erg s^{-1}). QSOs have a relatively featureless spectrum, spanning from radio wavelengths to hard X-rays. Fig. 1.6 shows a schematic example of a broadband AGN SED with most of the typical features, though not all are observed in individual AGN (Image credit: Collinson et al. (2017)). Under the generally accepted AGN scenario, UV emission in a QSO is produced by viscous dissipation in an accretion disk where the gravitational energy of the infalling material is partially transformed into radiation (Shakura and Sunyaev, 1973). The UV photons are Comptonised to

X-rays by a corona of hot relativistic electrons around the accretion disk (Haardt and Maraschi, 1993). These X-rays can illuminate the accretion disc, being reflected back towards the observer. The observational signs of such reflection features are a Compton scattering hump, an iron emission line and an Fe K absorption edge. While features such as the Compton hump, soft excess and iron emission lines are frequently observed in lower luminosity AGN, particularly at lower redshift, they are not often observed in QSO as the very powerful emission continuum dominates (Scott et al., 2011, and references therein). This makes QSO very attractive as tracers.

1.3.2.3 QSO host

In addition to the immediate QSO engine environment including the accretion disc and torus, one must also consider the QSO host galaxy in terms of its impact on the QSO observed spectra as any LOS must include that part of the path. Similar to GRBs, the conventional approach in prior studies was to assume a QSO host environment that was neutral and at solar metallicity. Further, most studies assumed that all X-ray absorption, in excess of our Galaxy was due to the QSO host. In Chapter 5, we draw from the Quasars Probing Quasars series to develop a QSO host absorption model (e.g Hennawi et al., 2006; Prochaska and Hennawi, 2009; Hennawi and Prochaska, 2013; Prochaska et al., 2013). Given the additional potential complications in the QSO spectra from Compton humps and soft excess in X-ray (usually observed in very low redshift QSO and AGN), Chapter 5 robustly examines the QSO sample for such features and any impact on IGM derived properties.

1.3.2.4 QSOs as tracers

In conclusion, QSOs meet many of the ideal tracer criteria including extreme luminosity, observed over a huge redshift range, simple intrinsic continuum spectra and non-transient observation. They are observed in huge numbers and with an isotropic sky distribution. However, they have potentially complex host environments. Further, a disadvantage is that the bulk of QSOs observed have redshifts $0 \leq z \leq 2$, with a peak just greater than $z \sim 2$, followed by a rapid decline (Pâris et al., 2018).

1.3.3 Blazars

Blazars are powerful emitters across the entire electromagnetic spectrum with very strong radio emission ($\geq 10^{41}$ erg s^{-1}) and with a bolometric luminosity between $10^{46} - 10^{48}$ erg s^{-1}. A very large fraction of this luminosity ($\sim 20\%$) is emitted in the X-ray energy band which includes our main focus range of 0.3 - 10 keV.

1.3.3.1 Blazar engine model and features

Blazars are a special class of radio-loud AGN in which the relativistic plasma emerges from the galaxy core as a jet towards the observer. The observed luminosity is much greater than the isotropic emission due to relativistic beaming or boosting. The broad-band spectra of blazars feature two humps, similar to the AGN SED in Fig.1.6. The first hump typically has a peak located between infrared to far UV and sometimes soft X-ray frequencies, and is attributed to synchrotron processes. The second hump is found in X-ray to γ-ray frequencies and is a result of inverse Compton(IC) processes. The seed photons for the IC process can be intrinsic to the jet, or, if the seed photons originated from the accretion disc and are reprocessed by the broad-line region and/or the molecular torus, it is referred to as External Compton. Blazars are conventionally divided into two classes. Flat spectrum radio quasars (FSRQs) are characterized by strong QSO emission lines and higher radio polarization, while BL Lac objects exhibit featureless optical spectra. The distribution of the synchrotron peak frequency is very different for the two blazar classes. While the rest-frame energy distribution of FSRQs is strongly peaked at low frequencies ($\leq 10^{14.5}$ Hz), the energy distribution of BL Lacs is shifted to higher values (Padovani et al., 2012). FSRQs can be found out to high redshift and have a much higher median redshift than BL Lacs (Sahakyan et al., 2020).

The intrinsic continuum of blazars is relatively simple and typically modelled as a simple power law. However, many blazar are better modelled with variations on the power law slope including log-parabolic and broken power law models (continuum power law models are covered in Section 1.5.1.1). Otherwise, the spectra are featureless in the range of this thesis, primarily 0.3 - 10 keV. Some spectra do exhibit a soft excess. There is no consensus on the cause of this feature. Further, blazar spectra show large variability with time. Therefore, in Chapter 4, we robustly examine the potential impact of soft excess and spectral variability on derived IGM properties.

1.3.3.2 Blazar host

Blazars are AGN in which the relativistic jet is pointing towards the observer. Blazars are therefore thought to have negligible X-ray absorption on the LOS within the host galaxy, swept by the kpc-scale relativistic jet. This aspect makes them more attractive as tracers than GRBs or QSOs.

1.3.3.3 Blazars as tracers

Blazars are potentially the best tracer in terms of satisfying the ideal tracer criteria. They are extremely luminous, available over a very large redshift range and are not transient. They are isotropic across the sky. They generally have simple featureless intrinsic continuum spectra. Further, they are thought to sweep out any host galaxy features in their spectra. However, they show time variability in their spectra and potentially occasional soft excess.

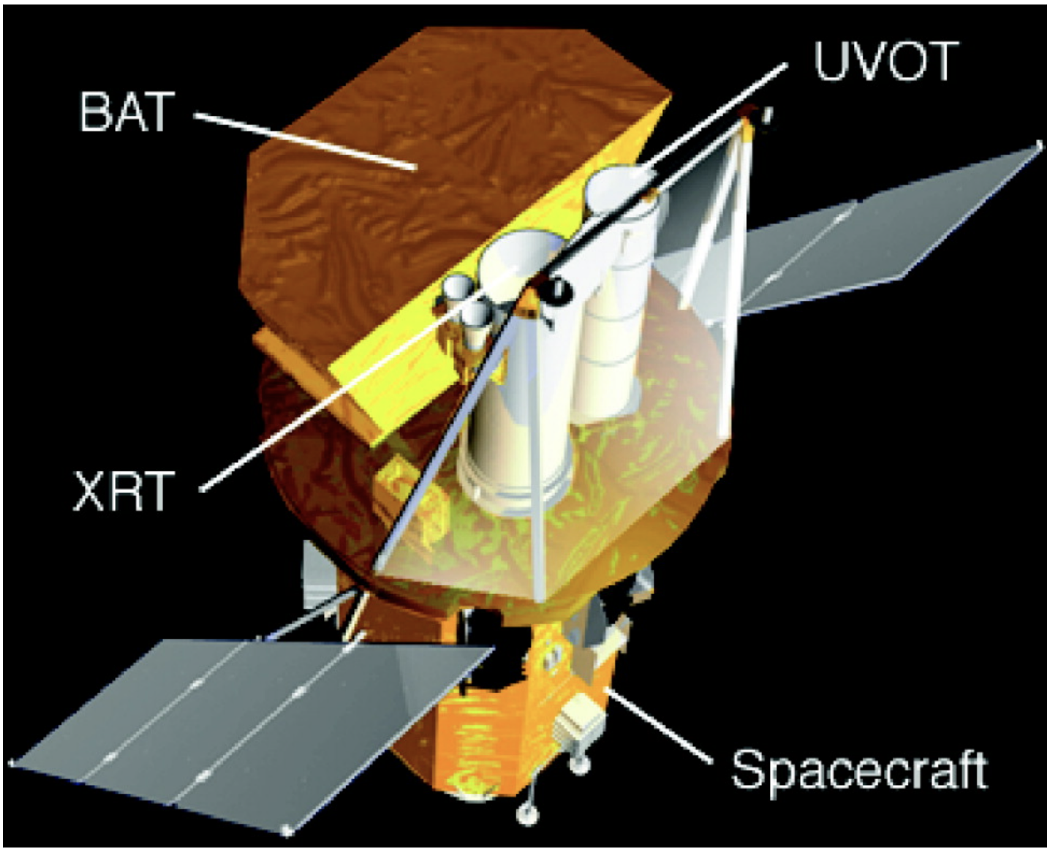

Figure 1.7: *Swift* satellite showing the BAT, XRT and UVOT instruments (image credit: Gehrels et al. (Fig. 2 2004))

1.4 Instruments and datasets used

In this section, I provide details of the two instruments used to provide X-ray observational data for the thesis. For GRBs, all data is taken from the UK *Swift* Science Data Centre* repository (hereafter *Swift*; Gehrels et al., 2004) . For Blazars, the main analysis is based on *Swift* data, while part of the robustness tests completed use data from the *XMM-Newton* European Photon Imaging Camera (Strüder et al., 2001) (hereafter *XMM-Newton*). All QSO data is taken from *XMM-Newton*. The data selection and methodology specific to each tracer are provided in Chapters 2, 3, 4 and 5.

---

*http://www.swift.ac.uk/xrtspectra

1.4.1 Swift

Launched in 2004, *Swift* is a multi-wavelength observatory with the primary mission to observe and study GRBs. *Swift* carries three instruments: the Burst Alert Telescope (BAT), the X-ray Telescope (XRT) and the Ultraviolet/Optical Telescope (UVOT) (see Fig. 1.7, Image credit: Gehrels et al. (2004)). The primary purpose of the BAT is to search the sky for new GRBs. On discovery of a GRB candidate, it triggers a spacecraft slew to bring the burst into XRT and UVOT fields of view. *Swift* revolutionised early-time multi-wavelength follow-up of GRBs. It also enables ground-based facilities and other satellites, including *XMM-Newton* to initiate early-time follow-up observations.

As this thesis uses X-ray spectral data, I draw from the results of the XRT instrument. The XRT is dedicated to the observation of light curves, spectra and fluxes of GRBs afterglows in the 0.2 - 10keV energy range. XRT provides automated source detection and position reporting. It can also measure the redshifts of GRBs using spectral features. There is a known instrument feature at ~ 2 keV due to the gold coated mirrors. This is accounted for in the Redistribution Matrix Files (RMF) and Ancilliary Response Files (ARF), so it is not usually apparent in the spectra unless there are high spectral counts available.

1.4.2 XMM-Newton

XMM-Newton was launched by the European Space Agency in December 1999 with the ability to simultaneously obtain X-ray and optical data. *XMM-Newton* has three mirror assemblies, one of which feeds the EPIC-pn detector, and the other two mirrors assigned to the EPIC-MOS and RGS detectors. The EPIC-pn detector has a 0.2-12 keV bandpass. The RGS instrument can resolve lines down to a full width at half maximum resolution of 2.9 eV at 1.0 keV while EPIC-pn has a resolution of 55 eV at 1.0 keV. Though the RGS instrument has superior spectral resolution, it has a limited 0.4-2.5 keV bandpass. Given this thesis is examining the full LOS to tracers, and also due to the general limited spectral counts for individual objects, I use the EPIC-pn data primarily. The EPIC and MOS cameras have a known systematic instrumental feature at ~ 7.8 and 2keV, associated with the Si K and Au M edges respectively. This is observed in most of my QSO sample spectra in Chapter 5.

1.5 Spectral analysis software

In this thesis work, all spectral fitting for both *Swift* and *XMM-Newton* data is done using various model components of XSPEC (Arnaud, 1996). XSPEC is an X-ray spectral-fitting program, designed to be completely detector-independent so that it can be used for any X-ray spectrometer.

Within specific instrument channels (I), a spectrometer obtains photon counts (C). This observed photons are related to the actual spectrum of the source (*f(E)*), such that:

$$C(I) = \int_0^\infty f(E)R(I,E)dE \tag{1.1}$$

where *R(I,E)* is the instrumental response and is proportional to the probability that an incoming photon of energy E will be detected in channel *I*. As it is not possible in general to directly infer the actual spectrum, a model spectrum is chosen based on knowledge of the source. The chosen model will have parameters which can be either fixed or variable. XSPEC then fits the model to the data obtained by the spectrometer. For a given observation, XSPEC uses two files: the data file, and the background file. The data file informs XSPEC how many total photon counts were detected by the instrument per channel. The background file is then used to derive a background-subtracted counts in units of counts per second per channel. For each model, a predicted count spectrum (*Cp(I)*) is calculated and compared to the observed data. A fit statistic is computed from the comparison, which is used to determine whether the model spectrum matches the data obtained by the spectrometer. When fitting models to spectra, chi-squared (χ^2) is the conventionally used statistical method. However, deep field X-ray sources from *Swift* and *XMM-Newton* in the data samples used in this thesis can have a small number of photon counts, well into the Poisson regime. The χ^2 regression approach is usually inappropriate in these circumstances (Buchner et al., 2014), and the maximum likelihood C-statistic (Cash, 1979), based on the Poisson likelihood, is preferred. The model parameters are varied to find the parameter values that gives the lowest fit Cash statistic. The final values are then referred to as the best-fit parameters.

As I am fitting my absorption models to the total continuum absorption in X-ray, and not any individual features, there is scope for degeneracy between the parameters including column density, temperature and metallicity. This can cause the fitting algorithm to get stuck in local probability maxima i.e. there may be multiple, separate, adequate solutions. I use Markov chain Monte Carlo (MCMC) and the STEPPAR function in XSPEC to overcome this problem, though it can still leave some degeneracy. I also use MCMC to generate the confidence intervals, and to produce integrated probability plots, which are analogous to contour plots, to examine the potential degeneracy.

1.5.1 Model components

The XSPEC components used in the spectral fitting attempt to model the full LOS to each tracer and consist of:

- Tracer intrinsic continuum
- Tracer host absorption and other possible features
- IGM absorption
- Our Galactic absorption

In this thesis, metal abundances from Wilms et al. (2000) are used which take into account H_2 and dust in the interstellar medium of galaxies. This is reasonable for our Galaxy and other galaxies and the CGM. However, the relative abundances may not be appropriate for some parts of the IGM e.g in voids and at higher redshifts. Some studies using simulations claim that early Population III stars are metal free and form in pristine gas (e.g. Pallottini et al., 2014). This study suggested that at $z > 4$, $> 90\%$ of the IGM is pristine. If this does prove to be the case, then the assumption that ionised metals are the main absorbers seen in X-rays may not hold.

1.5.1.1 Tracer intrinsic continuum

As reviewed in Section 1.3, the tracers chosen for this thesis had a selection criteria that the spectral shape be as simple as possible. Even so, as detailed in Chapters 2 to 5, various power law models are trialled including a simple power law, log-parabolic and broken power laws. The log-parabolic power law contains an extra curvature term (β), while the broken power law contains an energy break and a second power law.

1.5.1.2 Tracer host

As summarised in Section 1.3, and examined in detail in Chapters 2 to 5, correctly modelling the impact of the tracer host on the spectra is essential. Conventionally, the tracer host is assumed to be neutral and with solar metallicity. Further, all absorption in excess of our Galaxy is assumed to occur in the tracer host. The model ZTBABS is often used for host absorption (Wilms et al., 2000). The relevant host model components used in this thesis depending on the tracer host environment are:

- TBVARABS (Wilms et al., 2000) which is the same as TBABS with additional parameters for redshift of the source, metallicity and dust in the tracer host.

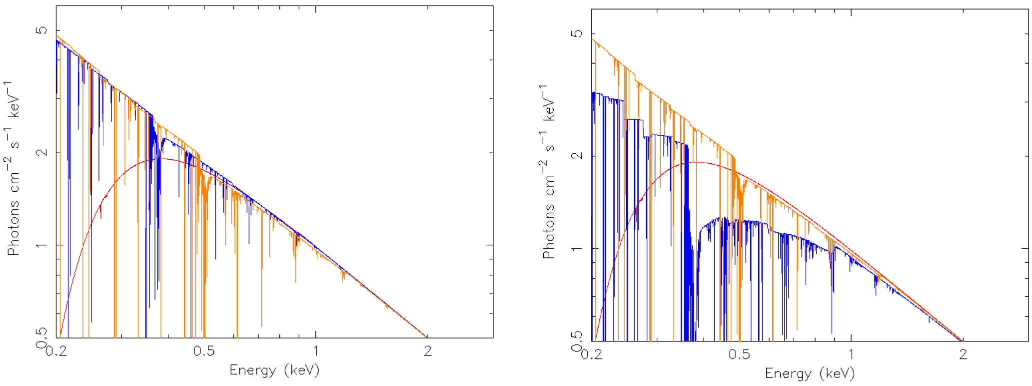

Figure 1.8: QSO host exaggerated scenarios with the QSO at $z = 1$, absorption in our Galaxy is fixed and no IGM absorption. The host absorption column is assumed to be $\log(N_{\text{HX}}/\text{cm}^{-2}) = 21.5$. In both panels, the orange curve assumes a neutral host using TBVARABS, and the blue curve is for an ionised CGM environment using HOTABS. The reds curves are our Galaxy absorption. In the left panel, metallicity in the QSO host is $Z/Z_{\odot} = 0.05$ and in the right panel $Z/Z_{\odot} = 0.3$.

It assumes a neutral host environment.

- HOTABS is used to model the CGM for QSO hosts (Kallman et al., 2009). It is a CIE model with free parameters for density, metallicity and temperature. These are discussed in Chapter 5.
- Possible impact on the tracer spectra for individual tracer host specific features such as Compton hump (PEXRAV (Magdziarz and Zdziarski, 1995)) and soft excess (ZBBODY).

In Fig. 1.8, exaggerated scenarios are given to show absorption in the QSO host under two scenarios. For both scenarios, the QSO is at $z = 1$, absorption in our Galaxy is fixed and there is no IGM absorption. The host absorption column is assumed to be $\log(N_{\text{HX}}/\text{cm}^{-2}) = 21.5$. In both panels, the orange curve is assuming a neutral host using TBVARABS, and the blue curve is for an ionised CGM environment using HOTABS. The red curve is the same for both panels being our Galaxy absorption. In the left panel, metallicity in the QSO host is $Z/Z_{\odot} = 0.05$ and in the right panel $Z/Z_{\odot} = 0.3$. As can be seen in the figure, metallicity in the host has a large impact on the absorption levels, with the impact being larger for an ionised environment. Below 1 keV, N, O, and Ne are the dominant absorption features. The model examples are trialled prior to the actual fitting for each tracer, and in the example of Fig 1.8, are not fitted to any spectrum. Therefore, they show all possible absorbing features in the model components. In the actual spectra, due to the redshift smearing over the LOS and resolution, generally no individual ion features can be observed. Therefore, the fitting is to the whole continuum curvature.

1.5.1.3 Galactic absorption

For Galactic absorption, I use TBABS (Wilms et al., 2000, hereafter W00) fixed to the values based on Willingale et al. (2013). These column densities are estimated using 21 cm radio emission maps from (Kalberla et al., 2005). They include a molecular hydrogen column density component. TBABS calculates the cross-section for X-ray absorption by our Galaxy ISM as the sum of the cross sections for the gas, molecules and grains. In reality, uncertainties exist on Galactic absorption measurements e.g. intrinsic radio map uncertainties and relating to molecular hydrogen (Kalberla et al., 2005; Willingale et al., 2013). Campana et al. (2014b) explored the impact of ignoring such uncertainties on column densities and found that the impact was not significant.

1.5.1.4 IGM absorption

Having carefully isolated the impacts of the various LOS contributions to the tracer spectra, I attribute the remaining absorption to the IGM. I model the IGM assuming a thin uniform plane parallel slab geometry in thermal and ionisation equilibrium. This is a simple approximation which is generally used for a homogeneous medium (e.g. Savage et al., 2014; Nicastro et al., 2017; Khabibullin and Churazov, 2019; Lehner et al., 2019). This slab is placed at half the tracer redshift as an approximation of the full LOS medium.

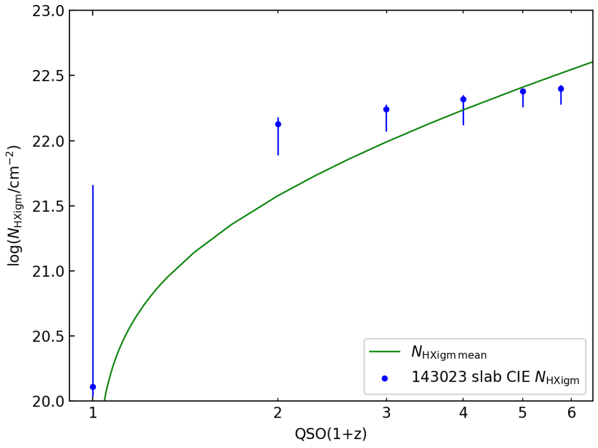

Figure 1.9: The impact on NHXIGM for 143023.73+420436.5 by moving the IGM slab from $z = 0$ to 4.71, freezing log(T/K) = 6 and [X/H] = −1. The green line is the simple IGM model.

I use observed 0.3-10 keV spectra in this thesis, so for higher redshift tracers, the slab location assumption results in lower keV absorbing ions being redshifted out of the observed spectral range. Most X-ray absorption occurs below 2 keV in the rest frame. Placing the slab at less than half the tracer redshift may better trace the low keV X-ray absorption, but would not reflect the impact on the observed cross-section which scales approximately as $E^{-2.5}$.Therefore for redshifted absorbers with a fixed observed energy window, the cross section scales as $\sim (1+z)^{-2.5}$. To show the impact of placing the slab at different redshifts, I used QSO 143023.73+420436.5 which is located at $z = 4.71$ as an example. The spectrum was fitted moving the IGM slab from $z = 0$ to 4.71, freezing log(T/K) = 6 and [X/H] = −1. The NHXIGM is not substantially affected by the choice of redshift location, apart from at $z = 0$ which would not reflect any IGM absorption (see Fig. 1.9). The uncertainties are small as there are less free parameters than the full free model.

As discussed in Section 1.2.2, equilibrium conditions in the IGM are assumed. Prior to modelling and fitting the first tracers, GRBs, I reviewed the impact on potential IGM absorption of variations in the model free parameters such as metallicity, redshift, temperature (CIE) and photoionisation (PIE). This was done using trans-

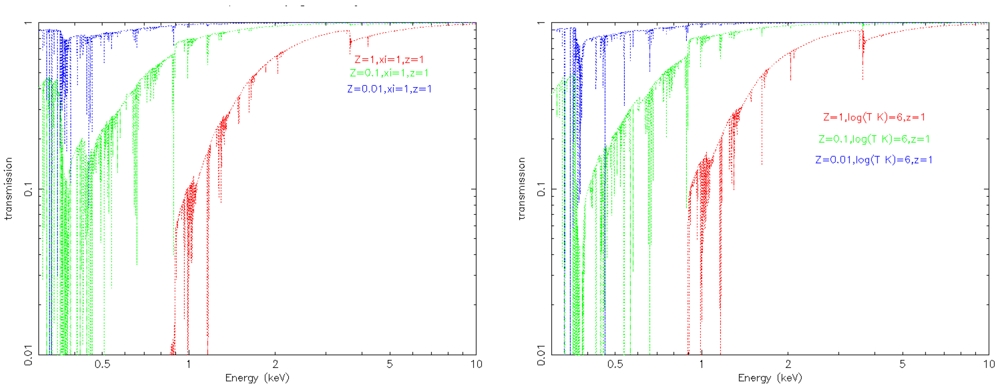

Figure 1.10: Impact of varying metallicity on transmission in the IGM. Left panel assumes PIE with redshift and ξ (xi in the plot legend) fixed. Right panel assumes CIE with temperature and redshift fixed

mission plots generated with XSPEC, with certain parameters fixed and varying a single IGM parameter of interest. In the following subsections, I give a sample of plots produced highlighting the differing impacts of the IGM parameter values on transmission.

(i) Metallicity For an IGM equilibrium scenario, the opacity ($\tau_{IGM}(E, z, Z)$ of metallicity (Z) relative to solar at observed photon energy E for a source at redshift z is (from Starling et al., 2013), adapted from (Behar et al., 2011)

$$\tau_{IGM}(E, z, Z) = \frac{n_0 c}{H_0} \int_0^z (\sigma_{HHe}(E, z) + \sigma_{metals}(E, z, Z)) \times \frac{(1+z)^2 dz}{[\Omega_M (1+z)^3 + \Omega_\Lambda]^{\frac{1}{2}}} \tag{1.2}$$

where n_0 is the hydrogen density at redshift zero, H_0 is the Hubble constant, Ω_M and Ω_Λ are the matter and dark energy fractions of the critical energy density of the Universe. As the metallicity in the IGM reduces, the potential absorption by ions decreases. In Fig. 1.10 left panel, the impact on transmission is shown for a PIE IGM model with redshift and ionisation parameter (ξ or xi in the legend) fixed and three different values of metallicity. When the plots were repeated using the CIE model with a fixed temperature and redshift, it was noted that the metallicity variations had very similar impacts on transmission (Fig. 1.10 right panel).

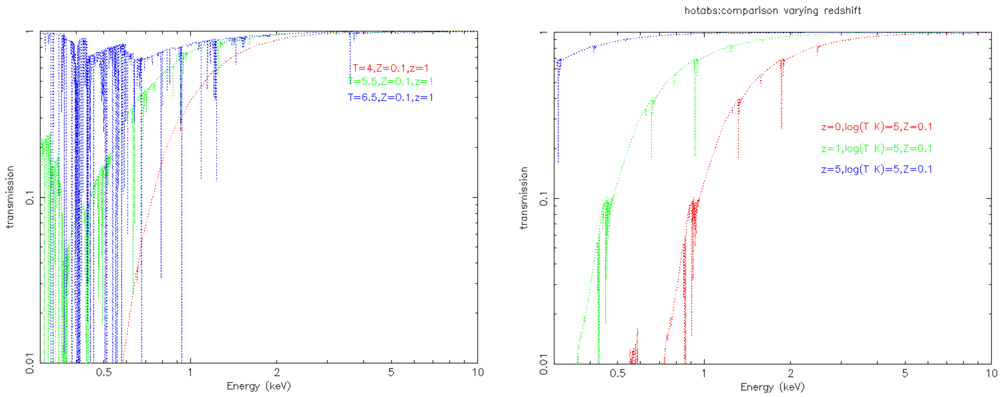

Figure 1.11: Impact of varying temperature and redshift on transmission in the IGM for CIE. Left panel assumes metallicity and redshift fixed with T at different values. Right panel assumes metallicity and temperature fixed with different redshift values. Z is in solar units.

(ii) CIE redshift and temperature impact In Fig 1.11, I show the impact of varying temperature and redshift for a CIE IGM model on transmission, with metallicity fixed. In the left panel, with redshift and metallicity fixed, transmission is far greater at log(T/K) = 6 compared to 4. In the right panel, the significant impact of redshift on transmission is clear, where the IGM slab redshift is given for $z = 0$, 1 and 5.

In summary, initial trials using XSPEC to generate transmission plots for IGM models using the slab approach were useful in understanding the impact on transmission in the IGM under different CIE and PIE scenarios.

1.6 My contribution to the field

This thesis derives values for IGM properties by fitting models to the X-ray spectra of highly luminous distant tracers i.e. baryon densities, metallicity, temperature and ionisation parameters. My contributions include demonstrating that these tracers can indeed be used to generate and anlayse such IGM parameters. An essential part of this work is examining each tracer host environment, modelling it realistically, in order to isolate IGM absorption. Further, the use of different tracer objects, across a substantial redshift range enables comparative analysis to determine if the tracers show consistent results that can more robustly parameterise the properties of the IGM. The results are also used to examine whether they are consistent with or challenge the current ΛCDM concordance model e.g. in terms of column density and redshift. I will demonstrate that the IGM contributes significantly to column density in tracers, proportional to redshift. My contribution also includes examining the impact of the prior conventional assumptions used for IGM tracers, and a better understanding of the reliability of the results given the risk of unrealistic assumptions, degeneracies and limitations of current instrument signal to noise and spectral resolution.

CHAPTER 2

Gamma-ray bursts as tracers of the IGM using realistic host galaxy metallicities

This paper was published as Dalton T., Morris S. L., 2020, MNRAS, 495, 2342, and reproduced here with minor formatting changes.

2.1 Summary

It is known that the gamma-ray burst (GRB) equivalent hydrogen column density (*N*HX) changes with redshift and that, typically, *N*HX is greater than the GRB host neutral hydrogen column density. We have compiled a large sample of data for GRB *N*HXIGM and metallicity [*X*/H]. The main aims of this paper are to generate improved *N*HX for our sample by using actual metallicities, dust corrected where available for detections, and for the remaining GRB, a more realistic average intrinsic metallicity using a standard adjustment from solar. Then, by approximating the GRB host intrinsic hydrogen column density using the measured neutral column adjusted for the ionisation fraction (*N*H I,IC), we isolate a more accurate estimate for the intergalactic medium (IGM) contribution. The GRB sample mean

metallicity is $= -1.17 \pm 0.09$ rms (or 0.07 ± 0.02 $Z/Z_\odot$) from a sample of 36 GRB with a redshift $1.76 \leq z \leq 5.91$, substantially lower than the assumption of solar metallicity used as standard for many fitted $N\textsc{hx}$. Lower GRB host mean metallicity results in increased $N\textsc{hx}$ estimated with the correction scaling with redshift as $\Delta\log(N\textsc{hx}\ \mathrm{cm}^{-2}) = (0.59 \pm 0.04)\log(1 + z) + 0.18 \pm 0.02$. Of the 128 GRB with data for both $N\textsc{hx}$ and $N\textsc{h i,ic}$ in our sample, only 6 have $N\textsc{h i,ic} > N\textsc{hx}$ when revised for realistic metallicity, compared to 32 when solar metallicity is assumed. The lower envelope of the revised $N\textsc{hx} - N\textsc{h i,ic}$, plotted against redshift can be fit by $\log(N\textsc{hx} - N\textsc{h i,ic}\ \mathrm{cm}^{-2}) = 20.3 + 2.4 \log(1 + z)$. This is taken to be an estimate for the maximum IGM hydrogen column density as a function of redshift. Using this approach, we estimate an upper limit to the hydrogen density at redshift zero (n_0) to be consistent with $n_0 = 0.17 \times 10^{-7}$ cm^{-3}.

2.2 Introduction

GRBs are among the most powerful explosions known in the universe, see Schady (2017, hereafter S17) for a recent general review of GRB. Given the huge range of redshifts and distances for GRBs, and their high luminosities combined with the broad energy range of observed emissions, GRBs provide a valuable probe of all baryonic matter along the line-of-sight (LOS). X-ray absorption yields information on the total absorbing column density of the matter between the observer and the source because any element that is not fully ionised contributes to the absorption of X-rays (scattering by electrons becomes important at high energy above 10keV (Wilms et al., 2000, hereafter W00). Although the X-ray absorption cross-section is often dominated by metals, with hydrogen and helium contribution being minimal but not nil (Fig.1 W00), it is typically reported as an equivalent hydrogen column density. $N\textsc{hx}$ consists of contributions from the local GRB environment, the IGM, and our own Galactic medium. However, X-ray absorption cannot reveal the redshift of the matter in the column due to a lack of spectral resolution and signal to noise. It is important to note that the common practice is to make the simplifying assumption that all X-ray absorption in excess of Galactic is at the redshift of the host, neglecting any IGM contribution (e.g Watson et al., 2007; Starling et al., 2013, hereafter S13). The GRB N_{HX} versus redshift relation has been investigated for many years. Early reports were based on small samples (e.g. Campana et al., 2010; Behar et al., 2011; Watson et al., 2013). A claimed strong correlation with redshift has recently been updated and confirmed with a much larger GRB sample by Rahin and Behar (2019). It has also been reported in many papers that the neutral intrinsic hydrogen column (N_{HI}) in GRB DLAs has no significant correlation with redshift (e.g. Watson et al., 2007). Further, it was also noted in these papers, that N_{HX} exceeds N_{HI} in GRB, often by over an order of magnitude.

The cause of an N_{HX} excess over N_{HI}, and the N_{HX} correlation with redshift is the source of much debate. One school of thought argues that the GRB host accounts for all the excess and evolution, e.g. a dense environment near the burst location (Campana et al., 2012, hereafter C12), ultra-ionised gas in the environment of the GRB (Schady et al., 2011, hereafter S11), dust extinction bias (Watson and Jakobsson, 2012), dense Helium He II regions close to the GRB (Watson et al., 2013), and/or a host galaxy mass N_{HX} relation (Buchner et al., 2017). Models for GRB N_{HX} being produced exclusively by gas intrinsic to the GRB host galaxy have required extreme conditions to be present within the absorbing material. The other school of thought argues that some of the excess N_{HX} and redshift correlation is due to the full integrated LOS including the diffuse IGM and intervening objects. Behar et al. (2011) modelled the effects of a cold, neutral, highly metal-enriched IGM model and showed that, at high redshift, this could produce the dominant excess X-ray absorption component. S13 modelled a more realistic warm IGM (WHIM) with temperature of between $10^5 - 10^{6.5}$K and metallicity of $\sim 0.2Z/Z_{\odot}$. Campana et al. (2015) used cosmological simulations to model the WHIM. Their results suggested that most of the excess N_{HX} absorption arises from discrete over-densities along the LOS to GRB, supporting the possibility of a significant contribution of the IGM to the NHX - redshift relation.

All of the theories thus far have relied upon key assumptions (listed below) which, if unrealistic, will substantially affect the results.

2.2.1 Metallicity

It is known that GRB galaxy hosts have, on average, sub-solar metallicity, and that assuming solar metallicity in the X-ray fits introduces a systematic error, and generates an NHX that is effectively, a minimum (Krühler et al., 2015; Tanga et al., 2016, S13). Further, models for the WHIM integrated gas density along the LOS heavily rely on the assumed gas metallicity of the WHIM. It is standard practice currently to assume solar metallicity when fitting models to GRB X-ray spectra. The main reasons for this historically were the small numbers of reliable metallicity measurements and poor constraints on any redshift metallicity evolution (S13). Even an assumption of solar metallicity, however, can lead to inconsistencies, as research improves the knowledge of solar abundances. The solar abundances of the key metals reported in the literature have undergone considerable changes in recent decades, for a useful review see Asplund et al. (2009). The X-ray fitting software XSPEC[*] (Arnaud, 1996) is the most commonly used for GRB. Within XSPEC, the default solar abundances are those of Anders and Grevesse (1989). However, there are six other options for solar abundance in XSPEC. The more commonly used is that of W00. S13 noted that their results using W00 abundances were consistently higher than the NHX reported in the UK Swift Science Data Centre[†] repository (hereafter *Swift*), which at the time were based on Anders and Grevesse (1989). These have since been updated using W00.

Some comments have been made in literature as to how NHX scales with metallicity e.g. S13 stated that NHX scales approximately with metallicity, and Krongold and Prochaska (2013) stated that the X-ray estimated oxygen column density has a

---

[*] https://heasarc.gsfc.nasa.gov/xanadu/xspec/

[†] www.swift.ac.uk

linear dependence on metallicity and density. Metallicity is the main focus of this paper and Section 2.4 examines the impact of the assumed metallicity on the derived N_{HX} in some detail.

2.2.2 Location of excess absorption

It is standard practice, when fitting models to GRB spectra, to assume all absorption in excess of the Galactic contribution is at the redshift of the GRB. X-ray optical depth is a function of frequency or energy, due to the frequency dependence of the cross-section (Morrison and Mccammon, 1983). The scaling relation between the observed amount of X-ray absorption for GRB and redshift was found by Campana et al. (2014b) to be approximated by

$$N_{\mathrm{H}}(z = 0) = \frac{N_{\mathrm{H}}(\mathrm{z})}{1 + z^{a}}, a = 2.4 \tag{2.1}$$

The error in X-ray column density produced by assuming the total absorption is at the GRB redshift arises from the difference in redshift between the GRB and any intervening contributor. Hence, the potential error in N_{HX} increases with redshift of the GRB, dependant on the amount of IGM absorption, its location, and any error in the scaling law assumed. The IGM hydrogen column estimation is highly uncertain as the metal pollution is very poorly determined (e.g Fumagalli, 2014; Maiolino and Mannucci, 2019).

2.2.3 Neutral fraction

The value found for the column density is almost always determined assuming a 100 per cent neutral absorbing gas (e.g Behar et al., 2011, S11, S13). An ionised absorber would have a lower cross-section at X-ray energies, and a larger column density would be required to produce the same opacity. Therefore, the neutral assumption could cause N_{HX} to be underestimated (S11).

2.2.4 Galactic absorption

Column densities for GRB reported have normally had the Galaxy contribution *N*HGal removed. The most common references for the *N*HGal are the Leiden Argentine Bonn (LAB) H I survey (Kalberla et al., 2005) and Willingale et al. (2013).

In conclusion, *N*HX, based on an assumed solar metallicity and 100 per cent neutral absorbing gas should be considered as a lower limit. Further, the inconsistent use or lack of reporting of the assumed metallicity, neutral fraction, and scaling factors can add uncertainty to any analysis using published data.

The hypothesis of this paper is that the IGM contributes to the total hydrogen column density, with the contribution increasing with redshift, as observed in GRB *N*HX, and that by correcting the GRB *N*HX using a more realistic GRB intrinsic metallicity, and estimating the host *N*H using the measured neutral intrinsic *N*HI adjusted for ionisation fraction (from optical spectra rest-frame UV of GRB afterglow), we can isolate a more accurate *N*HIGM contribution. The objectives of this paper are: (i) A review of the literature on the metallicities of GRB host environments to obtain improved values to use when estimating *N*HX, (ii) To present a revised GRB *N*HX, using these more realistic metallicities and hence to update the *N*HX – redshift relation. (iii) To isolate the IGM contribution to the total *N*HX in GRB, by using GRB ionised corrected *N*H I,IC as an estimate of the GRB intrinsic *N*HX and plotting *N*HX – *N*H I,IC against redshift, after the improved metal corrections have been used. (iv) To compare an estimated *N*HIGM based on a simple model of the IGM with our lower envelope for *N*HX based on realistic metallicities and with the intrinsic *N*H I,IC removed. Section 2.3 sets out the methodology, data selection approach, and the data used. Section 2.4 presents the results with a discussion and an analysis. Section 2.5 sets out the main conclusions. The Appendix to chapter 2 gives further details on the Section 2.4 analysis, including the metallicity and the resulting fractional increase in *N*HX with redshift. Throughout this paper, the term 'metallicity' is used synonymously with metal abundance $[X/\mathrm{H}]$*. Where relevant, the ΛCDM cosmology variables used are $H_0 = 70$ km s^{-1} Mpc^{-1} , $\Omega_m = 0.3$, and $\Omega_\Lambda = 0.7$ unless otherwise stated.

2.3 Methodology and Data Selection

The full sample used here consists of all *Swift* X-ray Telescope (XRT) (Burrows et al., 2005)(hereinafter *Swift*) observed GRB with spectroscopic redshift available up to 2019 July 31, plus GRB090429B which has a photometric redshift of 9.4 (Cucchiara et al., 2011). The vast majority of the *N*HX data is taken from the *Swift* repository to ensure a homogeneous data set (S13). Alternative sources were used only where detections with measured errors were available, and where *Swift* has only reported column density lower limits consistent with zero, or where the errors reported in the alternative source were smaller e.g. Arcodia et al. (2016) used a stricter methodology by selecting specific time intervals when hardness ratios were constant to minimize spectral variations. For all sources, we endeavoured to ensure the methodology and selection criteria were consistent in terms of confidence level and XSPEC models used. Data from the *Swift* repository for *N*HX were taken from the Photon Counting Late Time mode, as they are most likely to be a more stable, final value since spectral slope evolution is more prevalent at early times, leading to poor quality fits using a single power law (Page, K., private communication). All *N*HX error bars reported are the 90 per cent confidence range, unless otherwise stated.

We follow the *Swift* repository reporting conventions for *N*HX i.e. we treat as an upper limit the cases where the best fit *N*HX is zero. Further, where the lower limit of the 90 per cent confidence interval includes zero, we use the best-fitting *N*HX but use a different symbol for these objects in our figures. Where we refitted spectra for analysis, XSPEC v12.10.1 was used. Spectra were fitted with a power

---

*$[X/\mathrm{H}] = \log(X/\mathrm{H}) - \log(X/\mathrm{H})$ solar, where X is the metal element, and H is Hydrogen

law in the X-ray band from 0.3 to 10.0 keV, which is suitable for the vast majority of GRB and again is consistent with the *Swift* repository (S13). A fixed Galactic component is taken from *Swift* based on Willingale et al. (2013). The model used in XSPEC was TBABS*ZTBABS*PO where the initial assumption we want to use is that all absorption in excess of Galactic is at the host redshift. TBABS is the Galactic ISM absorption model, ZTBABS is the same model placing the absorption at a fixed redshift and PO is the power-law intrinsic spectral model. Isotopic abundances from W00 were used with the assumption of solar metallicity initially. In Section 2.4, where we examine more realistic metallicities for GRBs, the XSPEC model TBVARABS was used instead of ZTBABS which allows the individual metal abundances to be varied from solar values. Cash statistics (Cstat) were used in XSPEC as this is required for spectra with low count rates, and is consistent with the *Swift* repository (Cash, 1979).

The selection of a sample can introduce bias. Perley et al. (2015) found that GRB with measured redshifts tend to be found in brighter galaxies, which could produce such a bias. However, Rahin and Behar (2019) compared the NHX versus redshift trend for that paper's (smaller) unbiased sample with the full *Swift* sample and found no notable difference. In, Section 2.4, where we require that GRB have both optical and X-ray spectra, this requirement can introduce a selection effect against dim or highly dust extinguished GRBs (S11). It is estimated that between 25 and 40 percent of GRBs are undetected in the optical wavelength range as a result of dust extinction (e.g. Greiner et al., 2011). Therefore, the conclusions in that section may not apply to dust extinguished or dim GRBs.

All data for NHI were taken from Tanvir et al. (2019b). Of the 140 objects in their sample, we have used 128 which have NHX data in our analysis. In Section 2.4, we adjust the NHI for the ionisation fraction for log(NHI cm^{-2}) $\leq$ 20. The redshift range in our full GRB NHX sample is from 0.03 to 9.4, while the NHI sample redshift range is from 1.6 to 6.73. The lower NHI redshift cut-off is due to the requirement that the observed wavelength of the Ly α absorption line be in the

Table 2.1: The GRB full sample (extract shown here - see the online version of this paper for the complete table with all values listed). Column (1) GRB identification, (2) spectroscopic redshift (photometric for GRB090429B), (3) log(NHX/cm^{-2}) , (4) Refs for log(NHX/cm^{-2}) (note all are from the *Swift* repository if no ref given), (5) log(NHI/cm^{-2}) (all from Tanvir et al. (2019b)). Those with 'IC' have been corrected for ionisation fraction, (6) [X/H], (7) refs for [X/H].

GRB	z	$\log(\frac{N\mathrm{HX}}{\mathrm{cm}^{-2}})$	NHX Ref	$\log(\frac{N\mathrm{HI,IC}}{\mathrm{cm}^{-2}})$	$[X/\mathrm{H}]$	$[X/\mathrm{H}]$ Ref.
090926A	2.11	$21.74^{+0.19}_{-0.17}$	1	21.55 ± 0.10	-1.97 ± 0.11	2
090809	2.74	$21.85^{+0.27}_{-0.85}$	-	21.70 ± 0.20	-0.86 ± 0.13	2
080210	2.64	$21.32^{+0.21}_{-0.32}$	-	21.90 ± 0.10	-1.21 ± 0.16	3
090313	3.38	$21.64^{+0.13}_{-0.18}$	-	21.30 ± 0.20	-1.40 ± 0.30	2
120909A	3.93	$21.41^{+0.16}_{-0.24}$	-	21.70 ± 0.10	-1.06 ± 0.20	2

Table 1 Refs: (1) (Zafar et al., 2018), (2) (Bolmer et al., 2019), (3) (Arabsalmani et al., 2018)

visible/UV band.

In Section 2.4.5, we analyse the impacts on NHX of using metallicities that more realistically reflect the LOS absorption through the entire host galaxy. X-ray absorption is dominated by the metals and H and He are relatively unimportant. Below 1 keV, C, N, O, and Ne are the main absorbers, while above 1 keV, Si, S, and Fe dominate (W00). W00 also note that interpreting X-ray observations is subject to the uncertainties remaining in the atomic data. Data for metallicities in Table 2.1 are all UV/optical absorption line based. Absorption metallicities measure the metal enrichment of gas along the LOS from the GRB through the galaxy.

Table 2.1 contains the data for an extract of the full GRB sample for redshift, NHX, NH I,IC and metallicity where data are available. We list in the table extract, a sample of five GRB with data for all columns (see the online version of this paper for the complete table with all values listed). (See Appendix chapter 2 for an investigation about whether a flux limited sample would introduce any substantial bias).

2.4 Results and Analysis

In this section, we examine the distributions of GRB NHX and NHI with redshift, and the use of adjusted NHI,IC as an approximation for the GRB host intrinsic contribution to the total integrated hydrogen column density to isolate the IGM column density. We then examine GRB host metallicity to derive a more accurate metallicity to use in XSPEC fitting to get an improved NHX. Finally, we replot the distributions of revised NHX and NHX − NHI,IC with redshift to get the lower envelope of GRB NHX as a step towards constraining NHXIGM.

2.4.1 NHX and redshift

Fig. 2.1 shows the distribution of NHX with redshift (based on the standard assumptions of solar metallicity and that all the absorption, NHX is at the GRB redshift) for the full *Swift* observed sample with known spectroscopic redshift (with the exception of GRB090429B where the redshift is a photometric estimate). Where an estimate of the actual NHX was available from the *Swift* repository but the 90 per cent confidence interval included zero, these are plotted with a yellow dot. Yellow dots with arrows are the upper limits where the *Swift* repository has a best fit of zero NHX.

A relationship or dependence between NHX and redshift has been reported in several papers over the last decade (e.g. Behar et al., 2011, S13). The correlation statistics for the full 352 GRB sample are Pearson r = 0.29 and Spearman ρ = 0.55. For the detection only sample (226 GRB), the correlation results are Pearson r = 0.51 and Spearman ρ = 0.49. Both samples pass the null hypothesis test, indicating that the correlation seen is significant. However, when we used an error weighted least-squares fit to a linear model (χ^2), the reduced χ^2 was large, indicating either that a simple linear redshift relation is not a realistic model or that there is an additional substantial source of scatter. We checked for the impact of outliers with

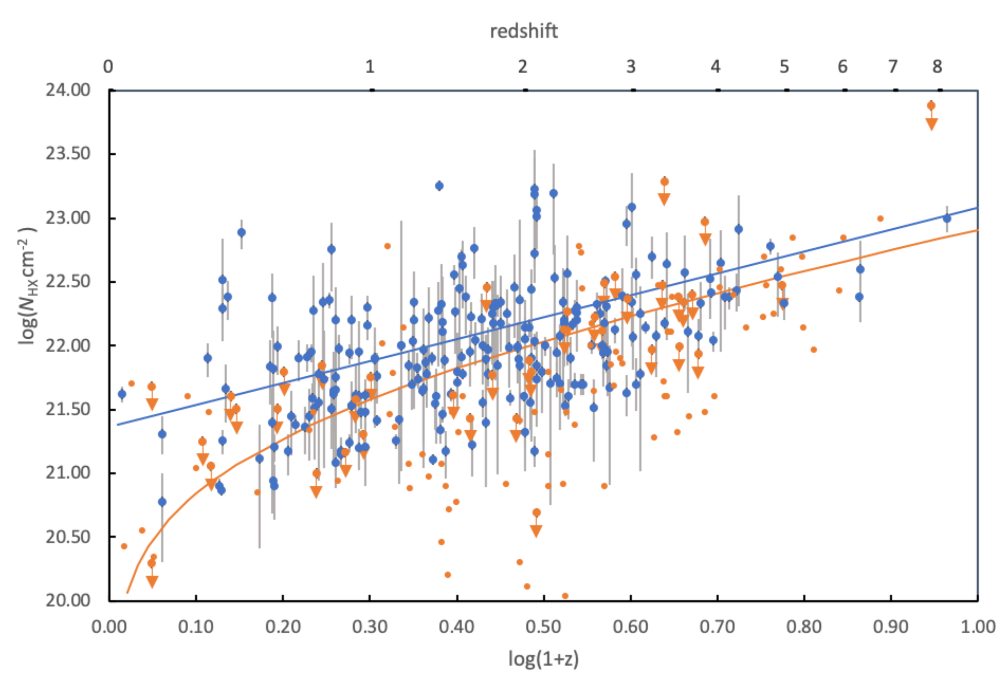

Figure 2.1: Distribution of intrinsic X-ray column densities with redshift for the full 352 GRB *Swift* observed sample. The blue dots represent the GRB detections with error bars. The orange dots are best fits where the 90 per cent confidence interval includes zero. The orange dots with arrows are the upper limits where *Swift* repository has a best fit of zero. The blue line is the χ^2 best fit with for the GRB data with error bars. The orange line represents the integrated hydrogen density (NHIGM) from a simple diffuse IGM model (see equation 2.2). The correlation statistics for the full 352 GRB sample are Pearson r = 0.29 and Spearman ρ = 0.55 (for the detection only sample (226 GRB) r = 0.51 and ρ = 0.49)

high NHX and very small error bars. To bring the reduced χ^2 close to 1 would have required the removal of over 10 per cent of the sample.

We include in Fig. 2.1 a simple model of the diffuse IGM following S13 (equation 5 in that paper) based on

$$N_{\mathrm{HXIGM}} = \frac{n_0 c}{H_0} \int_0^z \frac{(1+z)^2 dz}{[\Omega_M (1+z)^3 + \Omega_\Lambda]^{\frac{1}{2}}} \tag{2.2}$$

where n$_0$ is the hydrogen density at redshift zero, taken as 1.7×10^{-7} cm^{-3} (Behar et al., 2011).

The solution to the integral from Shull and Danforth (2018)(equation 4 in that paper) is

$$\frac{2}{3\Omega_M}((\Omega_M(1+z)^3+\Omega_\Lambda)^{\frac{1}{2}}-1) \tag{2.3}$$

In Fig. 2.1, we can see the NHXIGM model runs through the GRB data points. If it is to represent the diffuse IGM only, we would expect all the GRB to be above this curve (if there were no measurement errors). Given the large error bars for many GRB, the IGM hypothesis could still be plausible where a small fraction, 10 per cent approximately given the 90 per cent confidence, are below the curve. A much higher fraction than 10 per cent are below the IGM curve in Fig.2.1. However, the IGM model is admittedly very simple and therefore could poorly represent the real Universe. Also, not all LOS will be at the mean density.

We note that our model is based on the mean hydrogen density as a simple model, so the metallicity uncertainty in the IGM does not affect it directly. In our next paper, the metallicity in different phases of the IGM will be reviewed in detail. We examine this further in Section 2.4.3 onwards.

2.4.2 NHI review with redshift

In this section, we review the most recent substantial GRB NHI sample from Tanvir et al. (2019b) which consists of new measurements combined with those from literature. We examine this latest sample for any relations between NHI and redshift, or with NHX.

Optical spectroscopy enables the approximate location of any neutral hydrogen absorber to be identified. GRB hosts are typically found to have high column densities of cold neutral gas, with a large fraction of GRB hosts containing a DLA system ($\log(N\text{HI}/\text{cm}^{-2}) > 20.3$) or sub-DLA ($19.0 < \log(N\text{HI}/\text{cm}^{-2}) < 20.3$) (S11). Much of the neutral gas component is found at a few hundred parsecs from the GRB (Ledoux et al., 2009). The term ”cold” in this sense has been found to be $T/K < 500$ (e.g. Neeleman et al., 2015; Heintz, 2019).

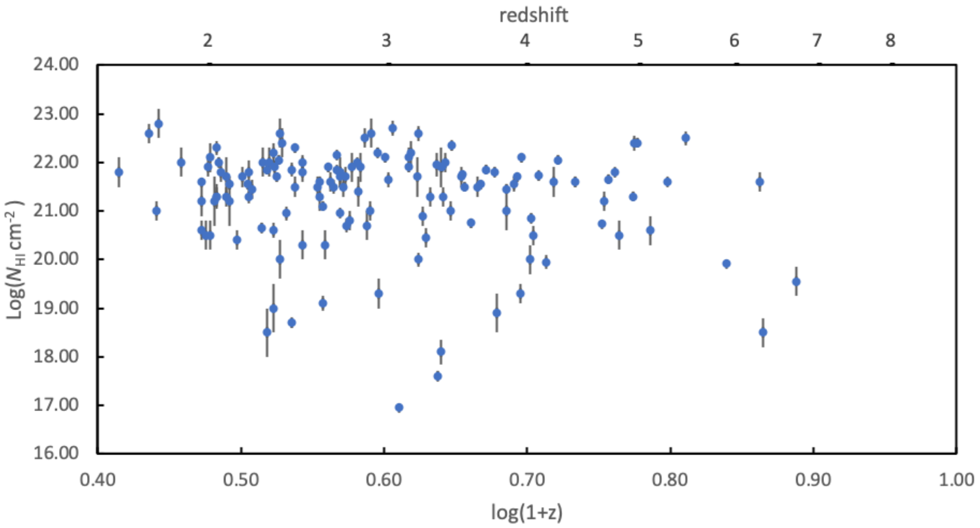

Figure 2.2: Distribution of *N*HI with redshift. No strong trends with redshift are visible.

Fig. 2.2 shows the distribution of the GRB *N*HI sample with redshift. Where not specified in literature, we have assumed the errors are Gaussian and correspond to one standard deviation. The Pearson r is -0.15 and Spearman ρ -0.10. Both fail the null hypothesis test i.e. there is no statistically significant correlation. The lack of a detectable redshift correlation for *N*HI is in contrast with the clear redshift correlation for *N*HX. Clearly, this does not provide support for the argument that redshift evolution in the GRB host properties is responsible for the redshift correlation for *N*HX. (See Appendix Chapter 2 for further review of any *N*HI correlation with *N*HX).

2.4.3 Using NHI,IC as proxy for the GRB intrinsic contribution to NHX

Part of the aim of this paper is to attempt to isolate an IGM contribution to *N*HX. Here, we investigate the plausibility of assuming that the host intrinsic hydrogen column density is equal to the measured ionised corrected intrinsic neutral column (*N*HI,IC) and examine the resulting residual column's dependence on redshift. To do this, we first make an ionisation correction (IC) to the hydrogen column density as measured by *N*HI using the approach described in Fumagalli et al. (2016) who

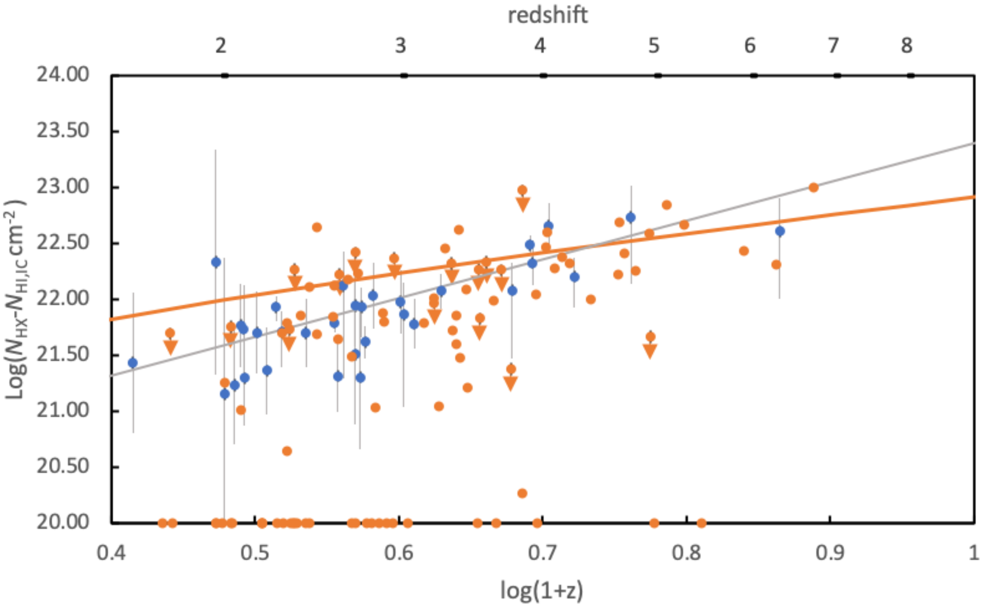

Figure 2.3: Distribution of total NHX minus localised NHI,IC (which is being used as a proxy of the intrinsic GRB hydrogen column density) in the sub-sample of 128 GRB with both NHX and NHI,IC. The blue dots are GRB detections for both NHX and NHI,IC . The orange dots are best fits where the 90 per cent confidence interval includes zero. The orange dots with arrows are the upper limits where *Swift* repository has a best fit of zero. Where NHX minus NHI,IC < 0 they are placed at 20.0 on the y-axis. The orange line represents the integrated hydrogen density (NHIGM) from a simple diffuse IGM model (see equation 2.2). A power law fit to the NHX minus NHI,IC < 0 versus redshift trend scales as $(1+z)^{3.5\pm0.1}$ (grey line with reduced $\chi^2 = 1.02$). Pearson and Spearman correlation coefficients are 0.75 and 0.69 respectively for the detections, and 0.55 and 0.59 for the full sample where NHX $>$ NHI,IC taking limits as detections.

observed that neutral fraction is a function of NHI. The neutral fraction drops rapidly from ~ 0.7 at log(NHI/cm^{-2}) ~ 20 to ~ 0.02 at ~log(NHI/cm $^{-2}$) ~ 18 with a 0.3 dex characteristic error. As the vast majority of GRB are in hosts with high column density DLAs, only 11 out of 128 GRB sample required an IC.

Of the 128 GRB with data for both NHX and NHI in our sample, 96 have NHX $>$ NHI,IC. In Fig.2.3, these are plotted, with the remaining 32 placed at the bottom of the figure for completeness. 32 of the GRB from this sub-sample (blue dots) are detections for both column densities. Where an estimate of NHX was available from the *Swift* repository but the confidence interval included zero, the object was plotted with a orange dot. The orange dots with arrows are the upper limits where *Swift* repository has a best fit of zero NHX. The correlation statistics for NHX and redshift for the sub-sample of 32 GRB detections with NHX > NHI are Pearson r = 0.75 and Spearman $\rho = 0.69$ (for the full 128 sub-sample taking limits as detections one gets r = 0.55, $\rho = 0.59$.) The NHX $-$ NHI,IC relation with redshift is much more significant than for a NHX alone. The reduced $\chi^2 = 1.02$ for a linear fit of the detection sample with the form NHX $-$ NHI,IC $\propto (1+z)^{3.5\pm0.1}$. It can be argued that this result supports the case for using NHI,IC as a proxy for the GRB intrinsic hydrogen column density, leaving the major remaining column density contribution being from the IGM. Note that there could be bias due to the exclusion of data with upper limits only. A further caveat is that a large part of the sub-sample has been excluded as the X-ray or UV column density was not measured. The fraction excluded because NHI,IC > NHX (32/128) is a cause for concern, as NHX is supposed to be the total column density. The large error bars on NHX may account for some of these. We can also see that the original NHIGM model is higher than the majority of the estimated intervening absorption. This may indicate that the IGM model is too simple e.g. it ignores LOS variation, or that the parameters used in the simple model need to be adjusted. However, the result could well be due to unrealistic assumptions of metallicity and ionisation for the GRB host galaxy. The next section examines the effects of assumptions about GRB host metallicity.

2.4.4 GRB host metallicity

GRB typically occur in sub-solar metallicity galaxy host environments (Cucchiara et al., 2015; Krühler et al., 2015, S13). Our sub-sample of 36 GRB with a range in redshift of $1.76 \leq z \leq 5.91$, and [X/H] from -2.18 to 0.25 is plotted in Fig. 2.4. Where data from multiple sources were available, we took those with the smallest reported errors. Further, we only used data with detections and error bars, and excluded those with lower limits only. This resulted in omitting most of the 55 GRB from Cucchiara et al. (2015, hereafter C15). The Pearson and Spearman

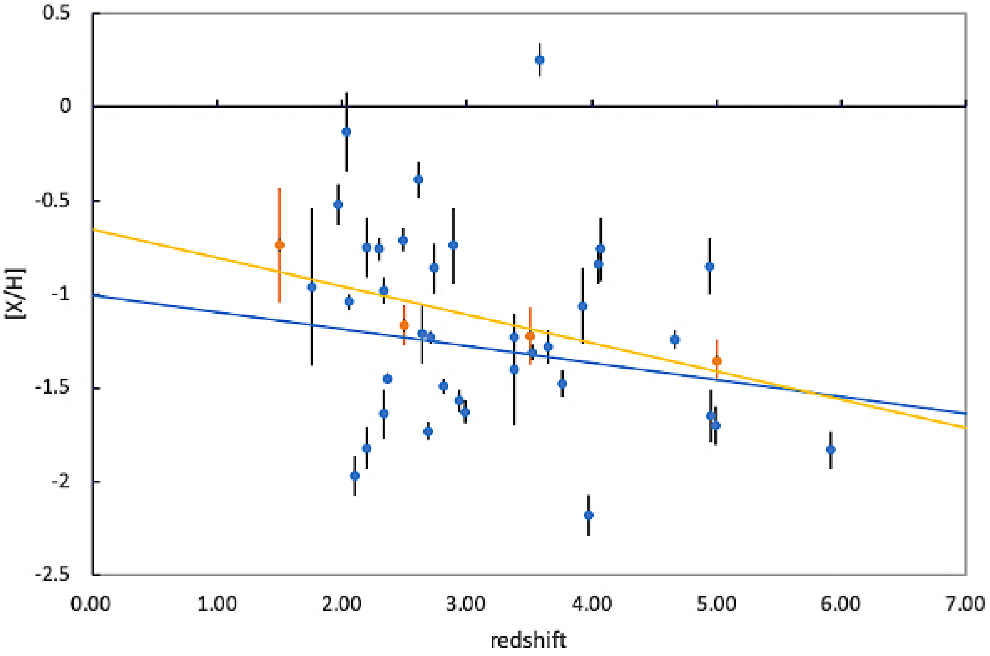

Figure 2.4: Distribution of the combined GRB absorption-based metallicities (blue dots) with redshift. The GRB absorption sample mean metallicity is -1.17 ± 0.09 (or $0.07 \pm 0.05 Z/Z_{\odot}$). The orange dots are the weighted average metallicity over specific redshift bins of bins $\Delta z = 1$ (except for $z = 4$ to 6 as there is only one GRB with $z > 5$) weighted by the total NHI. The Pearson and Spearman correlation coefficients are r = -0.24 and $\rho = -0.27$, both correlations failing the null hypothesis tests, indicating there is no statistically significant correlation between GRB metallicity and redshift. The blue line is the χ^2 linear fit to the blue dot data. The orange line is the best linear fit to the orange dots for the weighted average [X/H] and shows possible evolution (see Appendix Chapter 2 for more discussion).

correlation coefficients are r = -0.24 and $\rho = -0.27$. However, both correlations fail the null hypothesis test, indicating there is no statistically significant correlation between GRB metallicity and redshift. The blue line is the best linear fit to the data is

$$[X/H] = (-1.01 \pm 0.04) - (0.09 \pm 0.01)z \tag{2.4}$$

This possible mild metallicity evolution of GRB intrinsic gas with redshift is noted in some of the literature. For non-GRB absorption systems, stronger evolution is seen. For example, De Cia et al. (2018) reported evolution with a slope of $\sim 0.32z$.

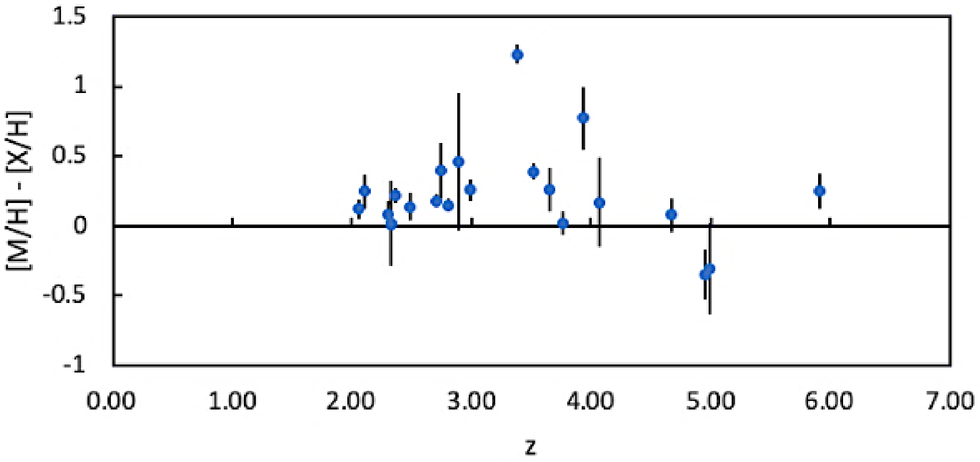

Figure 2.5: Plot of the dust correction to metallicities [M/H]-[X/H] by redshift for the Bolmer et al. (2019) GRB sample. The Pearson and Spearman coefficients are -0.14 and 0.03, respectively, and both fail the null hypothesis tests for a significant correlation. There is no detectable evolution.

However, GRB metallicity does not appear to evolve as much, if at all, based on our sample. This is consistent with C15, for example.

It is well known that dust depletion affects the determination of metallicity in GRBs (e.g. Savaglio, 2006; De Cia et al., 2013). In Bolmer et al. (2019), 22 GRB are studied at $z > 2$ for features including dust depletion measurements and any relation to redshift. Based on this sample, they found that, on average, the dust corrected metallicity $[M/\mathrm{H}] = -1.09 \pm 0.50$ compared with -1.27 ± 0.37 for the uncorrected metallicity (0.08 $Z/Z_{\odot}$ versus 0.05 $Z/Z_{\odot}$, respectively). This is an average correction of 0.2 dex which is considerably lower than found by De Cia (2018) (0.4-0.5 dex) for non-GRB objects. In Fig. 2.5, we plot the dust correction $[M/\mathrm{H}] - [X/\mathrm{H}]$ versus redshift for the Bolmer et al. (2019) sample, to see if there is any obvious evolution with redshift. No detectable evolution is seen. The Pearson and Spearman coefficients for Fig. 2.5 are -0.14 and 0.03, respectively and both fail the null hypothesis tests for a significant correlation.

Where actual dust corrections are not available, an argument can be made for using a standard dust correction to metallicity for XSPEC fitting for example, based on the Bolmer et al. (2019) mean value of 0.2 dex. This mean correction increases the average metallicity in our sample from 0.07 to $0.11 Z/Z_\odot$.

While this is an important correction to [X/H], the impact on revised NHX is very small as the corrected metallicity is still << solar [X/H]. Testing a sample of GRBs at redshift from 1 to 7, the change in $\log(N\text{HX}/\text{cm}^{-2})$ after making a dust correction was 0.03 to 0.06 dex. Further, how any dust correction is estimated and used in the literature is not always clear. In conclusion, given that the impact of an average dust correction to NHX is very small, we do not consider that a standard dust correction to the metallicity adjustment is appropriate.

In conclusion, from our GRB metallicity review, the GRB absorption sample mean metallicity is equal to -1.17 ± 0.09 or ($0.07 \pm 0.02\ Z/Z_\odot$). In further analysis therefore, we use the actual metallicity, dust corrected, for detections where available. While noting that some of the literature claims that there is possible mild redshift evolution in GRB host absorption, for the reasons outlined, we chose to use the average metallicity, without evolution or dust correction, of $0.07\ Z/Z_\odot$ for the remaining GRB. This is certainly a more realistic value than simply assuming solar metallicity in revisiting the NHX for the full GRB sample in the next section.

2.4.5 Impact of metallicity assumptions on NHX

We wish to examine the impact on GRB NHX fits in XSPEC of using actual dust corrected metallicities for GRB detections where available. For the remaining GRB, we examine a more realistic average host metallicity than solar, and importantly, look at the variation with redshift. To do this, we used an XSPEC model TBABS*TBVARABS*PO for the X-ray data from GRB151027A (a very high S/N GRB), varying the modelled host redshift between 0 and 10 and testing for metallicities $Z/Z_\odot = 0.07$ (the mean from our sample in Section 2.4.4), and solar. A lower metallicity results in an increased fitted NHX, with the increase varying with redshift (see Appendix chapter 2 for more details). In order to see whether this correction is consistent for different GRB X-ray spectra, we plotted the fractional increase in fitted NHX with redshift for a test sample of three high S/N GRB spectra with differing reported redshifts and NHX. Again, we varied the redshifts between 0 and 10 and used metallicity = 0.07 $Z/Z_{\odot}$ compared with the value assuming solar metallicity. The fractional increase in NHX with redshift is very similar for the three GRB. A power law-fit to the increase for GRB151027A is (orange line in Appendix Fig. 2.11)

$$\Delta\log(N\text{HX}/\text{cm}^{-2}) = (0.59 \pm 0.04)\log(1+z) + (0.18 \pm 0.02) \tag{2.5}$$

A more accurate power law could be obtained from a combined fit for the three GRB. However, this fit is deemed sufficient for the purposes of analysing the impact of a more realistic general metallicity assumption when calculating NHX.

2.4.6 GRB NHX revised for realistic host metallicity

Using actual metallicities, dust corrected where available, and the above power law relation for the remaining GRB, we use the new NHX for our full GRB sample and replot the relation with redshift in Fig. 2.6.

The Pearson and Spearman correlation coefficients are 0.59 and 0.61, respectively, for GRB detections in Fig. 2.6, which are stronger than prior to the correction for a low metallicity. The blue dots are GRB detections. The orange dots with arrows are upper limits where the fitted NHX are 0, and orange dots are where the 90 per cent confidence interval includes zero. The orange line in Fig. 2.6 is the simple model IGM line from equation 2.2. The blue line is an estimate of the GRB lower envelope based on a requirement of having 90 per cent of detections including their error bars to be above the envelope.

$$\log(N\text{HX}/\text{cm}^{-2}) = 20.3 + 2.4\log(1+z) \tag{2.6}$$

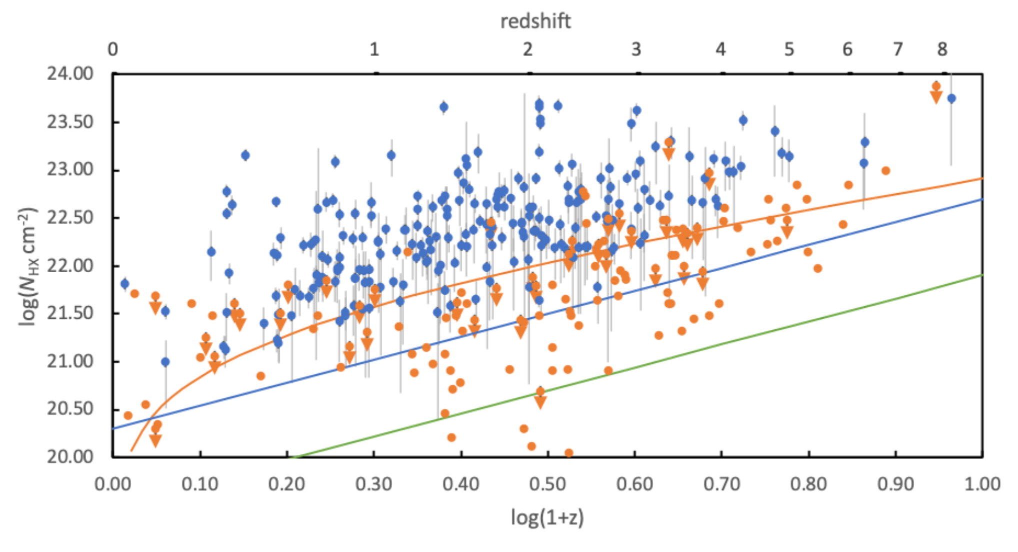

Figure 2.6: GRB *N*HX revised using actual metallicities, dust corrected where available and a mean metallicity of 0.07 $Z/Z_\odot$ for the remaining GRB. The blue dots represent the GRB detections with error bars. The orange dots are best fits where the 90 per cent confidence interval includes zero. The orange dots with arrows are the upper limits where *Swift* repository has a best fit of zero. The orange line represents the integrated hydrogen density (*N*HIGM) from a simple diffuse IGM model (see equation 2.2). The blue line is the GRB lower envelope based on the requirement for 90 per cent of detections, including error bars to be above the envelope, with $\log(N\text{HX}(z = 0)/\text{cm}^{-2}) = 20.3$. The green line is the envelope with the requirement that 99 per cent of all GRB, ignoring error bars, are above the envelope, which has $\log(N\text{HX}(z = 0)/\text{cm}^{-2}) = 19.5$ following the rule of thumb in Campana et al. (2015). Both these envelopes are plotted with assumed slopes of $(1 + z)^{2.4}$ (Campana et al., 2014a). The Pearson and Spearman correlation coefficients are 0.59 and 0.61, respectively, for GRB detections and 0.62 and 0.62 for the full sample treating the limits as detections

The green line is an estimate of the lower envelope based on the requirement that 99 per cent of all GRB measurements, ignoring error bars and treating any upper limits as detections, are above the envelope, using the rule of thumb in Campana et al. (2015) (note that they put *N*HX at the top of the 90 per cent confidence interval where the 90 per cent confidence interval of a fit includes zero, whereas we use the *Swift* best estimate *N*HX which is lower, except for those with best estimates equal to zero).

$$\log(N\text{HX}/\text{cm}^{-2}) = 19.5 + 2.4\log(1 + z) \tag{2.7}$$

The envelope fits may give an indication of the maximum NHXIGM potential contribution to NHX. Both the envelopes have been assumed to scale with redshift as $(1 + z)^{2.4}$ (Campana et al., 2014a), and we note that this may only be realistic for a cold absorber and not for a warm absorber (S13). The GRB LOS goes through a wide range of environments with different temperatures and densities. This will change the effective absorption cross-section at different frequencies. However, we will retain the cold absorber approximation for the current analysis. Using a χ^2 fit, the revised NHX for the detections scale as $N\text{HX} \propto (1 + z)^{1.94\pm0.04}$. However, a large reduced χ^2 indicates that the relationship is not a simple power law or that the data has a large additional source of scatter. We explore this further in Section 2.4.7. Of 226 GRB detections, only 11 are now below the NHIGM curve, not taking error bars into account.

2.4.7 Revised GRB NHX – NHI,IC

As before, to isolate the IGM contribution to NHX, we subtract from the revised NHX the GRB NHI adjusted for an ionisation correction, as a proxy for intrinsic hydrogen column density, as we did in Section 2.4.3, and plot the result against redshift in Fig. 2.7. Of the 128 GRB with data for both NHX and NHI in our sample, 122 now have $N\text{HX} > N\text{HI,IC}$. The $N\text{HX} - N\text{HI,IC}$ for GRB detections now has a best-fitting power-law slope of $(1+z)^{3.1\pm0.3}$ (grey line - with reduced $\chi^2 = 2.6$). The Pearson and Spearman correlation coefficients are 0.65 and 0.67, respectively, for the GRB detections, and 0.53 and 0.62 for the full sample with best fits being treated as detections, where upper limits are treated as detections where the best fit equals zero, and where $N\text{HX} > N\text{HI,IC}$.

This final figure is our best representation of the use of GRB X-ray spectral fits to potentially constrain the IGM hydrogen column density. The blue line is the GRB lower envelope based on the requirement for 90 percent of detections (equation 2.6), including error bars, to be above the envelope. Using eq.2.2, the orange line is NHIGM for a mean hydrogen number density $n_0 = 1.7 \times 10^{-7}$ cm^{-3}. In Fig.

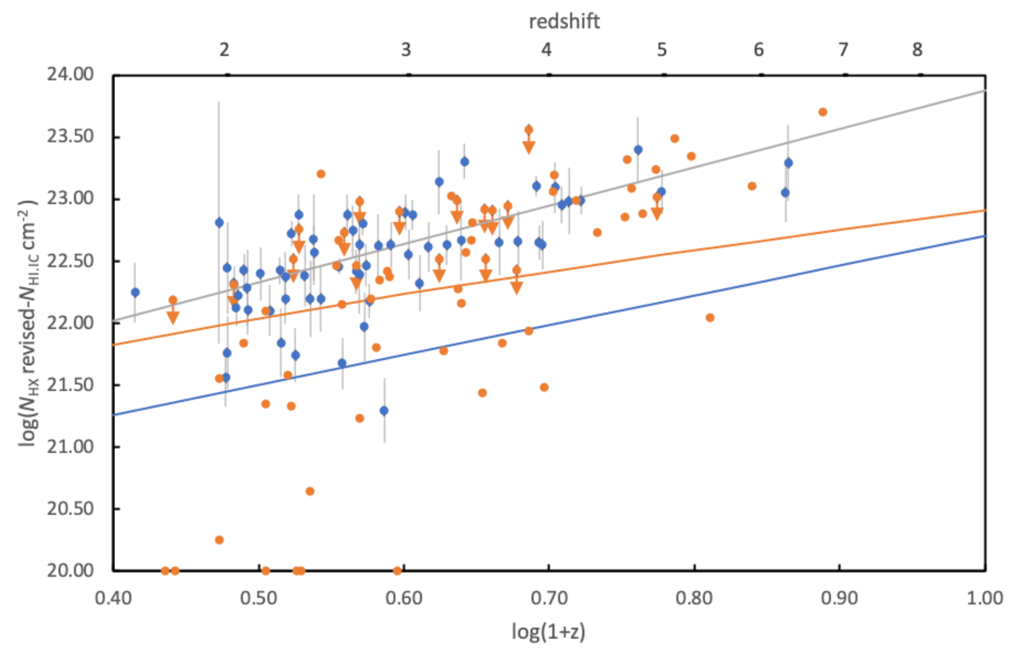

Figure 2.7: Distribution of GRB revised $N_{\rm HX} - N_{\rm HI,IC}$ with redshift. The blue dots are GRB detections and the orange with arrows are upper limits where the $N_{\rm HX}$ best fit is zero, or orange dots where the 90 per cent confidence interval of the X-ray fit includes zero. Where $N_{\rm HX} < N_{\rm HI,IC}$ the GRB are placed at the bottom of the figure for completeness. The orange line represents the integrated hydrogen density ($N_{\rm HIGM}$) from a simple diffuse IGM model (see equation 2.2). The blue line is the GRB lower envelope based on the requirement for 90 per cent of detections, including error bars to be above the envelope, with $\log(N_{\rm HX}(z = 0)/{\rm cm}^{-2}) = 20.3$. The $N_{\rm HX} - N_{\rm HI,IC}$ for GRB detections best fit has a power-law slope of $(1 + z)^{3.1\pm0.3}$ (grey line, reduced $\chi^2 = 2.6$). The Pearson and Spearman correlation coefficients are 0.65 and 0.67, respectively, for the GRB detections, and 0.53 and 0.62 for the full sample with limits treated as detections and where $N_{\rm HX} < N_{\rm HI,IC}$.

2.3, 32 GRB had $N_{\rm HX} < N_{\rm HI,IC}$ compared to only six based on the revised $N_{\rm HX}$ for our updated GRB host metallicity in Fig. 2.7. Therefore, the more realistic GRB metallicity generates a more plausible $N_{\rm HX}$, if it is assumed to represent the total hydrogen column density, which hence must be greater than the intrinsic column density. Several of the GRB $N_{\rm HX}$ have only upper limits (orange dots with arrows). Campana et al. (2015) used censored statistics to factor in both the GRB with error bars and those with upper limits only. The inclusion of the upper limit results was found to lower the resulting sample mean $N_{\rm HX}$. This may suggest that the requirement for high counts or sufficient resolution to determine fits with error

Table 2.2: Summary analysis for refitting of six GRB where the revised NHX < NHI,IC and one where the revised NHX − NHI,IC is substantially below NHIGM. (1) GRB name; (2) log(NHI cm^{-2}); (3) Measured metallicity from literature if available; (4) revised log(NHX cm^{-2}); (5) Whether the revised NHX > NHI,IC); (6) log(NHIGM cm^{-2}) at the GRB redshift; and (7) whether the revised NHX − NHI,IC is greater than NHIGM.

GRB	$\log(\frac{N\mathrm{HI}}{\mathrm{cm}^{-2}})$	Measured $Z/Z_\odot$	$\log(\frac{N\mathrm{HX}}{\mathrm{cm}^{-2}})$	New NHX >NHI,IC	$\log(\frac{N\mathrm{HIGM}}{\mathrm{cm}^{-2}})$ at GRB z	NHX − NHI,IC > IGM?
050922C	21.55 ± 0.10	0.15[a]	22.04*	Y	22.04	Y
120119A	22.60 ± 0.20	0.11[b]	22.45 ± 1.74	Y	21.91	Y
120815A	21.05 ± 0.10	0.04[c]	22.16*	Y	22.09	Y
121027A	22.80 ± 0.30	**	22.86 ± 1.20	Y	22.10	Y
160227A	22.40 ± 0.20	**	22.08 ± 1.15	Y	22.10	within errors
181020A	22.20 ± 0.10	0.27[c]	22.38 ± 1.25	Y	22.22	Y
180624A	22.50 ± 0.20	**	22.70 ± 3.40	Y	22.21	Y

Notes: $Z/Z_\odot$ references: [a] (Arabsalmani et al., 2018), [b] (Heintz et al., 2019), [c] (Bolmer et al., 2019), *log(NHX) lower error bar not with 90 per cent confidence, **metallicity unknown so 0.07 $Z/Z_\odot$ used in fitting.

bars may introduce bias.

We examined the six GRB where the fitted NHX was less than NHI,IC. For these objects, Table 2.2 lists: (1) GRB name; (2) log(NHI/cm^{-2}); (3) Measured metallicity from literature if available; (4) revised log(NHX/cm^{-2}); (5) Whether the revised NHX > NHI,IC); (6) log(NHIGM/cm^{-2}) at the GRB redshift; and (7) whether the revised NHX − NHI,IC is greater than NHIGM. We also include GRB180624A in the table, which had a revised NHX − NHI,IC substantially below NHIGM.

We refitted each GRB in XSPEC using TBABS*TBVARABS*PO using the actual reported metallicity, or 0.07$Z/Z_\odot$ otherwise. As can be seen from Table 2.2, all GRB now have NHX > NHI,IC. Further, all show NHX − NHI,IC (GRB160227A within error bars) as proxy for the host intrinsic column density, being greater than NHIGM. The refitting using the actual redshift and metallicity (or 0.07 otherwise) gives a higher corrected NHX as the power-law correction approximation marginally understates the actual relation between metallicity correction and redshift for redshift between 0.3 <log$(1 + z)$ < 0.8 (see Appendix chapter 2). Of the 67 GRB detections, five lie below the NHIGM curve in Fig. 2.7. None lie below the NHIGM curve after refitting for more realistic or actual metallicity.

In conclusion, by using actual metallicities, dust corrected where available, and a more realistic average GRB metallicity than the standard solar assumption for the remainder, we have shown that the revised larger NHX is greater than an ionisation corrected NHI for our entire sample of 128 GRB, where measurements of both are available, together with a spectroscopic redshift. Further, the lower envelope of NHX − NHI,IC is potentially a useful constraint on the IGM contribution to NHX. Finally, the metallicity revised NHX − NHI,IC for detections are mostly above the simple model NHIGM curve further suggesting that this is a useful constraint on the IGM hydrogen column density.

2.5 Conclusion

We compiled a large sample of all *Swift* X-ray Telescope observed GRB with spectroscopic redshifts up to 2019 July 31 (with a photometric redshift only for GRB090429B). Of this sample of 352 GRB with fitted X-ray equivalent hydrogen column densities, 128 have also have intrinsic neutral hydrogen column density measurements. We have also compiled a sample of absorption-based metallicity data. The main aims of this paper are to generate improved NHX for our sample by using more realistic host metallicity and, by approximating the host intrinsic hydrogen column density as equal to the measured NHX, with an ionisation correction applied, to isolate the more accurate IGM column density contribution.

We analysed the impacts on NHX of using metallicities that more realistically reflect the LOS absorption through the host galaxy than the standard use of the solar abundance. We discussed the possibility of using an average dust correction where actual measurements were not available but it had an insignificant effect on NHX.

Our main findings and conclusions are:

1. While some of the literature notes that GRB metallicity shows a mild evolution with redshift, the Pearson, and Spearman correlation coefficients for our sample are -0.24 and -0.27, respectively, and both correlations fail the null hypothesis test, indicating there is no detected trend. Further, the large reduced χ^2 of the fit means either that a linear model is not a good description of any potential relation or that there is a large additional source of scatter. Hence we do not find a statistically significant relation between GRB metallicity and redshift.

2. The GRB absorption sample mean metallicity is $[X/\mathrm{H}] = -1.17 \pm 0.09$ (or $0.07 \pm 0.02\ Z/Z_\odot$). This is substantially lower than the assumption of solar metallicity used as standard for many fitted NHX.

3. We find that using a lower GRB host metallicity results in increasing the fitted NHX with the correction scaling with redshift. In order to determine this relation at mean metallicity $0.07\ Z/Z_\odot$, we plotted the fractional increase in NHX with redshift for some trial fits. We find that the fractional increase in NHX with redshift is very similar for a range of GRB fits. The power-law relation for GRB151027A, used as a standard GRB for metallicity $0.07\ Z/Z_\odot$ is $\Delta\ \log(N\mathrm{HX}\ \mathrm{cm}^{-2}) = (0.59 \pm 0.04)\log(1 + z) + (0.18 \pm 0.02)$. A more accurate power law could be obtained from a combined fit of a large sample of GRB. However, this is sufficient for our purposes of analysing the impacts of a more realistic general metallicity assumption for calculating NHX.

4. Using actual metallicities, dust corrected where available, and, for the remaining GRB, our power-law relationship for the mean GRB host metallicity of $0.07\ Z/Z_\odot$, we revised the NHX for our full GRB sample and replotted the relation with redshift. To more accurately isolate the IGM contribution to the total hydrogen column density, we subtracted from the revised NHX the GRB NHI after ionisation correction, as a proxy for the intrinsic hydrogen X-ray column density, and plotted the result against redshift. Of

the 128 GRB with data for both NHX and NHI in our sample, only six have NHI,IC greater than the revised NHX, compared to 32 when solar metallicity is assumed. Therefore, using more realistic GRB metallicities generates an improved NHX, if it is interpreted as representing the total hydrogen column density, which must be greater than the local neutral column density. The estimated NHX − NHI,IC for GRB detections now has a redshift dependence of $(1+z)^{3.1\pm0.3}$ for the GRB detections, compared with power laws of 3.5 ± 0.1 for NHX fitted assuming solar abundance. The Pearson and Spearman correlation coefficients are 0.65 and 0.67, respectively, for the GRB detections, and 0.53 and 0.62, respectively, for the full sample where NHX > NHI,IC.

5. The lower envelope of the revised NHX > NHI,IC plotted against redshift has log(NHX($z = 0$)) = 20.3 cm^{-2} for our GRB sample of revised NHX − NHI,IC. This is taken to be representative of the maximum IGM hydrogen column density, based on the requirement for 90 per cent of detections, including error bars, to be above the envelope. Using this approach, we estimate the IGM n_0 lower limit to be equal to 1.7×10^{-7} cm^{-3} for the NHIGM curve which is consistent with that used by Behar et al. (2011) and S13.

X-ray spectroscopy at higher resolution and at higher signal-to-noise than is currently available would be required to detect absorption edges from individual ions in GRB. Such observations in the future, will provide valuable data on the distribution of the material along the line of sight, including its temperature, composition, density, and ionisation state. The value found for the column density is almost always determined assuming a 100 per cent neutral absorbing gas. This neutral assumption would cause the NHX to be underestimated if incorrect. Therefore, we can further improve the NHX and GRBs as probes of the IGM when higher resolution X-ray spectroscopy becomes available. We plan to examine the properties of the IGM such as metallicity, temperature, and density in a subsequent paper to develop a better IGM model and compare it with the results of this paper.

Acknowledgements

We thank M. Fumagalli for useful comments, K. Page for information on the *Swift* repository, and R. Mahmaud and K. Arnaud for advice on XSPEC. We also thank the referee for providing valuable and constructive feedback. SLM also acknowledges support from the Science and Technology Facilities Council (ST/P000541/1)

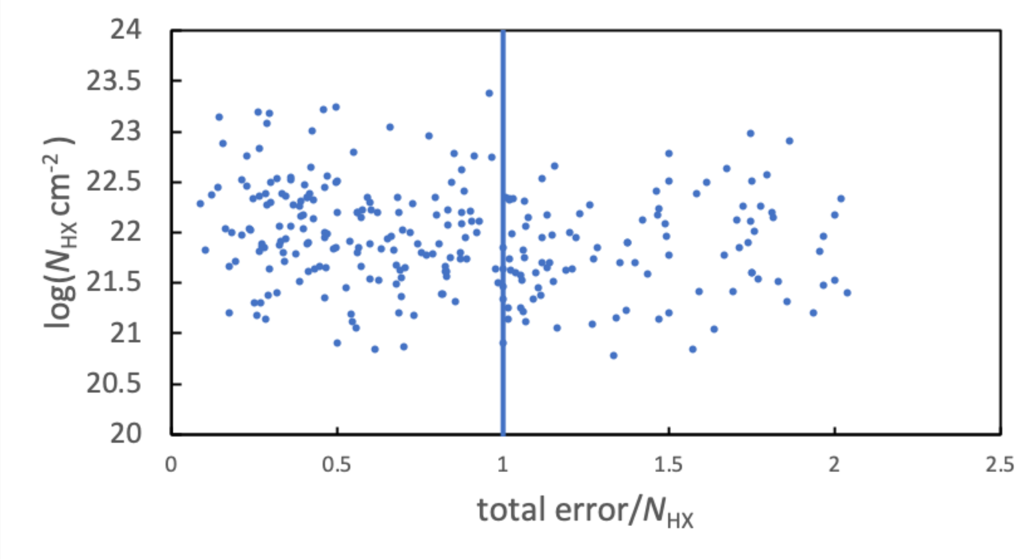

Figure 2.8: X-ray equivalent hydrogen column density against the ratio of the total error/NHX. The blue vertical line is where total error/NHX is 1. The scatter appears random

2.6 Appendix - Chapter 2

2.6.1 S/N bias review

As we are mainly using *Swift* detected GRB where a redshift is available, we wished to examine if an S/N limited sample would cause bias. As a proxy for S/N, we plotted the log(NHX) versus both log of total error in NHX and total error/NHX for all detections in Fig. 2.8. Fig. 2.8 plots the X-ray equivalent hydrogen column density against the ratio of the total error/NHX where the total error is the 90 per cent confidence range of the NHX fit. The scatter appears random so any cut-off by total error/NHX should not result in a bias in NHX. Fig. 2.9 plots the distribution of NHX against the total error for the detection. There is a clear strong correlation so any cut-off for an S/N limited sample based on total error could produce a bias towards low NHX GRB values. As a test of the impact of using a flux limited sample, we restricted a sub-sample to total error/NHX < 1 resulting in 163 GRB. This sub-sample had essentially the same properties as the GRB detection sample using the Pearson and Spearman correlation coefficients and the NHX versus redshift trend.

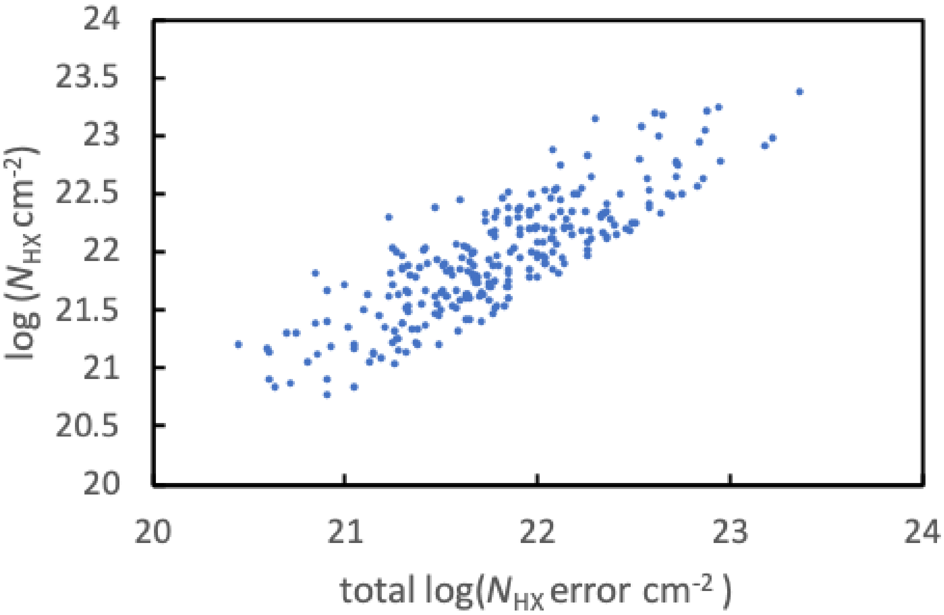

Figure 2.9: The distribution of NHX against the total error for the detection which shows a strong correlation. An S/N limited sample based on total error would introduce a bias to low NHX GRB values

Based on these results, we chose to use our full samples and not limit by a minimum flux.

2.6.2 NHX and NHI correlation review

In Fig. 2.10, we plot NHX and NHI,IC for the full sub-sample of 128 GRB with both NHX and NHI data. No strong correlation is detected using a null hypothesis test, with both Pearson and Spearman coefficients being 0.10. It can be argued that this result strengthens the case that it is the IGM that is causing the NHX redshift relation and is not intrinsic to the GRB host.

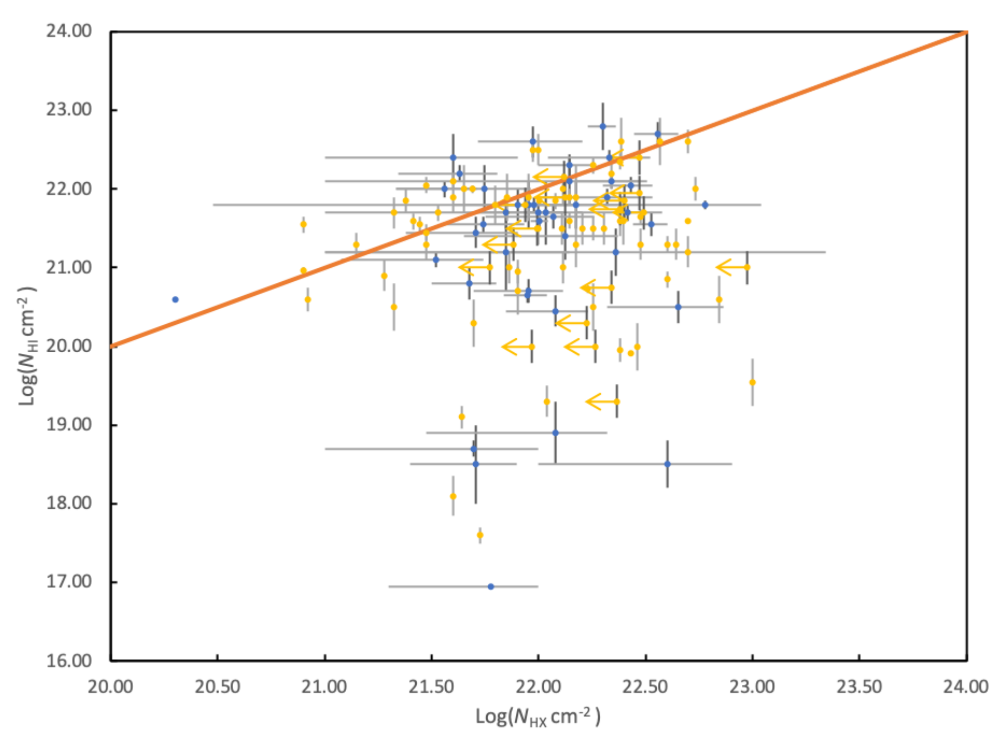

Figure 2.10: Plot of the log of the column densities for 128 GRB with both *N*HX and *N*HI data from Tanvir et al. (2019b) with ionisation corrections. The blue dots are GRB for which the *N*HX are detections. The orange dots are GRB best fits per *Swift* but where the 90 per cent confidence includes zero, and orange dots with arrows where the best-fitting *N*HX = 0. The line shows where *N*HI,IC is equal to *N*HX. There is no correlation.

2.6.3 Power law for metallicity redshift scaled adjustment to NHX

To examine the impact on GRB *N*HX fits in XSPEC using a more realistic mean GRB host metallicity than solar, and the variation with redshift, we used an XSPEC model TBABS*TBVARABS*PO for GRB151027A (a high S/N GRB). We varied the redshifts between 0 and 10 and used metallicity = 0.07 $Z/Z_{\odot}$ in fitting *N*HX. Fig. 2.11 shows a clear increasing metallicity adjusted log(*N*HX) with redshift (blue line for $Z/Z_{\odot}$ = 0.07). In order to determine this relationship, and see whether it is consistent for different GRB X-ray spectra, we plotted in Fig. 2.12 the fractional increase in *N*HX with redshift for a test sample of three high S/N GRB spectra with differing reported redshifts and *N*HX. The fractional increase in *N*HX with redshift is very similar for the three GRB. The power-law relation from a best-fitting least-

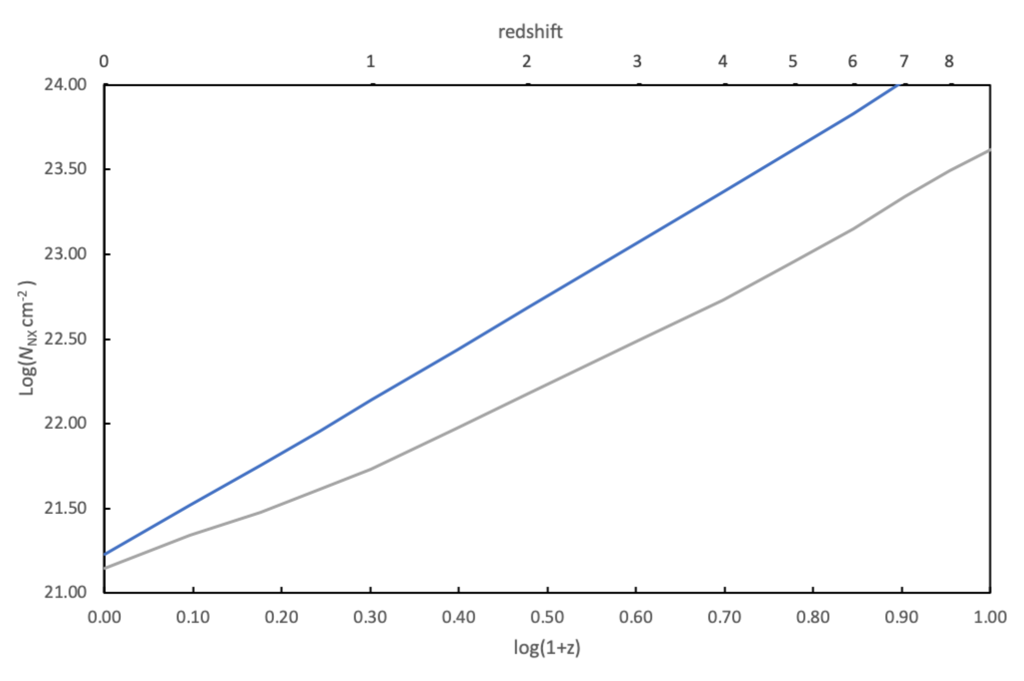

Figure 2.11: Impact on fitted NHX for GRB151027A varying the host redshift between 0 and 10 and using metallicities of 0.07 $Z/Z_{\odot}$ (mean from our sample in Section 2.4.4), and solar. The blue line is with $Z/Z_{\odot}$ = 0.07 and the grey $Z = Z_{\odot}$. A lower metallicity results in increasing the fitted NHX with the increased varying with redshift.

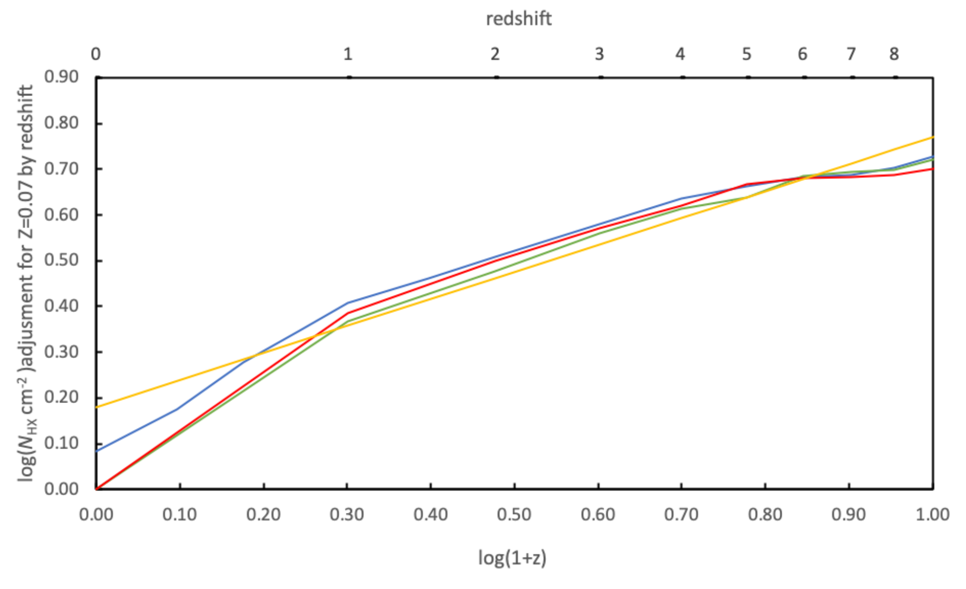

Figure 2.12: Comparison of the fractional increase in NHX with redshift for three high S/N GRB, blue is GRB151027A, red is GRB150403A, and green is GRB120909A. The power-law relation yellow line is from a least-squares best fit for GRB151027A, $\log(N\text{HX}) = (0.59 \pm 0.04)\log(1 + z) + (0.18 \pm 0.02)$

squares for GRB151027A is $\log(N_{\mathrm{HX}}) = (0.59 \pm 0.04)\log(1+z) + (0.18 \pm 0.02)$.

We note that in Fig. 2.12, the power-law curve is higher at $\log(1+z) < 0.2$ and $\log(1+z) > 0.8$. As a result, using this relation to adjust N_{HX} will result in marginally higher values than actual at low and high redshift but is a reasonable approximation for our purposes.

2.6.4 NHI weighted average metallicity of GRB hosts

The sample of metallicity measurements can be used to investigate the cosmic metallicity at different redshifts. A method to do this is to weight the average metallicity over a specific redshift bin with the total neutral hydrogen column density in the same redshift interval (C15). We used redshifts bins of $\Delta z = 1$ except for redshift 4 to 6 as there was only one GRB data point for metallicity greater than redshift 5 (see Fig.2.4). This weighted sample gives a marginally stronger evolution for metallicity than for the individual GRB.

$$[X/H]_{N_{\mathrm{HI}}weighted} = (0.65 \pm 0.07) - (0.15 \pm 0.06)z \tag{2.8}$$

Despite this possible mild evolution, in the high redshift range $z > 4$, all the GRB are metal enriched from 0.02 to 0.17 $Z/Z_{\odot}$, suggesting that substantial amounts of metals were already present in galaxies the early Universe. The lack of clear redshift evolution is in contrast with quasars (QSO) which show strong evolution (Rafelski et al., 2014). A possible explanation for the lack of evolution is that GRBs may be located in different environments to quasars (Fynbo et al., 2008, C15). However, while this would affect the emission line metallicity, it should impact less on the absorption metallicity which is tracing the average galaxy LOS (Arabsalmani et al., 2018). We need far more GRB at high redshift to increase the statistical significance of metallicity evolution. For this paper, we will not use the N_{HI} weighted average values as we wish to establish a metallicity to be applied to each GRB for the N_{HX} fitting.

Chapter 3

Probing the physical properties of the intergalactic medium using gamma-ray bursts

This paper was published as Dalton T., Morris S. L., Fumagalli, M., 2020, MNRAS 502, 5981–5996, and reproduced here with minor formatting changes.

3.1 Summary

We use Gamma-ray burst (GRB) spectra total continuum absorption to estimate the key intergalactic medium (IGM) properties of hydrogen column density (NHXIGM), metallicity, temperature and ionisation parameter over a redshift range of $1.6 \leq z \leq 6.3$, using photo-ionisation (PIE) and collisional ionisation equilibrium (CIE) models for the ionised plasma. We use more realistic host metallicity, dust corrected where available, in generating the host absorption model, assuming that the host intrinsic hydrogen column density is equal to the measured ionisation corrected intrinsic neutral column from UV spectra (NH I,IC). We find that the IGM property results are similar, regardless of whether the model assumes all PIE or CIE. The NHXIGM scales as $(1 + z)^{1.0 - 1.9}$, with equivalent hydrogen mean density

at $z = 0$ of $n_0 = 1.8^{+1.5}_{-1.2} \times 10^{-7}$ cm^{-3}. The metallicity ranges from $\sim 0.1Z_\odot$ at $z \sim 2$ to $\sim 0.001Z_\odot$ at redshift $z > 4$. The PIE model implies a less rapid decline in average metallicity with redshift compared to CIE. Under CIE, the temperature ranges between $5.0 < \log(T/\mathrm{K}) < 7.1$. For PIE the ionisation parameter ranges between $0.1 < \log(\xi) < 2.9$. Using our model, we conclude that the IGM contributes substantially to the total absorption seen in GRB spectra and that this contribution rises with redshift, explaining why the hydrogen column density inferred from X-rays is substantially in excess of the intrinsic host contribution measured in UV.

3.2 Introduction

The main objective of this paper is to estimate the key IGM parameters of column density, metallicity, temperature and ionisation, using the latest models for ionised absorbers on the line of sight (LOS) to GRBs. We examine past observations and simulations to set the parameters ranges and priors for our models. Our hypothesis is that the bulk of the excess in observed hydrogen column density in GRB spectra, inferred from X-rays over the intrinsic host contribution measured in the UV, is due to absorption in the IGM, and that this IGM column density increases with redshift.

Most baryonic matter resides in the IGM and in particular, the regions between galaxies. In the early universe, the fraction of baryons in the IGM was even higher, as less material had coalesced gravitationally from it (McQuinn, 2016, hereafter M16). IGM temperature varies widely over redshift and phase. Recent simulations predict that up to 50% of the baryons by mass have been shock-heated into a warm-hot phase (WHIM) at low redshift $z < 2$ with $T = 10^5 - 10^7$ K and $n_b = 10^{-6} - 10^{-4}$ cm^{-3} where n_b is the baryon density (e.g. Cen and Ostriker, 1999, 2006; Davé and Oppenheimer, 2007; Schaye et al., 2015). Martizzi et al. (2019, hereafter M19), using the IllustrisTNG simulations [*](Piattella, 2018), estimated that the cool

---

[*] http://www.tng-project.org/

diffuse IGM constitutes $\sim 39\%$ and the WHIM $\sim 46\%$ of the baryons at redshift $z = 0$. Observations of the cool diffuse IGM and WHIM are essential for effective tracing of matter across time and to validate the simulations (Danforth et al., 2016). We adopt the common temperature naming convention for IGM plasma: cool is $\log(T/\mathrm{K}) < 5$ and Warm-Hot, $\log(T/\mathrm{K}) \sim 5$ to 7 (M19). Though we concentrate on the very low density IGM, where relevant we use the common names for systems of different column densities: strong Lyα forest systems (SLFSs): $15 < \log N_{\mathrm{H\ I}} < 16.2$[*]; partial Lyman Limit Systems (pLLSs) $16.2 < \log N_{\mathrm{H\ I}} < 17.2$; Lyman Limit Systems (LLSs): $17.2 < \log N_{\mathrm{H\ I}} < 19$; super-LLSs (sLLSs) : $19.0 < \log N_{\mathrm{H\ I}} < 20.3$; and Damped Ly$\alpha$ Systems (DLAs) $\log N_{\mathrm{H\ I}} > 20.3$ (Fumagalli, 2014, hereafter F14).

Over the last several decades, observations of redshifted Lyα absorption in the spectra of quasars has provided a highly sensitive probe of the cool IGM (e.g. Morris et al., 1991; York et al., 2000; Harris et al., 2016; Fumagalli et al., 2020). In the cool phases of the IGM including voids, $40-60\%$ of the universe by mass has $[\mathrm{O/H}] > -3$ while, by volume, only 20% of the overdense universe has a metallicity $[\mathrm{C/H}] > -3$ (F14 and references therein). Both Schaye et al. (2003, hereafter S03) and Aguirre et al. (2008, hereafter A08) found virtually no evidence for metallicity evolution in the cool IGM in the range $z = 1.8 - 4.1$, but metallicity did have a strong dependency on density. S03 confirmed that collisional ionisation did not apply to the phases they studied.

A significant fraction of the cool gas probed by SLFSs, pLLSs, and LLSs has been associated with galaxy haloes and the circum-galactic medium (CGM) (Pieri et al., 2014; Fumagalli et al., 2013, 2016, hereafter F16). As we move from the diffuse IGM to virialised luminous matter, the metallicity rises from the very low values of $[\mathrm{X/H}] \sim -3$ to -2, to approximate values of -1.47 for SLFS, -1.3 for pLLSs, ≤ -2 for LLSs and > -1.5 for DLAs (Wotta et al., 2019, L19, F16). F16 noted considerable evolution in LLS metallicity. However, these systems contribute only $\sim 4\%$ to the cosmic metal density budget (L19). The intracluster medium (ICM)

---

[*] Throughout this chapter, logarithmic column densities are expressed in units of cm^{-2}

mean metallicity in the range $0 \le z \le 1.5$ is $Z = 0.23 \pm 0.01 Z_{\odot}$ (S12; McDonald et al., 2016). At the outer ICM, the metallicity falls to $< 0.01 \sim Z_{\odot}$ (Mernier et al., 2017), which is the start of the true IGM. Temperature in the ICM are typically $\log(T/\mathrm{K}) > 7$. However, the ICM only contains ~ 4% of cosmic metals (Shull et al., 2012, M16).

At higher temperatures, for some time since the first prediction of substantial baryons at low redshift, the expected baryons were not observed in the WHIM, giving rise to the ”missing” baryon problem (Danforth and Shull, 2005, 2008; Shull et al., 2012, 2014). Recent literature points to the CGM as reservoir for at least a fraction of this missing matter (Tumlinson et al., 2011, 2013; Werk et al., 2013; Lehner et al., 2016). Other claims to have detected the WHIM include possible detection of O VII lines, excess dispersion measure over our Galaxy and the host galaxy in Fast Radio Bursts (FRB), and stacked X-ray emission from cosmic web filaments using the thermal Sunyaev Zelodovich effect (e.g. Nicastro et al., 2018; Macquart et al., 2020; Tanimura et al., 2020b).

Detection of the WHIM is extremely challenging, as its emission is very weak, it lacks sufficient neutral hydrogen to be seen via Lyα absorption in spectra of distant quasars, and the X-ray absorption signal expected from the WHIM is extremely weak (Nicastro et al., 2018; Khabibullin and Churazov, 2019). There appears to be a consensus that, at least for $z < 2$, the predicted mean metallicity of the WHIM from simulations and O VI absorption studies is $\sim 0.1 Z_{\odot}$ (e.g. Wiersma et al., 2011; Danforth et al., 2016; Pratt et al., 2018, S12).

Post reionisation, the vast majority of hydrogen and helium is ionised in the IGM. Therefore, the observation of metals is essential for parameterising the IGM properties including density, temperature and metallicity. Huge work has been completed on individual systems from absorption-line studies that use the ionisation states of abundant heavy elements (e.g. Shull et al., 2014; Raghunathan et al., 2016; Selsing et al., 2016; Lusso et al., 2015). While these surveys have been very successful, most very highly ionised metals are not observed in optical to UV. High resolution

X-ray observations are required as they are sensitive to a broad range of cross-sections over the full integrated LOS. However, tracing individual features of the IGM metals in X-ray with current instruments is very limited. Athena, the proposed European Space Agency X-ray observatory, aims to study the IGM through detailed observations of O VII (E = 573 eV) and O VIII (E = 674 eV) absorption features (Walsh et al., 2020).

While we await this future mission, GRBs are currently one of the most effective observational methods to study the IGM as their X-ray absorption yields information on the total absorbing column density of the matter between the observer and the source (e.g. Galama and Wijers, 2001; Watson et al., 2007; Watson, 2011; Wang, 2013; Schady, 2017). GRBs are among the most powerful explosions known in the universe. GRBs exist over an extensive range of redshifts and distances, and have high luminosities combined with a broad energy range of observed emissions. Any element that is not fully ionised contributes to the absorption of X-rays. Though Thomson scattering is essentially energy independent, scattering by electrons only becomes important at energies above 10keV (Wilms et al., 2000, hereafter W00).

Although the X-ray absorption cross-section is mostly dominated by metals, with hydrogen and helium contribution being minimal but not nil (Fig.1 W00), it is typically reported as an equivalent hydrogen column density (hereafter *N*HX). *N*HX consists of contributions from the local GRB environment, the IGM, and our own Galactic medium. With current instruments, GRB X-ray absorption cannot generally reveal the redshift of the matter in the column due to a lack of signal to noise and spectral resolution.

The two main results of earlier studies of the IGM using GRBs are the apparent increase in *N*HX with redshift, and that *N*HX exceeds the host intrinsic neutral hydrogen column density (*N*H I) in GRB, often by over an order of magnitude (e.g. Behar et al., 2011; Watson, 2011; Campana et al., 2012). *N*H I is generally obtained from observations of strong individual absorbers in the GRB host system. The cause of an *N*HXIGM excess over *N*H I, and the *N*HXIGM rise with redshift seen in GRBs has been the source of much debate over the last two decades. One school of thought argues that the GRB host accounts for all the excess and evolution e.g. dense Helium regions close to the GRB (Watson et al., 2013), ultra-ionised gas in the environment of the GRB (Schady et al., 2011), a dense environment near the burst location (Campana et al., 2012), dust extinction bias (Watson and Jakobsson, 2012), and/or a host galaxy mass *N*HXIGM relation (Buchner et al., 2017). The other school of thought argues that the IGM is the cause of excess absorption and redshift relation e.g. (Starling et al., 2013; Arcodia et al., 2016; Rahin and Behar, 2019). While we acknowledge that the GRB host may contribute to the excess absorption, it is the IGM that is the focus of this paper.

The convention in prior work using GRB was to use solar metallicity as a device used to place all of the absorbing column density measurements on a comparable scale. These works all noted that the resulting column densities were, therefore, lower limits as GRB typically have much lower metallicities. Dalton and Morris (2020, hereafter D20) used realistic GRB host metallicities to generate improved estimates of *N*HX. They confirmed the *N*HX redshift relation and that the revised *N*HX showed an even greater excess over *N*H I.

As the bulk of matter in the IGM is ionised and exists outside of gravitationally bound structures, in this paper we use a homogeneity assumption. We will use tracer objects that have LOS orders of magnitude greater than the large scale structure.

The sections that follow are: Section 3.3 describes the data selection and methodology; Section 3.4 covers the models for the IGM LOS including key assumptions and plausible value ranges for key parameters; Section 3.5 gives the results of GRB spectra fitting using collisional and photoionisation IGM models with free IGM key parameters; we discuss the results and compare with other studies in Section 3.6; and Section 3.7 gives our conclusions. Chapter 3 appendix covers model comparisons and investigating the robustness of the IGM model fits. We suggest for readers interested in the key findings on IGM parameters from fittings only, read Sections

3.5, 3.6 and 3.7. Readers interested in detailed spectra fitting methodology and model assumptions should also read Sections 3.3 and 3.4. Finally, for readers interested in more detailed examination of key IGM parameters, plus software model comparisons, read Appendix chapter 3.

3.3 Data selection and methodology

We used the D20 data for $N_{\rm HX}$ which consisted of all observed GRBs with spectroscopic redshift available up to 31 July 2019 from the UK *Swift* Science Data Centre* repository (hereafter *Swift*; Gehrels et al., 2004). Spectra from the *Swift* repository were taken from the Photon Counting Late Time mode. D20 investigated the plausibility of assuming that the host intrinsic hydrogen column density is equal to the measured ionisation corrected intrinsic neutral column from UV spectra. D20 used ionisation corrections from F16 who report on the values of the neutral fraction as a function of NHI. We follow their method for GRB host hydrogen column density. The GRB $N_{\rm H\,I}$ sample is taken from Tanvir et al. (2019a). Our sample criteria was that the GRB has detections with quantified uncertainties for $N_{\rm HX}$, $N_{\rm H\,I}$, and spectroscopic redshift. The selection criteria resulted in a total GRB sample of 61. We selected the best S/N sample representative of the range from $1.6 < z < 6.32$. D20 examined if a S/N limited sample would cause a bias by plotting log($N_{\rm HX}$) versus both log of total error in $N_{\rm HX}$ and total error/$N_{\rm HX}$ for all detections. The scatter appeared random so any selection by total error/$N_{\rm HX}$ should not result in a bias in $N_{\rm HX}$. The total final data sample consists therefore of 32 GRB (Table 3.2).

We refitted the GRB spectra using XSPEC v12.10.1 (Arnaud, 1996, hereafter A96), assuming an underlying power law in the X-ray band from 0.3 - 10.0 keV, which is suitable for the vast majority of GRB and again is consistent with the *Swift* repository (Starling et al., 2013, hereafter S13). The Galactic component is fixed to

---

*http://www.swift.ac.uk/xrtspectra

Swift values based on (Willingale et al., 2013, hereafter W13). Asplund et al. (2009) is generally regarded as providing the most accurate solar abundances. However, we used the solar abundances from W00 which take into account dust and H_2 in the interstellar medium in galaxies.

Most works on the WHIM use absorption line observations focusing on oxygen, carbon, nitrogen and neon because of their relatively high abundance, and because the strongest resonance lines in He and H-like ions are in a relatively 'clean' wavelength band, compared to typical X-ray spectra resolutions. Due to the small Doppler broadening, ignoring turbulence, the lines rapidly saturate. The challenge for X-ray spectroscopy in the IGM is to detect small equivalent widths (Richter et al., 2008, hereafter R08), which is only possible currently in the UV. Accordingly, we chose to base our work on total absorption by the ionised IGM as opposed to fitting individual line absorption, avoiding misidentifation of absorption features (Gatuzz et al., 2015, hereafter G15).

When fitting models to spectra, chi-squared (χ^2) is the generally used statistical method. However, deep field X-ray sources such as our sample from *Swift*, only have a small number of photon counts, well into the Poisson regime. The χ^2 regression approach is inappropriate in this circumstance (Buchner et al., 2014). The common practice of rebinning data to use a χ^2 statistic results in loss of energy resolution. The maximum likelihood C-statistic (Cash, 1979), based on the Poisson likelihood, does not suffer from these issues. For a spectrum with many counts per bin the C-statistic $\rightarrow \chi^2$, but where the number of counts per bin is small, the value for C-statistic can be substantially smaller than the χ^2 value (Kaastra, 2017). Accordingly, we use the C-statistic (Cstat in XSPEC).

Typically, when using XSPEC to fit models to spectra, local optimisation algorithms like the Levenberg-Marquardt algorithm are employed to iteratively explore the space from a starting point. However, given we are studying the IGM with X-ray spectra, we can expect some degeneracies between the parameters. Therefore, there may be multiple, separate, adequate solutions, i.e. local probability maxima.

In these circumstances, these algorithms cannot identify them or jump from one local maximum to the other. The STEPPAR function in XSPEC allows the forcing of parameters to specific ranges. This can overcome the local maximum problem to some degree. Markov chain Monte Carlo (MCMC) is a commonly employed integration method for Bayesian parameter estimation. However, MCMC also has difficulty finding and jumping between well-separated maxima (Buchner et al., 2014). Given the issues of goodness of fit and getting out of local probability maxima, we use a combination of the STEPPAR function and confirmation with MCMC to validate our fitting and to provide confidence intervals on Cstat. We prefer this approach over alternatives such as the Akaike Information Criterion (AIC). The AIC, popular in astrophysics is $AIC = \chi^2 + 2k$ where k is the number of parameters of the model. However, as it is based on χ^2, it suffers from the same problems i.e. based on a Gaussian assumption for errors and requirung a high bin count.

We follow a similar MCMC methodology as Foreman-Mackey et al. (2013) for the number of walkers (× 10 free parameters), chain length and burn-in period. We use Goodman Weare MCMC (Goodman and Weare, 2010).

3.4 Models for the GRB LOS

In this section we describe the motivation and expected physical conditions in the IGM that lead to our choice of CIE and PIE models, the priors and parameter ranges.

In our models, we use different XSPEC (A96) absorption sub-routines for the absorbers on the LOS. For Galaxy absorption (NHXGAL), we use TBABS (W00) fixed to the values measured by W13. TBABS calculates the cross-section for X-ray absorption by the ISM as the sum of the cross sections for the gas, grain and molecules in the ISM. For the GRB host galaxy absorption, we use TBVARABS which is the same as TBABS but with metallicity, dust and redshift as free variables. We follow D20 for the metallicity of the GRB host galaxy i.e. using dust corrected actual metallicity where available, and otherwise their average GRB host value of $Z = 0.07Z_{\odot}$. The NHX for the GRB host is fixed to the NH I,IC values, following the D20 method. By fixing NHX for both our Galaxy and the GRB host, the excess absorption in the models is regarded as being produced by the IGM. W00 noted that the TBABS model does not include the effects of the warm phase or of the ionised phase of the ISM. We review the photoionisation (PIE) and collisional ionisation equilibrium (CIE) models available in XSPEC to determine which is best for our purposes of modelling the IGM. These are WARMABS (Kallman et al. 2009, hereafter K09) for PIE, HOTABS (K09), IONEQ (G15) and ABSORI (Done et al., 1992) for CIE. In earlier works on using tracers such as GRB and quasars for IGM absorption, ABSORI was generally used (e.g. Behar et al., 2011; Starling et al., 2013). While ABSORI was the best model available when it was developed in 1992, it is not self-consistent as it allows one to have both ionisation parameter and temperature as free parameters which would not occur in either PIE or CIE (Done, 2010). Other issues with ABSORI are that it only uses ionisation edges with no line absorption. The metals included are limited to H, He, C, N, O Ne, Mg, Si, S and Fe, and only Fe is allowed as a free parameter. Accordingly, we do not use it for PIE, but do for CIE to compare with earlier studies in the Appendix Chapter 3.

We chose to use WARMABS as a more sophisticated PIE model which is designed to determine the physical conditions in partially ionised gases. It calculates the absorption due to neutral and all ionised species of elements with atomic number $Z \leq 30$. While WARMABS does not account for self-shielding, this effect is negligible at high ionisation parameters (K09). For CIE, we chose HOTABS, a sophisticated code, similar to WARMABS except that it has temperature as the free parameter as opposed to ionisation. An alternative CIE model is IONEQ. It is similar to HOTABS except that it allows metallicity to vary for O, Ne and Fe only (G15). WARMABS, HOTSABS and IONEQ have turbulent velocity (vturb) as a free parameter. We examined varying vturb to assess impact on fittings. The broad range trialled

($0-150$ km s^{-1}) showed minimal variation in column densities or other parameters. Thus, we set vturb = 0.

We model the IGM assuming a thin uniform plane parallel slab geometry in thermal and ionisation equilibrium. This simplistic approximation is generally used to represent a LOS through a homogenous medium and is appropriate for our model (e.g. Savage et al., 2014; Nicastro et al., 2017; Khabibullin and Churazov, 2019; Lehner et al., 2019). This slab is placed at half the GRB redshift as an approximation of the full LOS medium. We examined placing the slab at half the redshift equivalent distance integral as an approximation of distance, but it did not change our results.

Any LOS to a GRB is likely to encounter many different intervening phases of matter, density, temperature and photoionisation levels. Given the current quality of the GRB spectra, the most pragmatic approach is to define the parameters ranges and priors from the past measurements and observations. The slab fit results will then characterise 'typical' conditions integrated along the LOS. We now review the physical processes and key conditions to pin down the range of parameters and models that are best suited for our analysis.

3.4.1 Ionisation processes and equilibrium conditions

Generally, there are two processes that determine the ionisation state of plasma in the IGM i.e. photoionisation and collisional ionisation. Different physical processes are therefore involved and any assumptions regarding whether collisional, photoionisation or a combination dominates will impact any attempts to model the IGM.

The photoionisation rate, $\Gamma_{\rm H\ I}$ depends on the ionising radiation field in the IGM provided by the cosmic ionising background (CIB). For photoionisation IGM modelling, the ionisation parameter ξ (the ratio of ionising photon density to electron density) is a key variable. We set the parameter range as $0 \leq \log(\xi) \leq 3$ for an ionised IGM (Starling et al., 2013). For IGM modelling with the collisional assumption for ionisation, temperature is a key variable. Collisions by thermal electrons ionise hydrogen to a high degree for gas temperatures $> 1.5 \times 10^4$ K. Metals require higher temperatures or ionisation. Therefore, we set the parameter range as $4 \leq \log(T/\mathrm{K}) \leq 8$.

We chose to use equilibrium based models. The relation between ionisation state or fraction and gas temperature and ionisation parameter explicitly assumes that the gas is in an ionisation equilibrium (R08). Opinions on the IGM equilibrium state differ greatly (e.g. Branchini et al., 2009; Nicastro et al., 2018). In non-equilibrium, the plasma remains over-ionised compared to CIE at any temperature, as recombination lags behind cooling (Gnat and Sternberg, 2007). While there is still debate on the equilibrium state of the WHIM, it is likely that a substantial part of the baryons in the Universe are in regions where extremely low densities and ionisation equilibrium conditions persist (M16). Importantly for IGM modelling, well outside the influence of galaxies and clusters, the radiation background becomes more important. Oppenheimer and Schaye (2013a) noted that non-equilibrium effects are smaller in the presence of the CIB, and are overestimated in CIE. However, they also showed that in the presence of AGN, a large fraction of the metal-enriched intergalactic medium may consist of non-equilibrium regions (Oppenheimer and Schaye, 2013b).

In summary, the equilibrium assumption could result in an underestimation of column density where the IGM plasma remains over ionised in non-equilibrium conditions.

3.4.2 Metallicity in the IGM phases

As we are using ionised metal absorption, we have to allow for a large range in the metallicity parameter as the LOS to the GRBs trace the various IGM phases. In our analysis, we include the highly ionised metals that dominate X-ray absorption given that H and He are relatively unimportant. Below 1 keV, C, N, O, and Ne are the main absorbers, while above 1keV, Si, S, and Fe dominate (W00). O VII & O VIII are the most abundant and Neon species also very important (Ne VII, Ne VIII, Ne IX, Ne X). Metallicity currently constitutes the main uncertainty of the IGM models (Branchini et al., 2009).

In Section 3.2, we noted that in the cool IGM phases, typical metallicity is observed to be at the very low range $-4 < [X/\mathrm{H}] < -2$ (e.g. Simcoe et al., 2004, S03, A04). In the hotter phases including the WHIM, the metallicity has been observed to be $[X/\mathrm{H}] \sim -1$ (e.g. Danforth et al., 2016; Pratt et al., 2018, S12). As we are modelling the LOS through the cool, warm and hot diffuse IGM, but noting that some contribution will come from overdense phases, we will set the XSPEC metallicity parameter range as $-4 < [X/H] < -0.7$ ($0.0001 < Z/Z_{\odot} < 0.2$).

3.4.3 Cosmic ionising background

The abundance of ionic species is partially dependent on the CIB. Many studies have been completed on the sources of the background radiation such as star forming galaxies and AGN with power laws in the range 1.4−2 (e.g. Haardt and Madau, 1996, 2012; De Luca and Molendi, 2004; Luo et al., 2011; Moretti et al., 2012). To explore uncertainties in the UV background, Crighton et al. (2015) and Fumagalli et al. (2016) introduced a free parameter αUV to account for the AGN-dominated (hard) to galaxy-dominated (soft) spectrum. A common practice is to adopt a fixed power law for the background radiation. This is a reasonable approach in calculating the ionisation balance.

ABSORI is the only XSPEC model which allows the background CIB as a free parameter. In WARMABS, HOTABS and IONEQ, the CIB photon index is set to 2 which is consistent with the work by Moretti et al. (2012). In many prior works on the IGM using ABSORI, general practice has been to set CIB photon index to 1.4 following (De Luca and Molendi, 2004). We examined the impact of different CIB indices on column density using ABSORI on GRB120909A in Fig. 3.1.

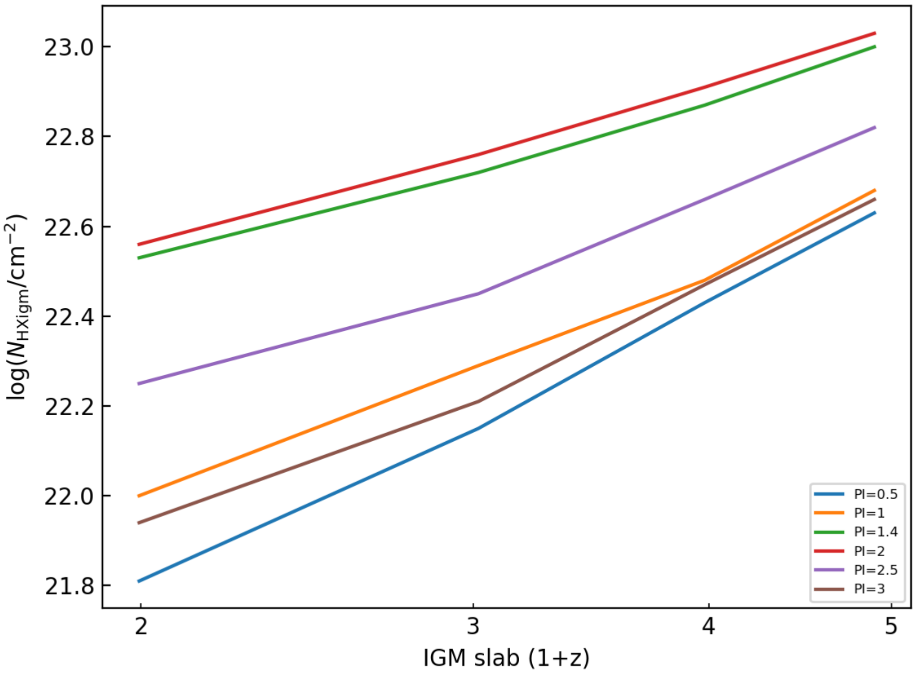

Figure 3.1: *N*HX and redshift relation for different CIB indices using ABSORI for GRB120909A. A power law of 2 produces the highest estimated column densities at all redshift, but only marginally greater than a photon index of 1.4

A photon index of 2 results in the highest estimated column density at all redshift. The lowest column densities resulted from a CIB photon index of 0.5 at logarithmic difference ∼ 0.5 lower than when the index is 2. However, the difference in the commonly observed CIB range of 1.4 − 2 is minimal. Accordingly, we set the photon index at 2 for ABSORI to allow comparison with the other models where it is fixed at 2.

3.4.4 Full models for the GRB LOS

Based on the extensive observations and simulations of the IGM to date, a combined CIE and PIE model for the IGM would be required for optimum fitting of the GRB spectra. However, given the quality of the spectra, we chose instead to examine the two extreme scenarios where all the IGM absorption is either in the CIE or

Table 3.1: Upper and lower limits for the free parameters in the IGM models. Power law slope and normalisation for the GRB spectrum were also free parameters. The fixed parameters are Galactic and host $\log(N_{\rm HX}/{\rm cm}^{-2})$, GRB redshift, the IGM slab at half the GRB redshift, and host metallicity at the observed dust corrected value, or $Z = 0.07 Z_{\odot}$.

IGM parameter	equilibrium model	range in XSPEC models
column density	PIE & CIE	$20 \le \log(N_{\rm HX}/{\rm cm}^{-2}) \le 23$
temperature	CIE	$4 \le \log(T/{\rm K}) \le 8$
ionisation	PIE	$0 \le \log(\xi) \le 3$
metallicity	PIE & CIE	$-4 \le [X/{\rm H}] \le -0.7$

PIE phase. As WARMABS and HOTABS are the most sophisticated PIE and CIE models, these are used for generating the final results of the IGM parameters of density, metallicity, temperature and ionisation parameter in Section 3.5. We then investigated robustness and validity of models and assumptions, together with a comparison of the various ionisation model results (Appendix chapter 3).

The parameters ranges that were applied to the PIE and CIE models are summarised in Table 3.1. The full multiplicative models (*) which we trialled for the absorbers on the LOS and including the GRB spectra power law (po) in XSPEC terminology are:

PIE: TBABS*WARMABS*TBVARABS*PO

CIE: TBABS*HOTABS*TBVARABS*PO

CIE: TBABS*IONEQ*TBVARABS*PO

CIE: TBABS*ABSORI*TBVARABS*PO

Fig. 3.2 shows an example of the model components for the full LOS absorption using HOTABS for IGM CIE absorption. The model example is for a GRB at redshift $z = 2$, with $[X/{\rm H}] = 0.1$ for the IGM. For our Galaxy and the GRB host, $\log(N_{\rm HX}/{\rm cm}^{-2}) = 21$, and $\log(N_{\rm HXIGM}/{\rm cm}^{-2}) = 22$ (to represent the column density of the IGM LOS cumulatively to $z = 2$). The absorption by the GRB host is minimal compared to the ISM of our Galaxy and the IGM. This is because of the redshift

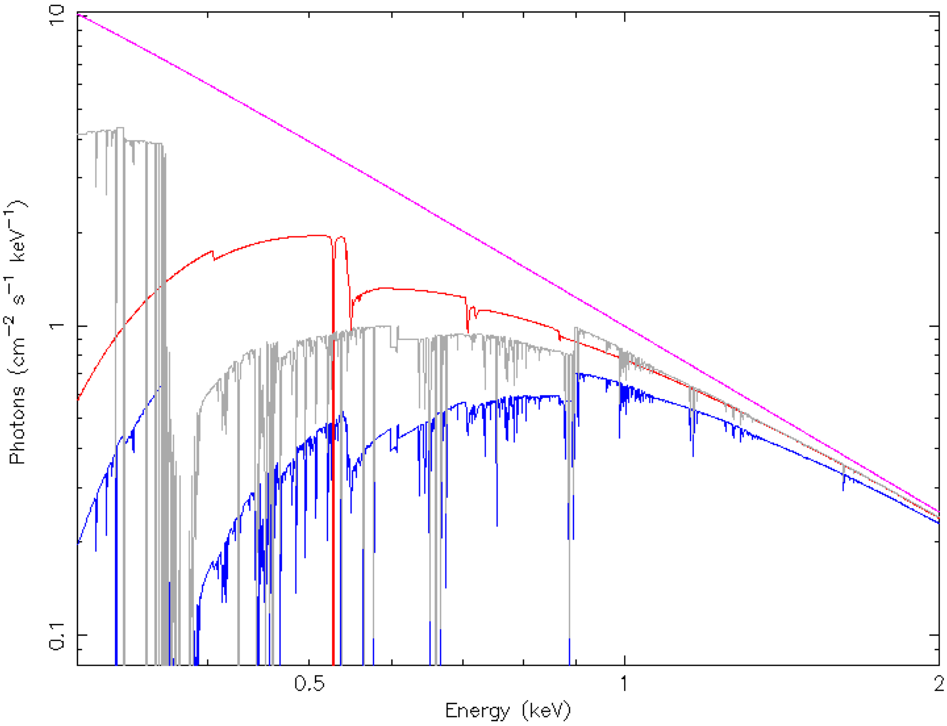

Figure 3.2: Model components for the LOS absorption using HOTABS for IGM CIE absorption in the energy range 0.3 - 2.0keV (*Swift* GRB spectra extend to 10keV). The model example is for a GRB at redshift $z = 2$, with $[X/H] = -1.0$ for the IGM, $\log(N_{HX}/\text{cm}^{-2}) = 21$ for our Galaxy and the GRB host. The IGM $\log(N_{HXIGM}/\text{cm}^{-2}) = 22$ approximates the total column density of the IGM LOS to $z = 2$. Most absorption is due to the IGM (grey) and our Galaxy (red). The GRB host has little contribution due to its redshift and low metallicity (magenta). The total absorption from all three components is the blue line.

$z = 2$ and low metallicity $Z = 0.07Z_\odot$ of the GRB host. The sample transmission plots using HOTABS and WARMABS show the impact of different key parameters and redshift for both PIE and CIE models are available in the online supplementary material.

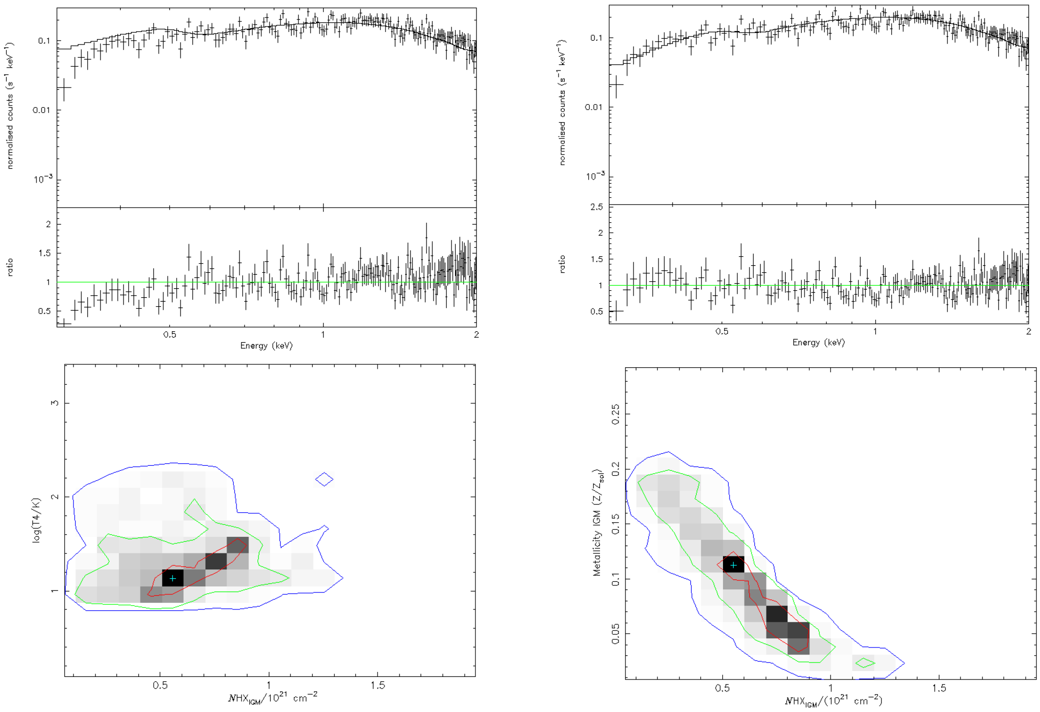

Figure 3.3: Impact of adding additional model components to a simple power law in fitting GRB150403A. Top-left panel is with *N*HXGal only. Top-right panel is with the addition of a fixed host component and CIE IGM absorption component. The spectrum fit shows improvement in low energy absorption over the simple power law fit with *N*HXGal. The bottom-left and right panels show the MCMC integrated probability results for $N_{\rm HXIGM}$ with temperature and metallicity respectively. The red, green and blue contours represent $68\%, 95\%$ and 99% ranges for the two parameters respectively, with grey-scale showing increasing integrated probability from dark to light. On the y-axis in the bottom-left panel T4 means the log of the temperature is in units of 10^4 K.

3.5 Results using CIE and PIE IGM models with key parameters free

In Section 3.5, we firstly discuss the impact of using additional model components on a sub-sample in Section 3.5.1, then give the results for the full sample using the CIE IGM absorption model in Section 3.5.2 and using the PIE IGM model in Section 3.5.3.

3.5.1 GRB model improvement results

We started by fitting a sub-sample of GRB from our full sample, to examine the impact of adding additional model components leading to the full model including the ionised IGM. We show the fitting results in Fig. 3.3 for GRB150403A at redshift $z = 2.06$ as an example of typical results. We initially fitted with a simple model of power law and absorption only from our Galaxy. The top-left panel in Fig. 3.3 shows residuals at low energy with a Cstat of 737.6 for 684 degrees of freedom (dof). We then add a fixed GRB host absorber equal to the measured ionised corrected intrinsic neutral column from UV spectra as detailed in Section 3.3 plus a variable IGM component. The IGM component is either the CIE or PIE model. The top-right panel of Fig. 3.3 shows the result for the model with the CIE IGM component. The spectral fit is visually improved compared with the Galaxy only model, with much less low energy residual. The Cstat for the full model with the CIE IGM component is 655.0 (680 dof), and for the PIE model 652.8 (680 dof). The Fig. 3.3 bottom-left and right panels show the MCMC integrated probability results for N_{HXIGM} with temperature and metallicity respectively. The red, green and blue contours represent $68\%, 95\%$ and 99% ranges for the two parameters respectively. On the y-axis bottom-left panel, log(T4/K) means that 0 is $\log(T/\mathrm{K}) = 4$.

All the fittings in the sub-sample for both CIE and PIE model components showed Cstat results as good as or better than the simple models where all the absorption in excess of our Galaxy was assumed to be at the GRB host redshift. Accordingly, we proceeded to fit the full GRB sample with our CIE and PIE models and give the results for the IGM parameters in Sections 3.5.2 and 3.5.3. In these scenarios, we use HOTABS for CIE and WARMABS for PIE with N_{HX}, metallicity and temperature or ionisation parameters all free. The error bars for all fits are reported with a 90% confidence interval. In the plots of N_{HX} and redshift, the green line is the mean hydrogen density of the IGM based on the simple model used in D20 and references

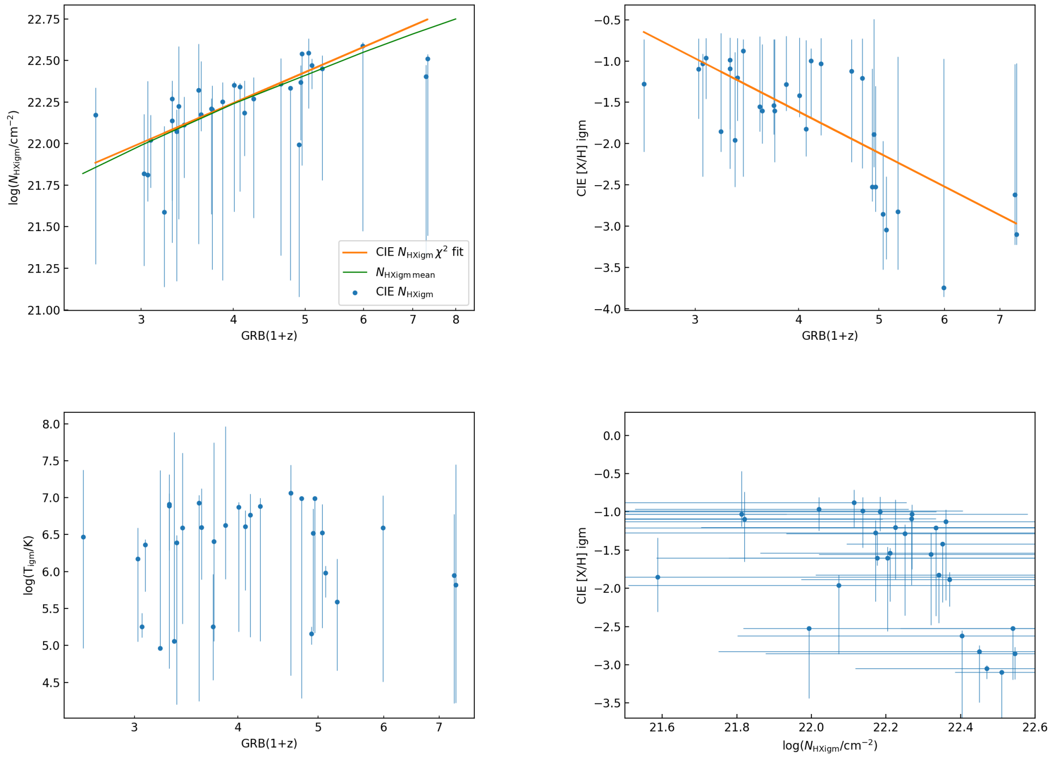

Figure 3.4: Results of the IGM parameters using the CIE (HOTABS) model . The error bars are reported with a 90% confidence interval. The green line is the simple IGM model using a mean IGM density. Top-left panel is NHX and redshift. Top-right panel is [X/H] and redshift. Bottom-left panel is temperature and redshift. Bottom-right panel is [X/H] and NHX. The orange line is the 1 sigma χ^2 fit. We do not include a χ^2 curve in the temperature-redshift plot, or the [X/H] and NHX plot as the fit was poor due to a large scatter and error bars.

therein.

$$N_{\mathrm{HXIGM}} = \frac{n_0 c}{H_0} \int_0^z \frac{(1+z)^2 dz}{[\Omega_M(1+z)^3 + \Omega_\Lambda]^{\frac{1}{2}}} \tag{3.1}$$

where n$_0$ is the hydrogen density at redshift zero, taken as 1.7×10^{-7} cm^{-3} (Behar et al., 2011). This value is based on 90% of the baryons being in the IGM. Values for this IGM fraction in the literature vary e.g. $0.5 - 0.7$ (S12) and 0.84 (Zhang et al., 2020).

3.5.2 Results for IGM parameters using a CIE IGM component

We give the key detailed results for the IGM parameters from fitting our model CIE model to the GRB spectra in our sample (See Table 3.2).

Modelling the IGM using HOTABS for CIE with parameters NHX, Z and T free, results in NHXIGM showing similar values and correlation with redshift as the mean IGM density model in Fig. 3.4 (top left). A power law fit to the NHXIGM versus redshift trend scales as $(1 + z)^{1.9\pm0.2}$. The reduced $\chi^2 = 0.34$ indicates a good fit. The mean hydrogen density at $z = 0$ from the sample is $n_0 = 1.8^{+1.5}_{-1.2} \times 10^{-7}$ cm^{-3}, providing a good constraint on this important IGM parameter. Nearly all GRB fits are proximate to both the χ^2 fit and mean IGM density curve. However, there are a few notable outliers, especially the lowest redshift GRB140430A with $z = 1.6$. This fit has much higher NHXIGM than both the mean density curve and the χ^2 fit. This could be due to a strong absorber on the LOS. To test this, we removed the cap of $Z = 0.2\ Z_\odot$ as the there is covariance between column density and metallicity parameters i.e. a higher metallicity results in a lower column density. The best fit then for GRB140430A was with $Z \approx 0.4\ Z_\odot$ with a much lower column density similar to the mean IGM model density at $z = 1.6$. At the highest redshift $z > 6$, the two GRB fits are well below the cosmic mean density and χ^2 fit. There is some dispersion in the GRB data points at $z \leq 2$. This could indicate that at these redshifts, the GRB host contribution is dominant over the IGM absorption, while at higher redshifts, the host contribution becomes diluted by the IGM, therefore showing a smaller dispersion of results. It is notable that most of the GRB fits sit at the high end of the 90% confidence interval error bars. XSPEC failed to fit two GRB from sample of 32. This was either because the best fit was at the limit of the parameters or the error bars were at one or both parameter limits. This could be due to poor spectra resolution or that the parameter range was too narrow.

The top-right panel of Fig. 3.4 shows the dependence of $[X/\mathrm{H}]$ with redshift. A power law fit to the $[X/\mathrm{H}]$ versus redshift trend scales as $(1+z)^{-5.2\pm1.0}$. The reduced

Table 3.2: GRB sample. For each GRB, the columns give the redshift and IGM fitted parameter results for the CIE and PIE free parameter models: NHXIGM, [X/H], temperature (CIE) or ionisation paramater (PIE)

		CIE model			PIE model		
GRB	z	$\log(\frac{N\text{HXIGM}}{\text{cm}^{-2}})$	$[X/\text{H}]$	$\log(\frac{\text{T}}{K})$	$\log(\frac{N\text{HXIGM}}{\text{cm}^{-3}})$	$[X/\text{H}]$	$\log(\xi)$
140430A	1.60	$22.17^{+0.17}_{-0.90}$	$-1.28^{+0.54}_{-0.82}$	$6.47^{+0.91}_{-1.50}$	$22.36^{+0.18}_{-0.96}$	$-2.02^{+1.27}_{-0.38}$	$1.87^{+0.91}_{-1.71}$
081203A	2.03	$21.82^{+0.36}_{-0.56}$	$-1.10^{+0.37}_{-0.60}$	$6.17^{+0.42}_{-1.12}$	$21.87^{+0.45}_{-0.41}$	$-0.81^{+0.09}_{-0.94}$	$1.46^{+0.82}_{-1.2}$
150403A	2.06	$21.81^{+0.56}_{-0.16}$	$-1.03^{+0.12}_{-1.37}$	$5.26^{+018}_{-0.17}$	$22.02^{+0.15}_{-0.41}$	$-0.99^{+0.49}_{-0.49}$	$1.80^{+0.27}_{-0.63}$
150206A	2.09	$22.02^{+0.15}_{-0.29}$	$-0.96^{+0.24}_{-0.49}$	$6.36^{+0.07}_{-0.63}$	$22.18^{+0.06}_{-0.37}$	$-1.05^{+0.53}_{-0.15}$	$1.93^{+0.07}_{-0.48}$
100728B	2.11	No	CIE	fit	No	PIE	fit
110205A	2.22	$21.59^{+0.52}_{-0.45}$	$-1.85^{+1.19}_{-0.24}$	$4.96^{+2.41}_{-0.01}$	$22.41^{+0.17}_{-0.91}$	$-1.92^{+1.07}_{-0.48}$	$1.18^{+1.68}_{-1.01}$
180325A	2.25	No	CIE	fit	$22.31^{+0.15}_{-0.48}$	$-1.14^{+0.31}_{-0.84}$	$2.52^{+0.32}_{-1.88}$
060124	2.3	$22.14^{+0.18}_{-0.48}$	$-0.99^{+0.27}_{-0.84}$	$6.89^{+0.43}_{-0.60}$	$22.03^{+0.35}_{-0.65}$	$-1.64^{+0.79}_{-0.41}$	$1.86^{+1.00}_{-1.73}$
121024A	2.30	$22.27^{+0.11}_{-0.87}$	$-1.09^{+0.06}_{-1.21}$	$6.91^{+0.15}_{-2.22}$	$22.38^{+0.19}_{-0.12}$	$-1.77^{+1.06}_{-0.53}$	$2.38^{+0.45}_{-2.16}$
070110	2.35	$22.07^{+0.13}_{-0.90}$	$-1.96^{+1.07}_{-0.56}$	$5.06^{+2.83}_{-0.01}$	$21.90^{+0.62}_{-0.44}$	$-1.4^{+0.65}_{-0.35}$	$2.85^{+0.08}_{-1.95}$
080905B	2.37	$22.23^{+0.36}_{-0.68}$	$-1.20^{+0.48}_{-0.52}$	$6.38^{+0.10}_{-2.68}$	No	PIE	fit
080310	2.43	$22.11^{+0.17}_{-0.32}$	$-0.88^{+0.14}_{-1.52}$	$6.56^{+1.18}_{-0.17}$	$22.11^{+0.35}_{-0.59}$	$-0.86^{+0.15}_{-0.84}$	$2.10^{+0.82}_{-1.65}$
080721	2.59	$22.32^{+0.28}_{-0.93}$	$-1.55^{+0.85}_{-0.30}$	$6.93^{+0.11}_{-2.68}$	$22.29^{+0.29}_{-0.17}$	$-1.57^{+0.40}_{-1.43}$	$2.22^{+0.67}_{-0.50}$
050820A	2.61	$22.18^{+0.32}_{-0.10}$	$-1.60^{+0.80}_{-0.40}$	$6.60^{+0.52}_{-0.71}$	$21.99^{+0.61}_{-0.68}$	$-1.43^{+0.59}_{-0.29}$	$1.63^{+1.33}_{-1.29}$
140206A	2.73	$22.21^{+0.06}_{-0.64}$	$-1.54^{+0.80}_{-0.35}$	$5.26^{+0.71}_{-0.72}$	$22.14^{+0.11}_{-0.08}$	$-1.12^{+0.23}_{-0.52}$	$0.02^{+1.06}_{-0.01}$
090809	2.74	$22.20^{+0.14}_{-0.96}$	$-1.60^{+0.87}_{-0.62}$	$6.41^{+1.34}_{-1.35}$	$22.00^{+0.45}_{-0.83}$	$-1.06^{+1.18}_{-1.16}$	$1.56^{+1.12}_{-1.41}$
180624A	2.86	$22.25^{+0.12}_{-1.07}$	$-1.28^{+0.59}_{-0.32}$	$6.63^{+1.34}_{-0.73}$	$21.98^{+0.66}_{-0.62}$	$-0.88^{+0.14}_{-0.97}$	$1.93^{+0.79}_{-1.63}$
090715B	3.01	$22.35^{+0.02}_{-0.76}$	$-1.42^{+0.70}_{-0.26}$	$6.87^{+0.07}_{-1.68}$	$22.22^{+0.14}_{-0.48}$	$-1.10^{+0.53}_{-0.60}$	$2.04^{+0.62}_{-0.64}$
060607A	3.08	$22.34^{+0.02}_{-0.63}$	$-1.82^{+1.08}_{-0.33}$	$6.61^{+0.22}_{-0.86}$	$22.29^{+0.06}_{-0.24}$	$-1.82^{+0.36}_{-0.48}$	$1.64^{+0.27}_{-1.42}$
140703A	3.14	$22.18^{+0.19}_{-0.26}$	$-1.00^{+0.17}_{-0.68}$	$6.77^{+0.29}_{-1.65}$	$22.24^{+0.33}_{-0.80}$	$-1.68^{+0.83}_{-0.48}$	$0.23^{+2.62}_{-0.06}$
140423A	3.26	$22.27^{+0.13}_{-0.72}$	$-1.03^{+0.31}_{-0.87}$	$6.88^{+0.12}_{-1.82}$	$22.25^{+0.22}_{-0.47}$	$-1.36^{+0.73}_{-0.74}$	$1.95^{+0.94}_{-0.84}$
070721B	3.63	$22.36^{+0.15}_{-1.03}$	$-1.12^{+0.39}_{-1.10}$	$7.06^{+0.38}_{-2.47}$	$22.44^{+0.16}_{-0.67}$	$-1.68^{+0.98}_{-0.42}$	$2.90^{+0.07}_{-2.67}$
060605	3.77	$22.33^{+0.01}_{-1.16}$	$-1.21^{+0.48}_{-1.09}$	$6.99^{+0.02}_{-2.70}$	$22.23^{+0.35}_{-0.63}$	$-2.10^{+0.99}_{-0.60}$	$2.45^{+0.52}_{-2.15}$
060210	3.91	$21.99^{+0.01}_{-0.91}$	$-2.52^{+1.43}_{-0.18}$	$5.16^{+0.10}_{-0.15}$	$22.26^{+0.22}_{-0.07}$	$-1.74^{+0.24}_{-0.26}$	$1.11^{+0.56}_{-1.00}$
120909A	3.93	$22.37^{+0.10}_{-0.35}$	$-1.89^{+1.19}_{-0.40}$	$6.52^{+0.33}_{-1.33}$	$22.22^{+0.14}_{-0.12}$	$-1.40^{+0.01}_{-0.24}$	$1.52^{+0.75}_{-0.70}$
140419A	3.96	$22.54^{+0.01}_{-0.67}$	$-2.52^{+1.20}_{-0.30}$	$6.99^{+0.02}_{-1.82}$	$22.40^{+0.11}_{-0.59}$	$-2.32^{+1.40}_{-0.27}$	$2.00^{+0.84}_{-1.79}$
151027B	4.06	$22.55^{+0.09}_{-0.33}$	$-2.85^{+0.89}_{-0.67}$	$6.53^{+0.39}_{-1.29}$	$22.41^{+0.04}_{-0.70}$	$-1.62^{+0.37}_{-0.90}$	$1.95^{+0.51}_{-1.82}$
090516	4.11	$22.47^{+0.04}_{-0.14}$	$-3.05^{+0.65}_{-0.36}$	$5.98^{+0.10}_{-0.33}$	$22.29^{+0.19}_{-0.06}$	$-1.92^{+0.15}_{-1.08}$	$0.98^{+0.65}_{-0.86}$
050505	4.27	$22.45^{+0.08}_{-0.67}$	$-2.82^{+1.88}_{-0.70}$	$5.59^{+0.58}_{-0.93}$	$22.51^{+0.04}_{-0.16}$	$-3.96^{+1.42}_{-0.04}$	$0.81^{+0.67}_{-0.69}$
111008A	4.99	$22.59^{+0.02}_{-1.11}$	$-3.74^{+2.77}_{-0.11}$	$6.59^{+0.44}_{-2.08}$	$22.50^{+0.13}_{-0.58}$	$-2.96^{+2.13}_{-0.13}$	$1.64^{+1.01}_{-1.63}$
050904	6.29	$22.40^{+0.07}_{-1.10}$	$-2.62^{+1.58}_{-0.60}$	$5.95^{+0.83}_{-1.73}$	$22.58^{+0.30}_{-0.94}$	$-1.62^{+0.59}_{-0.78}$	$0.71^{+2.13}_{-0.56}$
140515A	6.32	$22.51^{+0.03}_{-1.06}$	$-3.10^{+2.07}_{-0.12}$	$5.82^{+1.91}_{-0.71}$	$22.41^{+0.46}_{-0.75}$	$-2.48^{+1.45}_{-0.56}$	$0.85^{+1.99}_{-0.78}$

$\chi^2 = 1.3$ indicates a plausible linear fit. Metallicity ranges from [X/H] ~ -1 ($0.1Z_\odot$) at $z = 2$ to [X/H] ~ -3 ($0.001Z_\odot$) at high redshift ($z > 4$).

There is a large range in the fitted temperature $5.0 < \log(T/\mathrm{K}) < 7.1$, with substantial error bars in the Fig. 3.4 bottom-left panel. The mean temperature over the full redshift range is $\log(T/\mathrm{K}) = 6.3^{+0.6}_{-1.3}$. These values are consistent with the generally accepted WHIM range. It is interesting to note that even at the highest redshifts $z > 4$, temperatures of $\log(T/\mathrm{K}) > 5$ appear to give good fits. Further, there is no apparent general decline in temperature with redshift. It should be noted, however, that the fits are for the integrated LOS and not representative of any individual absorber temperature.

In nearly all GRB fits, the Cstat was at least as good as, or better than simple fits with all absorption in addition to that in our Galaxy assumed to be at the GRB host. The MCMC integrated plots were consistent with the STEPPAR results. In conclusion, with the caveats of low GRB X-ray resolution, small data sample and the slab model to represent to full LOS, there are reasonable grounds for arguing that the CIE model using HOTABS is plausible for modelling the warm/hot component of the IGM at all redshifts. The results are consistent with a mean hydrogen density of $n_0 = 1.7 \times 10^{-7}$ cm^{-3}, providing constraints on this IGM parameter of $n_0 = 1.8^{+1.5}_{-1.2} \times 10^{-7}$ cm^{-3}. However, cosmological simulations suggest that the fraction of mass contained in the warm-hot IGM phase is a strong function of redshift being $\sim 49\%$ at $z = 0$, dropping by a factor of 20 by $z = 4$, while the diffuse cooler IGM becomes dominant (Martizzi et al., 2019). Our model indicates a decline in the average metallicity on the LOS, with a significant drop in metallicity at the highest redshifts. The temperature range of $\log(T/\mathrm{K}) \sim 5 - 7$ and mean of $6.3^{+0.6}_{-1.3}$ are consistent with the expected values from simulations for a warm/hot phase. We discuss the results further and compare with other studies in Section 3.6.

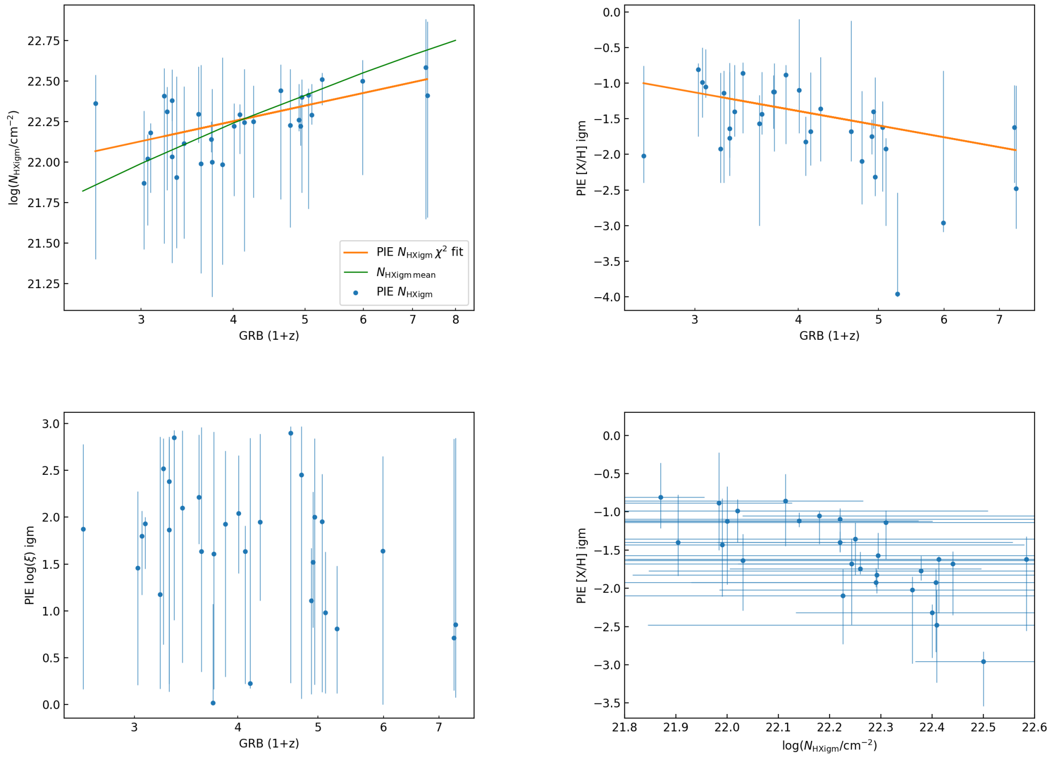

Figure 3.5: Results for the PIE IGM parameters using PIE (WARMABS) models. The error bars are reported with a 90% confidence interval. The green line in the top-left panel is the simple IGM model using a mean IGM density. Top-left panel is NHX and redshift. Top-right panel is [X/H] and redshift. Bottom-left panel is ionisation parameter and redshift. Bottom-right panel is [X/H] and NHX. The orange line is the χ^2 fit. We do not include a χ^2 curve in the ionisation-redshift plot , or the [X/H] and NHX plot as the fit was poor due to a large scatter.

3.5.3 Results for IGM parameters using a PIE IGM component

Modelling the IGM using WARMABS for PIE with NHXIGM, Z and ξ as free parameters results in values for NHXIGM and correlation with redshift comparable to the mean IGM density model (the top-left panel of Fig. 3.5). The data points appear to show less dispersion and are marginally below the mean IGM density model at higher redshift $z > 3$, though with large error bars. A power law fit to the NHXIGM versus redshift trend scales as $(1 + z)^{1.0\pm0.3}$, flatter than for CIE. The reduced χ^2 of 0.67 indicates a reasonable fit. Only 2 GRB failed to be fit in XSPEC out of our sample of 32. The mean hydrogen density at $z = 0$ from the sample is

$n_0 = 1.8^{+1.4}_{-1.2} \times 10^{-7}$ cm^{-3}, providing a similar constraint on the IGM density parameter to our CIE model. It is notable that the lowest redshift GRB140430A $z = 1.6$ in our sample has a best fit NHXIGM again considerably higher than the mean density curve, similar to the CIE model. Again, this could indicate a higher metallicity absorber along the LOS.

Fig. 3.5 top-right panel is a plot of [X/H] versus redshift with a trend scaling as $(1+z)^{-2.1\pm0.8}$. The reduced χ^2 of 1.84 indicates a reasonable linear fit. The metallicity is approximately [X/H] ~ -1.0 ($0.1Z_\odot$) at $z \sim 2$ falling to [X/H] ~ -2.4 ($0.004Z_\odot$) at $z > 4$. At higher redshift, the average LOS metallicity value appears to decline more rapidly, but with large error bars. This could suggest that there was very little higher metallicity aborption at those redshifts. However, there are very few high redshift GRB in the sample.

There is a large range in the fitted ionisation parameter $0.0 < \log(\xi) < 2.9$, with substantial error bars in Fig. 3.5 (bottom left). The mean ionisation parameter over the full redshift range is $\log(\xi) = 1.6^{+0.9}_{-1.2}$. We note that these values are the LOS average and not representative of any individual absorber or redshift.

As discussed in Section 3.3, we use Cstat minimization due to small number of photon counts, well into the Poisson regime. Thus, χ^2 and AIC are inappropriate. If the model improvement criteria is any improvement in Cstat when compared with the model with all excess absorption over Galactic assumed at the host redshift, then 26/30 CIE, 23/30 PIE, 27/30 combined show improvements. If we adopt the approach that a reduction of Cstat> 2.71, > 4.6, and > 6.25 for one, two and three additional interesting parameters corresponds to 90% significance (Reeves and Turner, 2000; Ricci et al., 2017), and our IGM inclusive XSPEC models have 3 extra free parameters, 12/30 for CIE and 9/30 for PIE are significantly improved, combined 15/30.

In conclusion, with the same caveats as for CIE, there are reasonable grounds for arguing that the PIE model using WARMABS is plausible for modelling the cool diffuse IGM. The results are similar to the mean hydrogen density of $n_0 = 1.7\times10^{-7}$ cm^{-3}. The PIE model results show a decline with redshift in the average metallicty values along the integrated LOS. The ionisation range and mean are consistent with the expected values from simulations. It is not possible to conclude whether PIE or CIE is the better single model for the IGM at all redshift. From the outset, it was noted that a combined model is likely but this requires better data. The results may indicate that we are seeing different IGM phases along the LOS, though we are examining the extremes of CIE an PIE models separately.

Given that it is typically not possible to fit the spectra with both PIE and CIE models due to spectral resolution, and that the results for the IGM parameters are very similar using CIE and PIE models, in subsequent chapters, I will use only the CIE model when modelling the IGM.

3.6 Discussion and comparison with other studies

In both CIE and PIE IGM scenarios, the IGM is highly ionised with either high temperatures or high ionisation parameters. We find that under both scenarios for the IGM, the average metallicity along the LOS declines with redshift, with the caveat that we are using a cumulative LOS absorption. The decline in average metallicity is less in the PIE model. It may be that at lower redshift regions of higher metallicity such as the WHIM may be dominant, while at higher redshift, the diffuse cool IGM becomes dominant, diluting the average metallicity, but we would require a combined CIE/ PIE model to establish this. Fixing metallicity to any value gave poor and unreliable results (see Appendix chapter 3). Most prior studies were based on simplistic assumptions of solar metallicity, and all absorption in excess of our Galaxy being at the host redshift(e.g. Behar et al., 2011; Campana et al., 2010, 2012). Further, the absorber was assumed to be neutral. Later studies used ABSORI which has only 10 metals, and only Fe variable (Starling et al., 2013; Campana et al., 2015). The use of solar metalicity leads to underestimate of column density, while the assumption of all excess absorption at the host redshift leads to overestimation of the column density.

Our analysis, using the more sophisticated models for PIE and CIE, shows that substantially higher metallicity is indicated at lower redshifts compared to higher redshifts. As noted in more detail in Sections 3.2 and 3.4, there is some consensus for the diffuse cool IGM metallicity with redshifts $z = 2-4$ at $Z = 0.001Z_{\odot}$ ($[X/\mathrm{H}] = -3$), but with little or no observed evolution. However, these are either in Lyα forest regions or more dense systems such as LLSs or DLAs (e.g. S03, A08, F14, F16). At lower redshift $z = 0-2$, in the WHIM and the ICM, there is some consensus that the predicted mean metallicity is $Z \sim 0.1Z_{\odot}$ (e.g. Wiersma et al., 2011; Danforth et al., 2016, S12), though it is unlikely that many GRB LOS pierce the ICM. Our CIE and PIE models in Section 3.5 show that regardless of the IGM model, both CIE and PIE are picking up substantial absorption by highly ionised absorbers. This use of sophisticated ionised absorber models for GRB has not been completed previously.

Campana et al. (2015) completed simulations of IGM absorption using GRBs and quasars. For GRBs, their simulations indicated that the LOS does not contain any absorbers with over-density $\Delta > 100$, $\log(T/\mathrm{K}) \sim 5-7$ and mean metallicity $Z = 0.03Z_{\odot}$. As we are tracing the full LOS and not any individual absorber, we cannot compare our results directly with Campana et al. (2015) in terms of overdensities. Their result for temperature range is consistent with ours for the CIE model. However, we find that a decline in metallicity is observed in both CIE and PIE scenarios for the IGM. In contrast, using AGNs, their simulations showed prevalence of absorption systems with large over-densities ($\Delta > 300$) at $z \sim 0.5-1.2$, temperature of $\sim (3-15) \times 10^6$ K and mean metallicity in these regions of $Z = 0.3 \pm 0.1Z_{\odot}$. We would agree with their speculation that it is unlikely that GRB trace different LOS to AGN through the diffuse IGM and that therefore, these large overdensities and high metallicity may be proximate to the AGNs, e.g. in their CGM.

Behar et al. (2011) noted that in their GRB sample the observed opacity at low energies, while high at low redshift, tended toward an asymptotic value at $z \sim 2$. They interpreted this as possible evidence for the detection of absorption by a diffuse, highly ionised intergalactic medium. This interpretation would solve the problems of the lack of correlation observed between the NHX and NH I in GRB afterglows, and the very low apparent dust-to-metals ratios. Rahin and Behar (2019) extended this earlier work to include all GRB up to 2019 and found very similar results.

There have been some claims in recent years to have found the missing baryons in the WHIM using different tracers. We now compare our work with some of these studies. Arcodia et al. (2018) used blazars as potential IGM absorption tracers. They modelled IGM absorption using IGMABS in XSPEC. This is based on ABSORI, with solar abundance and limited number of metals. Only 4 blazars were fitted. Their resulting average $n_0 = 1.01^{+0.53}_{-0.72} \times 10^{-7}$ cm^{-3} is lower than our result. Their temperature $\log(T/\mathrm{K}) = 6.45^{+0.51}_{-2.12}$ and ionisation $\log(\xi) = 1.47 \pm 0.27$ (note $\log(\xi)$ was tied to n_0) are consistent with our results. They derived a value of $Z_{IGM} = 0.59^{+0.31}_{-0.42} Z_{\odot}$ based on an average IGM density from their fittings, as compared to $n_0 = 1.7 \times 10^{-7}$ cm^{-3} which is substantially higher than our results but they noted this should only be viewed as a consistency check.

Macquart et al. (2020) used FRB dispersion measure (DM) to measure the total electron column density on the LOS to the FRB host. Their sample is limited to 5 FRB in the redshift range 0.12 to 0.52. To isolate the possible IGM component, they fix the Galactic DM to values measured by Cordes and Lazio (2002) with an additional fixed component to represent the Galactic halo of 50 pc cm^{-3}. They also assumed a fixed FRB host at $\mathrm{DM}_{host} = 50/(1+z)$ pc cm $^{-3}$. They add that further analysis of their sample mildly favors a median host galaxy contribution of ~ 100 pc cm^{-3} with a factor of two dispersion around this value. This is the conventional approach in FRB i.e. to fix the FRB host DM with the assumption that all excess DM is then due to the IGM. This is very different to the traditional GRB approach of assuming all absorption in excess of our Galaxy is at the host redshift. Their resulting baryon fraction is a median value of $\Omega_b h_{70} = 0.056$ and a 68% confidence interval spanning $[0.046, 0.066]$. Based on this result they claim that their FRB DM measurements confirm the presence of baryons with the density estimated from the CMB and Big Bang Nucleosynthesis, and are consistent with all the missing baryons being present in the ionised intergalactic medium. Our median value for the baryon fraction for both CIE and PIE models is $\Omega_b h_{70} = 0.043$ and a 90% confidence interval spanning $[0.014, 0.079]$ (CIE) and $[0.014, 0.077]$ (PIE) which is consistent with their results. Their approach to fixing the host DM component is also analogous to our approach with GRB.

Nicastro et al. (2018) claim to have observed the WHIM in absorption. Only 1 to 2 strong O VII absorbers are predicted to exist per unit redshift. Nicastro et al. (2018) reported observations of two O VII systems. System 1 ($z = 0.43$) had $T = 6.8^{+9.9}_{-3.6} \times 10^5$ K, $N\textsc{hxigm} = 1.6^{+0.8}_{-0.5}/(Z/Z_\odot) \times 10^{19}$ cm^{-2}. System 2 ($z = 0.36$) had $T = 5.4^{+9.0}_{-1.7} \times 10^5$ K, $N\textsc{hxigm} = 0.9^{+1.5}_{-0.9}/(Z/Z_\odot) \times 10^{19}$ cm^{-2}. With $Z = 0.1Z_\odot$, and with an average of 1.5 systems per unit redshift, this gives $N\textsc{hxigm} \sim 1.9 \times 10^{20}$ cm^{-2} for $z \sim 1$. While the temperatures are consistent with our results, the column densities are an order of magnitude lower than our results and that of Arcodia et al. (2018) and Macquart et al. (2020) for blazars and FRB respectively. This could be interpreted as supporting the contribution of the IGM to absorption over and above individual strong WHIM absorbers.

It is not possible at present to detect the individual filaments using the thermal Sunyaev–Zeldovich (tSZ) effect as the signal is much smaller than both the noise in the latest CMB experiments, and compared to the sensitivity of Planck(Planck Collaboration et al., 2020). Tanimura et al. (2020b, hereafter T20) used gas filaments between the Luminous Red Galaxy (LRG) pairs relying on stacking the individual frequency maps for 88000 pairs in the low redshift range $z < 0.4$. The stacking removes the CMB component while the dust foreground becomes homogeneous. Their stacked tSZ signal, with an assumed temperature of 5×10^6 K for the filaments, gives an electron overdensity of ~ 13 , based on electron number density today to be $n_{e0} = 2.2 \times 10^{-7}$ cm^{-3}. This is consistent with (Cen and Ostriker, 2006) and M19 simulations for the WHIM. Our results for the mean density and temperature ranges in the CIE scenario are consistent with these results, with the caveat that the IGM slab in our model is placed at half the GRB redshift i.e. at much higher redshifts than the T20 sample.

While there are GRB at low redshift with high NHX, the bulk of low redshift GRB are consistent with our work. The mean NHX (revised for $Z = 0.07Z_\odot$ or actual metallicity, dust-corrected if available) for $z < 1$ taken from D20 is 5.3×10^{21} cm^{-2}. GRB NH I do not show any relation with redshift. The mean for a sample again from D20 with $z < 2$ is 4.9×10^{21} cm^{-2}. Following our method of approximating the GRB host column density as equal to NH I, this leaves only a small absorption difference 0.4×10^{21} cm^{-2}. At $z \sim 0.5$, the mean IGM from our work is $\sim 1.5 \times 10^{21}$ cm^{-2}.

Some GRB at low redshift have very high X-ray absorption e.g. GRB190114C. The host-galaxy system of GRB190114C is composed of two galaxies, a close pair merger system (de Ugarte Postigo et al., 2020). Drawing from their observations, there are several possible factors which may explain the very high intrinsic NHX in this low redshift GRB. The GRB exploded within the central cluster of the host galaxy, where the density is higher, at a projected distance of ~ 170 pc from the core. The GRB location is indicative of a denser environment than typically observed for GRBs. The host system stellar mass is an order of magnitude higher than the median value of GRB hosts at $0 < z < 1$ as measured for the BAT6 host sample. Finally, the GRB host has a much higher metallicity at 0.43 than the average GRB host at 0.07 from D20. Campana et al. (2021) found that the NHX was decreasing with time which would be strong evidence the bulk of the column density was intrinsic as the IGM NHX should not vary with time.

Our results show that substantial absorption probably occurs in the IGM in both the PIE and CIE scenarios. Most fits have consistently, if marginally better Cstat results compared to the simple model with all excess absorption occurring at the GRB host redshift. We would argue that while some excess absorption is attributable to the GRB host, and that better host models may identify this host excess absorption, the IGM contributes substantially to the total absorption seen in GRB spectra, and that it indeed rises with redshift. This IGM absorption at least partly explains why NHXIGM seen in GRB full LOS afterglow spectra is substantially in excess of the intrinsic NH I in GRB hosts. However, the CGM in the GRB host may also contribute to the NHXIGM, and future models incorporating more advanced modelling for a warm/hot CGM component in GRB hosts are needed to explore the relative contribution of the IGM and the host CGM to the observed absorption.

3.7 Conclusions

The main aim of this paper is to probe the key parameters of density, metallicity, temperature and photo-ionisation of the IGM using sophisticated software models for the ionised plasma. We use spectra from *Swift* for GRBs as our tracers with a redshift range of $1.6 \leq z \leq 6.3$. We isolated the IGM LOS contribution to the total absorption for the GRBs by assuming that the GRB host absorption is equal to ionised corrected intrinsic neutral column NH I,IC estimated from the Lyα host absorption. We use more realistic host metallicity, dust corrected where available in generating the host absorption model. We model the IGM assuming a thin uniform plane parallel slab geometry in thermal and ionisation equilibrium to represent a LOS through a homogeneous isothermal medium. We use XSPEC fitting with STEPPAR and MCMC to generate best fits to the GRB spectra. Our work uses the continuum total absorption to model plasma as opposed to fitting individual line absorption as the required resolution is not available currently in X-ray. We set the XSPEC metallicity parameter range as $-4 < [X/\mathrm{H}] < -0.7$ ($0.0001 < Z/Z_{\odot} < 0.2$), with temperature for CIE at $4 < \log(T/\mathrm{K}) < 8$ and ionisation parameter between

$0 \leq \log(\xi) \leq 3$. The CIB photon index is fixed at 2.

Our main findings and conclusions are:

1. Modelling the IGM using HOTABS for CIE with parameters NHX, Z and T free appears to present plausible results for NHXIGM with an equivalent mean hydrogen density at $z = 0$ of $n_0 = 1.8^{+1.5}_{-1.2} \times 10^{-7}$ cm^{-3}. It shows similar values and correlation with redshift as the mean IGM density model, Fig. 3.4 top-left panel. A power law fit to the NHXIGM versus redshift trend scales as $(1 + z)^{1.9\pm0.2}$.

2. A power law fit to the $[X/\mathrm{H}]$ and redshift trend for CIE scales as $(1+z)^{-5.2\pm1.0}$, Fig. 3.4 top-right panel. Metallicity ranges from $[X/\mathrm{H}] = -1$ ($Z = 0.1Z_\odot$) at $z \sim 2$ to $[X/\mathrm{H}] \sim -3$ ($Z = 0.001Z_\odot$) at high redshift $z > 4$. This could suggest that at low redshift, the higher metallicity warm-hot phase is dominant with $Z \sim 0.1Z_\odot$, while at higher redshift the low metallicity IGM away from knots and filaments is dominant.

3. The CIE temperature range is $5.0 < \log(T/\mathrm{K}) < 7.1$, Fig. 3.4 bottom-left panel indicating that very highly ionised metals are prominent absorbers over the LOS. The mean temperature over the full redshift range is $\log(T/\mathrm{K}) = 6.3^{+0.6}_{-1.3}$. These values are consistent with the generally accepted WHIM range and with the latest simulations.

4. Modelling the IGM using WARMABS for PIE with NHXIGM, Z and ξ as free parameters appears to present plausible results though with more scatter at lower redshift compared to our CIE model . The PIE NHXIGM shows values and rise with redshift comparable to the mean IGM hydrogen density model in Fig. 3.5 top-left panel. A power law fit to the NHXIGM versus redshift trend scales as $(1+z)^{1.0\pm0.3}$, a much flatter power law than for CIE. The mean hydrogen density equivalent from this model at $z = 0$ is $n_0 = 1.8^{+1.4}_{-1.2} \times 10^{-7}$ cm^{-3}, very similar to the CIE result.

5. In the PIE scenario, there is a power law fit to the [X/H] and redshift trend scaling as $(1+z)^{-2.1\pm0.8}$, a slower decline than under the CIE IGM model. The metallicity is approximately [X/H] $= -1.0$ ($Z = 0.1Z_\odot$) at $z \sim 2$ falling to [X/H]$= -2.4$ ($Z = 0.004Z_\odot$) at $z > 4$.

6. The PIE ionisation parameter range from fits is $0.1 < \log(\xi) < 2.9$, Fig. 3.5 bottom-left panel. The mean ionisation parameter over the full redshift range is $\log(\xi) = 1.6^{+0.9}_{-1.2}$.

7. Regardless of the assumed ionisation state of the IGM, both models pick up considerable highly ionised absorption.

8. We compared our CIE model with ABSORI in Appendix chapter 3 which was generally used in prior studies using GRBs as IGM tracers. ABSORI is limited with only 10 metals, all fixed to solar metallicity except Fe. Our CIE and PIE IGM models use software which include all metals and ionisation species up to $Z \leq 30$, with variable metallicity. In conclusion, ABSORI is no longer a preferred model for IGM absorption and the results of earlier studies using it for IGM modelling may not be reliable.

9. All our GRB spectra have fits as good as or better than the model with all excess absorption assumed to occur at the GRB host redshift. While some excess absorption may be attributable to the GRB host and its CGM, in our models the IGM contributes substantially to the total absorption seen in GRB spectra, and it rises with redshift. We provide clear evidence that a complete model should also account for a (possibly dominant) fraction of intervening IGM material.

   This study is based on observations of GRB X-ray spectra, and provides results on the IGM parameters. The constraints will only be validated when observations are available from instruments with large effective area, high energy resolution, and a low energy threshold in the soft X-ray energy band e.g. Athena which will study the IGM through detailed observations of O VII and O VIII absorption features with equivalent width > 0.13 eV and > 0.09 eV respectively.

3.8 Appendix chapter 3 - Model comparisons and investigating robustness of CIE and PIE free parameter fits

3.8.1 Metallicity fixed to $Z = 0.01Z_\odot$

To test the selected PIE and CIE models, we conducted trials freezing one key parameter at a time. We limited the sample data size to 15 covering the full redshift range 1.6 – 6.3. For the first trial we froze the metallicity of the IGM to $Z = 0.01Z_\odot$ as representative of the diffuse IGM. Most studies of the cooler PIE IGM in Lyα regions found virtually no evidence for metallicity evolution in the range z $\sim 2-4$ (e.g. S03, A08) so it is reasonable to test this scenario. The green line for all models is the mean density of the IGM based on the simple model from eq. 3.1.

3.8.1.1 warmabs (PIE)

In Fig. 3.6 left, the expected increase of NHXIGM with redshift does not arise with WARMABS when the metallicity is frozen to $Z = 0.01Z_\odot$. The low redshift NHXIGM is substantially higher than the expected mean IGM density, while at higher redshifts it is below the IGM mean density. This could indicate that a fixed metallicity assumption is unrealistic, or the PIE model is not appropriate for the LOS to the GRB. In Fig. 3.6 middle panel, we see a wide range of ionisation parameters with substantial error bars at lower redshift. There appears to be a negative trend with redshift, though this may be due to the metallicity being fixed.

Fig. 3.6 right panel shows an example of the a MCMC integrated probability plot for the WARMABS PIE NHXIGM and ξ. Most MCMC integrated probability plots are reasonably consistent with STEPPAR, indicating a good fit with low Cstat, but some are not. In this example, there are a few islands of high probability. As for

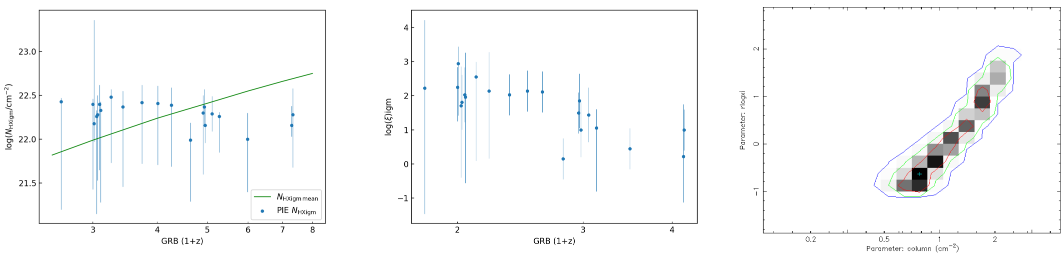

Figure 3.6: Results for the IGM parameters using the PIE warmabs model with $Z = 0.01Z_{\odot}$. The error bars are reported with a 90% confidence interval. Left panel is *N*HX and redshift. The green line is the simple IGM model using the mean IGM density. Middle panel is ionisation parameter versus redshift. Right panel is an example of an integrated MCMC plot. The red, green and blue contours represent $68\%, 95\%$ and 99% ranges for the two parameters respectively, with greyscale showing increasing integrated probability from dark to light. On the y-axis rlogxi = log(ξ).

several of the GRB, its shows that the best fit could have occurred at the low or high end of the confidence range. In conclusion, primarily due to the result for column density, it is likely, that a fixed metallicity warmabs based PIE model for the IGM is not realistic.

3.8.1.2 hotabs (CIE)

Similar to the WARMABS PIE model, the expected increase of *N*HXIGM with redshift in Fig. 3.7 left panel does not arise with HOTABS when the metallicity is frozen to $Z = 0.01Z_{\odot}$. This could indicate that a fixed metallicity assumption is unrealistic, or that the CIE model is not appropriate. Again, at low redshift, the *N*HXIGM is much greater than the mean density model, while at high redshift it is much lower. The error bars are very large. In Fig. 3.7 middle panel, we see a wide range of temperatures with substantial error bars. The best fit data points appear to favour either the high or low end of the 90% confidence range. Finally, Fig. 3.7 right panel shows an example of the MCMC integrated probability plot for the HOTABS CIE *N*HXIGM and T. In this example, there is a characteristic S shape where, at high column density, a range of temperatures at a similar column density could fit, while at low temperature, there is a different range of column densities that could

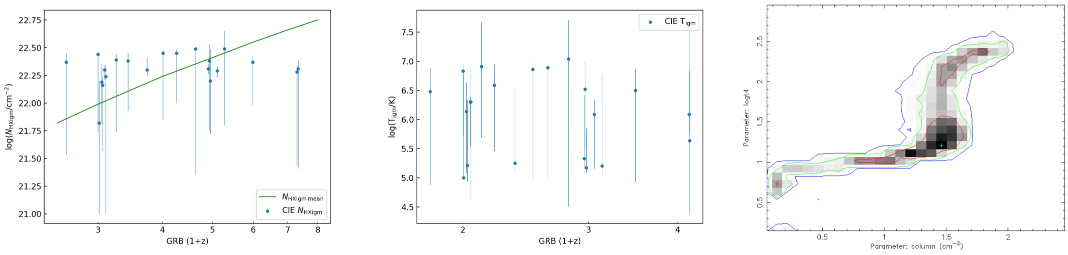

Figure 3.7: Results for the IGM parameters using the CIE HOTABS model with $Z = 0.01_{\odot}$CIE Z=0.01. The error bars are reported with a 90% confidence interval. Left panel is NHX and redshift. The green line is the simple IGM model using the mean IGM density. Middle panel is temperature versus redshift. Right panel is an example of an integrated MCMC plot. The red, green and blue contours represent $68\%, 95\%$ and 99% ranges for the two parameters respectively, with grey-scale showing increasing integrated probability from dark to light. On the y-axis in the bottom-left panel T4 means the log of the temperature is in units of 10^4 K.

fit. There is a single high maximum but there are a couple of islands of 1 sigma probability.

In conclusion, it is likely, that a fixed metallicity HOTABS based CIE model for the IGM is not realistic.

3.8.1.3 ioneq (CIE)

Modelling the IGM using IONEQ with a fixed metallicity appears to present plausible results for NHXIGM in Fig. 3.8 left panel, showing a similar rise with redshift as the mean IGM density model, except at very high redshift. A power law fit to the NHXIGM versus redshift trend scales as $(1 + z)^{1.8 \pm 0.5}$. We note that all metals included in the IONEQ model, except O, Ne and Fe, are fixed to the solar abundance, an unrealistic value for the diffuse IGM. IONEQ is currently being updated to allow all metals as free parameters but was not available for this paper (Gatuzz, E., private communication). As with HOTABS, the error bars on temperature with redshift in Fig. 3.8 middle panel are substantial, but the best fits do not favour the high or low end of the confidence interval.

Most MCMC integrated probability plots for IONEQ fittings show large degeneracy

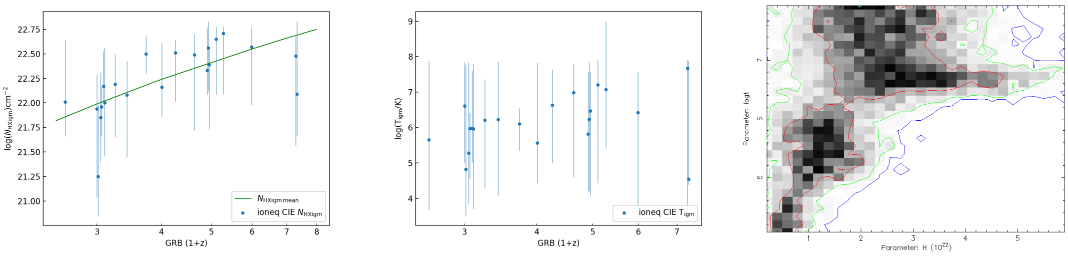

Figure 3.8: Results for the IGM parameters using the IONEQ CIE model with IGM $Z = 0.01\ Z_\odot$. The error bars are reported with a 90% confidence interval. Left panel is NHX and redshift. The green line is the simple IGM model using the mean IGM density. Middle panel is temperature versus redshift. Right panel is an example of an integrated MCMC plot. The red, green and blue contours represent $68\%, 95\%$ and 99% ranges for the two parameters respectively, with grey-scale showing increasing integrated probability from dark to light.

as seen in the example in Fig. 3.8 right panel, with many local maxima. The Cstat fits to the GRB spectra are as good as for WARMABS and HOTABS. In conclusion, the plots suggest that a CIE IGM model with fixed metallicity of $Z = 0.01\ Z_\odot$ may be plausible. However, due to the MCMC showing substantial degeneracies, and the unrealistic solar metallicities, we have not used this model.

3.8.1.4 absori

Fig. 3.9 left panel shows the results for NHXIGM using ABSORI for the IGM absorption with metallicity fixed again at $Z = 0.01\ Z_\odot$. In ABSORI, only Fe is affected as the other 9 metals in the model are fixed to solar. The ionisation parameter was fixed at $\xi = 0$, so only temperature was allowed to vary as a CIE model. The fits were very poor, errors could not be generated in XSPEC, and the MCMC runs failed to generate plausible results. No apparent redshift correlation can be seen, similar to WARMABS and HOTABS. Due to the poor fits, it cannot be said whether this is due to the ABSORI model being limited to 10 metals, having all metals, except Fe at solar, edge absorption only or the model not being self-consistent. Fig 3.9 right panel shows the IGM temperatures from the fittings. As with all models, it shows a large scatter. In conclusion, ABSORI is no longer an ideal model for IGM

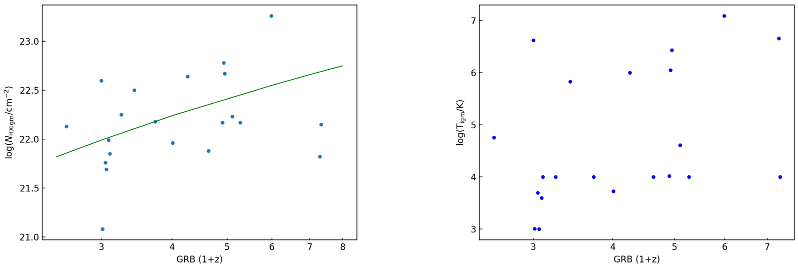

Figure 3.9: Results for the IGM parameters using the ABSORI CIE model with the IGM $Z = 0.01_{\odot}$. Left panel is NHX and redshift. The green line is the simple IGM model using the mean IGM density. Right panel is temperature and redshift. No error bars could be generated by XSPEC.

absorption.

In summary, WARMABS and HOTABS are the most sophisticated models, and the MCMC integrated probability plots were the most consistent with the STEPPAR results and have plausible integrated probability plots. Most show a single deep maximun, but there is degeneracy with several possible parameter fit solutions. Accordingly, we decided to proceed only with WARMABS and HOTABS, and not IONEQ nor ABSORI for the remaining tests. However, the fixing of metallicity for both PIE and CIE IGM models with redshift is not appropriate for any model.

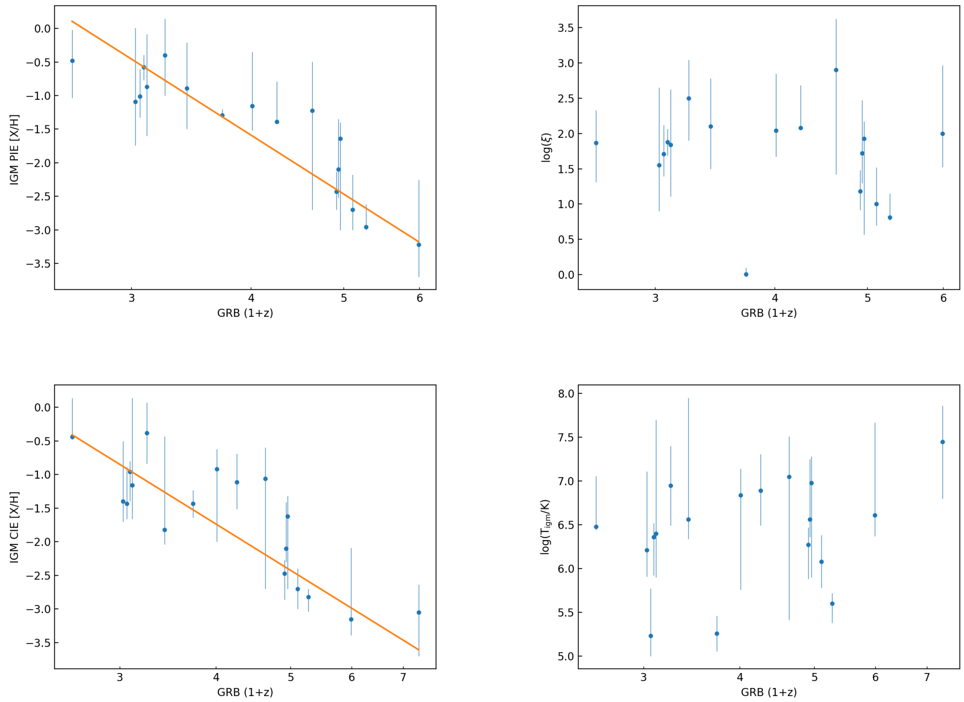

Figure 3.10: Results for the IGM parameters with NHXIGM fixed at the mean IGM density. The error bars are reported with a 90% confidence interval. Top-left panel is $[X/H]$ versus redshift for the PIE model. Top-right panel is ionisation versus redshift for PIE. Bottom-left panel is the CIE model $[X/H]$ versus redshift. Bottom-right panel is $\log(T/\mathrm{K})$ versus redshift for CIE. The orange line is the χ^2 fit. We do not include a χ^2 curve in the temperature-redshift plot (bottom-right) as the fit had very large uncertainties.

3.8.2 Forcing N_{HXIGM} to equal the mean IGM density

The next approach investigated was to freeze the NHXIGM parameter at the value for mean IGM density integrated to the GRB redshift using eq.3.1 . Metallicity and ionisation parameters (PIE) or temperature (CIE) were free.

For both PIE and CIE, nearly all fits were consistent with STEPPAR and showed good integrated probability plots. There is a requirement for strong metallicity evolution in both scenarios with power law fits to the $[X/\mathrm{H}]$ versus redshift trend scaling as $(1+z)^{-9.1\pm0.7}$ and $(1+z)^{-7.1\pm0.8}$ for PIE (Fig. 3.10 top-left panel) and CIE (Fig. 3.10 bottom-left panel) respectively. The 90% confidence range was much improved for the $[X/\mathrm{H}]$ fits as compared with the fixed metallicity scenario fits

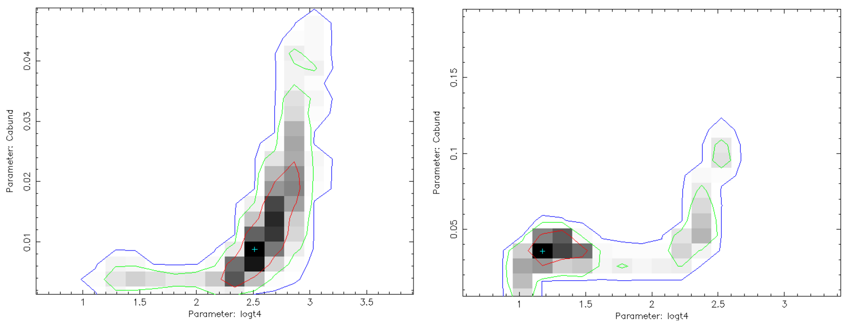

Figure 3.11: Sample MCMC integrated probability plots with hotabs CIE IGM for two GRB with N_{HXIGM} equal to the mean density. The red, green and blue contours represent $68\%, 95\%$ and 99% ranges for the two parameters respectively, with grey-scale showing increasing integrated probability from dark to light. On the x-axis T4 means the log of the temperature is in units of 10^4 K. On the y-axis all metals are tied to the $Z/Z_{\odot}$ for Carbon.

for NHXIGM. The ionisation parameter for the PIE fits varied widely between $0 < \log(\xi) < 3$ without any simple trend with redshift. The temperature parameter for the CIE fits also varied widely between $5 < \log{(T/\text{K})} < 7.5$ without any simple trend with redshift.

Fig. 3.11 shows two examples of MCMC integrated probability plots for the CIE scenario. Both show the patterns that most GRB showed in this scenario of NHXIGM fixed to the mean density where at high temperature, a range of metallicity could fit, while at low metallicity, there is a range of temperature that could fit.

In conclusion, if the scenario where the average density model of the IGM is valid for the GRB sight lines, it requires strong metallicity evolution for both CIE and PIE. It is not possible to determine which scenario (CIE versus PIE) is more plausible from the fits apart from the fact that the high redshift $z = 6.32$ GRB140505 was well fitted with CIE but not with PIE. The results support the Section 4 free parameter fit model scenarios for both PIE snd CIE IGM and could be interpreted as validity check.

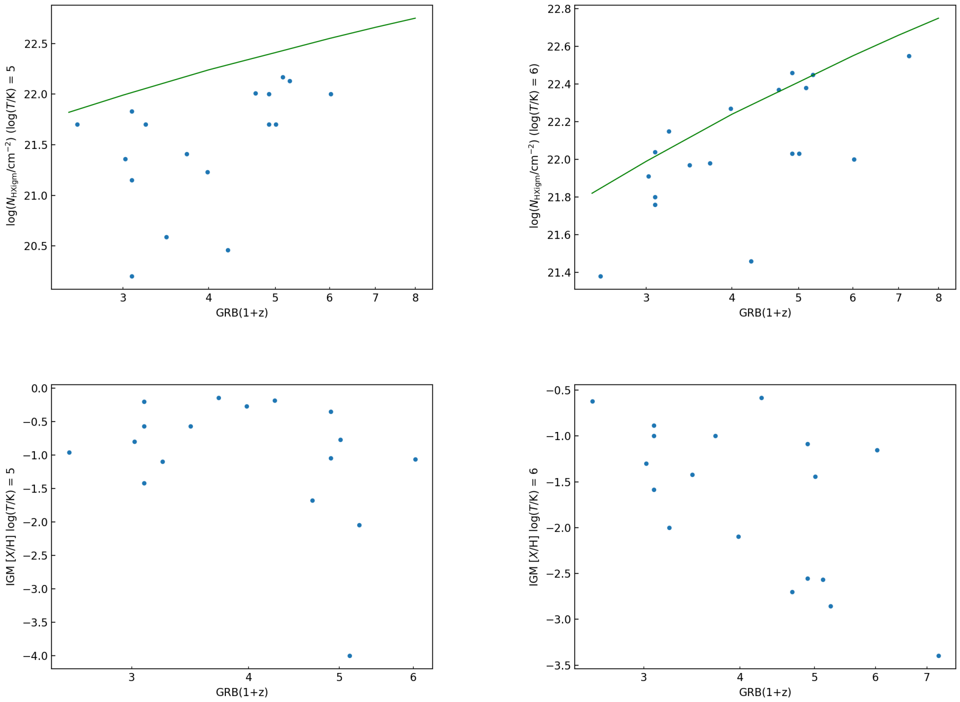

Figure 3.12: Results for the IGM parameters using the HOTABS CIE model with fixed temperatures. The green curve is the simple IGM model using the mean IGM density. Top-left panel is *N*HXIGM versus redshift and bottom-left panel is [X/H] versus redshift for the CIE model with log(T/K) = 5. Top-right panel is *N*HXIGM versus redshift and bottom-right panel is [X/H] versus redshift for the CIE model with log(T/K) = 6. We do not include error bars as the plots are not plausible models.

3.8.3 Freezing temperature for CIE and ionisation parameter for PIE

The next test was to freeze temperature for CIE and ionisation parameter for PIE and leave *N*HXIGM and metallicity free. For temperature in the CIE HOTABS model, we froze temperature at log(T/K) = 5 and 6 as representative of the cooler and hotter CIE phases.

The fits for *N*HXGM with temperature fixed at log(T/K) = 5, are much lower than the mean IGM model in Fig. 3.12 top-left panel, with considerable scatter. In Fig. 3.12 top-right panel with log(T/K) = 6, some fits are similar to the mean IGM model and show a suggestion of a rise with redshift with some outliers. However, several are well below the mean density. The metallicity plots for both fixed temperatures

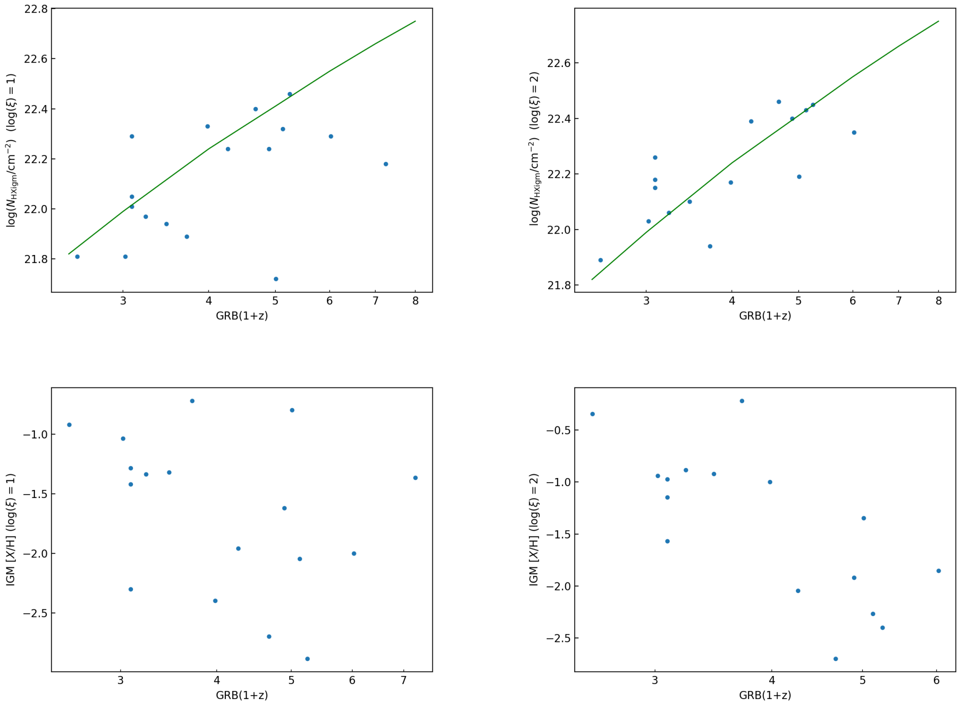

Figure 3.13: Results for the IGM parameters using the WARMABS PIE model with fixed ionisation parameters. The green curve is the simple IGM model using the mean IGM density. Top-left panel is *N*HXIGM and redshift and bottom-left panel is [X/H] and redshift for the PIE model with log(ξ) = 1. Top-right panel is *N*HXIGM and redshift and bottom-right panel is [X/H] and redshift for the PIE model with log(ξ) = 2. We do not include error bars as the plots are not meant to be representative of plausible models.

show no apparent relation with redshift. The higher temperature log(T/K) = 6 CIE model appears more realistic if the IGM mean density model is appropriate for the IGM. However, it is unlikely that a fixed average temperature approach is appropriate for our CIE IGM modelling.

For PIE, the ionisation parameter was frozen at log(ξ) = 1 and 2. At both log(ξ) = 1 and 2, there is a possible *N*HXIGM rise with redshift in Fig. 3.13 top-left and right panels. Further, the fits for both are similar to the mean density model, with log(ξ) = 2 being closer. There is a suggestion of metallicity evolution at log(ξ) = 2. It is not possible to say whether freezing ionisation parameter is a reasonable approach but the fits and overall results for log(ξ) = 2 are better, with lower Cstat.

In summary, freezing the ionisation parameter gives somewhat more plausible results in the PIE scenarios than the CIE scenarios with fixed temperatures. However, overall, the scenarios with such fixed parameters are not preferred and therefore, we suggest that our free parameter IGM scenarios are more realistic in Section 3.5.

The WARMABS and HOTABS models are more sophisticated than the current version of IONEQ and ABSORI, again supporting our model choices in Section 3.5.

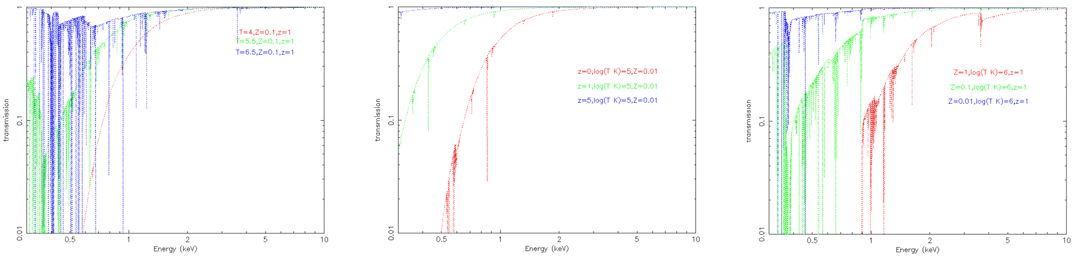

Figure 3.14: HOTABS transmission models showing the impact of variations for metallicity, temperature and redshift on transmission.

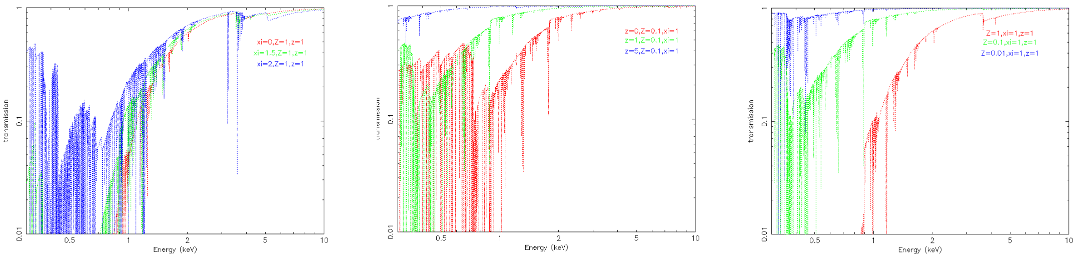

Figure 3.15: WARMABS transmission models showing the impact of variations for metallicity, ionisation parameter and redshift on transmission.

3.8.4 Sample transmission plots

The figures show the impact on transmission using models for CIE and PIE varying the parameters for temperature, redshift, metallicity and ionisation.

Chapter **4**

Probing the physical properties of the intergalactic medium using blazars

This paper was published as Dalton T., Morris S. L., Fumagalli, M., Gatuzz, E., 2021, MNRAS 508, 2, 1701, and reproduced here with minor formatting changes

4.1 Summary

We use *Swift* blazar spectra to estimate the key intergalactic medium (IGM) properties of hydrogen column density (NHXIGM), metallicity and temperature over a redshift range of $0.03 \leq z \leq 4.7$, using a collisional ionisation equilibrium (CIE) model for the ionised plasma. We adopted a conservative approach to the blazar continuum model given its intrinsic variability and use a range of power law models. We subjected our results to a number of tests and found that the NHXIGM parameter was robust with respect to individual exposure data and co-added spectra for each source, and between *Swift* and *XMM-Newton* source data. We also found no relation between NHXIGM and variations in source flux or intrinsic power laws. Though some objects may have a bulk Comptonisation component which could

mimic absorption, it did not alter our overall results. The NHXIGM from the combined blazar sample scales as $(1+z)^{1.8\pm0.2}$. The mean hydrogen density at $z = 0$ is $n_0 = (3.2 \pm 0.5) \times 10^{-7}$ cm^{-3}. The mean IGM temperature over the full redshift range is $\log(T/\mathrm{K}) = 6.1 \pm 0.1$, and the mean metallicity is $[X/\mathrm{H}] = -1.62 \pm 0.04$ ($Z \sim 0.02$). When combining with the results with a gamma-ray burst (GRB) sample, we find the results are consistent over an extended redshift range of $0.03 \leq z \leq 6.3$. Using our model for blazars and GRBs, we conclude that the IGM contributes substantially to the total absorption seen in both blazar and GRB spectra.

4.2 Introduction

The main objective of this paper is to estimate key IGM parameters of column density, metallicity, and temperature, using a model for ionised absorption on the line of sight (LOS) to blazars. Our hypothesis is that there is significant absorption in the diffuse IGM, and that this IGM column density increases with redshift. Our approach is different to most other blazar studies which focus primarily on the intrinsic curvature of the X-ray spectral flux, or where works attribute to the host only, any spectral hardening due to excess absorption over our Galaxy (e.g Bottacini et al., 2010; Paliya et al., 2016; Ricci et al., 2017). Instead, we focus on the possible absorption due to the IGM using a sophisticated highly ionised absorption component in addition to best fit intrinsic curvature models. We test the robustness of our result from a number of perspectives. Finally, we combine our blazar sample with an extended redshift GRB sample to enable cross tracer comparison.

Most baryonic matter resides in the IGM (McQuinn, 2016). Simulations predict that up to 50% of the baryons by mass have been shock-heated into a warm-hot phase (WHIM) at $z < 2$, with $T = 10^5 - 10^7$ K and $n_b = 10^{-6} - 10^{-4}$ cm^{-3} where n_b is the baryon density (e.g Cen and Ostriker, 1999, 2006; Davé and Oppenheimer, 2007; Schaye et al., 2015). Martizzi et al. (2019), using the IllustrisTNG simulations

[*](Piattella, 2018), estimated that the cool diffuse IGM constitutes $\sim 39\%$ and the WHIM $\sim 46\%$ of the baryons at redshift $z = 0$. Observations of the cool diffuse IGM and WHIM are required to trace matter across time and to validate the simulations (Danforth et al., 2016).

A significant fraction of the cool gas probed by strong Lyα forest systems (SLFSs): $15 < \log N_{\rm H\,I} < 16.2$[†]; partial Lyman Limit Systems (pLLSs): $16.2 < \log N_{\rm H\,I} < 17.2$; Lyman Limit Systems (LLSs): $17.2 < \log N_{\rm H\,I} < 19$; super-LLSs (sLLSs): $19.0 < \log N_{\rm H\,I} < 20.3$; and Damped Ly$\alpha$ Systems (DLAs) $\log N_{\rm H\,I} > 20.3$ (Fumagalli, 2014) has been associated with galaxy haloes and the circum-galactic medium (CGM) (Pieri et al., 2014; Fumagalli et al., 2013, 2016). Over the last several decades, observations of redshifted Lyα absorption in the spectra of quasars has provided a highly sensitive probe of the cool IGM (e.g. Morris et al., 1991; York et al., 2000; Harris et al., 2016; Fumagalli et al., 2020). At higher temperatures, for some time, the expected baryons were not detected in the WHIM, giving rise to the "missing" baryon problem (Danforth and Shull, 2005, 2008; Shull et al., 2012, 2014). Recent literature points to the CGM as the reservoir for at least a fraction of this missing matter (Tumlinson et al., 2011, 2013; Werk et al., 2013; Lehner et al., 2016). Other claims to have detected the WHIM include possible detection of O VII lines, excess dispersion measure over our Galaxy and the host galaxy in Fast Radio Bursts (FRB), using the thermal Sunyaev Zelodovich effect, and X-ray emission from cosmic web filaments (e.g. Nicastro et al., 2018; Macquart et al., 2020; Tanimura et al., 2020b).

Detection of the WHIM is extremely challenging, as its emission is very faint, it lacks sufficient neutral hydrogen to be seen via Lyα absorption in spectra of distant quasars, and the X-ray absorption signal expected from the WHIM is extremely weak (Nicastro et al., 2018; Khabibullin and Churazov, 2019). The vast majority of hydrogen and helium is ionised in the IGM post reionisation. Therefore, the

---

[*] http://www.tng-project.org/

[†] Throughout this chapter, logarithmic column densities are expressed in units of cm^{-2}

observation of metals is essential for exploring the IGM properties including density, temperature and metallicity. Absorption-line studies in optical to UV, of individual systems that use the ionisation states of abundant heavy elements, have been very successful (e.g. Shull et al., 2014; Raghunathan et al., 2016; Selsing et al., 2016; Lusso et al., 2015). However, most very highly ionised metals are not observed in optical to UV. Tracing individual features of the IGM metals in X-ray with current instruments is very limited. Although the X-ray absorption cross-section is mostly dominated by metals, it is typically reported as an equivalent hydrogen column density (hereafter NHX).

Extremely energetic objects such as active galactic nuclei (AGN) and GRBs are currently some of the most effective tracers to study the IGM as their X-ray absorption provides information on the total absorbing column density of matter between the observer and the source (e.g. Galama and Wijers, 2001; Watson et al., 2007; Watson, 2011; Wang, 2013; Schady, 2017; Nicastro et al., 2017, 2018). NHX consists of contributions from the host local environment, the IGM, and our own Galactic medium. The Galactic component is usually known from studies such as Kalberla et al. (2005); Willingale et al. (2013, hereafter W13).

One of the main results of earlier studies of the IGM using high redshift tracers is the apparent increase in excess of NHX with redshift (e.g. Behar et al., 2011; Watson, 2011; Campana et al., 2012). The cause of the NHX rise with redshift seen in high redshift tracers has been the source of much debate over the last two decades. One school of thought argues that the object host accounts for all the excess and evolution (e.g Schady et al., 2011; Watson et al., 2013; Buchner et al., 2017) . The other school of thought argues that while the host can have an absorption contribution, the IGM contributes substantially to the excess absorption and is redshift related (e.g Starling et al., 2013; Arcodia et al., 2016; Rahin and Behar, 2019; Dalton and Morris, 2020; Dalton et al., 2021a, hereafter D20, D21). The convention in earlier studies using AGN and GRBs was to use solar metallicity for a neutral absorber, as a device used to place all of the absorbing column density measurements on a comparable scale. These studies all noted that the resulting column densities were, therefore, lower limits as GRBs typically have much lower metallicities. D20 used realistic GRB host metallicities to generate improved estimates of N_{HX}. They confirmed the N_{HX} redshift relation.

While GRBs can have significant host absorption, blazars are thought to have negligible X-ray absorption on the LOS within the host galaxy, swept by the kpc-scale relativistic jet (Arcodia et al., 2018, hereafter A18). This makes blazars ideal candidates for testing the absorption component of the IGM. Despite the suitability of blazars as IGM tracers, A18 is the only previous study to use them to explore IGM absorption as the cause of spectral curvature. Blazars are a special class of radio-loud AGN in which the relativistic plasma emerges from the galaxy core as a jet towards the observer. The broad-band spectra of blazars are characterized by two humps. The first hump produces a peak located between infrared to X-ray frequencies and is attributed to synchrotron processes. The second hump is typically found in X-ray to γ-ray frequencies and relates to inverse Compton (IC) processes. The seed photons for the IC process can be intrinsic to the jet, emitted through synchrotron processes at low frequencies called Synchrotron Self-Compton (SSC) (e.g Ghisellini and Maraschi, 1989). Alternatively, if the seed photons originated from the accretion disc and are reprocessed by the broad-line region and/or the molecular torus, it is referred to as External Compton (EC) (e.g. Sikora et al., 1994). Blazars are conventionally classified as either flat spectrum radio quasars (FSRQs) characterized by strong quasar emission lines and higher radio polarization, or BL Lac objects exhibiting featureless optical spectra (Urry and Padovani, 1995). The distribution of the synchrotron peak frequency is significantly different for the two blazar classes. While the rest-frame energy distribution of FSRQs is strongly peaked at low frequencies ($\leq 10^{14.5}$ Hz), the energy distribution of BL Lacs is shifted to higher values by at least one order of magnitude (Padovani et al., 2012). FSRQs have a much higher median redshift than BL Lacs, and can be found out to high redshift (Sahakyan et al., 2020). Therefore, we focus primarily on FSRQ blazars in this study.

The sections that follow are: Section 4.3 describes the data selection and methodology; Section 4.4 covers the models for the IGM LOS including key assumptions and parameters, and blazar continuum models; Section 4.5 gives the results of blazar spectra fits using collisional IGM models with free IGM key parameters; in Section 4.6 we investigate and test the robustness of the IGM model fits; in Section 4.7 we combine a GRB sample with our blazar sample for cross-tracer analysis. We discuss the results and compare with other studies in Section 4.8, and Section 4.9 gives our conclusions. We suggest for readers interested in the key findings on IGM parameters from fits only, read Sections 4.5, 4.7 and 4.9. Readers interested in detailed spectra fitting methodology and model assumptions should also read Sections 4.3 and 4.4. Finally, for readers interested in more detailed examination of robustness of the blazar spectra fitting and comparison with other studies, read Sections 4.6 and 4.8.

4.3 Data selection and methodology

The total number of confirmed blazars by means of published spectra as of 2020 was 2,968 (1,909 FSRQ and 1,059 BL Lac) per the Roma-BZCAT Multifrequency Catalogue (Roma), which is regarded as the most comprehensive list of blazars (Paggi et al., 2020; Massaro et al., 2015). The vast majority of blazars are at $z < 2$, with less than 4% at $z > 2$ and 1.2% at $z > 2.5$ (Sahakyan et al., 2020). As our objective is to examine possible absorption by the IGM in blazar spectra, our percentage coverage is greater at higher redshift than lower redshift i.e. $\sim$ 13% of blazars with $z > 2$ and $\sim$ 25% of blazars at $z > 2.5$ based on the Roma Catalogue numbers. Our sample criteria requires blazars with confirmed redshift whose spectra have high counts for spectral analysis with a spread across redshift up to $z = 4.7$. Table 4.1 gives the counts for each blazar in the sample. The counts range from 361 to 139, with the highest redshift blazars ($z > 3$) accounting for most of the counts below 1000. We reviewed literature which studied large numbers of blazars (e.g. Perlman et al., 1998; Donato et al., 2005; Eitan and Behar, 2013; Ighina et al., 2019; Marcotulli et al., 2020) and, within our criteria, selected objects randomly for our sample. Our sample has 14 with $z > 2$, a high fraction of the total available as noted above. To keep a reasonable spread across the redshift range which is a log scale, we randomly selected 9 from $1 < z < 2$, with 17 with $z < 1$. The sample selection method requiring high counts could introduce possible biases. I investigate this in Chapter 5 for the larger QSO sample.

A key part of our research is the comparative analysis with the GRB sample from D20 and D21 which was taken primarily from the UK *Swift* Science Data Centre[*] repository (hereafter *Swift*; Gehrels et al., 2004). To ensure a homogeneous dataset across Blazars and GRBs, our main sample of 40 blazars is drawn from the *Swift* 2SXPS Catalogue (Evans et al., 2020), using their XRT data products generator. *Swift* was designed for GRBs which are thought to explode randomly across the sky and blazars are totally unrelated to these sources. Therefore, *Swift* provides a highly unbiased, all sky, serendipitous database of blazars. *Swift* recovers much of the comparative sensitivity with *XMM − Newton* even though it has a lower effective area and smaller field of view (Evans et al., 2020).

Swift has proven to be an excellent multi-frequency observatory for blazar research. Our sample spectra from the *Swift* repository were taken from the Photon Counting mode with high photon count. High signal-to-noise X-ray spectra are necessary to properly assess the presence of a curved spectrum in distant extra-galactic sources and its components. Therefore, where multiple observations of the same object were available, we use co-added spectra. Our sample is representative of the range from $0.03 < z < 4.7$ and details are available in Table 4.1.

---

[*] http://www.swift.ac.uk/xrtspectra

Table 4.1: *Swift* blazar sample. For each blazar, the columns give the name, type, redshift, number of counts in 0.3-10 keV range and count rate (s^{-1}). Co-added spectra for each blazar are used which often are observed over a number of years, so we do not provide individual observation information.

Blazar	Type	z	Total counts	Mean count rate (s^{-1})
Mrk 501	BL Lac	0.03	4398	4.471 ± 0.009
PKS 0521-365	BL Lac*	0.06	17076	0.673 ± 0.004
BL Lac	BL Lac	0.07	78117	0.360 ± 0.001
1ES 0347-121	BL Lac	0.18	2318	1.158 ± 0.018
1ES 1216+304	BL Lac	0.18	26601	1.404 ± 0.007
4C +34.47	FSRQ	0.21	9631	0.345 ± 0.006
1ES 0120+340	BL Lac	0.27	13358	0.987 ± 0.007
S50716+714	FSRQ	0.31	69783	0.596 ± 0.002
PKS 1510-089	FSRQ	0.36	60630	0.264 ± 0.001
J1031+5053	BL Lac	0.36	5653	1.022 ± 0.009
3C 279	FSRQ	0.54	139130	0.462 ± 0.001
1ES 1641+399	FSRQ	0.59	13752	0.168 ± 0.002
PKS 0637-752	FSRQ	0.64	4767	0.192 ± 0.003
PKS 0903-57	FSRQ	0.70	361	0.116 ± 0.004
3C 454.3	FSRQ	0.86	83571	1.259 ± 0.002
PKS 1441+25	FSRQ	0.94	2282	0.072 ± 0.002
4C +04.42	FSRQ	0.97	1831	0.108 ± 0.003
PKS 0208-512	FSRQ	1.00	8218	0.085 ± 0.008
PKS 1240-294	FSRQ	1.13	944	0.126 ± 0.005
PKS 1127-14	FSRQ	1.18	5950	0.167 ± 0.002
NRAO 140	FSRQ	1.26	5673	0.305 ± 0.004
OS 319	FSRQ	1.40	1180	0.004 ± 0.001
PKS 2223-05	FSRQ	1.40	1765	0.078 ± 0.002
PKS 2052-47	FSRQ	1.49	1360	0.094 ± 0.003
4C 38.41	FSRQ	1.81	20962	0.145 ± 0.001
PKS 2134+004	FSRQ	1.93	1394	0.090 ± 0.003
PKS 0528+134	FSRQ	2.06	8779	0.060 ± 0.001
1ES 0836+710	FSRQ	2.17	54675	0.664 ± 0.002
PKS 2149-306	FSRQ	2.35	16986	0.415 ± 0.003
J1656-3302	FSRQ	2.40	1365	0.113 ± 0.003
PKS 1830-211	FSRQ	2.50	13367	0.208 ± 0.002
TXS0222+185	FSRQ	2.69	4461	0.207 ± 0.003
PKS 0834-20	FSRQ	2.75	826	0.038 ± 0.001
TXS0800+618	FSRQ	3.03	647	0.057 ± 0.002
PKS 0537-286	FSRQ	3.10	4205	0.079 ± 0.001
PKS 2126-158	FSRQ	3.27	7280	0.225 ± 0.003
S50014+81	FSRQ	3.37	2051	0.112 ± 0.002
J064632+445116	FSRQ	3.39	569	0.029 ± 0.001
J013126-100931	FSRQ	3.51	592	0.055 ± 0.002
B3 1428+422	FSRQ	4.70	488	0.049 ± 0.002

*The classification of PKS0521-365 is disputed as being either a FSRQ, BL Lac or even a non-blazar (e.g. Urry and Padovani, 1995; Zhang et al., 2021, A18)

Table 4.2: *XMM-Newton* sub-sample for individual observation comparison with *Swift* co-added spectrum results. For each blazar, the columns give Observation ID, redshift, total counts and count rate for 0.3-10 keV.

Blazar	Observation ID	z	Total counts	Mean count rate (s^{-1})
3C 454.3	mean	0.86	261165	24.86
	0401700201			
	0401700401			
	0401700501			
	0103060601			
PKS 2149-306	0103060401	2.35	39152	1.91
PKS 2126-158	0103060101	3.26	39504	2.62
PKS 0537-286	mean	3.10	44938	1.40
	0114090101			
	0206350101			
1ES 0836+710	0112620101	2.17	236705	10.08
TXS 0222+185	mean	2.69	528277	6.80
	0150180101			
	0690900101			
	0690900201			
PKS 0528+134	mean	2.06	18051	0.88
	0600121401			
	0600121501			
	0401700601			
	0103060701			

In section 4.6, as part of robustness testing, we use a sub-sample of 7 *XMM-Newton* spectra (Table 4.2). The *XMM-Newton* European Photon Imaging Camera-pn (Strüder et al., 2001) spectra were obtained in timing mode, using the thin filter. Data reduction, including background subtraction, was done with the Science Analysis System (SAS2, version 19.1.0) following the standard procedure to obtain the spectra.

While we fit 7 BL Lac, in our analysis of IGM parameters such as the *N*HXIGM redshift relation, we use only FSRQ and omit BL Lac. FSRQ are more powerful and therefore more likely to sweep out any host absorbers. Further, their spectra have less intrinsic features which may be degenerate with potential IGM absorption curvature.

We use XSPEC version 12.11.1 for all our fitting (Arnaud, 1996). We use the C-statistic (Cash, 1979) (Cstat in XSPEC). The common practice of rebinning data to use a χ^2 statistic results in loss of energy resolution. The maximum likelihood C-statistic, based on the Poisson likelihood, does not suffer from these issues. For a spectrum with many counts per bin C-statistic $\rightarrow \chi^2$, but where the number of counts per bin is small, the value for C-statistic can be substantially smaller than the χ^2 value (Kaastra, 2017).

Given we are studying the IGM with X-ray spectra, we can expect some degeneracies between the parameters. Therefore, there may be several local probability maxima with multiple, separate, adequate solutions. In these circumstances, the local optimisation algorithms like the Levenberg- Marquardt cannot identify them or jump from one local maximum to the other. Given the issues of goodness of fit and getting out of local probability maxima, we follow the same method as D21, and use a combination of the XSPEC STEPPAR function, and confirmation with Markov chain Monte Carlo (MCMC) to validate our fitting and to provide confidence intervals on Cstat.

Approximating a χ^2 criterion, we follow the approach that a reduction of Cstat$>$ 2.71, $>$ 4.6, and $>$ 6.25 for one, two and three additional interesting parameters corresponds to 90% significance (Reeves and Turner, 2000; Ricci et al., 2017). We follow this method in Section 4.5 when fitting continuum only models and full models with an IGM absorption component.

As the bulk of matter in the IGM is ionised and exists outside of gravitationally bound structures (apart from the CGM), in this paper we use a homogeneity assumption. We use blazars that have LOS orders of magnitude greater than the large scale structure.

4.4 Models for the Blazar LOS

In this section we describe the motivation and expected physical conditions in the IGM that lead to our choice of models, the priors and parameter ranges. We also describe the models and reasoning used for fitting the intrinsic spectra of the blazars.

4.4.1 Galactic absorption

For Galactic absorption (NHXGAL), we use TBABS (Wilms et al., 2000, hereafter W00) fixed to the values based on Willingale et al. (2013) i.e. estimated using 21 cm radio emission maps from (Kalberla et al., 2005) , including a molecular hydrogen column density component. TBABS calculates the cross-section for X-ray absorption by the ISM as the sum of the cross sections for the gas, grain and molecules in the ISM. Asplund et al. (2009) is generally regarded as providing the most accurate solar abundances, though this has been updated by Asplund et al. (2021). However, we used the solar abundances from W00 which take into account dust and H_2 in the interstellar medium in galaxies. Below 1 keV, N, O, and Ne are the dominant absorption features.

4.4.2 Continuum model

In the energy range we are studying for the main sample (0.3-10 keV), blazar spectra typically show curvature in soft X-ray. A log-parabolic spectrum (LOGPAR in XSPEC) can be produced by a log-parabolic distribution of relativistic particles (Paggi et al., 2009). This curved continuum shape could also arise from a power-law particle distribution with a cooled high energy tail (Furniss et al., 2013).

Similarly, a broken power law intrinsic curvature can be interpreted as relativistic electrons in the jet following a broken power law energy distribution with a low energy cut-off, or an inefficient radiative cooling of lower energy electrons producing few synchrotron photons (Gianní et al., 2011).

Given that it is very difficult to determine whether spectral softening is caused by absorption or is intrinsic to the blazar emission, we adopted a conservative approach. We first fitted our full sample spectra with three different power laws:

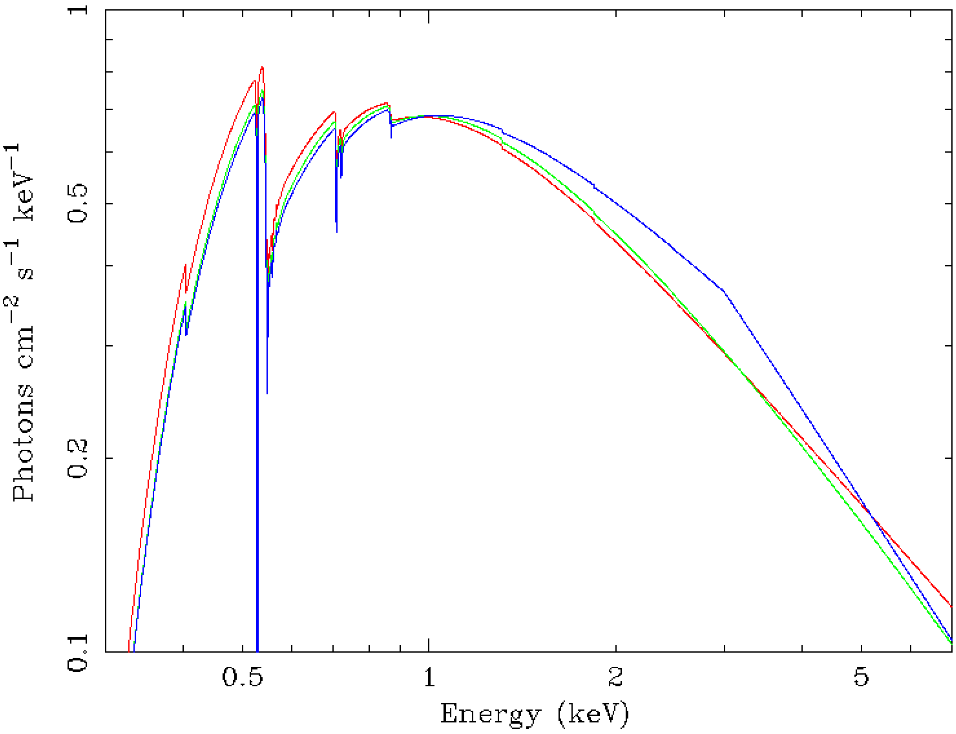

Figure 4.1: Intrinsic models with Galactic absorption only, in the energy range 0.3 - 2.0keV (*Swift* spectra extend to 10keV), simple power law (red), log-parabolic (green) and broken power law (blue). Below 1 keV, N, O, and Ne are the dominant absorption features.

simple power law, log-parabolic and broken power law. For all our sample, both log-parabolic and broken power laws provided better fits than the simple power law. We noted the best fit model and then proceeded to add an ionised absorption component to represent potential IGM absorption where we compare the Cstat results of the full models with the continuum only results. Fig 4.1 shows the impact of using the three different continuum power law models on intrinsic curvature with absorption assumed only from our Galaxy.

4.4.3 Ionised IGM

In earlier studies which examined the hypothesis of absorption causing the observed soft X-ray spectral hardening, only an intrinsic host absorption or some discrete intervening neutral absorbers (DLAs, LLS, etc) were considered. However, in blazars the host contribution is probably negligible, consistent with low levels of optical-UV extinction observed (Paliya et al., 2016). Further, strong intervening absorption by neutral absorbers (NHI) is too rare in blazar LOS to account for the observed curvature (e.g Elvis et al., 1994b; Cappi et al., 1997; Fabian et al., 2001; Page et al., 2005). Therefore, we omit any absorption contribution from the blazar host or low-column density intervening neutral Lyman absorbers (log(NHI) < 21) in our models. If there is a large known intervening absorber such as a galaxy (e.g. PKS 1830-211) or substantial DLA with log(NHI/cm^{-2}) > 21 then it was included in the model using XSPEC ZTBABS placed at the redshift of the intervening object. We note that it is possible that further unidentified individual strong absorbers may exist on the LOS to our sample which would then be included in the integrated NHXIGM derived from the fits.

D21 examined different ionisation models to represent diffuse IGM absorption including collisional ionised equilibrium models (CIE): HOTABS (Kallman et al., 2009), IONEQ (Gatuzz et al., 2015) and ABSORI (Done et al., 1992), and photionisation equilibrim (PIE) model WARMABS (Kallman et al., 2009). ABSORI allows one to have both ionisation parameter and temperature as free parameters which would not occur in either pure PIE or CIE (Done, 2010). In order to compare with CIE models, D21 froze the ionisation parameter leaving temperature as a free parameter required for CIE scenarios. In earlier works on using tracers such as GRBs and blazars for IGM absorption, ABSORI was generally used (e.g. Bottacini et al., 2010; Behar et al., 2011; Starling et al., 2013, A18). While ABSORI was the best model available when it was developed in 1992, it is not self-consistent, and is limited to 10 metals, all of which are fixed at solar metallicity except Fe (Done et al., 1992). D21 concluded that WARMABS and HOTABS are the most sophisticated of these models currently available, and the MCMC integrated probability plots were the most consistent with the STEPPAR results. We followed their methodology for the modelling the IGM absorption. Initially, we fitted a sub-sample of 20 blazars with both PIE and CIE absorption separately as extreme scenarios where all the IGM absorption is either in the CIE or PIE phase. Consistently with D21, we found that similar results were obtained for both models and that it is not possible to conclude whether PIE or CIE is the better single model for the IGM at all redshift, though a combination is the most physically plausible scenario. Given the fact that similar results are obtained for both PIE and CIE models, we proceeded only with fitting CIE model HOTABS. Therefore, the full models for each blazar in XSPEC language are (with the addition of ZTBABS for known intervening objects):

TBABS*HOTABS*LOGPAR

or

TBABS*HOTABS*BKNPO

We model the IGM assuming a thin uniform plane parallel slab geometry in thermal and ionisation equilibrium. This simple approximation is generally used for a homogeneous medium (e.g. Savage et al., 2014; Nicastro et al., 2017; Khabibullin and Churazov, 2019; Lehner et al., 2019). This slab is placed at half the blazar redshift as an approximation of the full LOS medium. The parameters ranges that were applied to the CIE models are taken from D21 and summarised in Table 4.3. We follow the same methodology as D21 in using HOTABS and the IGM parameter range for IGM density, temperature and metallicity. D21 provides detail on HOTABS which calculates the absorption due to neutral and all ionised species of elements with atomic number $Z \leq 30$. Further, D21 clarifies that the fitting method uses the continuum total absorption to model plasma as opposed to fitting individual line absorption as the required resolution is not available currently in X-ray. As we are modelling and fitting the continuum curvature and not specific lines or edges specifically, scope for degeneracy occurs. In the D21 Supplementary material, transmission figures are gives to show the impact of changes in temperature,

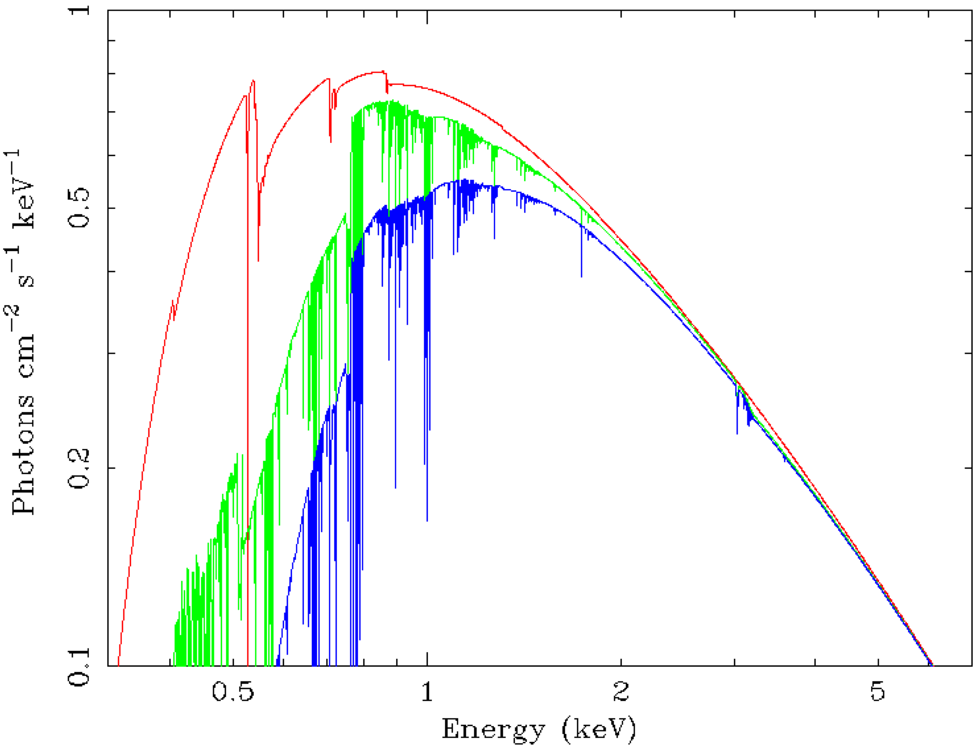

Figure 4.2: Model components for the LOS absorption to a blazar using a log-parabolic power law, HOTABS for IGM CIE absorption in the energy range 0.3 - 2.0keV (*Swift* spectra extend to 10keV). The model example is for a blazar at redshift $z = 2.69$, with $\log(N_{\rm HXIGM}/{\rm cm}^{-2}) = 22.28$, $[X/{\rm H}] = -1.59$, and $\log(T/{\rm K}) = 6.2$ for the IGM, $\log(N_{\rm HX}/{\rm cm}^{-2}) = 21.2$ for our Galaxy. The IGM CIE absorption curve is green, our Galaxy red and the total absorption from both components is the blue curve.

metallicity and redshift. In the cool IGM phases, typical metallicity is observed to be $-4 < [X/{\rm H}] < -2$ (e.g. Schaye et al., 2003; Simcoe et al., 2004; Aguirre et al., 2008). In the warmer phases including the WHIM, the metallicity has been observed to be higher $[X/{\rm H}] \sim -1$ (e.g. Danforth et al., 2016; Pratt et al., 2018). As we are modelling the LOS through the cool, warm and hot diffuse IGM, we will set the XSPEC metallicity parameter range following D21 as $-4 < [X/{\rm H}] < -0.7$.

Fig. 4.2 shows an example of the model components for the full LOS using HOTABS for IGM CIE absorption. The model example assumes a blazar at redshift $z = 2.69$ using a log-parabolic power law, HOTABS for CIE IGM absorption, $\log(N_{\rm HXIGM}/{\rm cm}^{-2}) = 22.28$, $[X/{\rm H}] = -1.59$, and $\log(T/{\rm K}) = 6.2$ for the IGM, and $\log(N_{\rm HX}/{\rm cm}^{-2}) = 21.2$

Table 4.3: Upper and lower limits for the free parameters in the IGM models. Continuum parameters were also free parameters. The fixed parameters are Galactic log(NHX), the IGM slab at half the blazar redshift, and any known intervening object log(NHX).

IGM parameter	range in XSPEC models
column density	$19 \leq \log(N\mathrm{HX}/\mathrm{cm}^{-2}) \leq 23$
temperature	$4 \leq \log(T/\mathrm{K}) \leq 8$
metallicity	$-4 \leq [X/\mathrm{H}] \leq -0.7$

for our Galaxy. The IGM CIE absorption curve is green, our Galaxy red and the total absorption from both components is the blue curve. In the model, the absorption lines are clearly visible. However, we would expect that these lines would not be detected due to instrument limitations and being smeared out over a large redshift range.

4.5 Spectral analysis results

In Section 4.5, we firstly discuss the impact of using different intrinsic blazar continuum models in Section 4.5.1, then give the results for IGM parameters for the full sample using the CIE IGM absorption model in Section 4.5.2. All spectral fits incude TBABS for Galactic absorption.

4.5.1 Spectra fit improvements from alternative continuum models and IGM component

We show the fit results in Fig.4.3 for J013126-100931 at redshift $z = 3.51$ as an example of typical results. We initially fitted a simple power law. The left panel in Fig. 4.3 shows residuals at low energy with a Cstat of 273.24 for 330 degrees of freedom (dof). We then tried both a log-parabolic and broken power law. The middle panel shows the fit with a broken power law which had a better result than both log-parabolic or simple power law, Cstat/dof = 262.88/328. An improved fit at soft energy can be seen. We then added a variable CIE IGM component to

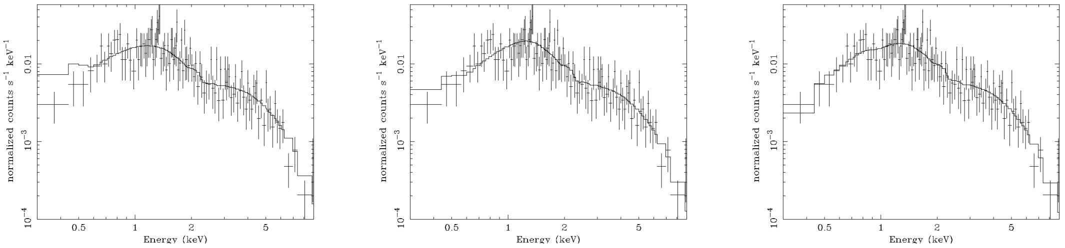

Figure 4.3: Impact of using different intrinsic curvature models and additional IGM absorption components for blazar J013126-100931. All fits include Galactic absorption. The left panel is a simple power law. The middle panel is with a broken power law. The right panel is a broken power law with a CIE IGM absorption component.

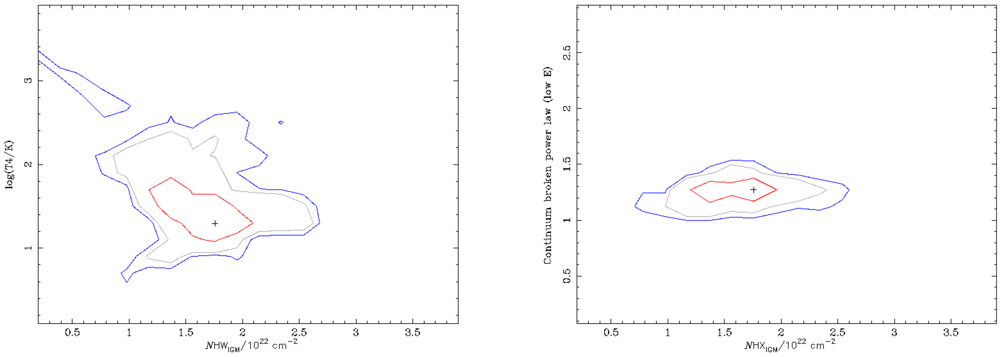

Figure 4.4: The left and right panels show the MCMC integrated probability results for J013126-100931 for N_{HXIGM} with temperature and broken power law (low energy) respectively. The red, grey and blue contours represent $68\%, 90\%$ and 95% confidence ranges for the two parameters respectively. On the y-axis in the left panel T4 means the log of the temperature is in units of 10^4 K.

the broken power law while allowing the intrinsic parameters to also vary shown in the right panel of Fig.4.3. The spectral fit is improved compared with the Galactic absorbed broken law only model, with less low energy residual, Cstat/dof = 256.98/326. Fig. 4.4 left and right panels show the MCMC integrated probability results for NHXIGM with temperature and broken power law index (low energy) respectively. The red, grey and blue contours represent $68\%, 90\%$ and 95% ranges for the two parameters respectively. On the y-axis left panel, log(T4/K) means that 0 is $\log(T/\text{K}) = 4$. The contours in both plots and particularly NHXIGM and the low energy power law provide reasonably tight ranges of parameter results at 2σ (95% confidence).

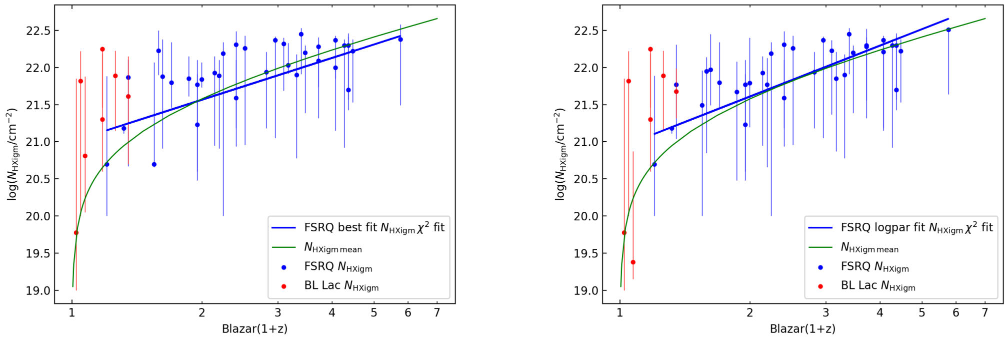

Figure 4.5: Results for the IGM *N*HX parameter and redshift using the CIE (HOTABS) model. The error bars are reported with a 90% confidence interval. The green line is the simple IGM model using a mean IGM density. Left panel is *N*HX and redshift selecting best Cstat results from the different power law intrinsic models. Right panel is the full sample with the IGM component and a log-parabolic power law only (best fit for 26/40).

4.5.2 IGM parameter results using a CIE IGM model

We now give the results for IGM parameters based on fitting the full sample of 40 blazars using HOTABS for CIE IGM (Table 4.4). The IGM *N*HX, metallicity and temperature parameters are all free, as are the power law parameters. The error bars for all fits are reported with a 90% confidence interval. In the plots of *N*HX and redshift, the green line is the mean hydrogen density of the IGM based on the simple model used in D20 and references therein (e.g. Starling et al., 2013; Shull and Danforth, 2018).

$$N_{\rm HXIGM} = \frac{n_0 c}{H_0} \int_0^z \frac{(1+z)^2 dz}{[\Omega_M (1+z)^3 + \Omega_\Lambda]^{\frac{1}{2}}} \tag{4.1}$$

where n$_0$ is the hydrogen density at redshift zero, taken as 1.7×10^{-7} cm^{-3} (Behar et al., 2011). This value is based on 90% of the baryons being in the IGM. When giving results for the mean hydrogen density at $z = 0$ (n_0), they are derived by rearranging equation 4.1 to give n_0. We then used our results for *N*HXIGM and actual redshift for each blazar to get their equivalent n_0. Finally, we took the mean of our full sample and the standard error.

We note that in all cases, the addition of the absorption component improved the

Cstat fit for all blazars in our sample indicating that the addition of the absorption component is required in the model. Overall, the best fit Cstat results were achieved using the IGM component with a log-parabolic power law (26/40 spectra). Only 6 blazars out of the sample with $z > 1$ (23), had a better fit with a broken power law. The continuum model fit favouring a log-parabolic or broken power law over a simple power law is consistent with prior studies (e.g. Bhatta et al., 2018; Sahakyan et al., 2020; Gaur, 2020, A18). Modelling the IGM using HOTABS for CIE with parameters NHXIGM, Z and T free, results in NHXIGM showing similar values and trend with redshift as the mean IGM density model. In Fig.4.5 left panel, we show the results for NHXIGM and redshift selecting the best fits from both log-parabolic and broken law (none were better with a simple power law). The right panel of Fig.4.5 are the results using the log-parabolic power law with the IGM component for comparison. Due to the differences between FSRQ (33/40 in our sample, blue) and BL Lac (red), we have plotted both categories coloured separately.

Based on best fit results, a power law fit to the NHXIGM versus redshift trend for the FSRQ objects scales as $(1 + z)^{1.8\pm0.2}$, reduced $\chi^2 = 1.69$, (p-value = 0.0011, root mean square (rms) = 0.39). However, given that the FSRQ sample redshift includes blazars as low as $z = 0.31$, a linear χ^2 fit is not appropriate as can be seen from the simple IGM curve. The mean hydrogen density using equation 4.1 at $z = 0$ from the FSRQ sample is $n_0 = (3.2 \pm 0.5) \times 10^{-7}$ cm^{-3}. This is higher than the value of 1.7×10^{-7} cm^{-3} for the simple IGM model (green line in Fig 4.5). Taking a sub-sample of FSRQ with $z > 1.6$, similar to the GRB sample in D21, gives $n_0 = (2.1 \pm 0.2) \times 10^{-7}$ cm^{-3}. While noting that many of the error bars are large, jointly the blazars would support any model that is proximate to the χ^2 fit which includes the mean IGM density curve. At low redshift, several blazars have higher NHXIGM than the simple IGM model. This may be evidence of the CGM in both our Galaxy and the host galaxy providing a minimum column density. While there is no observed significant evolution in neutral hydrogen column density in the CGM, there is evidence of evolution in total hydrogen column density including

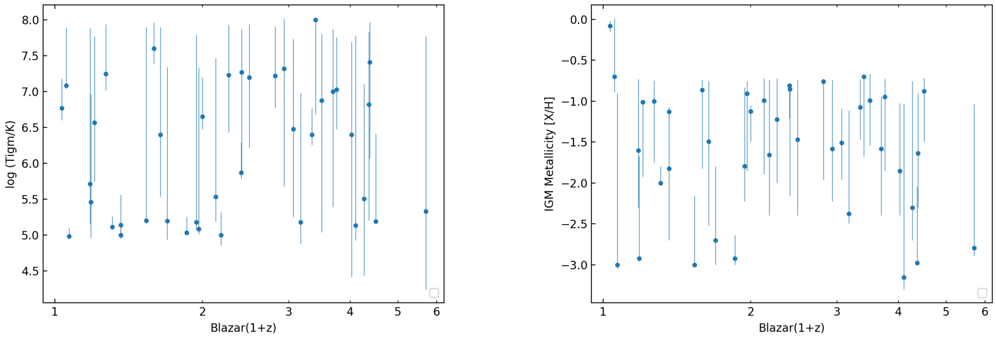

Figure 4.6: Results for the IGM parameters and redshift using the CIE (HOTABS) model best fit results from the various models. The error bars are reported with a 90% confidence interval. Left panel is temperature and redshift and right panel is the [X/H] and redshift. We do not include a χ^2 curve in the plots as the fit was poor due to a large scatter.

the partially ionised hydrogen column (Fumagalli et al., 2016; Lehner et al., 2016). Models incorporating more advanced modelling for a warm/hot CGM component are needed to explore the relative contribution of the IGM and the host CGM to the observed absorption in blazars and GRBs (D21). Das et al. (2021) claim to have detected three distinct phases in our Galaxy CGM, with a hot phase having log(T/K) ∼ 7.5 and log(NHX/cm^{-2}) ∼ 21. The BL Lacs dominate the sample at very low redshift and the majority appear to have high NHXIGM although with large error bars. This could be due to the overall model incorrectly describing the BL Lac spectra. The 4 BL Lac objects that most exceed the simple IGM curve are all high energy peaked blazars, known as HBLs. These objects have their peak synchrotron humps at energies that can appear in soft X-ray. Therefore, we have excluded the BL Lac in our derivation of the mean hydrogen density at $z = 0$ and the χ^2 fit for NHXIGM versus redshift trend.

There is a large range in the fitted temperature $5.0 < \log(T/\text{K}) < 8.0$, many with substantial error bars in Fig.4.6 left panel. The mean temperature over the full redshift range is $\log(T/\text{K}) = 6.1 \pm 0.1$. These values are consistent with the generally accepted WHIM. There is no apparent relation of temperature with redshift. It should be noted, however, that the fits are for the integrated LOS and not representative of any individual absorber temperature. Further, at high redshift, it is possible that the IGM comprises a cooler diffuse gas which is contributing to the absorption but not captured in this CIE model.

The right panel of Fig.4.6 shows no apparent relation of $[X/\mathrm{H}]$ with redshift. The mean metallicity over the full redshift range is $[X/\mathrm{H}] = -1.62 \pm 0.04$. Metallicity ranges from approximately $[X/\mathrm{H}] - 0.7$ ($0.2Z_{\odot}$) to $[X/\mathrm{H}] - 3$ ($0.001Z_{\odot}$) with one outlier. This is the BL Lac Mrk 501 at $z = 0.03$. The initial fitting went to the upper metallicity limit of $[X/\mathrm{H}] < -0.7$. We increased the upper limit to solar and the best fit was with $[X/\mathrm{H}] = -0.08$ ($0.8Z_{\odot}$). Our model may not be appropriate for this object.

In conclusion, with the caveats of low X-ray resolution, a CIE IGM component only and the slab model to represent to full LOS, there are reasonable grounds for arguing that the CIE model using HOTABS is plausible for modelling the warm/hot component of the IGM at all redshifts. In all fits, the Cstat was better than best fits for models with only Galactic absorption. Our CIE IGM component had three free parameters, *N*HXIGM, temperature and $[X/\mathrm{H}]$. There is scope for degeneracy as we model the continuum curvature and not specific absorption features as set out in Section 4.4 and D21. While there was a large range in Cstat improvements across the sample, the average Cstat improvement for the full sample per free IGM parameter was 3.9, with 20 out of 40 blazars exceeding ΔCstat> 6.25 for three interesting parameters. The model using a log-parabolic continuum model with a CIE IGM absorption appears to be more consistent with the simple IGM curve than the selected best fits from both log-parabolic and broken power laws. Overall, the results for *N*HXIGM using either a log-parabolic or broken power law are statistically indistinguishable indicating that IGM component is independent. Our temperature and metallicity results are consistent with the expected values from simulations for a warm/hot phase. However, as noted in Section 4.4, initial trials with a warm photionised IGM component gave similar results to a collisional ionised model. It is most likely that a combined model would be more physical,

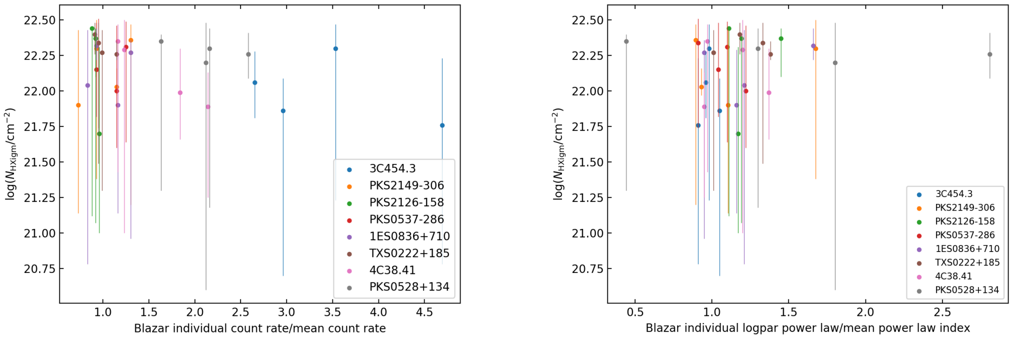

Figure 4.7: Testing for possible relation between *N*HXIGM and flux variability or spectral slope for four individual observations from the sub-sample of eight blazars. Objects are colour-coded to enable comparison of individual blazar results as well as overall possible relations. Left panel is *N*HXIGM and flux variability given as count rate over mean count rate . Right panel is *N*HXIGM and individual log-parabolic power law/ mean power law index for each object. The error bars are reported with a 90% confidence interval.

but testing this requires better data. We now test the robustness of the results in Section 4.6 and discuss the results further and compare with other studies in Section 4.8.

4.6 Tests for robustness of IGM parameter results

There are several alternative potential explanations for the curvature seen in blazar spectra which may not be partly or wholly attributable to IGM absorption. *N*HXIGM can be degenerate to some degree with spectral slope i.e. a harder spectrum slope can mimic higher *N*HXIGM and vice versa. Further, blazars can be highly variable in flux and spectral slope. Finally, some fits were nearly indistinguishable in terms of visual spectra ratio and/or Cstat i.e. there may be a concern about an a priori assumption of IGM absorption. Accordingly, we examine our results from a number of perspectives to test their robustness.

4.6.1 Flux variability

Blazars are known to have spectral variability (associated with flux variability). The physical causes of such variability can involve many processes, such as particle acceleration, injection, cooling, and escape, which contain a number of known and unknown physical parameters (Gaur, 2020). Also, a local absorber at the host can show variability, while an IGM absorber should not. An absorber that shows variability within a reasonable short time-frame cannot be on intergalactic length scales, and must therefore be attributed to the host, or to intrinsic variability of the source (Haim et al., 2019).

As noted in Section 4.3, we use co-added blazar spectra. To test for possible absorption variability and/or a relation between flux and spectral hardening, we selected a sub-sample of 8 blazars with a redshift range $0.86 \leq z \leq 3.26$ as representative of the full sample. For each, we selected four different individual observations taken at different dates, with high counts but which showed different flux rates to the mean co-added rate. We used the log-parabolic model for all 8 blazars. Table 4.5 in the Appendix chapter 4 reports the Observation ID, count rate over the mean count rate, NHXIGM and log-parabolic power law over the mean power law for each blazar observation.

In Fig. 4.7 left panel, we can see that there is no apparent relation between NHXIGM and flux across all the observations, with a χ^2 fit slope approximating zero (-0.09 ± 0.05). The blazars are individually colour-coded and there is no obvious relation between NHXIGM and flux for any individual blazar apart from possibly 4C 38.41. From Table 4.5, we can see that all the individual results for NHXIGM are consistent with the mean result within the errors for each blazar.

4.6.2 Column density and spectral slope degeneracy

Given the scope for degeneracy between NHXIGM and spectral hardening, for the sub-sample of 8 blazars we checked for any relation between these two parameters using the same four individual observations for each. As previously noted, due to the large variability frequently observed in blazars, non-simultaneous observations are expected to show different states of the object. Therefore, the log-parabolic parameters and normalizations were allowed free to vary. In Fig. 4.7 right panel, we show the NHXIGM using log-parabolic power law for all fits for the individual observations. There is no apparent relation between column density and power law indices with a χ^2 slope fit of 0.10 ± 0.06. We again colour code each blazar and there is no apparent relation between NHXIGM and power law index variability for any individual object.

Overall, our results are consistent with other studies (e.g. Haim et al., 2019, A18) which tested for a fixed absorber and noted that it did not change significantly across different observational times.

4.6.3 XMM-Newton spectra comparison

$XMM-Newton$ has excellent low energy response down to 0.15 keV, extreme sensitivity to extended emission, and large effective area facilitating analysis of the soft X-ray properties. We continued our robustness tests using *XMM-Newton* PN spectra for the same sub-sample of blazars with the exception of 4C 38.41 which was not available. We used the log-parabolic power law again with the CIE IGM component. We chose a selection of both individual spectra and co-added spectra as given in Table 4.2. We used the same energy range as *Swift* for consistent comparison (0.3 - 10 keV). We also separately fitted our model to an extended energy range of 0.16 - 13 keV given the excellent sensitivity of *XMM-Newton* over this range.

Table 4.6 in the Appendix reports the redshift, and NHXIGM for *Swift* 0.3-10keV, *XMM-Newton* 0.3-10keV and 0.16-13keV respectively for each blazar. The values for NHXIGM are consistent for each blazar within the errors. Fig. 4.8 left panel, shows NHXIGM for *Swift* and both *XMM-Newton* fits for each blazar. To enable the

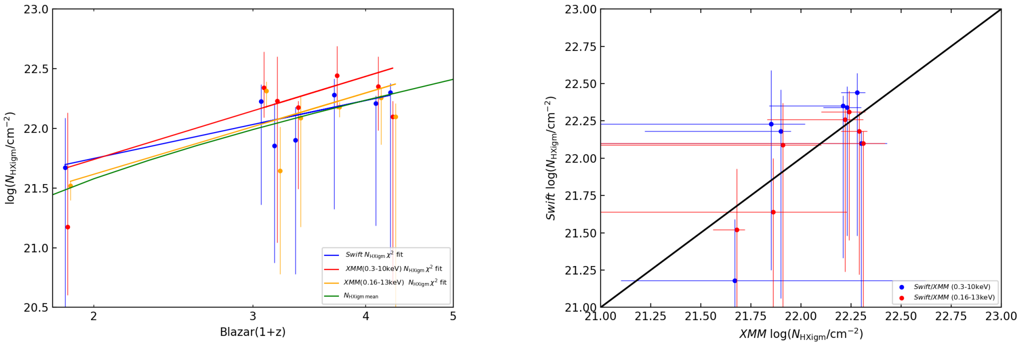

Figure 4.8: Comparing *N*HXIGM and redshift results for *Swift* (blue), *XMM-Newton* (0.3-10keV)(red) and (0.16-13keV)(orange) from a sub-sample of seven blazars (varied slightly on the left panel x-axis to enable error bar visibility). Left panel is *N*HXIGM and redshift. The green line is the simple IGM model using a mean IGM density. Right panel is *N*HXIGM for *XMM-Newton* on the x-axis (varied marginally for visibility) and *Swift* 0.3-10keV (blue) and 0.16-13keV (red) on the y-axis. The error bars are reported with a 90% confidence interval. The black line in the right panel is parity.

error bars to be separately visible, we have very slightly changed the redshift of the three spectra for each object. All *N*HXIGM are proximate to the simple IGM curve. We also plot the best χ^2 fit for the *Swift* and both *XMM-Newton* energy ranges. The slopes of both the *XMM-Newton* fits are very similar with 0.3-10 keV being 2.3 ± 1.0 and 0.16-13 keV being 2.3 ± 0.4 . The slope of the χ^2 fit for *Swift* is slightly less at 1.6±0.7. Overall, within the errors, the *Swift* and both *XMM-Newton* results are consistent.

In Fig. 4.8 right panel, we plot *N*HXIGM for *Swift* on the x-axis and *XMM-Newton* 0.3-10keV (blue) and 0.16-13keV (red) on the y-axis The black line in the right panel is parity. We have varied the *Swift* *N*HXIGM marginally to enable error bar visibility. All *Swift* and *XMM-Newton* data-points are proximate to the black parity line, with the possible exception of 3C 454.3 which has a reasonably higher *N*HXIGM with *Swift* than *XMM-Newton* 0.3-10keV, but consistent within the errors.

Fig. 4.9 show the MCMC integrated probability results for PKS0528+134 as a typical example of results for *N*HXIGM and log-parabolic power law for *Swift* and *XMM-Newton* 0.3-10keV respectively. While the *N*HXIGM best fit result is similar

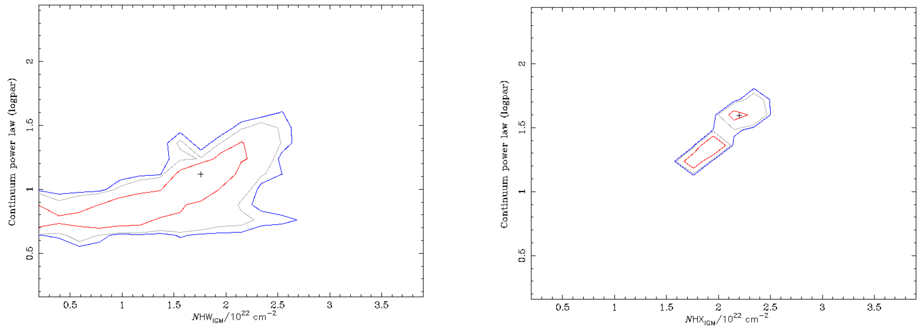

Figure 4.9: The left and right panels show the MCMC integrated probability results for PKS 0528+134 $N_{\rm HXIGM}$ and log-parabolic power law indices for *Swift* and *XMM-Newton* 0.3-10keV respectively. The red, grey and blue contours represent $68\%, 90\%$ and 95% ranges.

for both, due to the high resolution of *XMM-Newton*, the contours are much tighter.

Overall, our investigations demonstrate that our results are consistent for observations by both *Swift* and *XMM-Newton*. Further, they reinforce the findings from 4.6.2 that the IGM absorption results do not vary on a temporal basis.

4.6.4 Bulk Comptonisation

Some blazar spectra have a hump feature at soft X-rays, whose origin is still debated. Bulk Comptonisation (BC) has been suggested as an explanation where cold electrons could up-scatter cooler extreme ultraviolet photons from the disk and/or BLR to soft X-ray energies (e.g Sikora et al., 1994; Celotti et al., 2007). This BC related excess emission over the blazar continuum would appear as a hump in soft X-ray. Depending on the energy peak of this hump, it could mimic or mask absorption. If the the hump were to be in the region of ~ 3 keV, the apparent deficit at softer energies can mimic absorption (Kammoun et al., 2018, and references therein). This possible BC related feature has been modelled using a blackbody as a phenomenological representation (e.g Ricci et al., 2017).

Fig. 4.10 shows the spectrum of 3C 279 as an example of a FSRQ showing a second hump in soft X-ray where adding a blackbody component significantly improved

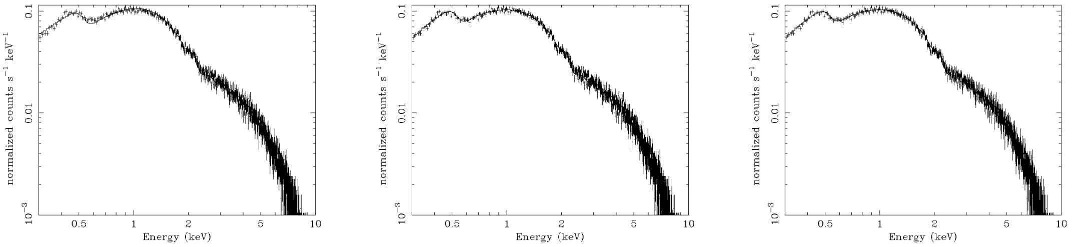

Figure 4.10: 3C 279 as an example of FSRQ spectrum showing second hump in soft X-ray. All fits are with a broken power law, the best intrinsic curvature. The left panel is with an IGM component. The middle panel is with a blackbody component. The right panel is with both an IGM absorption component and a blackbody.

the Cstat fit. All fits are with a broken power law which provided the best intrinsic curvature fit. The left panel is with an IGM component (Cstat 992.1/933). The middle panel is with no IGM but an additional blackbody emission component (Cstat 917.06/934), where a slight visual improvement in fit can be seen at ~ 0.6 keV. The right panel is with both an IGM and blackbody component (Cstat 916.03/931).

10 out of 40 in our blazar sample had a second soft X-ray hump where the Cstat was similar for both an IGM or blackbody component, and showed an improvement in Cstat with both components included. There was a large range in Cstat improvement for the model with both the IGM and blackbody components for the 10 blazars, with the average Cstat improvement per additional free blackbody parameter being 8.3, and 8 out of 10 blazars exceeding ΔCstat> 4.6 for two interesting parameters.

In 8/10, there was a reduction in *N*HXIGM in the combined IGM and BC model ranging up to one dex. 2/10 objects showed increased *N*HXIGM from 100% – 180%. Given this large impact on *N*HXIGM, we replotted the *N*HXIGM redshift relation omitting the 10 blazars possibly impacted by a BC component. In Fig. 4.11, we can see the clear *N*HXIGM redshift relation remains. In fact the power law fit to the *N*HXIGM versus redshift trend for the FSRQ objects scales as $(1+z)^{2.4\pm0.2}$ (p-value = 0.01, rms = 0.36) compared to $(1+z)^{1.8\pm0.2}$ from the full sample (Section

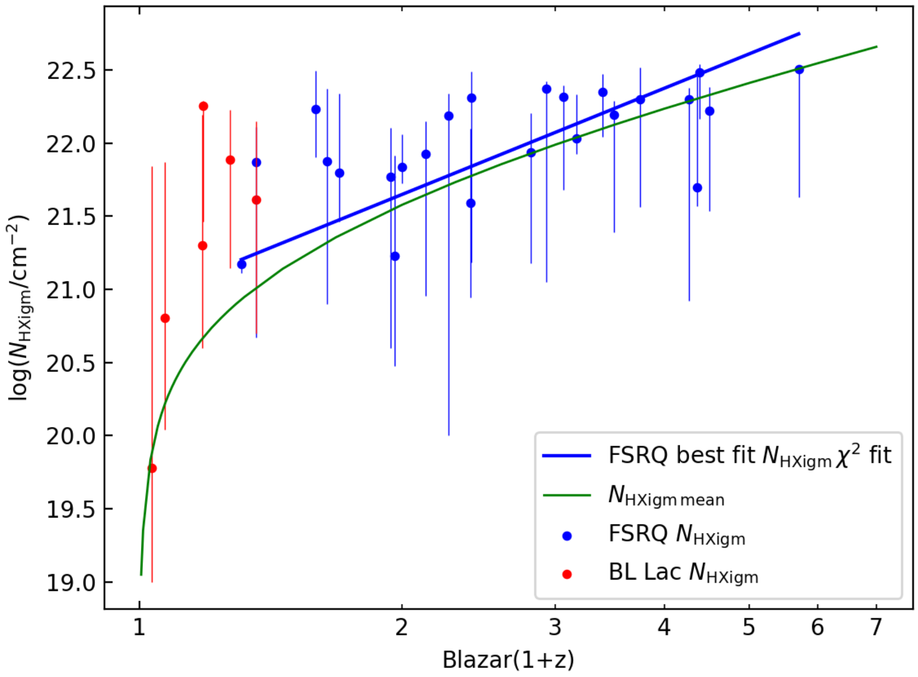

Figure 4.11: Results for the IGM NHX parameter and redshift omitting the 10 blazars where adding a bulk Comptonisation component improved the fit. The error bars are reported with a 90% confidence interval. The green line is the simple IGM model using a mean IGM density.

4.5). The hydrogen equivalent density at $z = 0$ is similar at $n_0 = (3.5 \pm 0.7) \times 10^{-7}$ cm^{-3}. Without the BC component, 5/10 favoured a log-parabloic power law over a broken power law. When the blackbody component was added, this changed to 9/10 favouring a broken power law.

Based on our investigations, it appears possible that in some cases BC could mimic absorption. On the other hand, depending on where the energy peak of the blackbody-like feature occurs, it could also mask actual absorption, appearing as an excess at soft X-ray. BC itself is still not generally accepted as the cause of this feature. The majority of our sample show improved fit statistics for an IGM component. Further, the clear NHXIGM redshift relation remains with the BC impacted blazars removed from the sample.

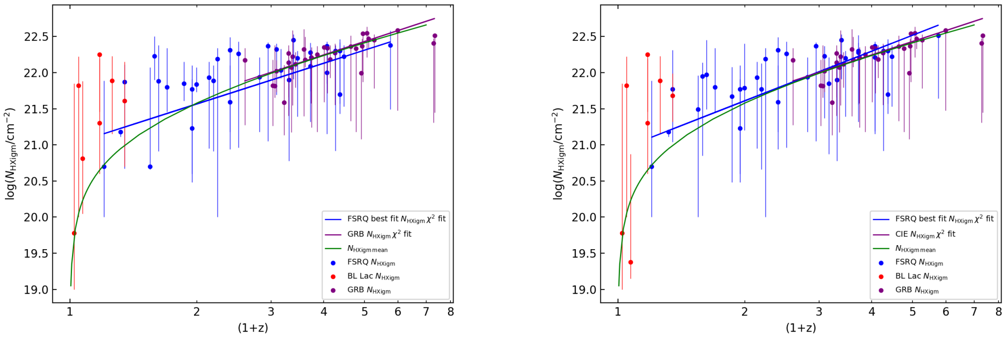

Figure 4.12: Results for the IGM *N*HX parameter and redshift using the combined GRB sample from D21 (purple) and our Blazar sample (FSRQ - blue and BL Lac - red) using the CIE (HOTABS) model. The blue and purple lines are χ^2 fits to the respective FSRQ and GRB samples. The error bars are reported with a 90% confidence interval. The green line is the simple IGM model using a mean IGM density. Left panel is *N*HX and redshift selecting best Cstat results for blazars from all three power law intrinsic models. Right panel is the full sample with the IGM component and a log-parabolic power law only (best fit for 26/40) for blazars.

4.7 Combined Blazar and GRB sample analysis

In this section, we combine the GRB sample from D21 with our full *Swift* blazar sample in a multiple tracer analysis across a redshift range $0.03 \leq z \leq 6.3$. In this paper, we used D21 results from their fits using HOTABS for CIE IGM for consistency. D21 isolated the IGM LOS contribution to the total absorption for the GRBs by assuming that the GRB host absorption was equal to ionised corrected intrinsic neutral column estimated from the Lyα host absorption. They used a realistic host metallicity, dust corrected where available, in generating the host absorption model.

As can be seen in Fig. 4.12, our results for blazars for a power law fit to the *N*HXIGM versus redshift trend scaling as $(1+z)^{1.8\pm0.2}$ (best cstat fit) is consistent with the GRBs in D21 which scale as $(1+z)^{1.9\pm0.2}$ over the extended redshift. In Fig. 4.12 left panel, we use the best Cstat fit results for blazars and in the right panel the log-parabolic only continuum results, in combination with the D21 GRB sample. The slopes of the χ^2 fits for GRB and blazar best cstat *N*HXIGM versus redshift are aligned, but the slope for the blazars using log-parabolic continuum power law in combination with the GRBs slightly better traces the simple IGM density curve over the full redshift.

The mean hydrogen density at $z = 0$ from the combined GRB and blazar samples is $n_0 = (2.2 \pm 0.1) \times 10^{-7}$ cm^{-3}. This is marginally higher than the value of 1.7×10^{-7} cm^{-3} for the simple IGM model (green line in Fig 4.12) and for the GRB only sample in D21 $n_0 = (1.8 \pm 0.1) \times 10^{-7}$ cm^{-3}. In section 4.5, we reported the mean hydrogen density at $z = 0$ from the blazar FSRQ sample as $n_0 = (3.2 \pm 0.5) \times 10^{-7}$ cm^{-3}. A possible explanation may be due to our assumption that there is no absorption in the blazar host due to the relativistic jet. In D21, it was also apparent that the lower redshift GRBs appeared to have higher NHXIGM that the simple IGM curve. As speculated in Section 4.5.2, this may be a sign of CGM absorption from a hot phase as proposed by (Das et al., 2021). At higher redshift, the IGM contribution to NHXIGM dominates any host contribution.

In Fig. 4.13, we show the combined GRB and blazar sample results for IGM temperature and metallicity. In the left panel, we can see that there is no detectable overall trend with redshift. Some objects in the blazar sample, appear to have a higher maximum temperature than the GRB sample, up to $\log(T/\mathrm{K}) \sim 7.5$. Das et al. (2021) have indicated that the Galaxy hot phase has a temperature of $\log(T/\mathrm{K}) \sim 7.5$. The mean temperature over the full redshift range for the combined samples is $\log(T/\mathrm{K}) = 6.2 \pm 0.1$ under the assumption of a CIE scenario.

In Fig. 4.13 right panel, we can see the IGM metallicity results for the combined GRB and blazar sample for $0.9 \leq z \leq 7$. We omitted blazars with $z < 0.9$ as they showed very large scatter in best fitted metallicity and with substantial errors. There appears to be a possible relation with redshift scaling as $(1+z)^{-2.9\pm0.5}$ (orange χ^2 line). The reduced χ^2 is 1.9, with a p-value = 0.00014 and rms = 0.60, indicating a modestly statistical relation. Visually, the metallicity redshift relation, if any, is not clear, or may indicate that a linear model may not be appropriate. For the GRB only sample, D21 reported a power law fit to the $[X/\mathrm{H}]$ and redshift

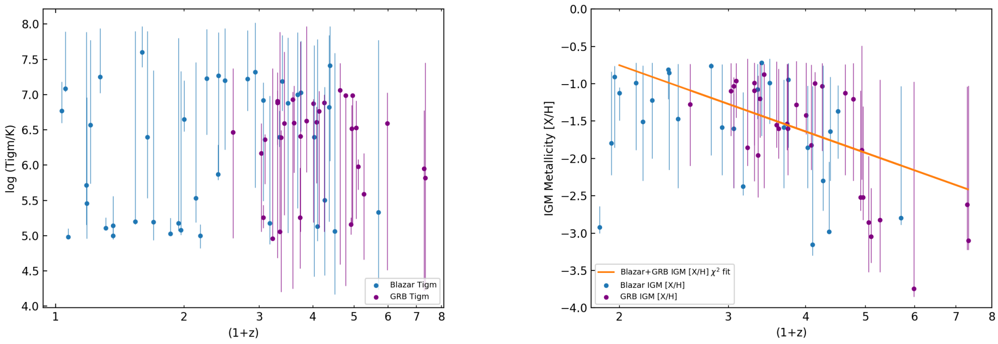

Figure 4.13: IGM parameter results using the combined GRB sample from D21 (purple) and our Blazar sample (blue). The error bars are reported with a 90% confidence interval. Left panel is temperature and redshift and right panel is the [X/H] and redshift. We do not include a χ^2 curve in the temperature plot as the fit was poor due to a large scatter. In the right panel, we show GRB and blazar combined χ^2 curve for $z > 0.9$ showing a possible redshift relation above this redshift.

trend as $(1 + z)^{-5.2\pm1.0}$, ranging from [X/H] = −1 ($Z = 0.1Z_\odot$) at $z \sim 2$ to [X/H] ~ -3 ($Z = 0.001Z_\odot$) at high redshift $z > 4$. They speculated that at low redshift, the higher metallicity warm-hot phase is dominant with $Z \sim 0.1Z_\odot$, while at higher redshift the low metallicity IGM away from knots and filaments is dominant. In the combined blazar and GRB sample for $z > 0.9$, the possible redshift metallicity relation is less pronounced. While there is a large range in the lower error bars, some of the blazars at lower redshift have upper metallicity error bars approaching our upper limit of [X/H] = −0.7.

Overall, the IGM parameter results from our blazar sample are consistent with the GRB sample from D21. Therefore, the combined sample gives improved robustness to our reported results for the IGM.

4.8 Discussion and comparison with other studies

The cause of spectral flattening seen in blazar spectra has been the subject of study and debate for some time. In early works, a cold local host absorber received favour (e.g. Cappi et al., 1997). Due to the low levels of optical-UV extinction seen in such blazars (e.g Elvis et al., 1994b; Sikora et al., 1994), subsequent studies favoured an intrinsic curvature explanation with models including log-parabolic, broken power law and variations on this. We accommodated this element of intrinsic curvature by fitting our sample with best fit from a simple power law, log-parabolic and broken power law. Further, when adding the IGM component, we allowed all parameters to vary. In Section 4.6, we explored any possible relation between IGM absorption and both spectral flux and power-law hardening. No such relation was apparent.

Several studies have tentatively explored absorption scenarios, either neutral or a warm absorption component, as a minor part of their work, typically placing the absorber at the blazar redshift (e.g. Bottacini et al., 2010; Paliya et al., 2016; Ricci et al., 2017; Marcotulli et al., 2020; Haim et al., 2019). Bottacini et al. (2010) found they could not constrain their photo-ionised model parameter better than an upper limit. They used ABSORI which is not as sophisticated as WARMABS, the photo-ionised equivalent of our CIE model using HOTABS. However, they reported that they found no evidence of absorption variability, consistent with our results. Ricci et al. (2017) used ZXIPCF, a photoionisation model to test a scenario of a warm absorber in the blazar host with metallicity fixed to solar. They found that only a small number of fits improved with the added warm absorber component. This differs from our model where we allow both metallicity and temperature to vary, as solar metallicity is highly unlikely to occur in the diffuse IGM (e.g. Schaye et al., 2003; Aguirre et al., 2008; Shull et al., 2012, 2014), and we place the absorber at an intermediate redshift.

The relation between spectral flattening and redshift has been reported by several authors (e.g. Yuan et al., 2006; Behar et al., 2011). The hypothesis of discrete intervening absorbers (DLA, LLS, sLLS, etc) has been investigated to explain this redshift relation (e.g. Wolf, 1987). Several studies concluded that the absorption from such cool neutral intervening systems is rare and insufficient to be the cause of observed spectral curvature (Gianní et al., 2011, and references therein), leaving the diffuse IGM as the alternative for non-localised intervening absorption.

Arguments against intervening IGM absorption are that intrinsic curvature is present in very low redshift blazars, or that absorption edges or lines are not observed in such very low redshift blazars (Watson and Jakobsson, 2012, and references therein), leading them to conclude that all the spectral flattening is due to intrinsic curvature at all redshifts. In general, most studies are focused on the blazar engine as the main or only cause of intrinsic curvature and leave out IGM absorption based on lack of significantly improved statistical fits. We would argue that it is highly likely that spectral curvature is due to a combination of both intrinsic factors as well as absorption, particularly at soft X-ray, given our findings for *N*HXIGM and the redshift relation. If the apparent absorption was actually intrinsic to the blazars, then there would have to be some explanation of the relation to redshift which is absent.

Detection of the WHIM is proving very challenging due to very weak emission and absorption. Nicastro et al. (2018) claim to have observed the WHIM in absorption. However, with only 1 to 2 strong O VII absorbers predicted to exist per unit redshift, the column densities they report are an order of magnitude lower than the simple IGM model, or the results for *N*HXIGM reported by D21. Our results for the FSRQ sample *N*HXIGM are consistent with the simple IGM model, though we note that many of the BL Lacs showed high *N*HXIGM. Haim et al. (2019) searched for absorption lines as signals of localised IGM absorption in RBS 315 at $z = 2.69$, one of the brightest FSRQ known. They could find no such line absorption and concluded that, if blazar curvature is at least partly attributable to the IGM, it is not localised but smeared over redshift, consistent with our hypothesis and findings.

A18 is, to our knowledge, the only previous study that was dedicated to exploring the IGM as part of the cause of spectral flattening in blazar spectra, and to use blazars to investigate IGM properties. They used an ABSORI based XPEC model (IGMABS) for the IGM absorption. They jointly fitted four blazars with IGM parameters of density, temperature and ionisation tied together. They reported that excess absorption is the preferred explanation over intrinsic curvature and that it is related to redshift. They give an IGM average density of $n_0 = 1.0^{+0.53}_{-0.72} \times 10^{-7}$ cm^{-3} and temperature $\log(T/\mathrm{K}) = 6.45^{+0.51}_{-2.12}$. Some caveats to their results are based on their solar metallicity assumption for the IGM and fixing the intrinsic power law parameters for some of their sample, which they adopted due to computational limits of their model which they noted would probably lead to upper limit measures for the IGM. Taking account of these factors, their results are broadly consistent with our results for IGM for n_0 and T, but not for our mean IGM metallicity of $[X/\mathrm{H}] = -1.62 \pm 0.04$ ($\sim 0.02 Z_\odot$). Their derived metallicity was $Z_{\mathrm{IGM}} = 0.59^{+0.31}_{-0.42}\ Z_\odot$, obtained from the ratio of their $n_0 \sim 1 \times 10^{-7}$ cm^{-3} result (based on solar metallicity) to the simple IGM model taken from (Behar et al., 2011) $n_0 = 1.7 \times 10^{-7}$ cm^{-3}. Campana et al. (2015) used simulations for intervening IGM absorption to AGN and GRBs. For GRBs, they reported $\log(T/\mathrm{K}) \sim 5 - 7$. To calculate the metal column density of the intervening IGM material, 100 LOS to distant sources were used through a $100h^{-1}$ comoving Mpc Adaptive Mesh Refinement cosmological simulation (Pallottini et al., 2013). The contribution by each cell was summed, with an absorbing column density weighted for its effective temperature dependent value. Metallicity was obtained by requiring that only 1% of their GRB and AGN sample fall below the simulated hydrogen column density redshift curve. Their mean metallicity $Z = 0.03 Z_\odot$ is consistent with our results.

A18 combined their results for blazars with GRBs and AGN from other studies. However, all those studies were based on the assumption that all absorption in excess of our Galaxy was at the host redshift, neutral and at solar metallicity. Our combined tracer results in Section 4.7 are more realistic as we use the GRBs from D21 which more accurately isolate the IGM absorption assuming that the GRB host absorption was equal to ionised corrected intrinsic neutral column estimated from the Lyα host absorption. D21 also used more realistic host metallicity, dust corrected where available in generating the host absorption model as opposed to the conventional solar assumption.

4.9 Conclusions

We used blazars as tracers of the IGM with the main aim to probe the key parameters of column density, metallicity and temperature using a sophisticated software model for collisionally ionised plasma. We used co-added spectra from *Swift* for 40 blazars as our tracers with a redshift range of $0.03 \leq z \leq 4.7$. Our focus is on FSRQ blazars as they are available over a broad redshift range, and the rest-frame energy distribution of FSRQs is strongly peaked at low frequencies, below soft X-ray, unlike BL Lacs. We adopted a conservative approach to the blazar continuum model and use three different intrinsic power law models. As blazars are thought to have a kpc-scale relativistic jet on our line of sight, we excluded any host absorption in our models. We fixed the Galactic absorption to known values and attributed the excess to the IGM. We model the IGM assuming a thin uniform plane parallel slab geometry in collisional ionisation equilibrium to represent a LOS through a homogeneous isothermal medium. We used XSPEC fitting with both the CIE IGM component and all power law parameters free to vary, and use STEPPAR and MCMC to generate best fits to the blazar spectra.

We subjected our results to a number of robustness tests using a sub-sample: comparison of individual observation fit results with our co-added spectra for possible temporal absorption variability; testing for a relation between column density and flux; investigating spectral slope degeneracy with column density; comparing results from using *XMM-Newton* with energy range 0.3-10 keV (as for *Swift*) and 0.16-13keV; and exploring the impact of using a blackbody like additional component to represent bulk comptonisation which could mimic absorption.

Finally, we combined our sample with the GRB sample from D21 to report results for an extended redshift range using the two different types of tracers.

Our main findings and conclusions are:

1. the best fit Cstat results for our blazar sample were achieved using an IGM

component with a log-parabolic power law (26/40 spectra) and appear to be more consistent with the simple model IGM curve than the selected best fits from both log-parabolic and broken power law.

2. Using blazars to model the IGM as being in highly ionised collisional equilibrium with free parameters for density, temperature and metallicity (as well as continnum parameters) appears to give plausible IGM property results. A power law fit to NHXIGM versus redshift trend for the FSRQ objects scales as $(1+z)^{1.8\pm0.2}$. The mean hydrogen density at $z = 0$ from the FSRQ sample is $n_0 = (3.2 \pm 0.5) \times 10^{-7}$ cm^{-3}, higher than the value of 1.7×10^{-7} cm^{-3} for the simple IGM model (Fig 4.5). Nearly all blazar fits are proximate to both the χ^2 fit and mean IGM density curve.

3. At low redshift, several blazars have higher NHXIGM than the simple IGM model. BL Lacs dominate the sample at very low redshift and the majority appear have high fitted NHXIGM. This may be due to CGM absorption.

4. The IGM temperature range is $5.0 < \log(T/\mathrm{K}) < 8.0$, with no apparent redshift relation in the Fig. 4.6 left panel. The mean temperature over the full redshift range is $\log(T/\mathrm{K}) = 6.1 \pm 0.1$. These values are consistent with the generally accepted WHIM range indicating that very highly ionised metals are plausible absorbers over the LOS.

5. The right panel of Fig. 4.6 shows no apparent relation of $[X/\mathrm{H}]$ with redshift (however, see Section 4.7 for possible metallicity redshift relation using combined blazar and GRB samples). The mean metallicity over the full redshift range is $[X/\mathrm{H}] = -1.62 \pm 0.04$ ($Z \sim 0.02$). Metallicity ranges from $[X/\mathrm{H}] = -0.7$ ($0.2Z_\odot$) to $[X/\mathrm{H}] = -3$ ($0.001Z_\odot$) with one outlier.

6. There was a large range in Cstat improvements across the sample, with the average Cstat improvement per free IGM parameter of 3.9. In our models the IGM contributes substantially to the total absorption seen in blazar spectra,

and it rises with redshift. We provide evidence that a complete blazar model should also account for absorption by intervening IGM material.

7. In Fig. 4.7 left panel, there is no apparent relation between *N*HXIGM and flux across all the observations. All the individual results for *N*HXIGM for each blazar are consistent with the mean result within the errors (Table 4.5).

8. There is no apparent relation between column density and power law index. Further, there was no temporal variation in IGM parameter results per blazar using observations over time.

9. For *Swift* 0.3-10 keV, *XMM-Newton* 0.3-10 keV and 0.16-13 keV respectively, the values for *N*HXIGM using log-parabolic power laws are consistent for each blazar within the errors. All *N*HXIGM are proximate to the simple IGM curve, Fig. 4.8 left panel. The slopes of both the *XMM-Newton* energy ranges are very similar. The slope of the χ^2 fit for *Swift* is less steep but consistent with *XMM-Newton* within the error. The *XMM-Newton* results reinforce the findings that the IGM absorption results do not vary on a temporal basis.

10. Bulk Comptonisation has been proposed as a cause of the hump feature at soft X-rays seen is some blazars. 10 out of 40 in our blazar sample had a second soft X-ray hump where the Cstat was similar for both an IGM or blackbody component. Based on our investigations, it appears possible that in some cases, BC could mimic absorption. On the other hand, depending on where the energy peak of the blackbody like feature occurs, it could also mask actual absorption, appearing as an excess at soft X-ray. We found that after omitting from the sample the blazars with possible BC, the *N*HXIGM relation with redshift remains and the results are consistent with those from our full sample.

11. Combining our blazar sample with the GRB sample from D21 gives consistent results for the IGM properties over an extended redshift range from $0.03 \leq z \leq 6.3$. The mean hydrogen density at $z = 0$ from the combined GRB and

blazar samples is $n_0 = (2.2 \pm 0.1) \times 10^{-7}$ cm^{-3}. This is marginally higher than the value of 1.7×10^{-7} cm^{-3} for the simple IGM model, but lower than the blazar only sample ($n_0 = (3.2 \pm 0.1) \times 10^{-7}$ cm^{-3}), perhaps indicating that the blazar relativisitc jet may not fully sweep out absorbing material in the host. Our blazar model assumes there is no host absorption which may be true for most FSRQ which are highly luminous, and hence probably more effective in removing host absorbing gas, but for the less luminous BL Lacs this may not completely happen. The mean temperature over the full redshift range is $\log(T/\mathrm{K}) = 6.1 \pm 0.1$, and the mean metallicity over the full redshift range is $[X/\mathrm{H}] = -1.62 \pm 0.04$ ($Z \sim 0.02$). These values are consistent with the generally accepted WHIM range indicating that very highly ionised metals are plausible absorbers over the LOS. There was no apparent temperature redshift relation. However, we found a possible relation for metallicity and redshift to be $(1 + z)^{-2.9\pm0.5}$.

This study is based on observations of blazar X-ray spectra, and provides results on the IGM parameters. The combination of blazars with the GRB sample gives consistent and more robust results for the IGM properties by using multiple tracer types. The IGM property constraints will only be validated when observations are available from instruments with large effective area, high energy resolution, and a low energy threshold in the soft X-ray energy band (e.g. Athena). We will continue our IGM exploration using other tracers in an upcoming paper and will combine the future results with those from this paper, D21 and D20.

4.10 Appendix chapter 4 - Tables reporting fit results for the main blazar sample and sub-samples

Table 4.4: *Swift* blazar sample. For each blazar, the columns give the name, type, redshift, IGM and continuum best cstat fitted parameter results: NHXIGM, $[X/\mathrm{H}]$, temperature, log parabolic power law and β, or broken power law low energy pewer law (PO1), Energy break (E_b) and high energy PO2, Cstat/dof

Blazar	Type	z	$\log(\frac{N_{\mathrm{HXIGM}}}{\mathrm{cm}^{-2}})$	$[X/\mathrm{H}]$	$\log(\frac{T}{K})$	PO or PO1	β or E_b	PO2	Cstat/dof
Mrk 501	BL Lac	0.03	$19.78^{+2.07}_{-0.78}$	$-0.08^{+0.06}_{-0.07}$	$6.77^{+0.41}_{-0.17}$	$1.92^{+0.06}_{-0.05}$	$0.23^{+0.14}_{-0.16}$		474.61/525
PKS 0521-365	BL Lac	0.06	$21.82^{+0.40}_{-1.82}$	$-0.70^{+0.70}_{-0.19}$	$7.08^{+0.81}_{-0.05}$	$1.47^{+0.03}_{-0.03}$	$0.15^{+0.05}_{-0.08}$		752.59/759
BL Lac	BL Lac	0.07	$20.81^{+1.07}_{-0.77}$	$-2.99^{+2.10}_{-0.05}$	$4.98^{+0.12}_{-0.01}$	$1.39^{+0.05}_{-0.06}$	$2.01^{+0.17}_{-0.23}$	$1.73^{+0.03}_{-0.04}$	874.68/917
1ES 0347-121	BL Lac	0.18	$21.30^{+0.90}_{-0.70}$	$-1.60^{+0.90}_{-0.70}$	$5.72^{+2.16}_{-0.56}$	$1.97^{+0.18}_{-0.11}$	$0.05^{+0.15}_{-0.21}$		375.95/443
1ES 1216+304	BL Lac	0.18	$22.25^{+0.04}_{-0.79}$	$-2.92^{+1.25}_{-0.04}$	$5.46^{+1.50}_{-0.05}$	$1.54^{+0.06}_{-0.02}$	$0.65^{+0.03}_{-0.03}$		681.87/724
4C +34.47	FSRQ	0.21	$20.70^{+1.19}_{-0.70}$	$-1.01^{+0.01}_{-0.91}$	$6.57^{+1.20}_{-0.93}$	$1.60^{+0.10}_{-0.06}$	$-0.15^{+0.08}_{-0.14}$		531.50/539
1ES 0120+340	BL Lac	0.27	$21.89^{+0.34}_{-0.74}$	$-1.00^{+0.25}_{-0.75}$	$7.25^{+0.69}_{-0.23}$	$1.71^{+0.03}_{-0.03}$	$0.24^{+0.06}_{-0.06}$		589.57/698
S50716+714	FSRQ	0.31	$21.18^{+0.15}_{-0.01}$	$-2.00^{+0.20}_{-0.00}$	$5.11^{+0.15}_{-0.01}$	$1.87^{+0.03}_{-0.10}$	$0.13^{+0.11}_{-0.04}$		824.04/822
PKS 1510-089	FSRQ	0.36	$21.87^{+0.24}_{-0.12}$	$-1.82^{+0.64}_{-0.88}$	$5.14^{+0.42}_{-0.11}$	$2.10^{+0.20}_{-0.47}$	$0.98^{+0.10}_{-0.06}$	$1.33^{+0.02}_{-0.03}$	868.77/922
J1031+5053	BL Lac	0.36	$21.63^{+0.54}_{-0.91}$	$-1.13^{+0.06}_{-0.08}$	$5.00^{+0.18}_{-0.05}$	$3.95^{+0.01}_{-1.42}$	$0.81^{+0.11}_{-0.11}$	$2.23^{+0.04}_{-0.11}$	463.45/525
3C 279	FSRQ	0.54	$20.70^{+1.37}_{-0.04}$	$-2.99^{+0.85}_{-0.01}$	$5.20^{+0.27}_{-0.04}$	$1.49^{+0.01}_{-0.02}$	$2.64^{+0.19}_{-0.26}$	$1.66^{+0.03}_{-0.03}$	992.21/933
1ES 1641+399	FSRQ	0.59	$22.23^{+0.27}_{-0.33}$	$-0.86^{+0.13}_{-0.96}$	$7.60^{+0.37}_{-0.21}$	$1.59^{+0.04}_{-0.03}$	$2.79^{+0.62}_{-0.37}$	$1.74^{+0.81}_{-0.47}$	681.57/739
PKS 0637-752	FSRQ	0.64	$21.88^{+0.50}_{-0.97}$	$-1.50^{+0.74}_{-1.03}$	$6.40^{+1.50}_{-0.87}$	$2.08^{+0.31}_{-0.24}$	$1.10^{+0.33}_{-0.29}$	$1.63^{+0.09}_{-0.08}$	535.08/629
PKS 0903-57	FSRQ	0.70	$21.80^{+0.54}_{-0.34}$	$-2.70^{+0.90}_{-0.30}$	$5.20^{+2.15}_{-0.26}$	$0.54^{+0.20}_{-0.18}$	$1.09^{+0.28}_{-0.24}$		371.01/433
3C 454.3	FSRQ	0.86	$21.85^{+0.30}_{-0.24}$	$-2.92^{+0.28}_{-0.08}$	$5.03^{+0.22}_{-0.03}$	$1.29^{+0.03}_{-0.03}$	$2.30^{+0.18}_{-0.03}$	$1.54^{+0.03}_{-0.03}$	935.16/926
PKS 1441+25	FSRQ	0.94	$21.77^{+0.33}_{-1.17}$	$-1.80^{+0.96}_{-0.43}$	$5.18^{+2.62}_{-0.11}$	$2.15^{+0.26}_{-0.16}$	$-0.03^{+0.29}_{-0.33}$		360.76/412
4C +04.42	FSRQ	0.97	$21.23^{+0.68}_{-0.75}$	$-0.90^{+0.15}_{-0.95}$	$5.08^{+2.25}_{-0.07}$	$1.53^{+0.15}_{-0.24}$	$-0.30^{+0.30}_{-0.15}$		505.29/537
PKS 0208+512	FSRQ	1.00	$21.84^{+0.23}_{-0.11}$	$-1.13^{+0.07}_{-0.37}$	$6.65^{+0.15}_{-0.17}$	$1.60^{+0.02}_{-0.06}$	$3.28^{+0.35}_{-0.12}$	$1.84^{+0.02}_{-0.06}$	575.64/668
PKS 1240-294	FSRQ	1.13	$21.93^{+0.22}_{-0.98}$	$-0.99^{+0.27}_{-0.90}$	$5.53^{+1.93}_{-0.34}$	$1.90^{+0.23}_{-0.75}$	$-0.31^{+0.84}_{-0.26}$		307.68/374
PKS 1127-14	FSRQ	1.18	$21.89^{+0.21}_{-0.98}$	$-1.51^{+0.75}_{-0.79}$	$5.00^{+0.16}_{-0.18}$	$2.37^{+1.59}_{-0.75}$	$0.59^{+0.27}_{-0.25}$	$1.41^{+0.05}_{-0.06}$	649.40/702
NRAO 140	FSRQ	1.26	$22.19^{+0.15}_{-2.19}$	$-1.22^{+0.50}_{-0.78}$	$7.23^{+0.70}_{-0.80}$	$1.11^{+0.12}_{-0.08}$	$0.36^{+0.09}_{-0.17}$		724.79/696
OS 319	FSRQ	1.40	$21.59^{+0.51}_{-0.65}$	$-0.81^{+0.02}_{-0.40}$	$5.87^{+0.42}_{-0.08}$	$1.86^{+0.11}_{-0.41}$	$0.20^{+0.31}_{-0.14}$		366.43/384
PKS 2223-05	FSRQ	1.40	$22.31^{+0.18}_{-1.13}$	$-0.85^{+0.01}_{-1.30}$	$7.27^{+0.61}_{-1.39}$	$1.42^{+0.19}_{-0.09}$	$0.28^{+0.13}_{-0.32}$		433.27/484
PKS 2052-47	FSRQ	1.49	$22.26^{+0.17}_{-1.30}$	$-1.47^{+0.73}_{-0.93}$	$7.20^{+0.74}_{-0.98}$	$1.33^{+0.13}_{-0.11}$	$0.20^{+0.18}_{-0.21}$		374.12/451
4C 38.41	FSRQ	1.81	$21.94^{+0.27}_{-0.96}$	$-0.76^{+0.04}_{-1.20}$	$7.22^{+0.16}_{-0.45}$	$1.37^{+0.03}_{-0.03}$	$0.17^{+0.04}_{-0.06}$		806.01/804
PKS 2134+004	FSRQ	1.93	$22.37^{+0.05}_{-1.32}$	$-1.59^{+0.84}_{-0.64}$	$7.32^{+0.07}_{-1.64}$	$1.45^{+0.16}_{-0.12}$	$0.25^{+0.16}_{-0.27}$		886.53/418
PKS 0528+134	FSRQ	2.06	$22.32^{+0.08}_{-0.64}$	$-1.60^{+0.47}_{-0.80}$	$6.92^{+0.25}_{-1.43}$	$0.88^{+0.33}_{-0.27}$	$1.59^{+0.28}_{-0.14}$	$1.52^{+0.08}_{-0.07}$	728.89/760
1ES 0836+710	FSRQ	2.17	$22.03^{+0.30}_{-0.11}$	$-2.38^{+1.26}_{-0.12}$	$5.18^{+1.80}_{-0.30}$	$1.15^{+0.03}_{-0.06}$	$2.15^{+0.15}_{-0.46}$	$1.35^{+0.03}_{-0.04}$	972.76/912
PKS 2149+306	FSRQ	2.35	$22.11^{+0.12}_{-0.21}$	$-1.08^{+0.34}_{-0.39}$	$6.40^{+0.37}_{-0.49}$	$2.13^{+0.42}_{-0.66}$	$1.02^{+0.15}_{-0.12}$	$1.27^{+0.03}_{-0.06}$	858.87/825
J1656-3302	FSRQ	2.40	$22.35^{+0.12}_{-0.03}$	$-0.72^{+0.02}_{-0.98}$	$7.19^{+0.65}_{-0.42}$	$0.12^{+0.46}_{-0.02}$	$1.50^{+0.62}_{-0.26}$	$1.36^{+0.13}_{-0.33}$	438.94/528
PKS 1830-211*	FSRQ	2.50	$22.20^{+0.10}_{-0.81}$	$-0.99^{+0.32}_{-0.55}$	$6.88^{+0.93}_{-1.84}$	$0.64^{+0.29}_{-0.23}$	$0.46^{+0.18}_{-0.25}$		784.65/858
TXS0222+185	FSRQ	2.69	$22.28^{+0.14}_{-0.96}$	$-1.59^{+0.64}_{-0.81}$	$7.00^{+0.88}_{-1.61}$	$0.99^{+0.18}_{-0.15}$	$0.36^{+0.15}_{-0.15}$		699.61/676
PKS 0834-20	FSRQ	2.75	$22.30^{+0.22}_{-0.74}$	$-0.95^{+0.22}_{-0.91}$	$7.03^{+0.73}_{-0.55}$	$0.88^{+0.40}_{-0.45}$	$0.54^{+0.47}_{-0.44}$		320.97/395
TXS0800+618	FSRQ	3.03	$22.37^{+0.06}_{-1.22}$	$-1.85^{+0.83}_{-0.54}$	$6.40^{+1.30}_{-1.98}$	$1.77^{+0.34}_{-0.80}$	$-0.61^{+0.87}_{-0.36}$		297.99/354
PKS 0537-286	FSRQ	3.10	$22.21^{+0.07}_{-1.02}$	$-2.99^{+2.21}_{-0.15}$	$5.13^{+2.65}_{-0.21}$	$1.16^{+0.13}_{-0.12}$	$0.04^{+0.16}_{-0.14}$		620.60/681
PKS 2126-158	FSRQ	3.27	$22.30^{+0.08}_{-1.38}$	$-2.30^{+1.54}_{-0.40}$	$5.51^{+1.60}_{-1.07}$	$1.10^{+0.15}_{-0.15}$	$0.34^{+0.18}_{-0.15}$		732.26/721
S50014+81	FSRQ	3.37	$21.70^{+0.76}_{-0.13}$	$-2.98^{+0.94}_{-0.00}$	$6.82^{+1.02}_{-1.62}$	$1.09^{+0.15}_{-0.11}$	$0.44^{+0.15}_{-0.18}$		492.23/582
J064632+445116	FSRQ	3.39	$22.45^{+0.09}_{-0.32}$	$-1.64^{+0.73}_{-0.66}$	$7.41^{+0.56}_{-1.35}$	$1.44^{+0.18}_{-0.17}$	$5.10^{+2.82}_{-1.20}$	$3.07^{+0.61}_{-1.65}$	289.92/309
J013126-100931	FSRQ	3.51	$22.22^{+0.16}_{-0.69}$	$-1.37^{+0.34}_{-0.63}$	$5.06^{+2.53}_{-0.89}$	$1.24^{+0.28}_{-0.59}$	$0.01^{+0.65}_{-0.32}$		256.98/326
B3 1428+422	FSRQ	4.70	$22.51^{+0.01}_{-0.87}$	$-2.80^{+1.76}_{-0.09}$	$5.33^{+2.44}_{-1.09}$	$1.76^{+0.34}_{-0.80}$	$-0.63^{+1.04}_{-0.40}$		249.06/286

*Intervening galaxy at $z = 0.89$ with NHX = 1.94×10^{22} included in fitting using ZTBABS

Table 4.5: SWIFT 2SXPS Catalogue sub-sample for individual observation comparison with co-added spectra results. For each blazar, the columns give Observation ID, redshift, count rate/mean count rate, fitted IGM $N_{\rm HXIGM}$ and log-parabolic power law/ mean power law.

Blazar	Observation ID	z	$\frac{\text{count rate}}{\text{mean rate}}$	$\log(\frac{N_{\rm HXIGM}}{\rm cm^{-2}})$	$\frac{\text{logpar power-law}}{\text{mean power-law}}$
3C 454.3	mean	0.86	1.00	$21.67^{+0.41}_{-1.19}$	1.00
	00035030001	0.86	2.65	$22.06^{+0.22}_{-0.25}$	0.96
	00030024001	0.86	4.69	$21.76^{+0.47}_{-0.98}$	0.91
	00030024002	0.86	2.96	$21.86^{+0.23}_{-1.16}$	1.05
	00035030005	0.86	3.53	$22.30^{+0.17}_{-1.07}$	0.98
PKS 2149-306	mean	2.35	1.00	$21.90^{+0.28}_{-1.12}$	1.00
	00031404001	2.35	0.73	$21.90^{+0.53}_{-0.76}$	1.11
	00031404015	2.35	1.15	$22.03^{+0.13}_{-0.06}$	0.93
	00035242001	2.35	0.93	$22.30^{+0.20}_{-0.92}$	1.68
	00031404013	2.35	1.30	$22.36^{+0.11}_{-1.16}$	0.89
PKS 2126-158	mean	3.26	1.00	$22.30^{+0.08}_{-1.38}$	1.00
	00036356001	3.26	0.92	$22.37^{+0.07}_{-0.27}$	1.45
	00036356003	3.26	0.92	$22.37^{+0.01}_{-1.30}$	1.19
	00036356004	3.26	0.88	$22.44^{+0.00}_{-1.32}$	1.11
	00036356002	3.26	0.96	$21.70^{+0.61}_{-0.70}$	1.17
PKS 0537-286	mean	3.10	1.00	$22.21^{+0.07}_{-1.02}$	1.00
	00035240001	3.10	0.93	$22.15^{+0.33}_{-0.33}$	1.04
	00035240002	3.10	0.95	$22.34^{+0.17}_{-0.60}$	0.91
	00036783001	3.10	1.25	$22.31^{+0.18}_{-0.67}$	1.10
	00030816005	3.10	1.15	$22.00^{+0.46}_{-0.40}$	1.22
1ES 0836+710	mean	2.17	1.00	$21.85^{+0.36}_{-0.98}$	1.00
	00035385001	2.17	1.16	$21.90^{+0.39}_{-0.76}$	1.16
	00036376012	2.17	0.93	$22.32^{+0.12}_{-0.10}$	1.66
	00080399002	2.17	1.30	$22.27^{+0.09}_{-1.31}$	0.95
	00036376005	2.17	0.83	$22.04^{+0.39}_{-1.26}$	1.21
TXS 0222+185	mean	2.69	1.00	$22.28^{+0.13}_{-0.96}$	1.00
	00080243001	2.69	1.15	$22.26^{+0.09}_{-0.04}$	1.38
	00080243002	2.69	0.91	$22.40^{+0.08}_{-0.14}$	1.18
	00030794003	2.69	0.95	$22.34^{+0.14}_{-0.85}$	1.33
	00030794002	2.69	0.99	$22.27^{+0.16}_{-0.97}$	1.01
4C 38.41	mean	1.81	1.00	$21.94^{+0.22}_{-0.76}$	1.00
	00036389050	1.81	1.23	$22.29^{+0.21}_{-1.29}$	1.20
	00036389059	1.81	2.14	$21.89^{+0.22}_{-0.64}$	0.95
	00032894004	1.81	1.84	$21.99^{+0.31}_{-0.33}$	1.37
	00036389052	1.81	1.16	$22.35^{+0.12}_{-0.92}$	0.97
PKS 0528+134	mean	2.06	1.00	$22.23^{+0.14}_{-0.86}$	1.00
	00035384002	2.06	1.63	$22.35^{+0.05}_{-1.05}$	0.44
	00035384003	2.06	2.12	$22.20^{+0.28}_{-1.60}$	1.80
	00035384005	2.06	2.16	$22.30^{+0.14}_{-1.12}$	1.30
	00035384006	2.06	2.58	$22.26^{+0.15}_{-0.17}$	2.81

Table 4.6: XMM-Newton (XMM), 0.3 - 10 keV and 0.16 - 13 keV, and Swift sub-sample IGM column density results. For each blazar, the columns give Blazar name, redshift, fitted IGM *N*hxigm for *Swift*, *XMM-Newton* 0.3-10 keV and 0.16-13 keV respectively.

		Swift 0.3-10 keV	*XMM* 0.3-10 keV	*XMM* 0.16-13 keV
Blazar	z	$\log(\frac{N_{\mathrm{HXIGM}}}{\mathrm{cm}^{-2}})$	$\log(\frac{N_{\mathrm{HXIGM}}}{\mathrm{cm}^{-2}})$	$\log(\frac{N_{\mathrm{HXIGM}}}{\mathrm{cm}^{-2}})$
3C 454.3	0.86	$21.67^{+0.41}_{-1.19}$	$21.18^{+0.95}_{-0.57}$	$21.52^{+0.04}_{-0.12}$
PKS2149-306	2.35	$21.90^{+0.28}_{-1.12}$	$22.18^{+0.05}_{-0.68}$	$22.09^{+0.19}_{-0.91}$
PKS2126-158	3.26	$22.30^{+0.08}_{-1.38}$	$22.10^{+0.13}_{-1.40}$	$22.11^{+0.11}_{-1.62}$
PKS0537-286	3.10	$22.21^{+0.07}_{-1.02}$	$22.35^{+0.02}_{-0.37}$	$22.26^{+0.09}_{-0.39}$
1ES0836+710	2.17	$21.85^{+0.36}_{-0.98}$	$22.23^{+0.17}_{-1.19}$	$21.64^{+0.37}_{-0.87}$
TXS0222+185	2.69	$22.28^{+0.13}_{-0.96}$	$22.44^{+0.04}_{-0.08}$	$22.18^{+0.04}_{-0.09}$
PKS0528+134	2.06	$22.23^{+0.14}_{-0.86}$	$22.34^{+0.07}_{-0.12}$	$22.31^{+0.08}_{-0.14}$

Chapter 5

Probing the parameters of the intergalactic medium using quasars

This paper was submitted to the MNRAS in January, 2022, and reproduced here with minor formatting changes.

5.1 Summary

We continue our series of papers on intergalactic medium (IGM) tracers using quasi-stellar objects (QSOs), having examined gamma-ray bursts (GRBs) and blazars in earlier studies. We have estimated the IGM properties of hydrogen column density (NHXIGM), metallicity and temperature using *XMM-Newton* QSO spectra over a redshift range of $0.114 \leq z \leq 6.18$, with a collisional ionisation equilibrium (CIE) model for the ionised plasma. We subjected our results to a number of tests and found that the NHXIGM parameter was robust with respect to intrinsic power laws, spectral counts, reflection hump and soft excess features. There is scope for a luminosity bias given both luminosity and NHXIGM scale with redshift, but we find this unlikely given the consistent IGM parameter results across the other tracer

types reviewed. The impact of intervening high column density absorbers was found to be minimal. The NHXIGM from the QSO sample scales as $(1+z)^{1.5\pm0.2}$. The mean hydrogen density at $z = 0$ is $n_0 = (2.8 \pm 0.3) \times 10^{-7}$ cm^{-3}, the mean IGM temperature over the full redshift range is $\log(T/\mathrm{K}) = 6.5 \pm 0.1$, and the mean metallicity is $[X/\mathrm{H}] = -1.3 \pm 0.1$ ($Z \sim 0.05$). Combining the results with our previous GRB and blazar tracers, we conclude that the IGM contributes substantially and consistently to the total absorption seen in QSO, blazar and GRB spectra.

5.2 Introduction

In our previous papers in this series (Dalton and Morris, 2020; Dalton et al., 2021a,b, hereafter D20, D21a and D21b), we studied GRBs and blazars as tracers of IGM properties and possible variation with redshift. We continue the series in this paper with the study of QSOs. Our main objective is to estimate the IGM parameters of column density, metallicity, and temperature, using a model for ionised absorption on the line of sight (LOS) to QSOs. Our continuing hypothesis is that there is significant absorption in the diffuse IGM, and that the integrated IGM column density increases with redshift. We analyse the possible absorption due to the IGM using a highly ionised absorption component in addition to examining appropriate host environment and continuum intrinsic models. We test the robustness of our results and combine our QSO sample with our GRB and blazar samples for cross tracer comparison.

Most baryonic matter residing in the intergalactic medium (IGM) is not in the form of luminous virialized matter (Shull et al., 2012). The vast majority of hydrogen and helium is ionised in the IGM following reionisation in the early Universe. In order to measure the IGM density, metallicity and temperature, the observation of metals is essential. Powerful cosmological sources such as GRBs, blazars and QSOs are currently some of the most effective targets to study the IGM as their X-ray absorption yields information on the total absorbing column density of the matter.

QSOs are extremely luminous form of Active Galactic Nuclei (AGN) observed over a huge cosmological range with the current most distant being J0313-1806 at z = 7.642 (Wang et al., 2020). Under the generally accepted scenario, UV emission in QSOs is produced by viscous dissipation in the accretion disk where the gravitational energy of the infalling material is partially transformed into radiation (Shakura and Sunyaev, 1973). The UV photons are Comptonised to X-rays by a corona of hot relativistic electrons around the accretion disk (Haardt and Maraschi, 1993). These X-rays can illuminate the accretion disc, being reflected back towards the observer. The observational signs of such reflection features are iron emission lines, Fe K absorption edge and Compton scattering hump. However, these are not always apparent or observed. While features such as the Compton hump, soft excess and iron emission lines are frequently observed in lower luminosity AGN, particularly at lower redshift, they are not often observed in QSOs where the very powerful emission continuum dominates (Scott et al., 2011, and references therein). QSOs have been extensively studied for many decades across a very wide band of frequencies from radio to X-ray. The availability of ultra-violet (UV) databases and catalogues enables broadband comparison with X-rays for our purposes. The clear non-linear relation between the UV and X-ray components has been measured in detail, and noted to be reasonably constant over redshift and luminosity ranges (e.g. Risaliti and Lusso, 2019; Salvestrini et al., 2019; Lusso et al., 2020, and references therein). Their very consistent spectra observed over an extensive redshift range make them attractive as IGM tracers, as it can then be hypothesised that deficits or softening in continuum curvature that are related to redshift could be interpreted as signatures of IGM absorption.

QSOs as X-ray tracers of the IGM have been well studied in the past (e.g. Wilkes and Elvis, 1987; Elvis et al., 1994a; Page et al., 2005; Behar et al., 2011; Starling et al., 2013). X-ray absorption is usually dominated by metal ions and reported as an equivalent hydrogen column density (N_{HX}). The early observations of excess absorption in QSOs at high redshift in X-ray over the known Galactic absorption

(*N*HXGAL) were unexpected, as in X-ray, the absorbing cross-section decreases as the observed spectral energy increases with redshift (e.g. Elvis et al., 1994a; Cappi et al., 1997; Fiore et al., 1998; Elvis et al., 1998). This excess absorption was initially assumed to be located in the QSO host. Reeves and Turner (2000) were among the first to strongly advocate a relation between excess absorption and redshift but noted that the assumption of all such excess being at the QSO rest-frame could lead to overestimation of column densities as the absorbing material could lie anywhere on the LOS. Later studies explored the possibility of the IGM contributing to the excess absorption and found to be related to redshift, indicating that at least some of the excess absorption may be attributable to the IGM and not entirely the host (e.g. Eitan and Behar, 2013; Starling et al., 2013). However, all such studies assumed by convention that the absorbers were neutral and at solar metallicity. As typical QSO hosts, and IGM absorbers are partially ionised and have low metallicity, the resulting reported column densities are, therefore, lower limits. In our previous studies on GRBs (D20 and D21a) and blazars (D21b), we used realistic parameter ranges for metallicity and temperature in collisional ionisation absorption models for the IGM. We found strong evidence for IGM absorption rising with redshift in the spectra of both GRBs and blazars. We now continue the series using similar IGM and continuum models to study QSO spectra. In this paper, all data is taken from the European Space Agency's *XMM – Newton* Photon Imaging camera (EPIC) (Strüder et al., 2001) which has excellent low energy response down to 0.15 keV, high sensitivity to extended emission, and large effective area enabling detailed analysis of soft X-ray properties.

The sections that follow are: Section 5.3 describes the data selection and methodology; Section 5.4 covers the models for the IGM LOS including assumptions and parameters, and QSO continuum models; Section 5.5 gives the results of QSO spectra fits using collisional IGM models with free IGM key parameters; in Section 5.6 we test the robustness of the IGM model fits including a review of the QSO UV spectra for any high density absorbers; in Section 5.7 we combine GRB and blazar samples with our QSO sample for cross-tracer analysis. In Section 5.8, we discuss the results and compare with other studies and Section 5.9 gives our conclusions. For those interested in the key findings on IGM parameters from fits, we suggest they read Sections 5.5, 5.7 and 5.9. Those interested in spectra fitting methodology and model assumptions should also read Sections 5.3 and 5.4. Finally, for readers interested in more detailed examination of robustness of the QSO spectra fitting and discussion on other studies, read Sections 5.6 and 5.8. In this paper where relevant, we adopt the cosmological parameters $\Omega_M = 0.3$, $\Omega_\Lambda = 0.7$, and $H_0 = 70$ km s^{-1} Mpc^{-1}.

5.3 Data selection and methodology

Our sample of QSOs is taken from the catalogue created by Lusso et al. (2020) based on the 14th Data Release of the *Sloan Digital Sky Survey* (SDSS-DR14) (York et al., 2000) which they cross-matched with 4*XMM-Newton* Data Release-9 data giving an initial sample of 24,947 QSOs. We applied a minimum threshold of X-ray counts > 500 to ensure high signal-to-noise spectra. As the number of QSOs with $z > 4$ deceases dramatically, we drew from samples in Page et al. (2005); Grupe et al. (2006); Eitan and Behar (2013); Nanni et al. (2017); Vito et al. (2019); Medvedev et al. (2021). For $z < 4$ QSOs, we selected those with highest counts, maintaining a redshift spread. We relaxed our minimum count cutoff requirement slightly above $z \sim 3.8$, with 3 QSOs have counts between $400 - 500$. Our final sample of 48 QSOs has a redshift range of $0.114 \leq z \leq 6.18$

Radio loudness (R) is typically defined as the ratio of the flux densities at rest-frame 5GHz and 4400 Å, with R ≥ 10 and R < 10 for radio-loud (RLQ) and radio-quiet (RQQ) respectively (Kellermann et al., 1989). We include both RLQ and RQQ in our sample but exclude broad absorption line QSOs as these are known to be highly absorbed in X-ray and could dominate any possible IGM absorption. In general, for a given optical luminosity, the X-ray emission from RLQs is about three times greater than that from RQQs which allows them to be studied out to higher redshifts (Scott et al., 2011, and references therin). As a result, 19 out of our 48 QSOs are RLQ which may be a source of bias given on average, approximately 10% of QSOs are RLQ (e.g Grupe et al., 2006). We explore this in Section 5.6.

Table 5.1: SDSS-DR14 and *4XMM-Newton-DR9* cross-correlation QSO sample. For each QSO, the columns give the name, radio type (radio loud - RLQ, radio quiet - RQQ, or unknown), redshift, number of counts in 0.3-10 keV range and count rate (s^{-1}). Co-added spectra for a number of QSOs are used, often observed over a period of time, so we do not provide individual observation information.

QSO	Radio type	z	Total counts	Mean count rate (s^{-1})
J142952+544717*	RLQ	6.18	725	0.046
022112.62-034252.2*	unknown	5.01	339	0.034
001115.23+144601.8	RLQ	4.96	2258	0.096
143023.73+420436.5	RLQ	4.71	13162	0.157
223953.6-055220.0	RQQ	4.56	450	0.015
151002.93+570243.3	RLQ	4.31	1395	0.15
133529.45+410125.9	RQQ	4.26	626	0.055
132611.84+074358.3	RQQ	4.12	947	0.025
163950.52+434003.7	RLQ	3.99	1158	0.029
021429.29-051744.8	RLQ	3.98	1126	0.018
133223.26+503431.3	RQQ	3.81	404	0.022
200324.1-325144.0	RLQ	3.78	3484	0.23
200324.1-135245.1	RLQ	3.77	2963	0.21
122135.6+280614.0	RLQ	3.31	2994	0.093
042214.8-384453.0	RLQ	3.11	1840	0.22
083910.89+200207.3	RLQ	3.03	4251	0.103
111038.64+483115.6	RQQ	2.96	741	0022
122307.52+103448.2	RQQ	2.75	535	0.029
115005.36+013850.7	unknown	2.33	954	0.014
121423.02+024252.8	RLQ	2.22	5394	0.077
112338.14+052038.5	RLQ	2.18	826	0.031
123527.36+392824.0	RQQ	2.16	553	0.017
134740.99+581242.2	RLQ	2.05	2978	0.112
095834.04+024427.1	RQQ	1.89	1444	0.023
093359.34+551550.7	RQQ	1.86	2309	0.09
133526.73+405957.5	RQQ	1.77	634	0.062
100434.91+411242.8	RQQ	1.74	9558	0.27
104039.54+061521.5	RLQ	1.58	946	0.019
083205.95+524359.3	RQQ	1.57	1303	0.016
112320.73+013747.4	RQQ	1.47	1801	0.078
091301.03+525928.9	RQQ	1.38	1221	0.44
121426.52+140258.9	RLQ	1.28	946	0.019
105316.75+573550.8	RQQ	1.21	2059	0.066
085808.91+274522.7	RQQ	1.09	3158	0.043
095857.34+021314.5	RQQ	1.02	1904	0.77
125849.83-014303.3	RQQ	0.97	7032	0.20

Table 5.2: Table 5.1 continued

QSO	Radio type	z	Total counts	Mean count rate (s^{-1})
082257.55+404149.7	RLQ	0.86	815	0.158
150431.30+474151.2	RQQ	0.82	1499	0.106
111606.97+423645.4	RQQ	0.67	2409	0.081
130028.53+283010.1	RLQ	0.65	6859	0.314
111135.76+482945.3	RQQ	0.56	4081	0.150
091029.03+542719.0	RQQ	0.53	2073	0.058
105224.94+441505.2	RQQ	0.44	1237	0.156
223607.68+134355.3	RQQ	0.33	3106	0.058
144645.93+403505.7	RQQ	0.27	15843	0.959
123054.11+110011.2	RQQ	0.24	6368	1.158
103059.09+310255.8	RLQ	0.18	37274	1.79
141700.81+445606.3	RQQ	0.11	29070	1.386

* These QSOs had poor high energy spectra above 2keV so the range taken was from 0.2 - 2.0 keV

The *XMM-Newton* EPIC spectra were obtained in timing mode and reduced with the Science Analysis System (SAS2, version 19.1.0) following the standard procedure. First, we processed each observation with the EPCHAIN SAS tool. We used only single-pixel events (PATTERN==0) while bad time intervals were filtered out for large flares applying a 1.0 cts s^{-1} threshold. In order to avoid bad pixels and regions close to CCD edges, we filtered the data using FLAG==0. We manually inspected the source and background subtraction region for each observation. ***XMM – Newton*** has three cameras, pn, MOS-1 and MOS-2. All our data is taken from pn except for our highest redshift QSOs where we included the MOS-1 and MOS-2 data to increase spectral counts.

For our fitting, we use XSPEC version 12.11.1 (Arnaud, 1996). We use the C-statistic (Cash, 1979) (Cstat in XSPEC) which is based on the Poisson likelihood and gives more reliable results where the number of counts per bin is small. As we are using total X-ray spectral absorption for the IGM, we can expect some degeneracy between the parameters. We therefore follow the same method as in our other papers in this series (D21a and D21b) using a combination of the STEPPAR function and Markov chain Monte Carlo to overcome the problem of local probability maxima, and to give confidence intervals on our IGM property results. We adopt the approach that a reduction of Cstat> 2.71, > 4.6, and > 6.25 for one, two and three additional interesting parameters corresponds to 90% significance (Reeves and Turner, 2000; Ricci et al., 2017). Spectra were binned to have a minimum of 1 count per bin to avoid empty channels so the Cstat value is independent of the count numbers (Nanni et al., 2017). We assume a homogeneous isotropic IGM as all our QSO sample have LOS much greater than the large scale structure, while acknowledging that large individual absorbers can still impact the LOS (tested in Section 5.6).

5.4 Models for the QSO continuum and LOS features

In this section we explain our choice of IGM models and parameter ranges. We also describe the models used for fitting the intrinsic spectra and absorption of the QSOs, and our Galaxy. We emphasise that we are not attempting to find a model fully consistent with the QSO spectrum, so long as our intrinsic model sufficiently represents spectral curvature and shape, with the remaining spectral features being attributable to the IGM. We, therefore, do not necessarily expect our modelling to yield any physical insight into the nature of the QSO engine itself. Given the moderate resolution of *XMM-Newton*, our spectral modelling and analysis pertains to the overall continuum absorption and not individual lines, edges or features (D21a and b).

5.4.1 Galactic absorption

We use TBABS (Wilms et al., 2000, hereafter W00) with *N*HXGAL fixed to the values based on Willingale et al. (2013) which are estimated using 21 cm radio emission maps from (Kalberla et al., 2005). We use W00 solar abundances which factor in dust and H_2 in the interstellar medium in galaxies.

5.4.2 Continuum models

In the energy range we are studying (0.3-10 keV), QSO spectra are typically modelled with a simple power law. Some studies add a high energy cut-off at ~ 100keV or higher (e.g. Ricci et al., 2017), but the typical values of such cut-off are well outside our X-ray energy range. Many QSOs show curvature, particularly in soft X-ray and a log-parabolic power law can be more appropriate. A Compton reflection hump is a common feature in QSOs, mainly RQQ. However, the visibility of this component in the observed spectra of QSOs is low, as their emission is mainly dominated by the luminous continuum (e.g. Reeves and Turner, 2000; Scott et al., 2011). In high luminosity QSOs, the reflection component may be intrinsically weaker due to possible ionisation of the inner accretion disc, reducing the neutral matter available to generate a reflection feature (Mushotzky et al., 1993). There is little observational evidence, particularly for higher redshift QSOs ($z > 2$) of the iron emission line, probably due to the dominant emission continuum (Page et al., 2005). QSOs sometimes show a soft excess, particularly at lower redshifts. This was initially postulated to be the hard tail of the UV 'big blue bump'. While there is no consensus on the origin of the soft excess, there are now several prominent theories e.g. an artifact of ionised absorption (e.g Gierliński and Done, 2004), Comptonisation of UV photons (e.g. Done et al., 2012), and relativistically blurred disc reflection (e.g. Crummy et al., 2006). In conclusion, as the soft excess rarely shows above redshift $z > 0.3$, and the reflection hump is also rarely seen in QSOs, we omit adding specific components for these features in our initial fitting.

Accordingly, we model the QSO continuum with a simple and a log-parabolic power law. In Section 5.6, we robustly explore whether the inclusion of model components for reflection and/or soft excess improves the fit and/or impacts any IGM absorption.

Finally, we note that there is a known systematic instrumental feature at 2keV which is observed in most of the QSO sample spectra. It is associated with the Au

M and Si K edges which occur in the pn and MOS instruments.

5.4.3 QSO host absorption

As noted in Section 5.2, by convention many X-ray QSO studies assume any absorption in excess of our Galaxy is located in the host galaxy, with the absorber assumed to be neutral and with solar metallicity. To more accurately isolate any absorption by the QSO host, we base our model on the findings in the Quasar Probing Quasar series (e.g Hennawi et al., 2006; Prochaska and Hennawi, 2009; Hennawi and Prochaska, 2013; Prochaska et al., 2013). Accordingly, our host model assumes collisionally ionised absorption (CIE) in the circum-galactic medium (CGM) at fixed parameters of $\log(N_{\rm HX}/{\rm cm}^{-2}) = 20$, $\log({\rm T/K}) = 6$ and $[X/{\rm H}] = -1$ ($Z/Z_{\odot} = 0.1$). We use the XSPEC CIE model HOTABS (Kallman et al., 2009). We note that there is evidence of metallicity evolution in QSOs (e.g. Prochaska et al., 2014, and references therein) but not sufficient to warrant leaving the metallicity parameter variable in the host model. Further, Damped Lyman α Systems (DLAs) have been observed on the LOS to QSOs. However, their very low incidence means they have limited potential impact on most QSO spectra. We examine this further in Section 5.6. Finally, we note that the incidence of QSOs with significantly reddened optical spectra is rare, indicating that the dust/gas ratio is low (Page et al., 2005). Therefore, we assume there is no dust impact on the assumed host absorption.

5.4.4 Ionised IGM component

We follow the D21a and D21b methodology for the modelling the IGM absorption. As extreme scenarios where all absorption in the IGM is either in the collisionally (CIE) or photoionised (PIE) phases, we initially fitted a sub-sample of QSOs with both PIE and CIE absorption separately. We found that similar results for $N_{\rm HXIGM}$ were obtained for both models, consistent with D21a and D21b. Some combination of CIE and PIE absorption is the most physically plausible scenario for the full LOS.

Table 5.3: Upper and lower limits for the free parameters in the IGM model. Continuum parameters were also left free. The fixed parameters are Galactic $\log(N_{\mathrm{HX}}/\mathrm{cm}^{-2})$, the IGM slab redshift at half the QSO redshift, and the QSO host CGM $\log(N_{\mathrm{HX}}/\mathrm{cm}^{-2})$, temperature and metallicity.

IGM parameter	range in XSPEC models
column density	$19 \leq \log(N_{\mathrm{HX}}/\mathrm{cm}^{-2}) \leq 23$
temperature	$4 \leq \log(T/\mathrm{K}) \leq 8$
metallicity	$-4 \leq [X/\mathrm{H}] \leq -0.7$

As it is not possible to determine which ionisation model is the better single model for the IGM at all redshifts, we follow D21b, fitting with the CIE model HOTABS only. As noted in Section 5.4, we are modelling and fitting the overall continuum curvature, and not specific absorption features. We note that this gives scope for possible degeneracy to occur. This degeneracy could arise from the relation between column density, temperature and metallicity, but also due to features such as soft excess and reflection humps. We examine the potential impact of such soft excess and reflection components in Section 5.6.

We assume a thin uniform plane parallel slab geometry in ionisation and thermal equilibrium to model the IGM LOS (e.g. Savage et al., 2014; Nicastro et al., 2017; Khabibullin and Churazov, 2019; Lehner et al., 2019). As an approximation of the full LOS IGM absorption, in a homogeneous medium, this slab is placed at half the QSO redshift.

We use the same IGM parameter ranges as D21a and D21b for density, temperature and metallicity as summarised in Table 5.3. The metallicity range is broad enough to cover the most diffuse low metallicty IGM regions, to the higher metallicity warm-hot IGM (WHIM) based on (e.g Schaye et al., 2003; Aguirre et al., 2008; Danforth et al., 2016; Pratt et al., 2018).

Fig. 5.1 shows an example of our model components for the LOS absorption to a QSO at $z = 3$. We show the model components separately using a log-parabolic power law for each line, as well as the full combined model: CIE IGM absorption (grey) for a slab at $z = 1.5$ $\log(N_{\mathrm{HXIGM}}/\mathrm{cm}^{-2}) = 22.00$, $Z = 0.05Z_{\odot}$, and $\log(T/\mathrm{K}) =$

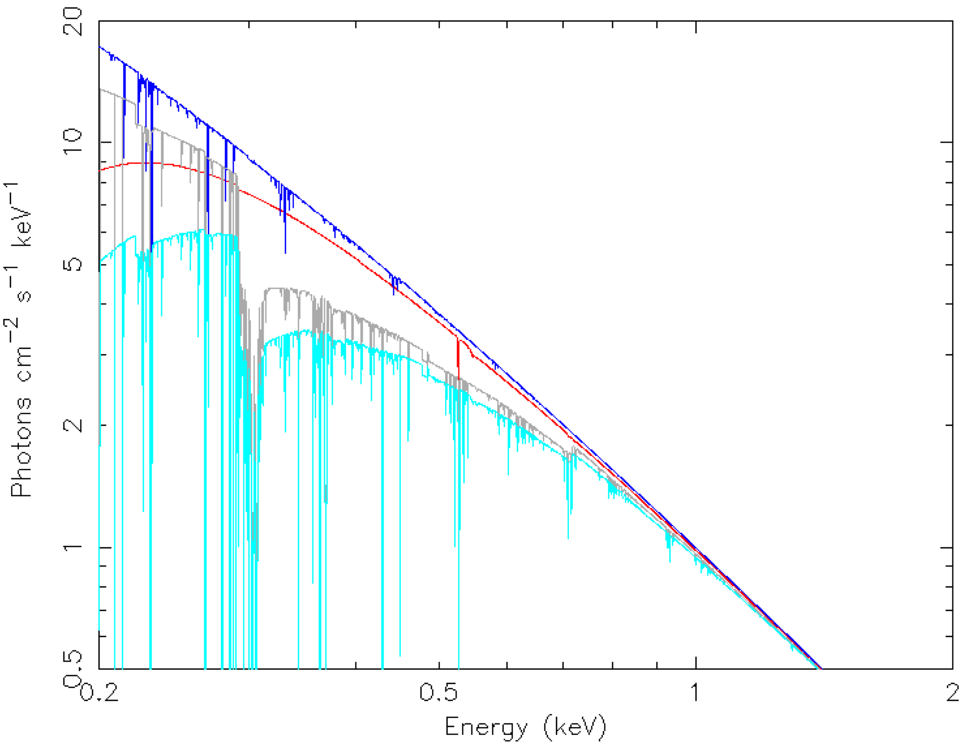

Figure 5.1: Model components for the LOS absorption to a QSO at $z = 3$, in the energy range 0.2 - 3keV. Each component is shown separately combined with a log-parabolic power law, as well as the full combined model: IGM CIE absorption (grey) of a slab at $z = 1.5$ $\log(N_{\mathrm{HXIGM}}/\mathrm{cm}^{-2}) = 22.00$, $Z = 0.05Z_{\odot}$, and $\log(T/\mathrm{K}) = 6.00$; $\log(N_{\mathrm{HX}}/\mathrm{cm}^{-2}) = 20$ for our Galaxy (red); $\log(N_{\mathrm{HX}}/\mathrm{cm}^{-2}) = 20$ with $Z = 0.1Z_{\odot}$ and $\log(T/\mathrm{K}) = 6.00$ for the QSO host CGM at $z = 3$ (blue). The full combined model is the light blue line.

6.00 fo a slab at $z = 1.5$; $\log(N_{\mathrm{HX}}/\mathrm{cm}^{-2}) = 20$ for our Galaxy (red); $\log(N_{\mathrm{HX}}/\mathrm{cm}^{-2}) = 20$ with $Z = 0.1Z_{\odot}$ and $\log(T/\mathrm{K}) = 6.00$ for the QSO host CGM (blue) at $z = 3$. The full combined model is the light blue line. The absorption lines are clearly visible in the model example, but these features would not be detected in a real spectrum being smeared out over a large redshift range and due to instrument limitations.

Substantial absorption by intervening neutral absorbers with $\log(N_{\mathrm{H\,I}}/\mathrm{cm}^{-2}) > 21.00$ is rare in QSO LOS, and insufficient to account for the observed spectral curvature unless there are several intervening DLA or a galaxy (e.g Elvis et al., 1994b; Cappi et al., 1997; Fabian et al., 2001; Page et al., 2005). Therefore, in our model, we omit any intervening absorption contribution from any such possible objects. In Section 5.6, we will examine all known DLA and intervening galaxies on the QSO LOS to see if they could account for any curvature in the sample spectra.

The full XSPEC models based on the above components are therefore:

TBABS(Galaxy)*HOTABS(IGM)*HOTABS(host CGM)*PO

or

TBABS(Galaxy)*HOTABS(IGM)*HOTABS(host CGM)*LOGPAR

5.5 QSO spectral analysis results

In this section, we firstly discuss the impact of using a log-parabolic power law compared to the more commonly used simple power law for the QSO intrinsic continuum in Section 5.5.1. We then give the results for IGM parameters for the full sample using the CIE IGM absorption model in Section 5.5.2. All spectral fits include TBABS for Galactic absorption and HOTABS for the QSO host CGM as described in Section 5.4.

5.5.1 Spectra fits using alternative continuum models

We fitted our full sample with a simple power law and a log-parabolic power law to see which has the best Cstat fit. In nearly all of the sample, the Cstat fit improved using the log-parabolic power law with 60% showing a significant improvement based on the criteria ΔCstat> 2.71. Accordingly, in fitting the QSO sample with the full CIE model, we used only a log-parabolic power law for consistency.

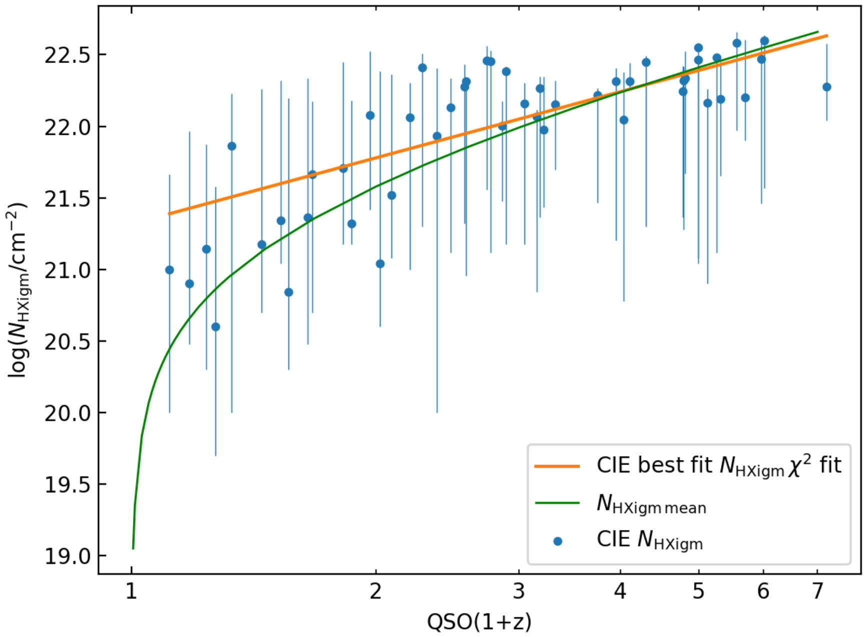

Figure 5.2: Results for the IGM NHX parameter versus redshift using the CIE (HOTABS) model. The error bars are reported with a 90% confidence interval. The green line is the simple IGM model using a mean IGM density (see eq. 5.1).

5.5.2 Results for IGM parameters using the CIE model

We give the results for the IGM parameters of log(NHX), temperature and metallicity using the CIE model component for our full QSO sample. These IGM parameters, as well as the power law parameters were left free to vary. The error bars are reported with a 90% confidence interval. The green line in the plots of NHX and redshift (Figs. 5.2 and 5.9), is the mean hydrogen density of the IGM based on D20, D21a and D21b and references therein (e.g. Starling et al., 2013; Shull and Danforth, 2018).

$$N_{\mathrm{HXIGM}} = \frac{n_0 c}{H_0} \int_0^z \frac{(1+z)^2 dz}{[\Omega_M (1+z)^3 + \Omega_\Lambda]^{\frac{1}{2}}} \tag{5.1}$$

where n$_0$ is the hydrogen density at $z = 0$, taken as 1.7×10^{-7} cm^{-3} (Behar et al., 2011). We used our results for NHXIGM and actual redshift for the QSOs to get their equivalent n_0 which are derived by rearranging equation 5.1 to give n_0. We then took the mean of n_0 for our full sample and calculated the standard error.

Table 5.6 gives the detailed results for our full QSO sample for the IGM and continuum parameters. In Fig. 5.2, we show the results for NHXIGM versus redshift.

A power law fit to the NHXIGM versus redshift for the full QSO sample scales as $(1 + z)^{1.5\pm0.2}$, reduced $\chi^2 = 0.58$. The sample includes QSOs with redshift as low as $z = 0.114$, so a linear χ^2 fit is only an approximation for the curve, as can be seen from the simple IGM model curve. The mean hydrogen density using equation 5.1 at $z = 0$ for the QSO sample is $n_0 = (2.8 \pm 0.3) \times 10^{-7}$ cm^{-3}, higher than the assumed value of 1.7×10^{-7} cm^{-3} for the plotted simple IGM model. A sub-sample of QSOs with $z > 1.6$, similar to the GRB sample in D21a, gives $n_0 = (2.1 \pm 0.3) \times 10^{-7}$ cm^{-3}.

As there is some evidence of evolution in the partially ionised column density in the CGM (Fumagalli et al., 2016; Lehner et al., 2016), more advanced modelling for a warm/hot CGM component is needed to explore the relative contribution of the host CGM compared to the observed absorption in QSOs, blazars (D21b) and GRBs (D21a).

There is a broad range in the temperature across the redshift range for the QSO sample $4.9 < \log(T/\mathrm{K}) < 8.0$, most with substantial error bars in Fig. 5.3. The mean temperature for the full QSO sample over the full redshift range is $\log(T/\mathrm{K}) = 6.5 \pm 0.1$. It is notable that very few of the QSOs have error bars that go below $\log(T/\mathrm{K}) < 5.0$ even though we allow the temperature parameter to vary down to $\log(T/\mathrm{K}) = 4.0$. A number of the QSOs have best fit temperatures close to the high or low parameter range limits, indicating that temperatures are not well determined.

There is no relation between temperature and redshift. It is possible that the IGM LOS includes a cooler photo-ionised gas which is contributing to the absorption but not captured in this CIE model. The fits are not representative of any individual absorber temperature, but instead represent the integrated LOS.

Fig. 5.4 shows no obvious relation of $[X/\mathrm{H}]$ with redshift. The mean metallicity over the full redshift range is $[X/\mathrm{H}] = -1.31 \pm 0.07$ ($0.05Z_\odot$). Metallicity ranges from

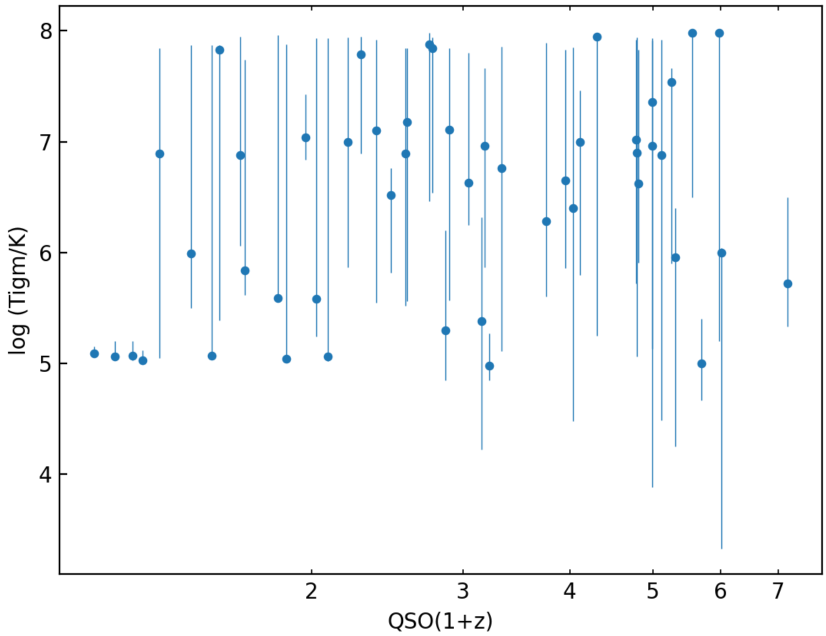

Figure 5.3: Results for the log(T/K) IGM versus redshift using the CIE (HOTABS) model. The error bars are reported with a 90% confidence interval. We do not include a χ^2 curve in the plot as the fit was poor due to a large scatter.

approximately $[X/\mathrm{H}] - 0.8$ ($0.16Z_\odot$) to $[X/\mathrm{H}] - 2.9$ ($0.001Z_\odot$). Most of the QSOs appear to favour metallicity in the range $-1 \geq [X/\mathrm{H}] \geq -2.0$, with only a small number favouring lower metallicities, generally at lower redshifts. This appears to be contrary to any expected evolution of metallicity, though our approach is based on the full LOS to the QSOs and not any particular absorber redshift.

There are reasonable grounds, based on our results, for arguing that the CIE model using HOTABS is plausible for modelling the warm/hot component of the IGM at all redshifts, with the caveats of using a CIE IGM component only, the slab model to represent to full LOS, and low X-ray resolution. In all fits, the Cstat was improved by using the IGM component. Further, 73% show a significant improvement with the IGM component added based on the criteria ΔCstat> 6.25 for three interesting parameters. There was a large range in Cstat improvements across the sample, with the average Cstat improvement for the full sample per free IGM parameter being

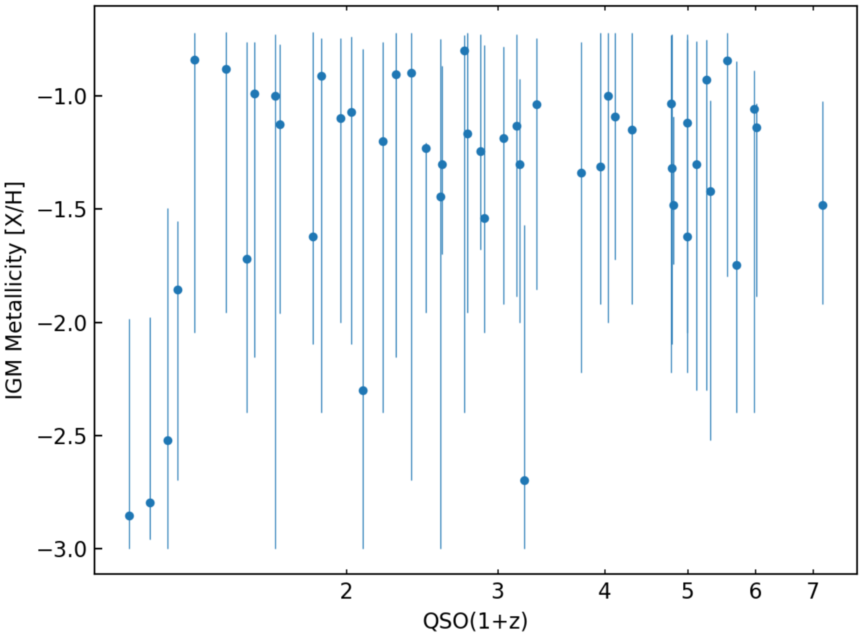

Figure 5.4: Results for the IGM metallicity versus redshift using the CIE (HOTABS) model. The error bars are reported with a 90% confidence interval. We do not include a χ^2 curve in the plot as the fit was poor due to a large scatter.

8.25. Our metallicity and temperature ranges and mean results are consistent simulations for a warm/hot phase. As our CIE IGM component had three free parameters, NHXIGM, temperature and [X/H], there is scope for degeneracy as we model the continuum curvature and not specific absorption features (D21a and D21b).

We now test the robustness of the results in Section 5.6 and discuss the results further and compare with other studies in Section 5.8.

5.6 Tests for robustness of IGM parameter results

We examine our results from a number of perspectives to test their robustness as there are several alternative potential explanations for the curvature seen in QSO spectra which may not be partly or wholly attributable to IGM absorption. AGN

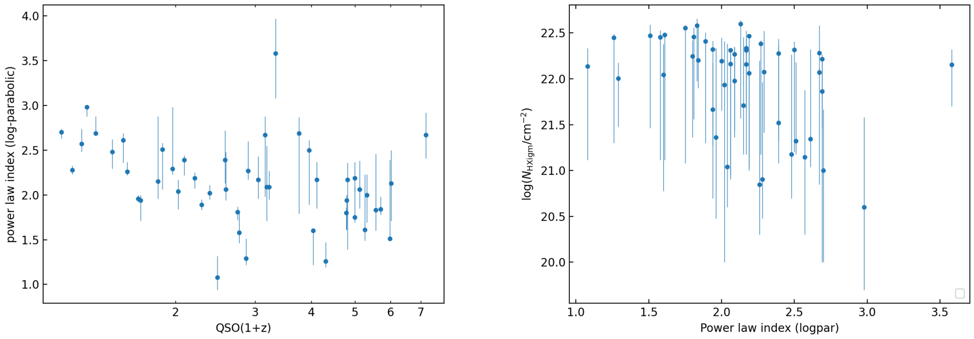

Figure 5.5: Testing for a possible relation between NHXIGM and the QSO intrinsic power law index (log-parabolic). Left panel is the QSO intrinsic power law index versus redshift. There is no apparent strong relation between the power law and redshift, other than that due to the dominance of RQQ below $z < 2$ which are known to have a higher power law index than RLQ. The right panel is NHXIGM and the QSO intrinsic power law index which does not show any apparent relation between the variables.

are generally known to have a Compton hump at higher energies. Similarly, at lower energies, a soft excess is sometimes observable in AGN spectra, whose cause is still debated. Both, or either, of these features, if present in a QSO spectra, may affect any absorption feature of the IGM. NHXIGM can be degenerate to some degree with continuum slope and intrinsic curvature. Further, QSO spectra have very large differences in total counts and count rates which could have an impact on or be linked to spectral curvature. There is a large range in luminosity of QSOs and this may be a source of the apparent NHXIGM redshift relation. Finally, we look for absorbers in UV and lensing galaxies to investigate their possible contribution to the column density.

5.6.1 IGM column density and intrinsic power law index

There is scope for degeneracy between NHXIGM and spectral slope and curvature. Therefore, we checked for any relation between these two parameters across the full QSO sample. To measure the unabsorbed continuum slope, we used a log-parabolic power law only. RQQ are dominant at $z < 2$, typically have a higher

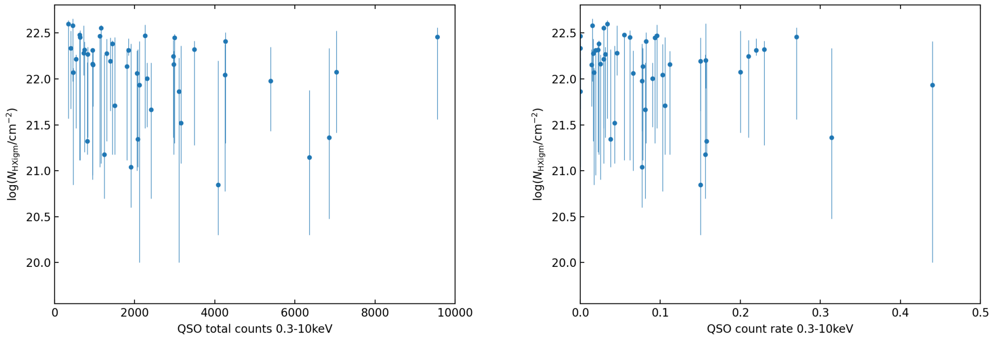

Figure 5.6: Left panel - testing for a possible relation between the QSO *N*HXIGM and total spectral counts. Right panel - testing for a possible relation between *N*HXIGM and spectral count rates. There is no apparent relation between the variables.

power index than RLQ which dominate above $z > 2$ (e.g. Scott et al., 2011; Page et al., 2005; Reeves and Turner, 2000), and is consistent with out results. Fig 5.5 left panel does not show a strong relation between the QSO power law index and redshift, other than that expected from the redshift spread of RQQ and RLQ. There have been many studies over the years examining possible evolution or relations of QSO continua with redshift. The results consistently have been that there is no such evolution or relation (e.g. Reeves and Turner, 2000; Page et al., 2005; Grupe et al., 2006; Risaliti and Lusso, 2019; Shehata et al., 2021). This supports the argument that the observed *N*HX redshift relation in our results is IGM related and not intrinsic to the QSO properties, as there is no apparent relation between our *N*HXIGM results and power law index in Fig. 5.5 right panel.

5.6.2 IGM column density and spectral counts

Since the QSO spectra and therefore *N*HXIGM will be better constrained for observations with higher statistics, total counts and count rates, this may lead to a bias. We check this by looking for any relation between the index and net counts and count rates. Fig 5.6 left panel shows no relation between the QSO *N*HXIGM and total counts. There is also no apparent relation between *N*HXIGM and count rates in Fig. 5.6 right panel, as expected given that there is no obvious physical reason

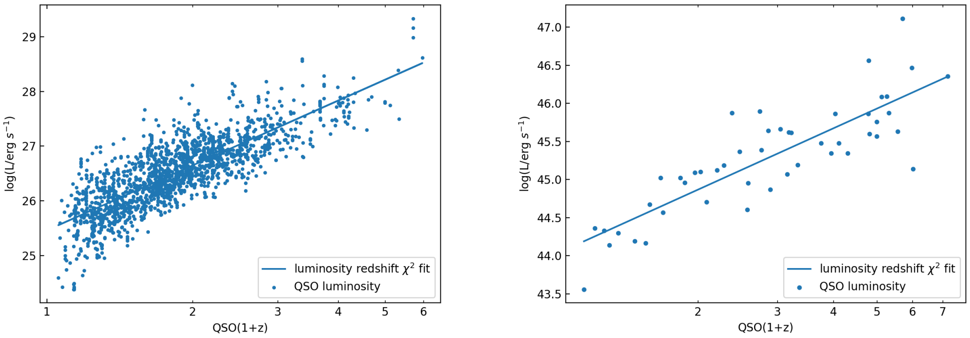

Figure 5.7: Left panel - Monochromatic luminosity (2keV) and redshift for the full SDSS-DR14 and *4XMM-DR9* with counts > 1000. Right panel - Our QSO sample luminosity for energy 2 - 10keV and redshift.

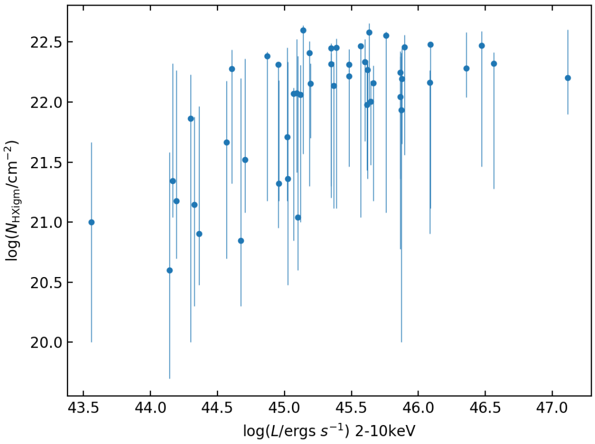

Figure 5.8: Testing for a possible relation between *N*HXIGM and luminosity.

why a higher flux should be linked to column density. This is consistent with prior studies (e.g. Shehata et al., 2021).

5.6.3 IGM column density and luminosity

The majority of QSOs are RQQ with only approximately 10% being RLQ, though this varies somewhat with redshift (e.g. Grupe et al., 2006). However, RQQ are mostly observed at $z < 2$. Given we are selecting the QSOs with the highest counts, and also out to the highest redshifts, there is scope for luminosity bias which may be degenerate with *N*HXIGM. In Fig 5.7 left panel, we plot the SDSS-DR14 and

4*XMM-Newton*-DR9 cross correlated catalogue with a cutoff of > 1000 counts. A clear luminosity redshift relation is notable. In Fig. 5.7 right panel, a plot our our QSO sample with redshift shows a similar luminosity redshift relation.

In Fig 5.8, we plot our QSO *N*HXIGM and luminosity. Given the luminosity bias in our sample, and the observed luminosity redshift relation in both our sample and the full SDSS-*XMM-Newton* catalogue, it is not surprising that there is also an apparent *N*HXIGM luminosity relation. This relation has been noted previously and it is not possible to determine which parameter of either luminosity or redshift, that *N*HXIGM is more closely related (Eitan and Behar, 2013; Shehata et al., 2021), or whether the luminosity relationship is causal in any way on *N*HXIGM. The results of *N*HXIGM redshift relations for other tracers in Section 5.7 should help clarify this point. In that section, we note that GRBs, blazars and QSOs all show a very similar consistent relation between *N*HXIGM and redshift supporting the argument that the rising *N*HXIGM is not caused luminosity.

5.6.4 Compton reflection hump

A Compton or reflection hump feature is common in AGNs at a rest frame of 30keV. Depending on the redshift, this could appear in the spectra observed frame between 0.3 – 10keV, especially above $z > 3$. The reflection is due to reprocessing of the primary X-ray continuum by circum-nuclear material. The most common model in XSPEC used for this feature is PEXRAV (Magdziarz and Zdziarski, 1995). There are more sophisticated reflection models available but the resolution in our sample does not warrant their use. PEXRAV assumes an optically thick, cold material, although with H and He fully ionised, distributed in a slab and covering a given fraction of the X-ray source. In our test fitting, we left the parameter R (slab scaling parameter) free, with the power law and normalisation tied to continuum power law, and with the other parameters set to default values following the conventional approach (e.g. Reeves and Turner, 2000; Ricci et al., 2017). Where there is reflection, and the model is appropriate, the value of the R parameter should be close to 1. Many studies choose to fix the R parameter to 1 but we wanted to see if this parameter preferred values close to 1 or 0, the latter indicating little or no reflection.

We refitted all our QSO sample with PEXRAV instead of our CIE IGM component. For most of the QSOs, the Cstat fit was worse with PEXRAV. For all QSOs with $z > 3$, the reflection parameter results were R $\ll 1$. For the small number of QSOs that had similar Cstat results as for the CIE IGM model, a visual inspection of the spectra indicated a possible Fe feature at a rest frame of $6 - 7$ keV. When refitted with the CIE IGM component added, the IGM parameters did not change i.e. the inclusion of the relection component did not impact the result. For the two lowest redshift QSOs, the Cstat fit improved significantly with both PEXRAV and our CIE IGM model included (being ΔCstat = 11.5 and 7.7 for QSOs 103059.09+310255.8 and 141700.81+445606.3 respectively). However, again, for these two low redshift QSOs, the IGM fit parameters did not alter substantially.

Our results are consistent with previous studies for QSOs which found that the reflection component was very weak or consistent with no reflection in both RQQ and RLQ and that this was inversely related to luminosity, known as the X-ray Baldwin effect (e.g. Reeves and Turner, 2000; Iwasawa and Taniguchi, 1993). This explains why the Fe line emission appears to be absent in the most luminous of QSOs. Risaliti and Lusso (2019) used simulations to calculate the error on the flux at 2 keV due to neglecting relection component and estimated it at a few per cent at most.

5.6.5 Soft excess

Many AGN show a soft excess in their X-ray spectra (e.g. Ricci et al., 2017). They found that over 50% of their AGN showed evidennce of soft excess. However, their AGN sample was restricted to $z < 0.3$ There is no consensus on the origin of the soft excess and theories include it being Comptonisation of UV photons, an artifact of ionised absorption, and blurred relativistic reflection (e.g. Done et al., 2012; Gierliński and Done, 2004; Crummy et al., 2006). The soft excess is typically modelled as a blackbody as a simple representation, with a peak rest frame temperature of ~ 0.1keV, and a range of $0.01 \leq kT \leq 0.3$keV (e.g. Scott et al., 2011; Reeves and Turner, 2000; Ricci et al., 2017).

We refitted all our sample with a redshifted blackbody, ZBBODY in XSPEC instead of the IGM component. None of our QSOs with $z > 0.3$ showed any evidence of a soft excess consistent with previous studies (e.g. Reeves and Turner, 2000). For the 4 QSOs with $z < 0.3$ the inclusion of a blackbody with a simple power law, did improve the Cstat fit. For the three lowest redshift QSOs, the inclusion of the IGM component using a log-parabolic power law as well as a blackbody component significantly improved the fit (ΔCstat > 6.25). The IGM fitted parameters did not alter substantially, with the exception of the lowest redshift QSO (141700.81+445606.3) where $\log(N_{\text{HXIGM}}/\text{cm}^{-2})$ increased from 21.0 to 21.6. Both of these values are well in excess of what would be expected from the simple IGM model absorption and may indicate that this QSO is somewhat obscured by its torus or have other host absorption.

5.6.6 Large absorbers on the line of sight

We have assumed that all absorption in excess of our Galaxy and the QSO host is due to the diffuse IGM. If there are any strong individual absorbers on the QSO LOS, they will contribute to the total absorption column.

One of the advantages of using QSOs as tracers is that they have been studied in depth in UV over the last several decades. The QSO LOS can encounter many types of hydrogen absorber from the lowest density Lyman α forest at $\log(N_{\text{H I}}/\text{cm}^{-2}) < 14$, to the most dense Lyman systems, the DLAs $\log(N_{\text{H I}}/\text{cm}^{-2}) > 20.3$. These dense systems have low column when compared to our results for $\log(N_{\text{HXIGM}})$ which start at 20.6 for our lowest redshift QSOs, and rise quickly to well above 21 by $z > 0.5$.

To test whether DLAs could account for some of the absorption on the LOS, we reviewed the SDSS spectra* for evidence of DLAs and cross-checked with the new catalogue based on SDSS DR16Q (Ho et al., 2021). Our results for DLAs on the QSO LOS were consistent with (Prochaska and Neeleman, 2018), who were investigating the average number of DLAs intersected by a LOS to a source at redshift out to $z \sim 5$. We found 1 QSO with a DLA between $2 \leq z \leq 3$, and 8 QSOs with DLAs between $3 \leq z \leq 5$. None had more than 2 DLAs on a particular QSO LOS. The QSO DLA mean $\log(N_{\mathrm{H\,I}}/\mathrm{cm}^{-2}) \sim 20$ tends to be lower than for GRBs at ~ 21.5 (Fynbo et al., 2009). This may be due to QSOs and GRBs probing differing LOS in their hosts. All of these QSOs in our sample, which showed DLAs from the SDSS, had $\log(N\mathrm{HXIGM}/\mathrm{cm}^{-2}) > 22$, and therefore the DLA contribution would be insignificant to the column.

Intervening lensing galaxies on the QSO LOS have been observed over the years. Earlier studies developed models predicting > 4% of high redshift QSOs would be lensed (e.g. Comerford et al., 2002; Wyithe and Loeb, 2002). However, the observed lensing fraction of such high redshift QSOs remains considerably lower than the model predicted amounts at ~ 0.2%, and could be due to survey incompleteness or model errors (Yue et al., 2021, and references therein). Bearing in mind that our sample covers low as well as high redshift QSOs, and based on the low observed lensed fraction, we could expect that less than 1 of our QSOs would be lensed, with perhaps around 2 or more if the models are correct. We reviewed literature and identified 2 of our sample QSOs with confirmed intervening lenses, 042214.8-384453.0 and 100434.91+411242.8. The neutral column through these lensing galaxies was estimated as $\log(N_{\mathrm{H\,I}}/\mathrm{cm}^{-2}) < 20$, two orders of magnitude lower that our measured NHXIGM (Chen et al., 2012; Carswell et al., 1996).

In conclusion, our robustness tests have demonstrated that, with the possible exception of luminosity, we have ruled out alternative explanations for the observed NHXIGM redshift relation including reflection hump, soft excess, power law index,

---

*http://skyserver.sdss.org/dr16/en/tools/explore/

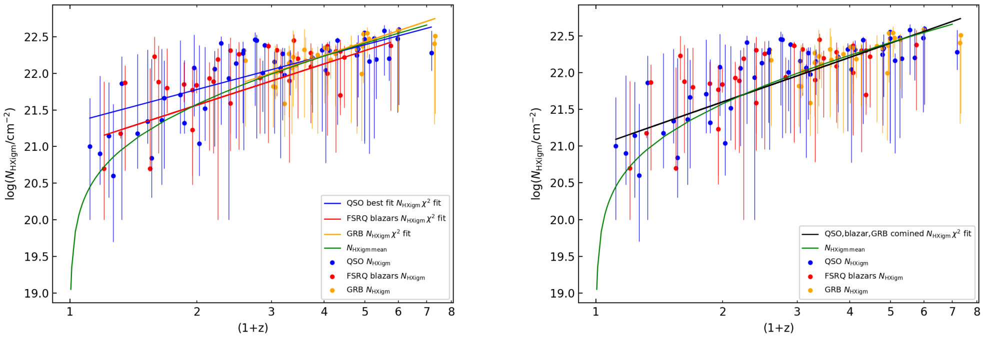

Figure 5.9: NHXIGM versus redshift for the full QSO sample (blue) combined with the FSRQ blazars from D21b (red) and the GRBs (yellow) from D21a. In the left panel, each tracer group has its own χ^2 line fit. The green line is the simple IGM model using a mean IGM density of $n_0 = 1.7 \times 10^{-7}$ cm^{-3} at $z = 0$ (see eq.5.1). In the right panel,the χ^2 line fit is for the entire tracer samples.

and spectral counts, intervening DLA and lensing galaxies. We note that the use of a log-parabolic power law may be showing an improved fit over a simple power law in all our QSO sample as either an intrinsic continuum feature, or or a slight signature of the reflection hump and soft excess. As for luminosity, in the next section we compare our QSO results with our previous GRB and blazar results to see if there are consistencies which would help rule out the luminosity degeneracy.

5.7 Combined QSO, GRB and blazar sample analysis

In this section, we bring together the results from our full series of papers on using different tracers to probe the IGM parameters of column density, temperature and metallicity. Given the differences in the tracer host environment, we adopted different approaches in estimating any host absorption.

In D20 and D21a, we assumed that the GRB host intrinsic hydrogen column density was equal to the UV measured ionisation-corrected intrinsic neutral column, using more realistic host galaxy metallicities, dust corrected where available. In D21b, we used blazars. For these tracers, we assumed no host absorption, relying on the fact that blazars are thought to have negligible X-ray absorption on the LOS within

Table 5.4: Summary results for the IGM parameters from the QSO, blazar and GRB samples from D21a and D21b, and this paper. The IGM parameters include the mean hydrogen density at $z = 0$ n_0 for the full redshift range and for $z > 1.6$, a power law fit to the *N*HXIGM versus redshift, mean temperature and metallicities, and the ranges.

Tracer	QSO	Blazar	GRB	All
		mean hydrogen density at $z = 0$ ($\times 10^{-7}$ cm^{-3})		
Full redshift range	2.8 ± 0.3	3.2 ± 0.5	1.8 ± 0.2	
$z > 1.6$	2.1 ± 0.3	2.1 ± 0.2	1.8 ± 0.2	2.0 ± 0.4
		power law fit to the *N*HXIGM versus redshift		
Slope index	1.5 ± 0.2	1.8 ± 0.2	1.9 ± 0.2	2.0 ± 0.1
		Temperature ($\log(T/K)$)		
Mean	6.5 ± 0.1	6.1 ± 0.1	6.3 ± 0.2	6.3 ± 0.3
Range	4.9 – 8.0	5.0 – 8.0	5.0 – 7.1	
		Metallicity [X/H]		
Mean	-1.3 ± 0.1	-1.6 ± 0.0	-1.8 ± 0.1	-1.5 ± 0.1
Range	−2.85 to −0.8	−3.0 to −0.08	−1.75 to −1.0	

the host galaxy, swept by the kpc-scale relativistic jet. Finally, in this paper using QSOs, as set out in Section 5.4, we assume a CGM model absorption. Apart from these differences in modelling the host absorption, all other methods and models are consistently used for the three tracers.

In Fig. 5.9, we plot the combined tracer samples for *N*HXIGM and redshift. In the left panel, the linear χ^2 fits are shown separately for each tracer. Though there are differences in the linear slopes, all three are reasonably close to the simple IGM curve. In the right panel, we show the combined tracer χ^2 linear fit. This fit is also close to the simple IGM curve. In Table 6.1, we give the main IGM parameter results from each tracer and in combination including the mean hydrogen density at $z = 0$ for the full redshift range and for $z > 1.6$ (our lowest GRB redshift), a power law fit to the *N*HXIGM versus redshift, mean temperature and metallicities, and the ranges.

The first IGM parameter, the mean hydrogen density at $z = 0$ is given for the full redshift range and also for our tracers with $z > 1.6$. Our GRB sample in D21a took $N_{\mathrm{H\ I}}$ data from Tanvir et al. (2019b) who had a cutoff at $z = 1.6$, as below this redshift, the observed Lyα transmission declines due to Earth's atmosphere. All of the values for n_0 are slightly higher than the simple IGM curve based on n_0 equal to 1.7×10^{-7} cm^{-3} (see Section 5.5). The overall mean across the three tracers for $z > 1.6$ is $2.0 \pm 0.4 \times 10^{-7}$ cm^{-3} which is consistent with the assumed density of the plotted IGM curve within the errors.

Assuming CIE, the mean IGM temperature across the tracers is $\log(T/K) = 6.3 \pm 0.3$ with a full range from 4.9 to 8.0. The mean IGM metallicity across the tracers is $[X/\mathrm{H}] = -1.5 \pm 0.1$ with a full range from -3.0 to -0.08. These values are consistent with the CIE predictions for a warm/hot IGM. There is no evidence for evolution or relation of temperature with redshift.

5.8 Discussion and comparison with other studies

Our work has found significant absorption in QSO spectra, in excess of that of our Galaxy and the QSO host. Excess X-ray absorption in QSOs has been reported in earlier studies, predominantly in RLQ rather than RQQ (e.g. Elvis et al., 1994b; Page et al., 2005; Reeves and Turner, 2000). Initial possible explanations included the absorption being related to the jet, which was thought to be responsible for the Doppler boosting of the X-ray continuum (e.g. Reeves and Turner, 2000). Most of these studies found the absorption tended to increase with QSO redshift. This would not support the jet absorption theory as the QSO jet luminosity was not found to increase with redshift (Scott et al., 2011). Eitan and Behar (2013) found that the optical depth increased with redshift for a sample of QSOs and GRBs, scaling as $(1+z)^{2.2\pm0.6}$. This is very close to our combined tracer result for N_{HXIGM} of $(1+z)^{2.0\pm0.1}$. Eitan and Behar (2013) postulated that their result could be explained by an ionised and clumpy IGM at $z < 2$, and a diffuse, cold IGM at higher redshift. This scenario was improved on by Starling et al. (2013), who used a warm-hot absorber scenario for the IGM. Starling et al. (2013) concluded that their warm-hot IGM scenario could account for most of their estimated X-ray column density for GRB at $z > 3$ for IGM parameters $\log(T/K) = 5 - 6$ and $Z/Z_\odot < 0.2$. The main differences and caveats on the results of Eitan and Behar (2013) and Starling et al. (2013), are that they used the conventional assumption that all excess absorption is at the host redshift, despite dealing with IGM absorption on the LOS . Further, while Eitan and Behar (2013) measured optical depth, Starling et al. (2013) used ABSORI which was compared with HOTABS for CIE modelling by D21a. Although ABSORI was the main XSPEC model used since it was developed in 1992, it is not self-consistent, and is limited to 10 metals fixed at solar metallicity except Fe (Done et al., 1992). D21a found HOTABS to be superior for modelling a CIE IGM.

Campana et al. (2015) examined intervening IGM absorption to AGN and GRBs using simulations. For GRBs, they reported $\log(T/\mathrm{K}) \sim 5 - 7$ and mean metallicity $Z = 0.03 Z_\odot$. In Section 5.7, we showed that our results across all our tracers, QSOs, blazars and GRBs are consistent for the IGM parameters. Our overall mean temperature and range for the IGM is $\log(T/\mathrm{K}) = 6.5 \pm 0.1$, and $4.9 < \log(T/\mathrm{K}) < 8.0$. Our mean metallicity and range on solar units is $0.05 Z_\odot$ and $0.16 Z_\odot$ to $0.001 Z_\odot$. These values are similar to Campana et al. (2015).

Arcodia et al. (2018, hereafter A18) used a blazar sample to investigate an IGM absorption scenario. Their IGM parameter results gave an average density ($z = 0$) of $n_0 = 1.0^{+0.53}_{-0.72} \times 10^{-7}$ cm^{-3} and temperature $\log(T/\mathrm{K}) = 6.45^{+0.51}_{-2.12}$. The temperature is very close to our results. Our average density at $z = 0$ across all tracers, limiting the sample to $z > 1.6$ to accommodate the GRBs, is $n_0 = 2.0 \pm 0.40 \times 10^{-7}$ cm^{-3}. A18's n_0 is less than the conventional simple IGM model of $n_0 = 1.7 \times 10^{-7}$ cm^{-3} (see Section 5.5). However, we do note that in our Fig. 5.9, some of the highest redshift tracers show NHXIGM, with equivalent n_0 at $z = 0$ below the simple IGM curve assumption. A18's lower result could be explained by their use of conventional assumptions of neutral and solar absorption in the IGM and their use of an older ABSORI based model. Alternatively, our combined results may indicate that a single uniform average density is over-simplistic across the full redshift range. The result is based on the homogeneity assumption and expansion of the Universe in the ΛCDM model. However, this does not factor in the structural changes and growth which are predicted to occur over redshift. For example, the fraction of matter in the IGM is expected to be much greater at higher redshift than lower redshift, as less matter had coalesced into galaxies and clusters (McQuinn, 2016).

One of our assumptions is that of CIE. The relation between ionisation state and plasma temperature explicitly assumes that the gas is in an ionisation equilibrium (Richter et al., 2008). Opinions on the IGM equilibrium state have differed over the years (e.g. Branchini et al., 2009; Nicastro et al., 2018). In non-equilibrium conditions, plasma remains over-ionised at any temperature, when compared to equilibrium, as recombination lags behind cooling (Gnat and Sternberg, 2007). There is ongoing debate on the equilibrium state of the WHIM, but it is likely that a substantial part of the baryons in the Universe are in regions where extremely low densities and ionisation equilibrium conditions persist (McQuinn, 2016). The equilibrium assumption may result in an underestimation of column density where the IGM gas remains over ionised in non-equilibrium conditions (D21a and references therein).

Generally, the fraction of RLQ to RQQ is $5 - 10\%$ and is possibly anti-correlated with redshift (Rusinek-Abarca and Sikora, 2021, and references therein). As RLQ tend to have far greater X-ray luminosity than RQQ, they are more frequently observed at higher redshift (Worrall et al., 1987; Page et al., 2005). In our study the fraction of RLQ is $\sim 40\%$ reflecting the X-ray loudness bias due to our higher redshift range and choice of QSOs with high counts. However, if we look at the sample below $z < 3$ in Fig. 5.2 where the RQQ are dominant, and the RLQ fraction is $\sim 26\%$, the redshift relation is still very clear indicating that the luminosity or high redshift RLQ bias is not driving the absorption redshift relation. A further point is that all of these prior studies make the same conventional assumptions of excess absorption being at the QSO redshift, and a neutral and solar metallicity absorber. Our analysis attempts to isolate any IGM absorption by using more realistic assumptions about the QSO host environment and then assuming the IGM absorption occurs in an isotropic, homogeneous intervening medium which is in CIE. We acknowledge that this is still a simplistic assumption but is appropriate given the X-ray resolution available. For example, Campana et al. (2015) using simulations of LOS to AGN, found a dominant contribution of absorption systems with large over-densities ($\Delta > 300$) at $z \sim 0.5 - 1.2$. However, they acknowledged that these absorbing systems may be proximate to the AGN and not common to all IGM tracers. This would be consistent with studies of neutral hydrogen systems in the CGM (e.g. Hennawi and Prochaska, 2013; Prochaska et al., 2013; Tumlinson et al., 2013; Lusso et al., 2018; Fumagalli et al., 2020).

It is possible that some additional absorption occurs in the QSO host over and above our assumed CGM amount i.e. intrinsic dust or gas in the host galaxy interstellar medium. Alternatively, absorption could occur in the inter-cluster medium as many QSOs are located in galaxy clusters (Elvis et al., 1994a). However, higher absorption if related to neutral gas would result in higher dust measurements which are not observed (Page et al., 2005).

Significant curvature is present in the spectra of many low redshift QSOs, below $z < 1$. This fact, or that absorption features are not observed in such low redshift tracers has been used as an argument against IGM absorption (Watson and Jakobsson, 2012, and references therein). From this, they concluded that at all redshifts, the spectral flattening is due to intrinsic curvature. In our QSO sample, many of the lowest redshift QSOs closely follow the simple IGM curve. We would argue that it is highly likely that spectral curvature is due to a combination of both intrinsic factors as well as IGM absorption, with the former dominant at low redshift, and the latter becoming dominant at higher redshift.

Comparing with an alternative tracer type, Macquart et al. (2020) used Fast Radio Burst (FRB) dispersion measure (DM) to measure the total electron column density on the LOS to the FRB host. Their sample is limited the redshift range 0.12 to 0.52, and just 5 FRB. They fix the Galactic DM to values measured by Cordes and Lazio (2002) with an additional 50 pc cm^{-3} to represent the Galactic halo. They assumed a fixed FRB host at $\mathrm{DM}_{host} = 50/(1+z)$ pc cm $^{-3}$. This is the standard approach in

FRB, i.e. to fix the FRB host DM with the assumption that all excess DM is then due to the IGM, similar to our approach. This is very different to the conventional QSO, blazar, GRB approach of assuming all absorption in excess of our Galaxy is at the host redshift. Their resulting baryon fraction is a median value of $\Omega_b h_{70} = 0.056$ (68% confidence interval $[0.046, 0.066]$). Based on this measurement, they conclude that their results are consistent with all the missing baryons being present in the ionised intergalactic medium. Our median value for the baryon fraction for all our tracers with $z > 1.6$ is $\Omega_b h_{70} = 0.048$ (68% confidence interval $[0.039, 0.058]$ (derived from $n_0 = 2.0 \pm 0.4 \times 10^{-7}$ cm^{-3}). For our full QSO sample only, the $\Omega_b h_{70} = 0.068$, (68% confidence interval $[0.061, 0.075]$). These values are consistent with Macquart et al. (2020).

A final observation on our results is that at highest redshifts $z > 3$ in Fig.5.9, while the numbers of tracers fall rapidly, some appear to have NHXIGM and error bars below the simple IGM curve. When plotting their distance modulus estimates versus redshift, Lusso et al. (2020) noted a deviation from the ΛCDM model appeared at higher redshift i.e. the distance modulus was lower than that predicted under the ΛCDM model at $z \geq 1.5$. They considered the explanation for the deviation as the possible evolution of the dark energy equation of state with the dark energy density increasing with time. In our simple IGM model, we calculate NHXIGM using the density at $z = 0$ and integrate over the redshift, which is based on eq.5.1. XSPEC performs a similar calculation using the redshift integral deriving column density from opacity. Though this redshift integral uses proper distance, while Lusso et al. (2020) use luminosity distance, if the distance is found to be lower than the ΛCDM model, then it may explain why the QSOs NHXIGM is below the simple IGM curve at higher redshift.

Alternatively, it could be due to an increasing influence of the Epoch of Reionisation (EoR) at the very highest redshifts. The EoR is considered to lie in the redshift range $\sim 6 - 10$ (see Bolan et al., 2021, and references therein, for a good sumary). If the Universe does indeed become more neutral at higher redshift, then there would be less highly ionised IGM for X-ray absorption. However, most research places the end of EoR at $z = 5 - 6$ and so would only affect the few tracers in our samples at this redshift or higher.

5.9 Conclusion

We used QSOs as tracers of the IGM with the main aim to probe the key parameters of column density, metallicity and temperature using a model for collisionally ionised plasma. We isolated the IGM LOS contribution to the total absorption for the QSOs by assuming that the QSO host absorption is based on a fixed model of CGM absorption. We used XSPEC fitting with both the CIE IGM component and all power law parameters free to vary. Our work uses the continuum total absorption to model plasma as opposed to fitting individual absorption features as the required resolution is not available currently in X-ray.

We subjected our results to a number of robustness tests covering: a relation between column density and flux; investigating spectral slope degeneracy with column density; reflection hump and soft excess impacts; luminosity column density relation, and any impact of large absorbers known of UV studies on the LOS.

Finally, we combined our sample with the blazar sample from D21b and the GRB sample from D21a to report results for an extended redshift range using the three different types of tracers.

Our main findings and conclusions are:

1. Our results for the IGM parameters are consistent across the three tracer types. The average results across the tracers for equivalent mean hydrogen density at $z = 0$ are $n_0 = 2.0 \pm 0.4 \times 10^{-7}$ cm^{-3} for $z > 1.6$. It shows similar values and correlation with redshift as the simple mean IGM density model, Fig. 5.9, right panel. A power law fit to the NHXIGM versus redshift scales as $(1 + z)^{2.0 \pm 0.1}$.

2. For our QSO sample for this paper, the equivalent mean hydrogen density at $z = 0$ is $n_0 = 2.8 \pm 0.3 \times 10^{-7}$ cm^{-3}. A power law fit to the NHXIGM versus redshift trend scales as $(1 + z)^{1.5\pm0.2}$.

3. The mean temperature across all the tracers for the CIE IGM is $\log(T/K) = 6.3 \pm 0.3$ with a full range from 4.9 to 8.0. The mean metallicity across the tracers for the CIE IGM is $[X/\mathrm{H}] = -1.5 \pm 0.1$ with a full range from -3.0 to -0.08. These values are consistent with the CIE predictions for a warm/hot IGM. There is no evidence for evolution with redshift.

4. The mean temperature across our QSOs only sample from this paper for the CIE IGM is $\log(T/K) = 6.5 \pm 0.1$ with a full range from 4.9 to 8.0. The mean metalicity across the QSO sample for the CIE IGM is $[X/\mathrm{H}] = -1.3 \pm 0.1$ with a full range from -2.9 to -0.8. These values are also consistent with the CIE predictions for a warm/hot IGM, and there is no evidence for evolution with redshift.

5. For the QSO sample, there is no obvious relation between NHXIGM and the robustness tested parameters for continuum power law index or spectral counts. Further, the possible effects of the reflection hump and soft excess were shown not to impact the results for NHXIGM, and only improved the fit for the two lowest redshift QSOs. There was insufficient evidence for DLAs or intervening lens systems on the LOS to account for the measured NHXIGM for the QSOs. Finally, there is an apparent NHXIGM luminosity relation due luminosity bias in our sample, which is due to our sample selection for high counts and the dominance of RLQ at $z > 3$, which are more X-ray luminous than RQQ. Both NHXIGM and luminosity rise with redshift. However, the results for NHXIGM are consistent across all three tracers and this would support the argument that the QSO result for NHXIGM is not dominated or caused by luminosity.

Overall in this series of papers D20, D21a and D21b, and this paper, we have demonstrated a consistent case for strong absorption in the IGM on the LOS to three different tracer types, QSOs, blazars and GRBs. We have taken a careful approach to isolating absorption by our Galaxy and and the tracer host, by examining the differing host environment conditions known to exist for the tracer types. We have also examined the possible contribution on the LOS due to large absorbers from UV QSO studies and have subjected our results to a series of robustness tests.

As we have demonstrated that there is substantial absorption in the IGM and it is related to redshift, using the conventional assumption that all excess absorption is in the tracer host, while investigating high redshift objects could lead to errors in deriving their properties including intrinsic absorption. Our results could also be used to test cosmological models through observations of IGM properties from these high redshift tracers. Our estimated IGM properties will be improved by instruments such as Athena, with higher energy resolution, lower energy threshold and larger effective areas in soft X-ray energies.

Acknowledgements

We would like to thank E. Lusso for making available the data from the SDSS DR14 and 4*XMM-Newton*-DR9 cross-correlation dataset, and E. Nardini for advice on using PEXRAV and ZBBODY for QSOs. This work made use of data supplied by *XMM–Newton*, an ESA science mission with instruments and contributions directly funded by ESA member states and NASA. S.L. Morris acknowledges support from STFC (ST/P000541/1). This project has received funding from the European Research Council (ERC) under the European Union's Horizon 2020 research and innovation programme (grant agreement No 757535) and by Fondazione Cariplo (grant No 2018-2329).

Data Availability

Data including spectra fit plots for all the QSO sample, and MCMC integrated probability plots are available on request - please contact Tony Dalton. The reduced *XMM-Newton* spectral files are available by contacting Efrain Gatuzz. *XMM-Newton* EPIC spectra data is available at http://xmm-catalog.irap.omp.eu/sources. SDSS data is available at http://skyserver.sdss.org/dr17.

5.10 Appendix - Chapter 5

Table 5.5: Full IGM model fitting results for the SDSS-DR14 and *4XMM-Newton-DR9* cross-correlation QSO sample. For each QSO, the columns give the name, redshift, IGM paramaters: NHXIGM, [X/H], temperature; Continuum log parabolic power law and curvature parameter β; Cstat/dof

QSO	z	$\log(\frac{N_{\rm HXIGM}}{\rm cm^{-2}})$	[X/H]	$\log(\frac{\rm T}{K})$	PO	β	Cstat/dof
J142952+544717	6.18	$22.28^{+0.30}_{-0.24}$	$-1.48^{+0.46}_{-0.44}$	$5.72^{+0.78}_{-0.39}$	$2.67^{+0.25}_{-0.26}$	$-0.96^{+1.42}_{-0.02}$	483.20/1940
022112.62-034252.2	5.01	$22.60^{+0.04}_{-1.03}$	$-1.14^{+0.11}_{-0.75}$	$7.91^{+0.04}_{-2.67}$	$2.13^{+0.37}_{-0.42}$	$0.94^{+0.00}_{-1.65}$	110.04/1940
001115.23+144601.8	4.96	$22.47^{+0.12}_{-1.01}$	$-1.06^{+0.17}_{-1.34}$	$7.98^{+0.00}_{-2.78}$	$1.51^{+0.88}_{-0.01}$	$0.64^{+0.22}_{-0.29}$	639.73/1940
143023.73+420436.5	4.71	$22.20^{+0.40}_{-0.31}$	$-1.75^{+0.90}_{-1.65}$	$5.00^{+0.40}_{-0.33}$	$1.84^{+0.14}_{-0.06}$	$-0.22^{+0.11}_{-0.14}$	1604.58/1940
223953.6-055220.0	4.56	$22.58^{+0.08}_{-0.61}$	$-0.84^{+0.12}_{-0.95}$	$7.98^{+0.01}_{-1.48}$	$1.83^{+0.63}_{-0.23}$	$-0.22^{+1.42}_{-0.02}$	483.20/1940
151002.93+570243.3	4.31	$22.19^{+0.25}_{-0.54}$	$-1.42^{+0.42}_{-1.10}$	$5.96^{+0.44}_{-1.71}$	$2.00^{+0.23}_{-0.31}$	$-0.59^{+0.41}_{-0.30}$	621.21/1940
133529.45+410125.9	4.26	$22.48^{+0.01}_{-1.37}$	$-0.93^{+0.18}_{-1.38}$	$7.54^{+0.12}_{-1.64}$	$1.61^{+0.62}_{-0.12}$	$0.15^{+0.28}_{-0.76}$	334.92/1940
132611.84+074358.3	4.12	$22.16^{+0.10}_{-1.26}$	$-1.30^{+0.54}_{-1.00}$	$6.88^{+1.04}_{-2.39}$	$2.06^{+0.32}_{-0.21}$	$-0.34^{+0.47}_{-0.34}$	352.29/1940
163950.52+434003.7	3.99	$22.55^{+0.03}_{-1.47}$	$-1.12^{+0.39}_{-0.93}$	$6.96^{+0.95}_{-2.08}$	$1.75^{+0.35}_{-0.06}$	$-0.09^{+0.45}_{-0.03}$	436.57/1940
021429.29-051744.8	3.98	$22.46^{+0.02}_{-1.42}$	$-1.62^{+0.87}_{-0.60}$	$7.36^{+0.57}_{-2.23}$	$2.19^{+0.18}_{-0.15}$	$-0.25^{+0.47}_{-0.38}$	516.95/1940
133223.26+503431.3	3.81	$22.34^{+0.19}_{-0.66}$	$-1.48^{+0.39}_{-0.26}$	$6.62^{+1.21}_{-0.71}$	$2.17^{+0.19}_{-0.78}$	$-0.50^{+1.00}_{-0.50}$	240.41/1940
200324.1-325144.0	3.78	$22.32^{+0.10}_{-1.04}$	$-1.32^{+0.59}_{-0.78}$	$6.90^{+1.04}_{-1.84}$	$1.94^{+0.06}_{-0.33}$	$-0.08^{+0.36}_{-0.07}$	757.08/1940
200324.1-135245.1	3.77	$22.25^{+0.18}_{-0.88}$	$-1.03^{+0.30}_{-1.19}$	$7.02^{+0.90}_{-1.30}$	$1.80^{+0.06}_{-0.18}$	$0.05^{+0.19}_{-0.08}$	735.85/1940
122135.6+280614.0	3.31	$22.45^{+0.04}_{-1.15}$	$-1.15^{+0.43}_{-0.77}$	$7.95^{+0.02}_{-2.70}$	$1.26^{+0.21}_{-0.07}$	$0.18^{+0.16}_{-0.18}$	843.48/1940
042214.8-384453.0	3.11	$22.31^{+0.13}_{-0.06}$	$-1.09^{+0.37}_{-0.63}$	$7.00^{+0.46}_{-1.20}$	$2.17^{+0.20}_{-0.32}$	$-0.12^{+0.37}_{-0.32}$	527.00/1940
083910.89+200207.3	3.03	$22.05^{+0.34}_{-1.27}$	$-1.00^{+0.28}_{-1.00}$	$6.40^{+1.45}_{-1.92}$	$1.60^{+0.03}_{-0.38}$	$-0.32^{+0.39}_{-0.06}$	1048.72/1940
111038.64+483115.6	2.96	$22.32^{+0.09}_{-1.11}$	$-1.31^{+0.59}_{-0.61}$	$6.65^{+1.18}_{-0.69}$	$2.50^{+0.11}_{-0.61}$	$-0.45^{+0.70}_{-0.27}$	333.61/1940
122307.52+103448.2	2.75	$22.22^{+0.05}_{-0.75}$	$-1.34^{+0.58}_{-0.89}$	$6.28^{+1.61}_{-0.68}$	$2.69^{+0.18}_{-0.90}$	$-0.79^{+1.27}_{-0.07}$	261.18/1940
115005.36+013850.7	2.33	$22.15^{+0.17}_{-0.45}$	$-1.04^{+0.29}_{-0.82}$	$6.76^{+1.10}_{-1.65}$	$3.58^{+0.39}_{-0.50}$	$-2.02^{+1.07}_{-0.65}$	316.75/1940
121423.02+024252.8	2.22	$21.98^{+0.37}_{-0.58}$	$-2.70^{+1.13}_{-0.30}$	$4.98^{+0.29}_{-0.13}$	$2.09^{+0.18}_{-0.14}$	$-0.48^{+0.21}_{-0.28}$	1256.46/1940
112338.14+052038.5	2.18	$22.27^{+0.08}_{-0.91}$	$-1.30^{+0.38}_{-0.70}$	$6.96^{+0.70}_{-1.09}$	$2.09^{+0.46}_{-0.38}$	$-0.27^{+0.48}_{-0.52}$	415.64/1940
123527.36+392824.0	2.16	$22.07^{+0.05}_{-1.22}$	$-1.13^{+0.40}_{-0.76}$	$5.38^{+0.94}_{-1.16}$	$2.67^{+0.21}_{-0.69}$	$-0.91^{+1.03}_{-0.24}$	270.33/1940
134740.99+581242.2	2.05	$22.16^{+0.14}_{-0.98}$	$-1.19^{+0.41}_{-0.73}$	$6.63^{+1.17}_{-0.38}$	$2.17^{+0.26}_{-0.21}$	$-0.23^{+0.16}_{-0.38}$	638.71/1940
095834.04+024427.1	1.89	$22.38^{+0.04}_{-1.21}$	$-1.54^{+0.76}_{-0.51}$	$7.11^{+0.73}_{-1.54}$	$2.27^{+0.33}_{-0.10}$	$-0.52^{+0.22}_{-0.47}$	500.15/1940
093359.34+551550.7	1.86	$22.04^{+0.17}_{-0.53}$	$-1.24^{+0.52}_{-0.43}$	$5.30^{+0.90}_{-0.45}$	$1.29^{+0.22}_{-0.07}$	$-1.00^{+0.00}_{-0.25}$	659.00 /1940
133526.73+405957.5	1.77	$22.45^{+0.08}_{-1.34}$	$-1.17^{+0.45}_{-0.79}$	$7.84^{+0.10}_{-1.42}$	$1.58^{+0.22}_{-0.12}$	$0.11^{+0.33}_{-0.28}$	303.33/1940
100434.91+411242.8	1.74	$22.46^{+0.10}_{-0.91}$	$-0.80^{+0.07}_{-1.60}$	$7.88^{+0.10}_{-1.42}$	$1.81^{+0.06}_{-0.09}$	$-0.07^{+0.21}_{-0.07}$	1002.61/1940
104039.54+061521.5	1.58	$22.31^{+0.02}_{-1.36}$	$-1.30^{+0.44}_{-0.40}$	$7.18^{+0.66}_{-1.62}$	$2.06^{+0.42}_{-0.12}$	$0.21^{+0.33}_{-0.73}$	360.88/1940
083205.95+524359.3	1.57	$22.28^{+0.16}_{-0.95}$	$-1.44^{+0.70}_{-1.56}$	$6.89^{+0.95}_{-1.37}$	$2.39^{+0.33}_{-0.26}$	$-0.28^{+0.49}_{-0.53}$	444.36/1940

Table 5.6: Table 5.5 continued

QSO	z	$\log(\frac{N_{\rm HXIGM}}{\rm cm^{-2}})$	$[X/{\rm H}]$	$\log(\frac{\rm T}{K})$	PO	β	Cstat/dof
112320.73+013747.4	1.47	$22.13^{+0.02}_{-1.02}$	$-1.23^{+0.02}_{-0.73}$	$6.52^{+0.24}_{-0.70}$	$1.08^{+0.24}_{-0.14}$	$1.12^{+0.51}_{-0.03}$	639.3/1940
091301.03+525928.9	1.38	$21.93^{+0.47}_{-1.93}$	$-0.90^{+0.18}_{-1.80}$	$7.10^{+0.82}_{-1.55}$	$2.02^{+0.09}_{-0.07}$	$-0.44^{+0.15}_{-0.17}$	595.67/1940
121426.52+140258.9	1.28	$22.41^{+0.10}_{-1.11}$	$-0.90^{+0.18}_{-1.25}$	$7.79^{+0.16}_{-0.90}$	$1.89^{+0.06}_{-0.06}$	$-0.21^{+0.17}_{-0.09}$	805.58/1940
105316.75+573550.8	1.21	$22.06^{+0.25}_{-1.06}$	$-1.20^{+0.44}_{-1.20}$	$7.00^{+0.94}_{-1.13}$	$2.19^{+0.06}_{-0.12}$	$-0.32^{+0.22}_{-0.20}$	588.84/1940
085808.91+274522.7	1.09	$21.52^{+0.84}_{-0.44}$	$-2.30^{+1.51}_{-0.70}$	$5.06^{+2.87}_{-0.04}$	$2.39^{+0.05}_{-0.17}$	$-0.33^{+0.34}_{-0.05}$	655.53/1940
095857.34+021314.5	1.02	$21.04^{+1..34}_{-0.44}$	$-1.07^{+0.33}_{-1.07}$	$5.58^{+2.35}_{-0.34}$	$2.04^{+0.13}_{-0.20}$	$-0.19^{+0.29}_{-0.19}$	553.17/1940
125849.83-014303.3	0.97	$22.08^{+0.45}_{-0.66}$	$-1.10^{+0.35}_{-0.90}$	$7.04^{+0.39}_{-0.20}$	$2.29^{+0.69}_{-0.06}$	$-0.23^{+0.10}_{-0.65}$	904.00/1940
082257.55+404149.7	0.87	$21.32^{+0.86}_{-0.15}$	$-0.91^{+0.17}_{-1.49}$	$5.04^{+2.84}_{-0.0}$	$2.51^{+0.07}_{-0.45}$	$-0.90^{+0.72}_{-0.05}$	365.24/1940
150431.30+474151.2	0.82	$21.71^{+0.74}_{-0.53}$	$-1.62^{+0.90}_{-0.48}$	$5.59^{+2.37}_{-0.00}$	$2.15^{+0.73}_{-0.19}$	$-0.11^{+0.44}_{-0.66}$	407.23/1940
111606.97+423645.4	0.67	$21.66^{+0.51}_{-0.96}$	$-1.13^{+0.36}_{-0.83}$	$5.84^{+1.90}_{-0.22}$	$1.94^{+0.06}_{-0.23}$	$-0.26^{+0.28}_{-0.08}$	680.82 /1940
130028.53+283010.1	0.65	$21.36^{+0.97}_{-0.89}$	$-1.00^{+0.27}_{-1.99}$	$6.88^{+1.07}_{-0.82}$	$1.96^{+0.04}_{-0.04}$	$-0.06^{+0.08}_{-0.10}$	971.87/1940
111135.76+482945.3	0.56	$20.85^{+1.35}_{-0.54}$	$-0.99^{+0.23}_{-1.17}$	$7.83^{+0.04}_{-2.44}$	$2.26^{+0.11}_{-0.04}$	$-0.12^{+0.13}_{-0.17}$	633.63/1940
091029.03+542719.0	0.53	$21.34^{+0.98}_{-0.30}$	$-1.72^{+0.96}_{-0.68}$	$5.07^{+2.80}_{-0.03}$	$2.61^{+0.08}_{-0.25}$	$-0.68^{+0.55}_{-0.04}$	599.13/1940
105224.94+441505.2	0.44	$21.18^{+1.09}_{-0.48}$	$-0.88^{+0.16}_{-1.08}$	$5.99^{+1.88}_{-0.49}$	$2.48^{+0.14}_{-0.19}$	$-0.40^{+0.44}_{-0.26}$	419.56/1940
223607.68+134355.3	0.33	$21.86^{+0.37}_{-1.87}$	$-0.84^{+0.12}_{-1.21}$	$6.89^{+0.95}_{-1.84}$	$2.69^{+0.19}_{-0.03}$	$-0.20^{+0.12}_{-0.45}$	510.23/1940
144645.93+403505.7	0.27	$20.60^{+0.98}_{-0.90}$	$-1.85^{+0.30}_{-1.85}$	$5.03^{+0.09}_{-0.01}$	$2.98^{+0.02}_{-0.10}$	$-0.71^{+0.19}_{-0.04}$	885.25/1940
123054.11+110011.2	0.24	$21.15^{+0.73}_{-0.85}$	$-2.52^{+1.03}_{-0.48}$	$5.07^{+0.13}_{-0.04}$	$2.57^{+0.17}_{-0.07}$	$-0.59^{+0.14}_{-0.07}$	679.62/1940
103059.09+310255.8	0.18	$20.90^{+1.06}_{-0.43}$	$-2.80^{+0.82}_{-0.16}$	$5.06^{+0.14}_{-0.01}$	$2.28^{+0.05}_{-0.06}$	$-0.53^{+0.08}_{-0.06}$	1514.88/1940
141700.81+445606.3	0.11	$21.00^{+0.66}_{-1.00}$	$-2.85^{+0.87}_{-0.15}$	$5.09^{+0.06}_{-0.03}$	$2.70^{+0.04}_{-0.07}$	$-0.57^{+0.10}_{-0.07}$	1216.11/1940

CHAPTER 6

Conclusion

6.1 Summary conclusions

In this thesis, I have used GRBs, blazars and QSOs as X-ray tracers of the IGM with the main aim to probe the key parameters of column density, metallicity and temperature using a model for collisionally ionised plasma. For GRBs, I also used a model for photoionised plasma which produced very similar results to the CIE model. I isolated the potential IGM absorption from the total continuum absorption by exploring different tracer host absorption models, as well as known Galactic absorption. I completed robustness tests to investigate other possible causes for the observed spectral curvature that may be degenerate with IGM absorption. For the QSO, I have examined the possible contribution on the LOS due to large absorbers from UV QSO studies and examining SDSS spectra.

The specific results for the IGM column density, temperature and metallicity from each tracer type are contained in Chapters 3, 4 and 5. Chapter 5.7 also gives the combined results which were found to be consistent across the different tracers (See Fig 5.9 for combined GRB, blazar and QSO samples NHXIGM vs. redshift plot). I have reproduced here, Table 6.1 from Chapter 5 for convenience which is a summary of IGM parameter results for each of the tracers as well as combined results. For n_0, I used the results for NHXIGM and actual redshift for the tracers to get their

Table 6.1: Summary results for the IGM parameters from the QSO, blazar and GRB samples from D21a and D21b, and this paper. The IGM parameters include the mean hydrogen density at $z = 0$ n_0 for the full redshift range and for $z > 1.6$, a power law fit to the *N*HXIGM versus redshift, mean temperature and metallicities, and the ranges.

Tracer	QSO	Blazar	GRB	All
mean hydrogen density at $z = 0$ ($\times 10^{-7}$ cm^{-3})				
Full redshift range	2.8 ± 0.3	3.2 ± 0.5	1.8 ± 0.2	
$z > 1.6$	2.1 ± 0.3	2.1 ± 0.2	1.8 ± 0.2	2.0 ± 0.4
power law fit to the *N*HXIGM versus redshift				
Slope index	1.5 ± 0.2	1.8 ± 0.2	1.9 ± 0.2	2.0 ± 0.1
Temperature ($\log(T/K)$)				
Mean	6.5 ± 0.1	6.1 ± 0.1	6.3 ± 0.2	6.3 ± 0.3
Range	$4.9 - 8.0$	$5.0 - 8.0$	$5.0 - 7.1$	
Metallicity [X/H]				
Mean	-1.3 ± 0.1	-1.6 ± 0.0	-1.8 ± 0.1	-1.5 ± 0.1
Range	-2.85 to -0.8	-3.0 to -0.08	-1.75 to -1.0	

equivalent n_0 which are are derived by rearranging equation 5.1 in Chapter 5 to give n_0. I then took the mean of n_0 for the full sample and calculated the standard error.

In summary, I have demonstrated a consistent case for strong absorption in the IGM on the LOS to three different tracer types, QSOs, blazars and GRBs, and that it is related to redshift. The results are also consistent with the ΛCDM cosmological model in terms of predicted baryonic content.

Given these results, I would recommend that studies of distant objects should not follow the convention of assuming all absorption in excess of that in our Galaxy is attributed to the host galaxy, that the host is neutral and has solar metallicity. Instead, particulary at higher redshift, absorption in the IGM should be included to give more accurate results for the tracer host properties.

6.2 Future work and related surveys

Further work on IGM absorption using other tracers should include FRB dispersion measure which gives the total electron column density on the LOS to the FRB host. I omitted these objects as, at the outset of this thesis in 2019, the total population was ~ 30, with only one localised repeating FRB which had a reliable redshift. As of now, the population is now over 600, with 24 repeaters and 14 with reliable redshift localised to host galaxies (Petroff et al., 2021). There are substantial efforts to increase this number e.g. CHIME (Newburgh et al., 2014; Pleunis et al., 2021; Amiri et al., 2021) and Australian Square Kilometre Array Pathfinder (ASKAP) (Macquart et al., 2010). FRBs can also yield valuable information on the CGM, foreground galaxy halos and the baryonic mass fraction in the IGM (e.g. Connor and Ravi, 2021; Simha et al., 2021; Dai and Xia, 2021). Therefore FRBs will prove to be very important IGM tracers.

Other techniques to study the IGM include using the stacked signal from the tSZ effect (e.g. Tanimura et al., 2020a) and the 21cm line, which is very important for studying the reionisation era as neutral hydrogen is abundant in the early Universe (e.g. Simcoe et al., 2020; Laporte et al., 2021; Villasenor et al., 2021).

Direct IGM observation of individual absorbers in X-ray is very limited but claims to have done so include Nicastro et al. (2018). With telescopes such as Athena, the proposed European Space Agency X-ray observatory (Walsh et al., 2020), far greater resolution and collecting area will be possible enabling absorption features in X-ray to be observed. Athena aims to study the IGM through detailed observations of O VII (E = 573 eV) and O VIII (E = 674 eV) absorption features. At lower redshifts, individual observations of IGM absorbers in the WHIM and LSS will be criticsl in parameterising IGM properties.

At very high redshifts, the recently launched James Web Space Telescope (JWST) will probe into the era of Reionisation. JWST will capture high-resolution images and multi-object spectroscopy in the infrared. In this thesis, I use tracers with redshifts up to $z \sim 6$. Moving to higher redshifts the impact of the reionisation era becomes increasingly important with the hydrogen ionisation fraction declining until the IGM becomes essentially neutral. In addition to surveying earliest galaxy formation and star formation rates, JWST will provide data on metallicities and ionisation at $z \sim 8$ and higher redshifts (Robertson, 2021, and references therein).

In X-ray then, we may expect that the observed relation noted in this thesis between column density and redshift will not hold for tracer objects located well into the reionisation epoch as the IGM becomes increasing neutral.

I hope my work will contribute to the study of IGM properties and look forward to continuing research into FRBs and using new data from CHIME, ASKAP and JSWT to name but a few.

Bibliography

A. Aguirre, L. Hernquist, J. Schaye, N. Katz, D. H. Weinberg, and J. Gardner. Metal Enrichment of the Intergalactic Medium in Cosmological Simulations. *ApJ*, 561(2):521–549, 2001. ISSN 0004-637X. doi: 10.1086/323370.

A. Aguirre, C. Dow-Hygelund, J. Schaye, and T. Theuns. Metallicity of the Intergalactic Medium Using Pixel Statistics. IV. Oxygen. *ApJ*, 689(2):851–864, 2008. ISSN 0004-637X. doi: 10.1086/592554.

M. Amiri, B. C. Andersen, K. Bandura, S. Berger, M. Bhardwaj, M. M. Boyce, P. J. Boyle, C. Brar, D. Breitman, T. Cassanelli, P. Chawla, T. Chen, A. Cook, D. Cubranic, A. P. Curtin, M. Deng, M. Dobbs, M. Fandino, E. Fonseca, B. M. Gaensler, U. Giri, D. C. Good, M. Halpern, A. S. Hill, G. Hinshaw, A. Josephy, J. F. Kaczmarek, Z. Kader, J. W. Kania, V. M. Kaspi, T. L. Landecker, D. Lang, C. Leung, D. Li, H.-h. Lin, K. W. Masui, R. Mckinven, J. Mena-parra, M. Merryfield, B. W. Meyers, D. Michilli, N. Milutinovic, A. Mirhosseini, A. Naidu, L. Newburgh, C. Ng, C. Patel, U.-l. Pen, T. Pinsonneault-marotte, Z. Pleunis, M. Rafiei-ravandi, M. Rahman, S. M. Ransom, A. Renard, P. Sanghavi, P. Scholz, J. R. Shaw, K. Shin, S. R. Siegel, A. E. Sikora, S. Singh, K. M. Smith, I. Stairs, C. M. Tan, S. P. Tendulkar, K. Vanderlinde, H. Wang, D. Wulf, and A. V. Zwaniga. The First CHIME/FRB Fast Radio Burst Catalog. *https://arxiv.org/abs/2106.04352*, 2021.

E. Anders and N. Grevesse. Abundances of the elements: Meteoritic and solar. *Geochimica et Cosmochimica Acta*, 53(1):197–214, 1989. ISSN 00167037. doi: 10.1016/0016-7037(89)90286-X.

M. Arabsalmani, P. Møller, D. A. Perley, W. Freudling, J. P. Fynbo, E. Le Floc'h, M. A. Zwaan, S. Schulze, N. R. Tanvir, L. Christensen, A. J. Levan, P. Jakobsson, D. Malesani, Z. Cano, S. Covino, V. D'Elia, P. Goldoni, A. Gomboc, K. E. Heintz, M. Sparre, A. de Ugarte Postigo, and S. D. Vergani. Mass and metallicity scaling relations of high-redshift star-forming galaxies selected by GRBs. *MNRAS*, 473 (3):3312–3324, 2018. ISSN 13652966. doi: 10.1093/mnras/stx2451.

R. Arcodia, S. Campana, and R. Salvaterra. The dependence of gamma-ray burst X-ray column densities on the model for Galactic hydrogen. *A&A*, 590:1–8, 2016. ISSN 14320746. doi: 10.1051/0004-6361/201628326.

R. Arcodia, S. Campana, R. Salvaterra, and G. Ghisellini. X-ray absorption towards high-redshift sources: probing the intergalactic medium with blazars. *A&A*, 616: A170, 2018. URL `http://arxiv.org/abs/1804.04668`.

K. Arnaud. XSPEC: The first ten years. *Astron. Data Anal. Softw. Syst.*, 101:17, 1996.

M. Asplund, N. Grevesse, A. J. Sauval, and P. Scott. The chemical composition of the Sun. *Annual Review of Astronomy and Astrophysics*, 47(481), 2009. ISSN 0004640X. doi: 10.1007/s10509-010-0288-z.

M. Asplund, A. M. Amarsi, and N. Grevesse. The chemical make-up of the Sun : A 2020 vision. *https://arxiv.org/abs/2105.01661*, 2021.

E. Behar, S. Dado, A. Dar, and A. Laor. Can the soft X-ray opacity toward high-redshift sources probe the missing baryons? *ApJ*, 734(1):26, 2011. ISSN 15384357. doi: 10.1088/0004-637X/734/1/26.

G. Bhatta, M. Mohorian, and I. Bilinsky. Hard X-ray properties of NuSTAR blazars. *A&A*, 619:1–19, 2018. ISSN 14320746. doi: 10.1051/0004-6361/201833628.

P. Bolan, B. C. Lemaux, C. Mason, M. Bradač, T. Treu, V. Strait, D. Pelliccia, L. Pentericci, and M. Malkan. Inferring the IGM Neutral Fraction at z ˜ 6-8 with Low-Luminosity Lyman Break Galaxies. *https://arxiv.org/abs/2111.14912*, 2021. URL `http://arxiv.org/abs/2111.14912`.

J. Bolmer, C. Ledoux, P. Wiseman, A. De Cia, J. Selsing, P. Schady, J. Greiner, S. Savaglio, J. M. Burgess, V. D'Elia, J. P. U. Fynbo, P. Goldoni, D. H. Hartmann, K. E. Heintz, P. Jakobsson, J. Japelj, L. Kaper, N. R. Tanvir, P. M. Vreeswijk, and T. Zafar. Evidence for diffuse molecular gas and dust in the hearts of gamma-ray burst host galaxies. *A&A*, 623:A43, 2019. ISSN 0004-6361. doi: 10.1051/0004-6361/201834422.

J. R. Bond, L. Kofman, and D. Pogosyan. How filaments of galaxies are woven into the cosmic web. *Nature*, 380(6575):603–606, 1996. ISSN 00280836. doi: 10.1038/380603a0.

E. Bottacini, M. Ajello, J. Greiner, E. Pian, A. Rau, E. Palazzi, S. Covino, G. Ghisellini, T. Krühler, A. Küpcü Yoldaş, N. Cappelluti, and P. Afonso. PKS 0537-286, carrying the information of the environment of SMBHs in the early universe. *A&A*, 509(1):1–8, 2010. ISSN 14320746. doi: 10.1051/0004-6361/200913260.

E. Branchini, E. Ursino, A. Corsi, D. Martizzi, L. Amati, J. W. Den Herder, M. Galeazzi, B. Gendre, J. Kaastra, L. Moscardini, F. Nicastro, T. Ohashi, F. Paerels, L. Piro, M. Roncarelli, Y. Takei, and M. Viel. Studying the warm hot intergalactic medium with gamma-ray bursts. *ApJ*, 697(1):328–344, 2009. ISSN 15384357. doi: 10.1088/0004-637X/697/1/328.

J. Buchner, A. Georgakakis, K. Nandra, L. Hsu, C. Rangel, M. Brightman, A. Merloni, M. Salvato, J. Donley, and D. Kocevski. X-ray spectral modelling of the AGN obscuring region in the CDFS: Bayesian model selection and catalogue. *A&A*, 564:1–25, 2014. ISSN 14320746. doi: 10.1051/0004-6361/201322971.

J. Buchner, S. Schulze, and F. E. Bauer. Galaxy gas as obscurer - I. GRBs x-ray galaxies and find an N H3 $\propto$ M * relation. *MNRAS*, 464(4):4545–4566, 2017. ISSN 13652966. doi: 10.1093/mnras/stw2423.

D. N. Burrows, J. E. Hill, J. A. Nousek, J. A. Kennea, A. Wells, J. P. Osborne, A. F. Abbey, A. Beardmore, K. Mukerjee, A. D. Short, G. Chincarini, S. Campana, O. Citterio, A. Moretti, C. Pagani, G. Tagliaferri, P. Giommi, M. Capalbi, F. Tamburelli, L. Angelini, G. Cusumano, H. W. Bräuninger, W. Burkert, and G. D. Hartner. The Swift X-ray telescope. *Space Science Reviews*, 120(3-4): 165–195, 2005. ISSN 00386308. doi: 10.1007/s11214-005-5097-2.

N. R. Butler, D. Kocevski, J. S. Bloom, and J. L. Curtis. A Complete Catalog of Swift Gamma-Ray Burst Spectra and Durations: Demise of a Physical Origin for Pre- Swift High-Energy Correlations . *ApJ*, 671(1):656–677, 2007. ISSN 0004-637X. doi: 10.1086/522492.

S. Campana, C. C. Thöne, A. de Ugarte Postigo, G. Tagliaferri, A. Moretti, and S. Covino. The X-ray absorbing column densities of Swift gamma-ray bursts. *MNRAS*, 402(4):2429–2435, 2010. ISSN 00358711. doi: 10.1111/j.1365-2966. 2009.16006.x.

S. Campana, R. Salvaterra, A. Melandri, S. D. Vergani, S. Covino, P. D'Avanzo, D. Fugazza, G. Ghisellini, B. Sbarufatti, and G. Tagliaferri. The X-ray absorbing column density of a complete sample of bright Swift gamma-ray bursts. *MNRAS*, 421(2):1697–1702, 2012. ISSN 00358711. doi: 10.1111/j.1365-2966.2012.20428.x.

S. Campana, M. G. Bernardini, V. Braito, G. Cusumano, P. D. Avanzo, V. D. Elia, G. Ghirlanda, G. Ghisellini, A. Melandri, R. Salvaterra, G. Tagliaferri, and S. D. Vergani. Effective absorbing column density in the gamma-ray burst afterglow X-ray spectra. *MNRAS*, 441(4):3634–3639, 2014a. doi: 10.1093/mnras/stu831.

S. Campana, M. G. Bernardini, V. Braito, G. Cusumano, P. D'avanzo, V. D'elia, G. Ghirlanda, G. Ghisellini, A. Melandri, R. Salvaterra, G. Tagliaferri, and S. D.

Vergani. Effective absorbing column density in the gamma-ray burst afterglow X-ray spectra. *MNRAS*, 441(4):3634–3639, 2014b. ISSN 13652966. doi: 10.1093/mnras/stu831.

S. Campana, R. Salvaterra, A. Ferrara, and A. Pallottini. Missing cosmic metals revealed by X-ray absorption towards distant sources. *A&A*, 575:A43, 2015. ISSN 0004-6361. doi: 10.1051/0004-6361/201425083. URL `http://arxiv.org/abs/1501.00913{%}0Ahttp://dx.doi.org/10.1051/0004-6361/201425083`.

S. Campana, D. Lazzati, R. Perna, M. Grazia Bernardini, and L. Nava. The variable absorption in the X-ray spectrum of GRB 190114C. *https://arxiv.org/abs/2103.05735*, 2021. ISSN 14320746. doi: 10.1051/0004-6361/202140439.

M. Cappi, M. Matsuoka, A. Comastri, W. Brinkmann, M. Elvis, G. Palumbo, and C. Vignali. Asca and rosat x-ray spectra of high-redshift radio-loud quasars. *ApJ*, 478(2):492, 1997.

R. F. Carswell, J. K. Webb, K. M. Lanzetta, J. A. Baldwin, A. J. Cooke, G. M. Williger, M. Rauch, M. J. Irwin, J. G. Robertson, and P. A. Shaver. The high-redshift deuterium abundance: the z= 3.086 absorption complex towards Q 0420 388. *MNRAS*, 278(2):506–518, 1996.

W. Cash. Parameter estimation in astronomy through application of the likelihood ratio. *ApJ*, 228:939, 1979. URL `???`

A. Celotti, G. Ghisellini, and A. C. Fabian. Bulk Comptonization spectra in blazars. *MNRAS*, 375(2):417–424, 2007. ISSN 00358711. doi: 10.1111/j.1365-2966.2006.11289.x.

R. Cen and j. p. Ostriker. Where are the baryons. *AJ*, 514:1–6, 1999.

R. Cen and J. P. Ostriker. Where Are the Baryons? II. Feedback Effects. *ApJ*, 650(2):560–572, 2006. ISSN 0004-637X. doi: 10.1086/506505.

B. Chen, X. Dai, C. S. Kochanek, G. Chartas, J. A. Blackburne, and C. W. Morgan. X-ray monitoring of gravitational lenses with Chandra. *ApJ*, 755(1), 2012. ISSN 15384357. doi: 10.1088/0004-637X/755/1/24.

M. Colless, G. Dalton, S. Maddox, W. Sutherland, P. Norberg, S. Cole, J. Bland-Hawthorn, T. Bridges, R. Cannon, C. Collins, W. Couch, N. Cross, K. Deeley, R. De Propris, S. P. Driver, G. Efstathiou, R. S. Ellis, C. S. Frenk, K. Glazebrook, C. Jackson, O. Lahav, I. Lewis, S. Lumsden, D. Madgwick, J. A. Peacock, B. A. Peterson, I. Price, M. Seaborne, and K. Taylor. The 2dF Galaxy Redshift Survey: Spectra and redshifts. *MNRAS*, 328(4):1039–1063, 2001. ISSN 00358711. doi: 10.1046/j.1365-8711.2001.04902.x.

J. S. Collinson, M. J. Ward, H. Landt, C. Done, M. Elvis, and J. C. McDowell. Reaching the peak of the quasar spectral energy distribution - II. Exploring the accretion disc, dusty torus and host galaxy. *MNRAS*, 465(1):358–382, 2017. ISSN 13652966. doi: 10.1093/mnras/stw2666.

J. M. Comerford, Z. Haiman, and J. Schaye. Constraining the Redshift z ∼ 6 Quasar Luminosity Function Using Gravitational Lensing . *ApJ*, 580(1):63–72, 2002. ISSN 0004-637X. doi: 10.1086/343116.

L. Connor and V. Ravi. A detection of circumgalactic gas with fast radio bursts. *https://arxiv.org/abs/2107.13692*, 2021. URL `http://arxiv.org/abs/2107.13692`.

J. M. Cordes and T. J. W. Lazio. NE2001.I. A New Model for the Galactic Distribution of Free Electrons and its Fluctuations. *arXiv preprint astro-ph/0207156*, 2002.

E. Costa, F. Frontera, J. Heise, M. Feroci, F. Fiore, M. Cinti, D. D. Fiume, L. Nicastro, M. Orlandini, E. Palazzi, and G. Zavattini. Discovery of an X-ray afterglow associated with the gamma-ray burst of 28 February 1997. *Nature*, 387(6635):783–785, 1997.

N. H. Crighton, J. F. Hennawi, R. A. Simcoe, K. L. Cooksey, M. T. Murphy, M. Fumagalli, J. Xavier Prochaska, and T. Shanks. Metal-enriched, subkiloparsec gas clumps in the circumgalactic medium of a faint z = 2.5 galaxy. *MNRAS*, 446 (1):18–37, 2015. ISSN 13652966. doi: 10.1093/mnras/stu2088.

J. Crummy, A. C. Fabian, L. Gallo, and R. R. Ross. An explanation for the soft X-ray excess in active galactic nuclei. *MNRAS*, 365(4):1067–1081, 2006. ISSN 00358711. doi: 10.1111/j.1365-2966.2005.09844.x.

A. Cucchiara, A. J. Levan, D. B. Fox, N. R. Tanvir, T. N. Ukwatta, E. Berger, T. Krühler, A. K. Yoldaş, X. F. Wu, K. Toma, J. Greiner, F. E. Olivares, A. Rowlinson, L. Amati, T. Sakamoto, K. Roth, A. Stephens, A. Fritz, J. P. Fynbo, J. Hjorth, D. Malesani, P. Jakobsson, K. Wiersema, P. T. O'Brien, A. M. Soderberg, R. J. Foley, A. S. Fruchter, J. Rhoads, R. E. Rutledge, B. P. Schmidt, M. A. Dopita, P. Podsiadlowski, R. Willingale, C. Wolf, S. R. Kulkarni, and P. D'Avanzo. A photometric redshift of z ~9.4 for GRB 090429B. *ApJ*, 736(1): 7, 2011. ISSN 15384357. doi: 10.1088/0004-637X/736/1/7.

A. Cucchiara, M. Fumagalli, M. Rafelski, D. Kocevski, J. X. Prochaska, R. J. Cooke, and G. D. Becker. Unveiling the secrets of metallicity and massive star formation using dlas along gamma-ray bursts. *ApJ*, 804(1):51, 2015. ISSN 15384357. doi: 10.1088/0004-637X/804/1/51.

J.-P. Dai and J.-Q. Xia. Reconstruction of Baryon Fraction in Intergalactic Medium through Dispersion Measurements of Fast Radio Bursts. *https://arxiv.org/abs/2103.08479*, 5(March):1–5, 2021. URL `http://arxiv.org/abs/2103.08479`.

T. Dalton and S. L. Morris. Using realistic host galaxy metallicities to improve the GRB X-ray equivalent total hydrogen column density and constrain the intergalactic medium density. *MNRAS*, 495(2):2342–2353, 2020. ISSN 0035-8711. doi: 10.1093/mnras/staa1321.

T. Dalton, S. L. Morris, and M. Fumagalli. Probing the physical properties of the intergalactic medium using gamma-ray bursts. *MNRAS*, 502(4):5981–5996, 2021a. ISSN 13652966. doi: 10.1093/mnras/stab335.

T. Dalton, S. L. Morris, M. Fumagalli, and E. Gatuzz. Probing the physical properties of the intergalactic medium using blazars. *MNRAS*, 508(2):1701, 2021b.

C. W. Danforth and J. M. Shull. The Low- z Intergalactic Medium. I. O vi Baryon Census . *ApJ*, 624(2):555–560, 2005. ISSN 0004-637X. doi: 10.1086/429285.

C. W. Danforth and J. M. Shull. THE LOW- z INTERGALACTIC MEDIUM . III . H i AND METAL ABSORBERS AT z $<$ 0 . 4. *ApJ*, 679(1):194, 2008.

C. W. Danforth, B. A. Keeney, E. M. Tilton, J. M. Shull, J. T. Stocke, M. Stevans, M. M. Pieri, B. D. Savage, K. France, D. Syphers, B. D. Smith, J. C. Green, C. Froning, S. V. Penton, and S. N. Osterman. AN HST / COS SURVEY OF THE LOW-REDSHIFT INTERGALACTIC MEDIUM . I . *ApJ*, 817(2): 111, 2016. ISSN 1538-4357. doi: 10.3847/0004-637X/817/2/111. URL `http://dx.doi.org/10.3847/0004-637X/817/2/111`.

S. Das, S. Mathur, A. Gupta, and Y. Krongold. The hot circumgalactic medium of the Milky Way: evidence for super-virial, virial, and sub-virial temperature, non-solar chemical composition, and non-thermal line broadening. *ApJ*, 918(2): 83, 2021. URL `http://arxiv.org/abs/2106.13243`.

R. Davé and B. D. Oppenheimer. The enrichment history of baryons in the Universe. *MNRAS*, 374(2):427–435, 2007. ISSN 00358711. doi: 10.1111/j.1365-2966.2006.11177.x.

A. De Cia. Metals and dust in the neutral ISM: The Galaxy, Magellanic Clouds, and damped Lyman-α absorbers. *A&A*, 613:2–5, 2018. ISSN 14320746. doi: 10.1051/0004-6361/201833034.

A. De Cia, C. Ledoux, S. Savaglio, P. Schady, and P. M. Vreeswijk. Dust-to-metal ratios in damped Lyman- α absorbers . *A&A*, 560:A88, 2013. ISSN 0004-6361. doi: 10.1051/0004-6361/201321834.

A. De Cia, C. Ledoux, P. Petitjean, and S. Savaglio. The cosmic evolution of dust-corrected metallicity in the neutral gas. *A&A*, 611:1–16, 2018. ISSN 14320746. doi: 10.1051/0004-6361/201731970.

A. De Graaff, Y. C. Cai, C. Heymans, and J. A. Peacock. Probing the missing baryons with the Sunyaev-Zel'dovich effect from filaments, 2019. ISSN 14320746.

A. De Luca and S. Molendi. The 2-8 keV cosmic X-ray background spectrum as observed with XMM-Newton. *A&A*, 419(3):837–848, 2004. ISSN 00046361. doi: 10.1051/0004-6361:20034421.

A. de Ugarte Postigo, C. C. Thöne, S. Martín, J. Japelj, A. J. Levan, M. J. Micha³owski, J. Selsing, D. A. Kann, S. Schulze, J. T. Palmerio, S. D. Vergani, N. R. Tanvir, K. Bensch, S. Covino, V. D'Elia, M. D. Pasquale, A. S. Fruchter, J. P. Fynbo, D. Hartmann, K. E. Heintz, A. J. Horst, L. Izzo, P. Jakobsson, K. C. Ng, D. A. Perley, A. Rossi, B. Sbarufatti, R. Salvaterra, R. Sánchez-Ramírez, D. Watson, and D. Xu. GRB190114C in the nuclear region of an interacting galaxy? A detailed host analysis using ALMA, HST and VLT. *A&A*, 633:A68, 2020.

D. Donato, R. M. Sambruna, and M. Gliozzi. Six years of BeppoSAX observations of blazars: A spectral catalog. *A&A*, 433(3):1163–1169, 2005. ISSN 00046361. doi: 10.1051/0004-6361:20034555.

C. Done. Observational characteristics of accretion onto black holes. *Accretion Processes In Astrophysics: XXI Canary Islands Winter School Of Astrophysics*, arXiv: 100:184–226, 2010. doi: 10.1017/CBO9781139343268.007.

C. Done, J. Mulchaey, R. Mushotzky, and K. Arnaud. An ionized accretion disk in Cygnus X-1. *ApJ*, 395:275, 1992.

C. Done, S. W. Davis, C. Jin, O. Blaes, and M. Ward. Intrinsic disc emission and the soft X-ray excess in active galactic nuclei. *MNRAS*, 420(3):1848–1860, 2012. ISSN 00358711. doi: 10.1111/j.1365-2966.2011.19779.x.

S. P. Driver, P. Norberg, I. K. Baldry, S. P. Bamford, A. M. Hopkins, J. Liske, J. Loveday, and J. A. Peacock. GAMA : towards a physical unde. *Astronomy and Geophysics*, 50(October), 2009.

A. Eitan and E. Behar. X-ray Absorption of High Redshift Quasars. *ApJ*, 774(1): 29, 2013.

M. Elvis, F. Fiore, B. Wilkes, J. McDowell, and J. Bechtold. Absorption in X-ray spectra of high-redshift quasars. *ApJ*, 422:60, 1994a. ISSN 0004-637X. doi: 10.1086/173703.

M. Elvis, B. Wilkes, J. McDowell, R. Green, J. Bechtold, S. Willner, M. Oey, E. Polomski, and R. Cutri. Atlas of quasar energy distributions. *The Astrophysical Journal Supplement Series.*, 1994b. ISSN 0067-0049. doi: 10.1086/312966.

M. Elvis, F. Fiore, P. Giommi, and P. Padovani. X-RAY SPECTRAL SURVEY OF WGACAT QUASARS. II. OPTICAL AND RADIO PROPERTIES OF QUASARS WITH LOW-ENERGY X-RAY CUTOFFS. *ApJ*, 492:91–97, 1998.

P. A. Evans, K. L. Page, J. P. Osborne, A. P. Beardmore, R. Willingale, D. N. Burrows, J. A. Kennea, M. Perri, M. Capalbi, G. Tagliaferri, and S. B. Cenko. 2SXPS: An Improved and Expanded Swift X-Ray Telescope Point-source Catalog. *ApJS*, 247(2):54, 2020. ISSN 0067-0049. doi: 10.3847/1538-4365/ab7db9.

A. C. Fabian, A. Celotti, K. Iwasawa, and G. Ghisellini. The blazar GB 1428+4217: A warm absorber at z = 4.72? *MNRAS*, 324(3):628–634, 2001. ISSN 00358711. doi: 10.1046/j.1365-8711.2001.04348.x.

F. Fiore, P. Elvis, M., Giommi, and P. Padovani. X-ray spectral survey of WGACAT quasars. I. Spectral evolution and low-energy cutoffs. *ApJ*, 492(1):79, 1998.

A. M. Flores, A. B. Mantz, S. W. Allen, and R. G. Morris. The History of Metal Enrichment Traced by X-ray Observations of High Redshift Galaxy Clusters. *https://arxiv.org/abs/2108.12051*, 2021.

D. Foreman-Mackey, D. W. Hogg, D. Lang, and J. Goodman. emcee : The MCMC Hammer . *PASP*, 125(925):306–312, 2013. ISSN 00046280. doi: 10.1086/670067.

M. Fumagalli. Metal abundances in the high-redshift intergalactic medium. *Memorie della Societa Astronomica Italiana*, 85:355, 2014.

M. Fumagalli, J. M. O'Meara, J. X. Prochaska, and G. Worseck. Dissecting the properties of optically thick hydrogen at the peak of cosmic star formation history. *ApJ*, 775(1):78, 2013. ISSN 15384357. doi: 10.1088/0004-637X/775/1/78.

M. Fumagalli, J. M. O'Meara, and J. Xavier Prochaska. The physical properties of z $>$ 2 Lyman limit systems: New constraints for feedback and accretion models. *MNRAS*, 455(4):4100–4121, 2016. ISSN 13652966. doi: 10.1093/mnras/stv2616.

M. Fumagalli, S. Fotopoulou, T. Avenue, and B. Bs. Detecting neutral hydrogen at z ? 3 in large spectroscopic surveys of quasars. *MNRAS*, 498:1951–1962, 2020. ISSN 0035-8711. doi: 10.1093/mnras/staa2388.

A. Furniss, M. Fumagalli, A. Falcone, and D. A. Williams. The blazar emission environment: Insight from soft X-ray absorption. *ApJ*, 770(2), 2013. ISSN 15384357. doi: 10.1088/0004-637X/770/2/109.

J. P. Fynbo, P. Jakobsson, J. X. Prochaska, D. Malesani, C. Ledoux, A. De Ugarte Postigo, M. Nardini, P. M. Vreeswijk, K. Wiersema, J. Hiorth, J. Sollerman, H. W. Chen, C. C. Thöne, G. Biörnsson, J. S. Bloom, A. J. Castro-Tirado, L. Christensen, A. De Cia, A. S. Fruchter, J. Gorosabel, J. F. Graham, A. O. Jaunsen, B. L. Jensen, D. A. Kann, C. Kouveliotou, A. J. Levan, J. Maund, N. Masetti, B. Milvano-Jensen, E. Palazzi, D. A. Perley, E. Pian, E. Rol, P. Schady, R. L. Starling, N. R. Tanvir, D. J. Watson, D. Xu, T. Augusteiin, F. Grundhal, J. Tilting, and P. O. Uirion. Low-resolution spectroscopy of gamma-ray burst optical afterglows: Biases in the swift sample and characterization of the absorbers. *ApJ*, 185(2):526–573, 2009. ISSN 00670049. doi: 10.1088/0067-0049/185/2/526.

J. P. U. Fynbo, J. X. Prochaska, J. Sommer-Larsen, M. Dessauges-Zavadsky, and P. Møller. Reconciling the Metallicity Distributions of Gamma-ray Burst, Damped Lyman-α, and Lyman-break Galaxies at z $\approx$ 3 . *Proc. Int. Astron. Union*, 4(S254):41–48, 2008. ISSN 1743-9213. doi: 10.1017/s1743921308027373.

T. J. Galama and R. A. M. J. Wijers. High Column Densities and Low Extinctions of Gamma-Ray Bursts: Evidence for Hypernovae and Dust Destruction. *ApJ*, 549(2):L209–L213, 2001. ISSN 0004637X. doi: 10.1086/319162.

E. Gatuzz, J. García, T. R. Kallman, C. Mendoza, and T. W. Gorczyca. ISMabs: A comprehensive X-ray absorption model for the interstellar medium. *ApJ*, 800 (1):29, 2015. ISSN 15384357. doi: 10.1088/0004-637X/800/1/29.

H. Gaur. X-ray spectral evolution of high energy peaked blazars. *Galaxies*, 8(3), 2020. ISSN 20754434. doi: 10.3390/GALAXIES8030062.

N. Gehrels, L. Piro, and P. J. . T. . Leonard. The Brightest Explosions in the Universe. *Scientific American*, 287(6):84–91, 2002.

N. Gehrels, G. Chincarini, P. Giommi, K. Mason, J. Nousek, A. Wells, N. White, S. Barthelmy, D. Burrows, L. Cominsky, and K. Hurley. The swift gamma-ray burst mission. *ApJ*, 611(2):1005, 2004.

G. Ghisellini and L. Maraschi. Bulk acceleration in relativistic jets and the spectral properties of blazars. *ApJ*, 340:181–189, 1989.

S. Gianní, A. De Rosa, L. Bassani, A. Bazzano, T. Dean, and P. Ubertini. An X-ray view of the INTEGRAL/IBIS blazars. *MNRAS*, 411(4):2137–2147, 2011. ISSN 00358711. doi: 10.1111/j.1365-2966.2010.17725.x.

M. Gierliński and C. Done. Is the soft excess in active galactic nuclei real? *MNRAS*, 349(1):7–11, 2004. ISSN 00358711. doi: 10.1111/j.1365-2966.2004.07687.x.

O. Gnat and A. Sternberg. Time-dependent Ionization in Radiatively Cooling Gas. *ApJS*, 168(2):213–230, 2007. ISSN 0067-0049. doi: 10.1086/509786.

R. S. Gonçalves, G. C. Carvalho, C. A. Bengaly, J. C. Carvalho, and J. S. Alcaniz. Measuring the scale of cosmic homogeneity with SDSS-IV DR14 quasars. *https://arxiv.org/abs/2010.06635*, 2020. ISSN 13652966. doi: 10.1093/MNRAS/STY2670.

J. Goodman and J. Weare. Ensemble Samplers With Affine. *Communications in Applied Mathematics and Computational Science*, 5(1):65–80, 2010.

J. R. Gott III, M. Jurić, D. Schlegel, F. Hoyle, M. Vogeley, M. Tegmark, N. Bahcall, and J. Brinkmann. A Map of the Universe. *ApJ*, 624(2):463–484, 2005. ISSN 0004-637X. doi: 10.1086/428890.

J. Greiner, T. Krühler, S. Klose, P. Afonso, C. Clemens, R. Filgas, D. H. Hartmann, A. K. Yolda, M. Nardini, , A. Rau, and A. Rossi. The nature of “ dark ” gamma-ray bursts. *A&A*, 526:A30, 2011.

D. Grupe, S. Mathur, , B. Wilkes, and P. Osmer. XMM-NEWTON OBSERVATIONS OF HIGH-REDSHIFT QUASARS. *AJ*, 131(1):55–69, 2006.

F. Haardt and P. Madau. Radiative Transfer in a Clumpy Universe. II. The Ultraviolet Extragalactic Background. *ApJ*, 461:20, 1996. URL `http://articles.adsabs.harvard.edu/full/gif/1996ApJ...461...20H/0000020.000.html`.

F. Haardt and P. Madau. Radiative transfer in a clumpy universe. IV. New synthesis models of the cosmic UV/X-RAY background. *ApJ*, 746(2), 2012. ISSN 15384357. doi: 10.1088/0004-637X/746/2/125.

F. Haardt and L. Maraschi. X-ray spectra from two-phase accretion disks. *ApJ*, 413:507, 1993.

S. B. Haim, E. Behar, and R. F. Mushotzky. X-Ray Spectrum of RBS 315: Absorption or Intrinsic Curvature. *ApJ*, 882(2):130, 2019. ISSN 0004-637X. doi: 10.3847/1538-4357/ab340f. URL `http://dx.doi.org/10.3847/1538-4357/ab340f`.

D. W. Harris, T. W. Jensen, N. Suzuki, J. E. Bautista, K. S. Dawson, M. Vivek, J. R. Brownstein, J. Ge, F. Hamann, H. Herbst, L. Jiang, S. E. Moran, A. D. Myers, M. D. Olmstead, and D. P. Schneider. The Composite Spectrum of BOSS Quasars Selected for Studies of the Lyman-alpha Forest. *AJ*, 151(6):1–20, 2016. ISSN 1538-3881. doi: 10.3847/0004-6256/151/6/155. URL `http://arxiv.org/abs/1603.08626{%}0Ahttp://dx.doi.org/10.3847/0004-6256/151/6/155`.

S. He, S. Alam, S. Ferraro, Y. C. Chen, and S. Ho. The detection of the imprint of filaments on cosmic microwave background lensing. *Nature Astronomy*, 2(5): 401–406, 2018. ISSN 23973366. doi: 10.1038/s41550-018-0426-z. URL `http://dx.doi.org/10.1038/s41550-018-0426-z`.

K. E. Heintz. *Galaxies through cosmic time illuminated by gamma-ray bursts and quasars*. 2019. ISBN 9789935947338. URL `http://arxiv.org/abs/1910.09849`.

K. E. Heintz, C. Ledoux, J. P. Fynbo, P. Jakobsson, P. Noterdaeme, J. K. Krogager, J. Bolmer, P. Møller, S. D. Vergani, D. Watson, T. Zafar, A. De Cia, N. R. Tanvir, D. B. Malesani, J. Japelj, S. Covino, and L. Kaper. Cold gas in the early Universe: Survey for neutral atomic-carbon in GRB host galaxies at $1 < z < 6$ from optical afterglow spectroscopy. *A&A*, 621:1–14, 2019. ISSN 14320746. doi: 10.1051/0004-6361/201834246.

J. F. Hennawi and J. X. Prochaska. Quasars probing quasars. IV. Joint constraints on the circumgalactic medium from absorption and emission. *ApJ*, 766(1), 2013. ISSN 15384357. doi: 10.1088/0004-637X/766/1/58.

J. F. Hennawi, J. X. Prochaska, S. Burles, M. A. Strauss, G. T. Richards, D. J. Schlegel, X. Fan, D. P. Schneider, N. L. Zakamska, M. Oguri, J. E. Gunn, R. H.

Lupton, and J. Brinkmann. Quasars Probing Quasars. I. Optically Thick Absorbers near Luminous Quasars. *ApJ*, 651(1):61–83, 2006. ISSN 0004-637X. doi: 10.1086/507069.

M. F. Ho, S. Bird, and R. Garnett. Damped Lyman-α absorbers from Sloan digital sky survey DR16Q with Gaussian processes. *https://arxiv.org/abs/2103.10964*, 2021. ISSN 13652966. doi: 10.1093/mnras/stab2169.

L. Ighina, A. Caccianiga, A. Moretti, S. Belladitta, R. Della Ceca, L. Ballo, and D. Dallacasa. X-ray properties of z > 4 blazars. *MNRAS*, 489(2):2732–2745, 2019. ISSN 13652966. doi: 10.1093/mnras/stz2340.

K. Iwasawa and Y. Taniguchi. The X-ray Baldwin effect. *ApJ*, 413:L15–18, 1993.

J. Japelj, S. D. Vergani, R. Salvaterra, P. D'Avanzo, F. Mannucci, A. Fernandez-Soto, S. Boissier, L. K. Hunt, H. Atek, L. Rodríguez-Muñoz, M. Scodeggio, S. Cristiani, E. Le Floc'h, H. Flores, J. Gallego, G. Ghirlanda, A. Gomboc, F. Hammer, D. A. Perley, A. Pescalli, P. Petitjean, M. Puech, M. Rafelski, and G. Tagliaferri. Are long gamma-ray bursts biased tracers of star formation? Clues from the host galaxies of the Swift/BAT6 complete sample of bright LGRBs: II. Star formation rates and metallicities at z < 1. *A&A*, 590, 2016. ISSN 14320746. doi: 10.1051/0004-6361/201628314.

J. S. Kaastra. On the use of C-stat in testing models for X-ray spectra. *A&A*, 605 (3):2–5, 2017. ISSN 14320746. doi: 10.1051/0004-6361/201629319.

P. M. Kalberla, W. B. Burton, D. Hartmann, E. M. Arnal, E. Bajaja, R. Morras, and W. G. Pöppel. The Leiden/Argentine/Bonn (LAB) survey of Galactic HI: Final data release of the combined IDS and IAR surveys with improved stray-radiation corrections, 2005. ISSN 00046361.

T. R. Kallman, M. A. Bautista, S. Goriely, C. Mendoza, J. M. Miller, P. Palmeri, P. Quinet, and J. Raymond. Spectrum synthesis modeling of the X-ray spectrum of GRO J1655-40 taken during the 2005 outburst. *ApJ*, 701(2):865–884, 2009. ISSN 15384357. doi: 10.1088/0004-637X/701/2/865.

E. S. Kammoun, E. Nardini, G. Risaliti, G. Ghisellini, E. Behar, and A. Celotti. Bulk Comptonization: New hints from the luminous blazar 4C+25.05. *Monthly Notices of the Royal Astronomical Society: Letters*, 473(1):L89–L93, 2018. ISSN 17453933. doi: 10.1093/mnrasl/slx164.

K. I. Kellermann, R. Sramek, M. Schmidt, D. B. Shaffer, and R. Green. VLA observations of objects in the Palomar Bright Quasar Survey. *AJ*, 98(4):1195, 1989. ISSN 00046256. doi: 10.1086/115207.

I. Khabibullin and E. Churazov. X-ray emission from warm-hot intergalactic medium: The role of resonantly scattered cosmic X-ray background. *MNRAS*, 482 (4):4972–4984, 2019. ISSN 13652966. doi: 10.1093/mnras/sty2992.

I. S. Khrykin, J. F. Hennawi, G. Worseck, and F. B. Davies. The first measurement of the quasar lifetime distribution. *MNRAS*, 505(1):649–662, 2021. ISSN 13652966. doi: 10.1093/mnras/stab1288.

R. Klebesadel, I. Strong, and R. Olson. Observations of gamma-ray bursts of cosmic origin. *ApJ*, 182:L85, 1973.

C. Kouveliotou, C. Meegan, G. Fishman, N. Bhat, M. Briggs, T. Koshut, and G. Paciesas, W.S. and Pendleton. Identification of two classes of gamma-ray bursts. *ApJ*, 413:L101, 1993.

Y. Krongold and J. X. Prochaska. An explanation for the different X-ray to optical column densities in the environments of gamma ray bursts: A progenitor embedded in a dense medium. *ApJ*, 774(2):115, 2013. ISSN 15384357. doi: 10.1088/0004-637X/774/2/115.

T. Krühler, D. Malesani, J. P. U. Fynbo, O. E. Hartoog, J. Hjorth, P. Jakobsson, D. A. Perley, A. Rossi, P. Schady, S. Schulze, N. R. Tanvir, VerganiS.D, K. Wiersema,

P. M. J. Afonso, J. Bolmer, Z. Cano, S. Covino, V. D'Eliia, A. Postigo, de Ugarte, R. Filgas, M. Friis, J. F. Graham, J. Greiner, P. Goldoni, A. Gomboc, F. Hammer, J. Japelj, D. A. Kann, Kaper, Klose, A. J. Levan, G. Leloudas, B. Milvang-Jensen, A. Guelbenzu Nicuesa, E. Palazzi, E. Pian, S. Piranomonte, R. Sánchez-Ramírez, S. Savaglio, J. Selsing, G. Tagliaferri, P. M. Vreeswijk, D. J. Watson, and D. Xu. GRB hosts through cosmic time-VLT/X-Shooter emission-line spectroscopy of 96 \$$\gamma$\$ − *ray* − *burst* − *selectedgalaxiesat*0.1<z<3.6. *A&A*, 581 : *A*125, 2015. *URL*.

N. Laporte, R. A. Meyer, R. S. Ellis, B. E. Robertson, J. Chisholm, M. Planck, J. Webb, and S. Telescope. Probing cosmic dawn : Ages and star formation histories of candidate z $>$ 9 galaxies. *MNRAS*, 505:3336–3346, 2021.

D. V. Lapparent, M. Geller, and J. Huchra. A slice of the Universe. *ApJ*, 302(21): L1, 1986.

C. Ledoux, P. Vreeswijk, A. Smette, A. Fox, P. Petitjean, S. Ellison, J. Fynbo, and S. Savaglio. Physical conditions in high-redshift GRB-DLA absorbers observed with VLT/UVES: Implications for molecular hydrogen searches. *A&A*, 506(2):661–675, 2009. ISSN 0004-6361. doi: 10.1051/0004-6361/200811572. URL `http://www.scopus.com/inward/record.url?eid=2-s2.0-70350448599{&}partnerID=40{&}md5=d11dfddbde0ba1380ffb52780f72911d`.

N. Lehner, J. M. O'Meara, J. C. Howk, J. X. Prochaska, and M. Fumagalli. the Cosmic Evolution of the Metallicity Distribution of Ionized Gas Traced By Lyman Limit Systems. *ApJ*, 833(2):283, 2016. ISSN 1538-4357. doi: 10.3847/1538-4357/833/2/283. URL `http://dx.doi.org/10.3847/1538-4357/833/2/283`.

N. Lehner, C. B. Wotta, J. C. Howk, J. M. O'Meara, B. D. Oppenheimer, and K. L. Cooksey. The COS CGM Compendium. III. Metallicity and Physical Properties of the Cool Circumgalactic Medium at z $\lesssim$ 1 . *ApJ*, 887(1):5, 2019. ISSN 1538-4357. doi: 10.3847/1538-4357/ab41fd. URL `http://dx.doi.org/10.3847/1538-4357/ab41fd`.

B. Luo, W. N. Brandt, Y. Q. Xue, D. M. Alexander, M. Brusa, F. E. Bauer, A. Comastri, A. C. Fabian, R. Gilli, B. D. Lehmer, D. A. Rafferty, D. P. Schneider, and C. Vignali. Revealing A population of heavily obscured active galactic nuclei at z $\approx$ 0.5-1 in the Chandra Deep Field-South. *ApJ*, 740(1), 2011. ISSN 15384357. doi: 10.1088/0004-637X/740/1/37.

E. Lusso, G. Worseck, J. F. Hennawi, J. X. Prochaska, C. Vignali, J. Stern, and J. M. O'Meara. The first ultraviolet quasar-stacked spectrum at z $\simeq$ 2.4 from WFC3. *MNRAS*, 449(4):4204–4220, 2015. ISSN 13652966. doi: 10.1093/mnras/stv516.

E. Lusso, M. Fumagalli, M. Rafelski, M. Neeleman, J. X. Prochaska, J. F. Hennawi, J. M. O'Meara, and T. Theuns. The Spectral and Environment Properties of z $\sim$ 2.0–2.5 Quasar Pairs . *ApJ*, 860(1):41, 2018. ISSN 0004-637X. doi: 10.3847/1538-4357/aac514. URL `http://dx.doi.org/10.3847/1538-4357/aac514`.

E. Lusso, G. Risaliti, E. Nardini, G. Bargiacchi, M. Benetti, S. Bisogni, S. Capozziello, F. Civano, L. Eggleston, M. Elvis, G. Fabbiano, R. Gilli, A. Marconi, M. Paolillo, E. Piedipalumbo, F. Salvestrini, M. Signorini, and C. Vignali. Quasars as standard candles III. Validation of a new sample for cosmological studies. *A&A*, 642:A150, 2020. URL `http://arxiv.org/abs/2008.08586`.

J. Macquart, M. Bailes, N. Bhat, G. Bower, J. Bunton, S. Chatterjee, T. Colegate, J. Cordes, L. D'Addario, A. Deller, and R. Dodson. The Commensal Real-Time ASKAP Fast-Transients (CRAFT) Survey. *PASA*, pages 272–282, 2010.

J. P. Macquart, J. X. Prochaska, M. McQuinn, K. W. Bannister, S. Bhandari, C. K. Day, A. T. Deller, R. D. Ekers, C. W. James, L. Marnoch, S. Oslowski, C. Phillips, S. R. Ryder, D. R. Scott, R. M. Shannon, and N. Tejos. A census of baryons in the Universe from localized fast radio bursts. *Nature*, 581(7809): 391, 2020. doi: 10.1038/s41586-020-2300-2. URL `http://arxiv.org/abs/2005.13161{%}0Ahttp://dx.doi.org/10.1038/s41586-020-2300-2`.

P. Magdziarz and A. Zdziarski. Angle-dependent Compton reflection of X-rays and gamma-rays. Monthly Notices of the Royal Astronomical Society, 273(3), pp.837-848. *MNRAS*, 273(8):837, 1995.

R. Maiolino and F. Mannucci. De Re Metallica: The cosmic chemical evolution of galaxies. *A&A*, 27(1):3, 2019. URL `http://arxiv.org/abs/1811.09642`.

L. Marcotulli, V. Paliya, M. Ajello, A. Kaur, S. Marchesi, M. Rajagopal, D. Hartmann, D. Gasparrini, R. Ojha, and G. Madejski. NuSTAR perspective on high-redshift MeV blazars. *ApJ*, 889(2):164, 2020. ISSN 0004-637X. doi: 10.3847/1538-4357/ab65f5.

D. Martizzi, M. Vogelsberger, M. C. Artale, M. Haider, P. Torrey, F. Marinacci, D. Nelson, A. Pillepich, R. Weinberger, L. Hernquist, J. Naiman, and V. Springel. Baryons in the Cosmic Web of IllustrisTNG - I: Gas in knots, filaments, sheets, and voids. *MNRAS*, 486(3):3766–3787, 2019. ISSN 13652966. doi: 10.1093/mnras/stz1106.

E. Massaro, A. Maselli, C. Leto, P. Marchegiani, M. Perri, P. Giommi, and S. Piranomonte. The 5th edition of the Roma-BZCAT. A short presentation. *Astrophysics and Space Science*, 357(1):1–5, 2015. ISSN 1572946X. doi: 10.1007/s10509-015-2254-2.

M. McDonald, E. Bulbul, T. de Haan, E. D. Miller, B. A. Benson, L. E. Bleem, M. Brodwin, J. E. Carlstrom, I. Chiu, W. R. Forman, J. Hlavacek-Larrondo, G. P. Garmire, N. Gupta, J. J. Mohr, C. L. Reichardt, A. Saro, B. Stalder, A. A. Stark, and J. D. Vieira. THE EVOLUTION OF THE INTRACLUSTER MEDIUM METALLICITY IN SUNYAEV ZEL'DOVICH-SELECTED GALAXY CLUSTERS AT $0 < z < 1.5$. *ApJ*, 826(2):124, 2016. ISSN 1538-4357. doi: 10.3847/0004-637x/826/2/124. URL `http://dx.doi.org/10.3847/0004-637X/826/2/124`.

M. McQuinn. The Evolution of the Intergalactic Medium. *Annual Review of Astronomy and Astrophysics*, 54:313, 2016. ISSN 0066-4146. doi: 10.1146/annurev-astro-082214-122355. URL `http://arxiv.org/abs/1512.00086{%}0Ahttp://dx.doi.org/10.1146/annurev-astro-082214-122355`.

P. Medvedev, M. Gilfanov, S. Sazonov, N. Schartel, and R. Sunyaev. XMM-Newton observations of the extremely X-ray luminous quasar CFHQS J142952+544717=SRGE J142952.1 + 544716 at redshift z = 6.18. *MNRAS*, 504(1):576–582, 2021. ISSN 13652966. doi: 10.1093/mnras/stab773.

F. Mernier, J. De Plaa, J. S. Kaastra, Y. Y. Zhang, H. Akamatsu, L. Gu, P. Kosec, J. Mao, C. Pinto, T. H. Reiprich, J. S. Sanders, A. Simionescu, and N. Werner. Radial metal abundance profiles in the intra-cluster medium of cool-core galaxy clusters, groups, and ellipticals. *A&A*, 603:1–27, 2017. ISSN 14320746. doi: 10.1051/0004-6361/201630075.

M. R. Metzger, S. G. Djorgovski, S. R. Kulkarni, C. C. Steidel, K. L. Adelberger, D. A. Frail, E. Costa, and F. Frontera. Spectral constraints on the redshift of the optical counterpart to the γ-ray burst of 8 May 1997. *Nature*, 387(6636):878–880, 1997. ISSN 00280836. doi: 10.1038/43132.

A. Moretti, S. Vattakunnel, P. Tozzi, R. Salvaterra, P. Severgnini, D. Fugazza, F. Haardt, and R. Gilli. Spectrum of the unresolved cosmic X-ray background: What is unresolved 50 years after its discovery. *A&A*, 548:1–11, 2012. ISSN 00046361. doi: 10.1051/0004-6361/201219921.

S. Morris, R. Weymann, B. Savage, and R. Gilliland. First results from the Goddard High-Resolution Spectrograph-The Galactic halo and the Ly-alpha forest at low redshift in 3C 273. *ApJ*, 377:L21–24, 1991. ISSN 1098-6596. doi: 10.1017/CBO9781107415324.004.

R. Morrison and D. Mccammon. Interstellar photoelectric absorption cross sections, 0.03-10 keV. *ApJ*, 270:119–122, 1983.

R. F. Mushotzky, C. Done, and K. a. Pounds. X-Ray Spectra and Time Galactic Nuclei. *Annual Review of Astronomy and Astrophysics*, 31(1):717, 1993.

R. Nanni, C. Vignali, R. Gilli, A. Moretti, and W. N. Brandt. The X-ray properties of z ˜ 6 luminous quasars . *A&A*, 603:A128, 2017. ISSN 0004-6361. doi: 10.1051/0004-6361/201730484.

M. Neeleman, J. X. Prochaska, and A. M. Wolfe. Probing the physical conditions of atomic gas at high redshift. *ApJ*, 800(1), 2015. ISSN 20418213. doi: 10.1088/0004-637X/800/1/7.

L. B. Newburgh, G. E. Addison, M. Amiri, K. Bandura, J. R. Bond, L. Connor, J.-F. Cliche, G. Davis, M. Deng, N. Denman, M. Dobbs, M. Fandino, H. Fong, K. Gibbs, A. Gilbert, E. Griffin, M. Halpern, D. Hanna, A. D. Hincks, G. Hinshaw, C. Höfer, P. Klages, T. Landecker, K. Masui, J. M. Parra, U.-L. Pen, J. Peterson, A. Recnik, J. R. Shaw, K. Sigurdson, M. Sitwell, G. Smecher, R. Smegal, K. Vanderlinde, and D. Wiebe. Calibrating CHIME: a new radio interferometer to probe dark energy. *Ground-based and Airborne Telescopes V*, 9145:91454V, 2014. ISSN 1996756X. doi: 10.1117/12.2056962.

F. Nicastro, Y. Krongold, S. Mathur, and M. Elvis. A Decade of WHIM Searches:Where do we Stand and Where do we Go? *Astronomische Nachrichten*, 338(2-3):281–286, 2017. URL `http://arxiv.org/abs/1611.03722`.

F. Nicastro, J. Kaastra, Y. Krongold, S. Borgani, E. Branchini, R. Cen, M. Dadina, C. Danforth, M. Elvis, F. Fiore, , and A. Gupta. Observations of the missing baryons in the warm–hot intergalactic medium. *Nature*, 558(7710):406, 2018. URL `https://arxiv.org/ftp/arxiv/papers/1806/1806.08395.pdf`.

B. D. Oppenheimer and J. Schaye. Non-equilibirum ionization and cooling of metal-enriched gas in the presence of a photoionization background. *MNRAS*, 434 (2):1043–1062, 2013a. ISSN 00358711. doi: 10.1093/mnras/stt1043.

B. D. Oppenheimer and J. Schaye. AGN proximity zone fossils and the delayed recombination of metal lines. *MNRAS*, 434(2):1063–1078, 2013b. ISSN 00358711. doi: 10.1093/mnras/stt1150.

B. Paczynski. Gamma-ray bursters at cosmological distances. *ApJ*, 308:L43, 1986.

P. Padovani, P. Giommi, and A. Rau. The discovery of high-power high synchrotron peak blazars. *Monthly Notices of the Royal Astronomical Society: Letters*, 422(1): 48–52, 2012. ISSN 17453933. doi: 10.1111/j.1745-3933.2012.01234.x.

K. L. Page, J. N. Reeves, P. T. O'Brien, and M. J. Turner. XMM-Newton spectroscopy of high-redshift quasars. *MNRAS*, 364(1):195–207, 2005. ISSN 00358711. doi: 10.1111/j.1365-2966.2005.09550.x.

A. Paggi, F. Massaro, V. Vittorini, A. Cavaliere, F. D'Ammando, F. Vagnetti, and M. Tavani. SSC radiation in BL Lacertae sources, the end of the tether. *A&A*, 504(3):821–828, 2009. ISSN 00046361. doi: 10.1051/0004-6361/200912237.

A. Paggi, M. Bonato, C. M. Raiteri, M. Villata, G. De Zotti, and M. I. Carnerero. A new multiwavelength census of blazars. *A&A*, 641:A62, 2020. ISSN 14320746. doi: 10.1051/0004-6361/202038430.

V. S. Paliya, M. L. Parker, A. C. Fabian, and C. S. Stalin. Broadband Observations of High Redshift Blazars. *ApJ*, 825(1):74, 2016. ISSN 0004-637X. doi: 10.3847/0004-637x/825/1/74. URL `http://dx.doi.org/10.3847/0004-637X/825/1/74`.

A. Pallottini, A. Ferrara, and C. Evoli. Simulating intergalactic quasar scintillation. *MNRAS*, 434(4):3293–3304, 2013. ISSN 00358711. doi: 10.1093/mnras/stt1249.

A. Pallottini, A. Ferrara, S. Gallerani, S. Salvadori, and V. D'odorico. Simulating cosmic metal enrichment by the first galaxies. *MNRAS*, 440(3):2498–2518, 2014. ISSN 13652966. doi: 10.1093/mnras/stu451.

I. Pâris, P. Petitjean, É. Aubourg, A. D. Myers, A. Streblyanska, B. W. Lyke, S. F. Anderson, É. Armengaud, J. Bautista, M. R. Blanton, M. Blomqvist, J. Brinkmann, J. R. Brownstein, W. N. Brandt, É. Burtin, K. Dawson, S. De La Torre, A. Georgakakis, H. Gil-Marín, P. J. Green, P. B. Hall, J. P. Kneib, S. M. LaMassa, J. M. Le Goff, C. MacLeod, V. Mariappan, I. D. McGreer, A. Merloni, P. Noterdaeme, N. Palanque-Delabrouille, W. J. Percival, A. J. Ross, G. Rossi, D. P. Schneider, H. J. Seo, R. Tojeiro, B. A. Weaver, A. M. Weijmans, C. Yèche, P. Zarrouk, and G. B. Zhao. The sloan digital sky survey quasar catalog: Fourteenth data release. *A&A*, 613, 2018. ISSN 14320746. doi: 10.1051/0004-6361/201732445.

D. A. Perley, T. Krühler, S. Schulze, A. D. U. Postigo, J. Hjorth, E. Berger, S. B. Cenko, R. Chary, A. Cucchiara, R. Ellis, W. Fong, J. P. U. Fynbo, J. Gorosabel, J. Greiner, P. Jakobsson, S. Kim, T. Laskar, A. J. Levan, M. J. Michałowski, B. Milvang-Jensen, N. R. Tanvir, C. C. Thöne, and K. Wiersema. The Swift Gamma-Ray Burst Host Galaxy Legacy Survey - I. Sample Selection and Redshift Distribution. *Perley, D.A., Krühler, T., Schulze, S., de Ugarte Postigo, A., Hjorth, J., Berger, E., Cenko, S.B., Chary, R., Cucchiara, A., Ellis, R. and Fong, W.F., 2016. The Swift gamma-ray burst host galaxy legacy survey. I. Sample selection and redshift distributio*, 817(1):7, 2015. doi: 10.3847/0004-637X/817/1/7. URL `http://arxiv.org/abs/1504.02482{%}0Ahttp://dx.doi.org/10.3847/0004-637X/817/1/7`.

E. S. Perlman, P. Padovani, P. Giommi, R. Sambruna, L. R. Jones, A. Tzioumis, and J. Reynolds. The Deep X-Ray Radio Blazar Survey. I. Methods and First Results. *AJ*, 115(4):1253–1294, 1998. ISSN 00046256. doi: 10.1086/300283.

E. Petroff, J. W. T. Hessels, and D. R. Lorimer. Fast radio bursts at the dawn of the 2020s. *https://arxiv.org/abs/2107.10113*, 2021. URL `http://arxiv.org/abs/2107.10113`.

C. Peroux and J. C. Howk. The Cosmic Baryon and Metal Cycles. *Annu. Rev. Astron. Astrophys*, 58:363–406, 2020.

O. F. Piattella. Lecture notes in cosmology. *Lecture notes in cosmology (Berlin: Springer.)*, page 417, 2018. ISSN 2198-7890. doi: 10.1007/978-3-319-95570-4.

M. Pieri, M. J. Mortonson, S. Frank, N. Crighton, D. H. Weinberg, K. G. Lee, P. Noterdaeme, S. Bailey, N. Busca, J. Ge, D. Kirkby, B. Lundgren, S. Mathur, I. Pâris, N. Palanque-Delabrouille, P. Petitjean, J. Rich, N. P. Ross, D. P. Schneider, and D. G. York. Probing the circumgalactic medium at high-redshift using composite boss spectra of strong Lyman α forest absorbers. *MNRAS*, 441(2):1718–1740, 2014. ISSN 13652966. doi: 10.1093/mnras/stu577.

T. Piran. The physics of gamma-ray bursts. *Reviews of Modern Physics*, 76(4): 1143–1210, 2004. ISSN 00346861. doi: 10.1103/RevModPhys.76.1143.

Planck Collaboration, N. Aghanim, Y. Akrami, M. Ashdown, J. Aumont, C. Baccigalupi, M. Ballardini, A. Banday, R. Barreiro, , N. Bartolo, and S. Basak. Planck 2018 results, 2020. ISSN 14320746.

Z. Pleunis, D. C. Good, V. M. Kaspi, R. Mckinven, S. M. Ransom, P. Scholz, K. Bandura, M. Bhardwaj, P. J. Boyle, C. Brar, T. Cassanelli, P. Chawla, Fengqiu, Dong, E. Fonseca, B. M. Gaensler, A. Josephy, J. F. Kaczmarek, C. Leung, H.-H. Lin, K. W. Masui, J. Mena-Parra, D. Michilli, C. Ng, C. Patel, M. Rafiei-Ravandi, M. Rahman, P. Sanghavi, K. Shin, K. M. Smith, I. H. Stairs, and S. P. Tendulkar. Fast Radio Burst Morphology in the First CHIME/FRB Catalog. *https://arxiv.org/abs/2107.10858*, 2021. URL `http://arxiv.org/abs/2106.04356`.

C. T. Pratt, J. T. Stocke, B. A. Keeney, and C. W. Danforth. The Spread of Metals into the Low-redshift Intergalactic Medium. *ApJ*, 855(1):18, 2018. ISSN 1538-4357. doi: 10.3847/1538-4357/aaaaac. URL `http://dx.doi.org/10.3847/1538-4357/aaaaac`.

J. X. Prochaska and J. F. Hennawi. Quasars probing quasars. III. New clues to feedback, quenching, and the physics of massive galaxy formation. *ApJ*, 690(2): 1558–1584, 2009. ISSN 15384357. doi: 10.1088/0004-637X/690/2/1558.

J. X. Prochaska and M. Neeleman. The astrophysical consequences of intervening galaxy gas on fast radio bursts. *MNRAS*, 474(1):318–325, 2018. ISSN 13652966. doi: 10.1093/mnras/stx2824.

J. X. Prochaska, J. F. Hennawi, K. G. Lee, S. Cantalupo, J. Bovy, S. G. Djorgovski, S. L. Ellison, M. W. Lau, C. L. Martin, A. Myers, K. H. Rubin, and R. A. Simcoe. Quasars probing quasars. VI. Excess HI absorption within one proper Mpc of z $\sim$ 2 quasars. *ApJ*, 776(2), 2013. ISSN 15384357. doi: 10.1088/0004-637X/776/2/136.

J. X. Prochaska, P. Madau, J. M. O'meara, and M. Fumagalli. Towards a unified description of the intergalactic medium at redshift z $\approx$ 2.5. *MNRAS*, 438(1):476–486, 2014. ISSN 00358711. doi: 10.1093/mnras/stt2218.

M. Rafelski, M. Neeleman, M. Fumagalli, A. M. Wolfe, and J. X. Prochaska. The rapid decline in metallicity of damped Ly α systems at z $\sim$ 5. *ApJ*, 782(2):L29, 2014. doi: 10.1088/2041-8205/782/2/L29.

S. Raghunathan, R. G. Clowes, L. E. Campusano, I. K. Söchting, M. J. Graham, and G. M. Williger. Intervening Mg II absorption systems from the SDSS DR12 quasar spectra. *MNRAS*, 463(3):2640–2652, 2016. ISSN 13652966. doi: 10.1093/mnras/stw2095.

R. Rahin and E. Behar. Cosmological evolution of the absorption of gamma-ray burst X-ray afterglows. *ApJ*, 885(1):47, 2019. ISSN 1538-4357. doi: 10.3847/1538-4357/ab3e34. URL `http://arxiv.org/abs/1908.10420`.

J. N. Reeves and M. J. Turner. X-ray spectra of a large sample of quasars with ASCA. *MNRAS*, 316(2):234–248, 2000. ISSN 00358711. doi: 10.1046/j.1365-8711.2000.03510.x.

C. Ricci, B. Trakhtenbrot, M. J. Koss, Y. Ueda, I. Delvecchio, E. Treister, K. Schawinski, S. Paltani, K. Oh, I. Lamperti, S. Berney, P. Gandhi, K. Ichikawa, F. E. Bauer, L. C. Ho, D. Asmus, V. Beckmann, S. Soldi, M. Baloković, N. Gehrels, and

C. B. Markwardt. BAT AGN spectroscopic survey – V. X-ray properties of the Swift/BAT 70-MONTH AGN catalog. *ApJS*, 233(2):17, 2017. ISSN 0067-0049. doi: 10.3847/1538-4365/aa96ad.

P. Richter, F. B. Paerels, and J. S. Kaastra. FUV and X-ray absorption in the warm-hot intergalactic medium. *Space Science Reviews*, 134(1-4):25–49, 2008. ISSN 00386308. doi: 10.1007/s11214-008-9325-4.

G. Risaliti and E. Lusso. Cosmological constraints from the Hubble diagram of quasars at high redshifts. *Nature Astronomy*, 3(3):272–277, 2019. ISSN 23973366. doi: 10.1038/s41550-018-0657-z.

B. E. Robertson. Galaxy Formation and Reionization: Key Unknowns and Expected Breakthroughs by the James Webb Space Telescope. *https://arxiv.org/abs/2110.13160*, 2021. URL `http://arxiv.org/abs/2110.13160`.

K. Rusinek-Abarca and M. Sikora. The dependence of the fraction of radio luminous quasars on redshift and its theoretical implications. *https://arxiv.org/abs/2109.07523*, 2021. URL `http://arxiv.org/abs/2109.07523`.

N. Sahakyan, D. Israyelyan, G. Harutyunyan, M. Khachatryan, and S. Gasparyan. Multiwavelength Study of High-Redshift Blazars. *MNRAS*, 498(2):2594, 2020. ISSN 0035-8711. doi: 10.1093/mnras/staa2477.

F. Salvestrini, G. Risaliti, S. Bisogni, E. Lusso, and C. Vignali. Quasars as standard candles II. The non-linear relation between UV and X-ray emission at high redshifts. *A&A*, 631:1–17, 2019. ISSN 14320746. doi: 10.1051/0004-6361/201935491.

R. Sari, T. Piran, and J. Halpern. Jets in GRBs. *ApJ*, 519:L17, 1999. doi: 10.1086/312109. URL `http://arxiv.org/abs/astro-ph/9903339{%}0Ahttp://dx.doi.org/10.1086/312109`.

B. D. Savage, T. S. Kim, B. P. Wakker, B. Keeney, J. M. Shull, J. T. Stocke, and J. C. Green. The properties of low redshift intergalactic OVIabsorbers determined from high S/N observations of 14 QSOs with the cosmic origins spectrograph. *ApJ*, 212(1), 2014. ISSN 00670049. doi: 10.1088/0067-0049/212/1/8.

S. Savaglio. GRBs as cosmological probes - Cosmic chemical evolution. *New Journal of Physics*, 8:195, 2006. ISSN 13672630. doi: 10.1088/1367-2630/8/9/195.

P. Schady. Gamma-ray bursts and their use as cosmic probes. *Royal Society open science*, 4(7):170304, 2017.

P. Schady, S. Savaglio, T. Krühler, J. Greiner, , and A. Rau. The missing gas problem in GRB host galaxies: evidence for a highly ionised component. *A&A*, 525:A113, 2011.

J. Schaye, A. Aguirre, T. Kim, T. Theuns, M. Rauch, and W. L. W. Sargent. Metallicity of the Intergalactic Medium Using Pixel Statistics. II. The Distribution of Metals as Traced by C iv . *ApJ*, 596(2):768–796, 2003. ISSN 0004-637X. doi: 10.1086/378044.

J. Schaye, R. A. Crain, R. G. Bower, M. Furlong, M. Schaller, T. Theuns, C. Dalla Vecchia, C. S. Frenk, I. G. Mccarthy, J. C. Helly, A. Jenkins, Y. M. Rosas-Guevara, S. D. White, M. Baes, C. M. Booth, P. Camps, J. F. Navarro, Y. Qu, A. Rahmati, T. Sawala, P. A. Thomas, and J. Trayford. The EAGLE project: Simulating the evolution and assembly of galaxies and their environments. *MNRAS*, 446(1): 521–554, 2015. ISSN 13652966. doi: 10.1093/mnras/stu2058.

M. Scodeggio, L. Guzzo, B. Garilli, B. R. Granett, M. Bolzonella, S. de la Torre, U. Abbas, C. Adami, S. Arnouts, D. Bottini, A. Cappi, J. Coupon, O. Cucciati, I. Davidzon, P. Franzetti, A. Fritz, A. Iovino, J. Krywult, V. Le Brun, O. Le Fèvre, D. Maccagni, K. Małek, A. Marchetti, F. Marulli, M. Polletta, A. Pollo, L. A. M. Tasca, R. Tojeiro, D. Vergani, A. Zanichelli, J. Bel, E. Branchini, G. De Lucia, O. Ilbert, H. J. McCracken, T. Moutard, J. A. Peacock, G. Zamorani, A. Burden, M. Fumana, E. Jullo, C. Marinoni, Y. Mellier, L. Moscardini, and W. J. Percival.

The VIMOS Public Extragalactic Redshift Survey (VIPERS). *A&A*, 609:A84, 2018. ISSN 0004-6361. doi: 10.1051/0004-6361/201630114.

A. E. Scott, G. C. Stewart, S. Mateos, D. M. Alexander, S. Hutton, and M. J. Ward. New constraints on the X-ray spectral properties of type 1 active galactic nuclei. *MNRAS*, 417(2):992–1012, 2011. ISSN 00358711. doi: 10.1111/j.1365-2966.2011.19325.x.

J. Selsing, J. P. U. Fynbo, L. Christensen, and J.-K. Krogager. An X-shooter composite of bright 1 < z < 2 quasars from UV to infrared. *A&A*, 585:a87, 2016. doi: 10.1051/0004-6361/201527096. URL `http://arxiv.org/abs/1510.08058{%}0Ahttp://dx.doi.org/10.1051/0004-6361/201527096`.

N. Shakura and R. Sunyaev. Black holes in binary systems. Observational appearance. *$\$aap, 24 : 337 - -355, 1973.

S. H. Shehata, R. Misra, A. M. Osman, O. M. Shalabiea, and Z. M. Hayman. Redshift evolution of X-ray spectral index of quasars observed by XMM-NEWTON/SDSS. Journal of High Energy Astrophysics*, 31:37–43, 2021. ISSN 22144048. doi: 10.1016/j.jheap.2021.04.003. URL `https://doi.org/10.1016/j.jheap.2021.04.003`.*

J. M. Shull and C. W. Danforth. The dispersion of fast radio bursts from a structured intergalactic medium at redshifts z < 1 . 5. ApJ*, 852(1):L11, 2018.*

J. M. Shull, B. D. Smith, and C. W. Danforth. The baryon census in a multiphase intergalactic medium: 30% of the BARYONS may still be missing. ApJ*, 759(1):23, 2012. ISSN 15384357. doi: 10.1088/0004-637X/759/1/23.*

J. M. Shull, C. W. Danforth, and E. M. Tilton. Tracing the cosmic metal evolution in the low-redshift intergalactic medium. ApJ*, 796(1), 2014. ISSN 15384357. doi: 10.1088/0004-637X/796/1/49.*

M. Sikora, M. Begelman, and M. Rees. Comptonization of diffuse ambient radiation by a relativistic jet: The source of gamma rays from blazars? ApJ*, 421:153, 1994.*

R. A. Simcoe. The carbon content of intergalactic gas at $z = 4.25$ and its evolution toward $z = 2.4$. ApJ*, 738(2), 2011. ISSN 15384357. doi: 10.1088/0004-637X/738/2/159.*

R. A. Simcoe, W. L. W. Sargent, and M. Rauch. The Distribution of Metallicity in the Intergalactic Medium at $z \sim 2.5$: O vi and C iv Absorption in the Spectra of Seven QSOs . ApJ*, 606(1):92–115, 2004. ISSN 0004-637X. doi: 10.1086/382777.*

R. A. Simcoe, M. Onoue, A.-C. Eilers, E. Banados, T. J. Cooper, G. Furesz, J. F. Hennawi, and B. Venemans. Interstellar and Circumgalactic Properties of an Unseen $z=6.84$ Galaxy: Abundances, Ionization, and Heating in the Earliest Known Quasar Absorber. https://arxiv.org/abs/2011.10582*, 2020. URL* `http://arxiv.org/abs/2011.10582`*.*

S. Simha, N. Tejos, J. X. Prochaska, K.-G. Lee, S. D. Ryder, S. Cantalupo, K. W. Bannister, S. Bhandari, and R. M. Shannon. Estimating the contribution of foreground halos to the FRB 180924 dispersion measure. https://arxiv.org/abs/2108.09881*, 2021. URL* `http://arxiv.org/abs/2108.09881`*.*

V. Springel, S. D. White, A. Jenkins, C. S. Frenk, N. Yoshida, L. Gao, J. Navarro, R. Thacker, D. Croton, J. Helly, J. A. Peacock, S. Cole, P. Thomas, H. Couchman, A. Evrard, J. Colberg, and F. Pearce. Simulations of the formation, evolution and clustering of galaxies and quasars. Nature*, 435(7042):629–636, 2005. ISSN 00280836. doi: 10.1038/nature03597.*

R. L. Starling, R. Willingale, N. R. Tanvir, A. E. Scott, K. Wiersema, P. T. O'Brien, A. J. Levan, and G. C. Stewart. X-ray absorption evolution in gamma-ray bursts: Intergalactic medium or evolutionary signature of their host galaxies. MNRAS*, 431(4):3159–3176, 2013. ISSN 00358711. doi: 10.1093/mnras/stt400.*

L. Strüder, U. Briel, K. Dennerl, R. Hartmann, E. Kendziorra, N. Meidinger, E. Pfeffermann, C. Reppin, B. Aschenbach, W. Bornemann, and H. Bräuninger. The European Photon Imaging Camera on XMM-Newton: The pn-CCD camera. A&A*, 365:L18, 2001.*

M. Tanga, P. Schady, A. Gatto, J. Greiner, M. G. H. Krause, R. Diehl, S. Savaglio, and S. Walch. Soft X-ray absorption excess in gamma-ray burst afterglow spectra : Absorption by turbulent ISM. A&A*, 595:A24, 2016.*

H. Tanimura, N. Aghanim, V. Bonjean, N. Malavasi, and M. Douspis. Density and temperature of cosmic-web filaments on scales of tens of megaparsecs, 2020a. ISSN 14320746.

H. Tanimura, N. Aghanim, A. Kolodzig, M. Douspis, and N. Malavasi. First detection of stacked X-ray emission from cosmic web filaments. A&A*, 643:1–7, 2020b. ISSN 14320746. doi: 10.1051/0004-6361/202038521.*

N. Tanvir, J. Grindlay, E. Berger, B. Metzger, S. Gezari, Z. Ivezic, J. Jencson, M. Kasliwal, A. Kutyrev, C. Macleod, G. Melnick, B. Purcell, G. Rieke, Y. Shen, and M. W. Vasey. GRBs as Probes of the Early Universe with TSO. arXiv preprint arXiv:1903.07835*, 2019a. URL `http://arxiv.org/abs/1903.07835`.*

N. R. Tanvir, J. P. Fynbo, A. De Ugarte Postigo, J. Japelj, K. Wiersema, D. Malesani, D. A. Perley, A. J. Levan, J. Selsing, S. B. Cenko, D. A. Kann, B. Milvang-Jensen, E. Berger, Z. Cano, R. Chornock, S. Covino, A. Cucchiara, V. D'Elia, A. Gargiulo, P. Goldoni, A. Gomboc, K. E. Heintz, J. Hjorth, L. Izzo, P. Jakobsson, L. Kaper, T. Krühler, T. Laskar, M. Myers, S. Piranomonte, G. Pugliese, A. Rossi, R. Sánchez-Ramírez, S. Schulze, M. Sparre, E. R. Stanway, G. Tagliaferri, C. C. Thöne, S. Vergani, P. M. Vreeswijk, R. A. Wijers, D. Watson, and D. Xu. The fraction of ionizing radiation from massive stars that escapes to the intergalactic medium. MNRAS*, 483(4):5380–5408, 2019b. ISSN 13652966. doi: 10.1093/mnras/sty3460.*

J. Tumlinson, C. Thom, J. K. Werk, J. X. Prochaska, T. M. Tripp, D. H. Weinberg, M. S. Peeples, J. M. O'Meara, B. D. Oppenheimer, J. D. Meiring, N. S. Katz, R. Davé, A. B. Ford, and K. R. Sembach. The large, oxygen-rich halos of star-forming galaxies are a major reservoir of galactic metals. Science, *334(6058): 948–952, 2011. ISSN 10959203. doi: 10.1126/science.1209840.*

J. Tumlinson, C. Thom, J. K. Werk, J. X. Prochaska, T. M. Tripp, N. Katz, R. Davé, B. D. Oppenheimer, J. D. Meiring, A. B. Ford, J. M. O'Meara, M. S. Peeples, K. R. Sembach, and D. H. Weinberg. THE COS-HALOS SURVEY: RATIONALE, DESIGN, AND A CENSUS OF CIRCUMGALACTIC NEUTRAL HYDROGEN. ApJ, *777(1):59, 2013. ISSN 15384357. doi: 10.1088/0004-637X/777/1/59.*

H. Umehata, M. Fumagalli, I. Smail, Y. Matsuda, A. M. Swinbank, S. Cantalupo, C. Sykes, R. J. Ivison, C. C. Steidel, A. E. Shapley, J. Vernet, T. Yamada, Y. Tamura, M. Kubo, K. Nakanishi, M. Kajisawa, B. Hatsukade, and K. Kohno. Gas filaments of the cosmic web located around active galaxies in a protocluster. Science, *366(6461):97–100, 2019. ISSN 10959203. doi: 10.1126/science.aaw5949.*

C. Urry and P. Padovani. Unified schemes for radio-loud active galactic nuclei. PASP, *107(715):803, 1995. ISSN 1098-6596.*

J. van Paradijs, P. J. Groot, T. Galama, C. Kouveliotou, R. G. Strom, J. Telting, R. G. Rutten, G. J. Fishman, C. A. Meegan, M. Pettini, N. Tanvir, J. Bloom, H. Pedersen, H. U. Nørdgaard-Nielsen, M. Linden-Vørnle, J. Melnick, G. Van Der Steene, M. Bremer, R. Naber, J. Heise, J. In't Zand, E. Costa, M. Feroci, L. Piro, F. Frontera, G. Zavattini, L. Nicastro, E. Palazzi, K. Bennet, L. Hanlon, and A. Parmar. Transient optical emission from the error box of the γ-ray burst of 28 february 1997. Nature, *386(6626):686–689, 1997. ISSN 00280836. doi: 10.1038/386686a0.*

B. Villasenor, B. Robertson, P. Madau, and E. Schneider. Inferring the Thermal History of the Intergalactic Medium from the Properties of the Hydrogen and Helium Lyman-alpha Forest. https://arxiv.org/abs/2111.00019, *2021. URL* `http://arxiv.org/abs/2111.00019`.

F. Vito, W. N. Brandt, F. E. Bauer, F. Calura, R. Gilli, B. Luo, O. Shemmer, C. Vignali, G. Zamorani, M. Brusa, F. Civano, A. Comastri, and R. Nanni. The X-ray properties of $z > 6$ *quasars: No evident evolution of accretion physics in the first Gyr of the Universe.* A&A, *630:1–16, 2019. ISSN 14320746. doi: 10.1051/0004-6361/201936217.*

S. Walsh, S. McBreen, A. Martin-Carrillo, T. Dauser, N. Wijers, J. Wilms, J. Schaye, and D. Barret. Detection capabilities of the Athena X-IFU for the warm-hot intergalactic medium using gamma-ray burst X-ray afterglows. A&A, *642(2019):A24, 2020. URL* `http://arxiv.org/abs/2007.10158`.

F. Wang, F. B. Davies, J. Yang, J. F. Hennawi, X. Fan, A. J. Barth, L. Jiang, X.-B. Wu, D. M. Mudd, E. Banados, F. Bian, R. Decarli, A.-C. Eilers, E. P. Farina, B. Venemans, F. Walter, and M. Yue. A Significantly Neutral Intergalactic Medium Around the Luminous z=7 Quasar J0252-0503. Harxiv.org/abs/2004.10877, *5, 2020. URL* `http://arxiv.org/abs/2004.10877`.

J. Wang. Evidence of contribution of intervening clouds to gamma-ray Burst's X-ray column density. ApJ, *776(2):96, 2013. ISSN 15384357. doi: 10.1088/0004-637X/776/2/96.*

D. Watson. The Galactic dust-to-metals ratio and metallicity using gamma-ray bursts. A&A, *533:16, 2011. ISSN 0004-6361. doi: 10.1051/0004-6361/201117120. URL* `http://adsabs.harvard.edu/abs/2011arXiv1107.6031W`.

D. Watson and P. Jakobsson. Dust extinction bias in the column density distribution of gamma-ray bursts: High column density, low-redshift GRBs are more heavily *obscured.* ApJ, *754(2):89, 2012. ISSN 15384357. doi: 10.1088/0004-637X/754/2/89.*

D. Watson, J. Hjorth, J. P. U. Fynbo, P. Jakobsson, S. Foley, J. Sollerman, and R. A. M. J. Wijers. Very Different X-Ray-to-Optical Column Density Ratios in \gray{} Burst Afterglows: Ionization in GRB Environments. ApJ, *660(2):L101–L104, 2007. ISSN 0004-637X. doi: 10.1086/518310. URL* `http://stacks.iop.org/1538-4357/660/i=2/a=L101{%}0Ahttp://adsabs.harvard.edu/abs/2007ApJ...660L.101W`.

D. Watson, T. Zafar, A. C. Andersen, J. P. Fynbo, J. Gorosabel, J. Hjorth, P. Jakobsson, T. Krühler, P. Laursen, G. Leloudas, and D. Malesani. Helium in natal H II regions: The origin of the X-ray absorption in gamma-ray burst afterglows. ApJ, *768(1):23, 2013. ISSN 15384357. doi: 10.1088/0004-637X/768/1/23.*

J. K. Werk, J. X. Prochaska, C. Thom, J. Tumlinson, T. M. Tripp, J. M. O'Meara, and M. S. Peeples. The cos-halos survey: An empirical description of metal-line absorption in the low-redshift circumgalactic medium. ApJ, *204(2):17, 2013. ISSN 00670049. doi: 10.1088/0067-0049/204/2/17.*

R. P. Wiersma, J. Schaye, and T. Theuns. The effect of variations in the input physics on the cosmic distribution of metals predicted by simulations. MNRAS, *415(1):353–371, 2011. ISSN 00358711. doi: 10.1111/j.1365-2966.2011.18709.x.*

B. J. Wilkes and M. Elvis. Quasar energy distributions. I - Soft X-ray spectra of quasars. ApJ, *323:243, 1987. ISSN 0004-637X. doi: 10.1086/165822.*

R. Willingale, R. L. Starling, A. P. Beardmore, N. R. Tanvir, and P. T. O'brien. Calibration of x-ray absorption in our galaxy. MNRAS, *431(1):394–404, 2013. ISSN 00358711. doi: 10.1093/mnras/stt175.*

J. Wilms, A. Allen, and R. McCray. On the Absorption of X-Rays in the Interstellar Medium. ApJ*, 542(2):914–924, 2000. ISSN 0004-637X. doi: 10.1086/317016.*

E. Wolf. Non-cosmological redshifts of spectral lines. Nature*, 326(26):363–365, 1987. ISSN 0028-0836. doi: 10.1038/326363a0.*

S. Woosley. Gamma-ray bursts from stellar mass accretion disks around black holes. ApJ*, 405:273, 1993.*

D. Worrall, P. Giommi, H. Tananbaum, and G. Zamorani. X-ray studies of quasars with the Einstein Observatory. IV-X-ray dependence on radio emission. ApJ*, 313:596, 1987. ISSN 1098-6596.*

C. B. Wotta, N. Lehner, J. C. Howk, J. M. O'Meara, B. D. Oppenheimer, and K. L. Cooksey. The COS CGM Compendium. II. Metallicities of the Partial and Lyman Limit Systems at $z \lesssim 1$ *.* ApJ*, 872(1):81, 2019. ISSN 1538-4357. doi: 10.3847/1538-4357/aafb74. URL* `http://dx.doi.org/10.3847/1538-4357/aafb74`*.*

J. S. B. Wyithe and A. Loeb. GRAVITATIONAL LENSING OF THE SLOAN DIGITAL SKY SURVEY HIGH-REDSHIFT QUASARS. ApJ*, 577:57–68, 2002.*

T. Yang, M. J. Hudson, and N. Afshordi. How dark are filaments in the cosmic web? MNRAS*, 498(3):3158–3170, 2020. ISSN 13652966. doi: 10.1093/mnras/staa2547.*

D. G. York, J. Adelman, J. E. Anderson, S. F. Anderson, J. Annis, N. A. Bahcall, J. A. Bakken, R. Barkhouser, S. Bastian, E. Berman, W. N. Boroski, S. Bracker, C. Briegel, J. W. Briggs, J. Brinkmann, R. Brunner, S. Burles, L. Carey, M. A. Carr, F. J. Castander, B. Chen, P. L. Colestock, A. J. Connolly, N. Csabai, P. C. Czarapata, J. E. Davis, M. Doi, T. O. M. Dombeck, D. Eisenstein, N. Ellman, B. R. Elms, M. L. Evans, X. Fan, G. R. Federwitz, L. Fiscelli, S. Friedman, J. A. Frieman, M. Fukugita, B. Gillespie, J. E. Gunn, V. K. Gurbani, E. D. E. Haas, *M. Haldeman, F. H. Harris, J. Hayes, T. M. Heckman, G. S. Hennessy, R. B. Hindsley, S. Holm, D. J. Holmgren, C.-h. Huang, C. Hull, D. O. N. Husby, S.-i. Ichikawa, T. Ichikawa, E. Ivezic, S. Kent, R. S. J. Kim, E. Kinney, M. Klaene, A. N. Kleinman, S. Kleinman, G. R. Knapp, J. Korienek, R. G. Kron, P. Z. Kunszt, D. Q. Lamb, B. Lee, R. F. Leger, S. Limmongkol, C. Lindenmeyer, D. C. Long, C. Loomis, J. O. N. Loveday, R. Lucinio, R. H. Lupton, B. Mackinnon, E. J. Mannery, P. M. Mantsch, B. Margon, P. Mcgehee, T. A. Mckay, A. Meiksin, A. Merelli, D. G. Monet, J. A. Munn, V. K. Narayanan, T. Nash, E. Neilsen, R. Neswold, H. J. O. Newberg, R. C. Nichol, T. O. M. Nicinski, M. Nonino, N. Okada, S. Okamura, J. P. Ostriker, R. Owen, A. G. Pauls, J. Peoples, R. L. Peterson, D. Petravick, J. R. Pier, A. Pope, R. Pordes, A. Prosapio, R. O. N. Rechenmacher, T. R. Quinn, G. T. Richards, M. W. Richmond, C. H. Rivetta, C. M. Rockosi, K. Ruthmansdorfer, D. Sandford, D. J. Schlegel, D. P. Schneider, M. Sekiguchi, G. Sergey, K. Shimasaku, W. A. Siegmund, S. Smee, J. A. Smith, S. Snedden, R. Stone, C. Stoughton, M. A. Strauss, C. Stubbs, M. Subbarao, A. S. Szalay, I. Szapudi, G. P. Szokoly, A. R. Thakar, C. Tremonti, D. L. Tucker, A. Uomoto, D. A. N. V. Berk, M. S. Vogeley, P. Waddell, S.-i. Wang, M. Watanabe, D. H. Weinberg, B. Yanny, and N. Yasuda. THE SLOAN DIGITAL SKY SURVEY: TECHNICAL SUMMARY.* AJ, *120(3):1579–1587, 2000.*

W. Yuan, A. C. Fabian, M. A. Worsley, and R. G. McMahon. X-ray spectral properties of high-redshift radio-loud quasars beyond redshift 4 - First results. MNRAS, *368(2):985–992, 2006. ISSN 00358711. doi: 10.1111/j.1365-2966.2006.10175.x.*

M. Yue, X. Fan, J. Yang, and F. Wang. Revisiting the Lensed Fraction of High-Redshift Quasars. https://arxiv.org/abs/2112.02821*, 2021. URL* `http://arxiv.org/abs/2112.02821`*.*

T. Zafar, D. Watson, P. Møller, J. Selsing, J. P. U. Fynbo, P. Schady, K. Wiersema, A. J. Levan, K. E. Heintz, A. De Ugarte Postigo, V. D 'elia, P. Jakobsson, J. Bolmer, J. Japelj, S. Covino, A. Gomboc, and Z. Cano. VLT/X-shooter

GRBs: Individual extinction curves of star-forming regions. MNRAS, *479(2): 1542, 2018. ISSN 13652966. doi: 10.1093/mnras/sty1380. URL* `https://arxiv.org/pdf/1805.07016.pdf`.

R. C. Zhang, B. Zhang, Y. Li, and D. R. Lorimer. On the energy and redshift distributions of fast radio bursts. https://arxiv.org/abs/2011.06151, *2020. URL* `http://arxiv.org/abs/2011.06151`.

Z. Zhang, A. C. Gupta, H. Gaur, P. J. Wiita, T. An, Y. Lu, S. Fan, and H. Xu. X-ray Intraday Variability of the TeV Blazar PKS 2155-304 with Suzaku During 2005-2014. ApJ, *902(2):103, 2021. URL* `http://arxiv.org/abs/2101.05977`.

Colophon

This thesis is based on a template developed by Matthew Townson and Andrew Reeves. It was typeset with LaTeX 2$_{\varepsilon}$. It was created using the *memoir* package, maintained by Lars Madsen, with the *madsen* chapter style. The font used is Latin Modern, derived from fonts designed by Donald E. Kunith.